

AD-A103 058

MISSISSIPPI UNIV UNIVERSITY
AN ANALYTICAL AND EXPERIMENTAL INVESTIGATION OF PLANAR DISCONTINUITIES--ETC(U)
MAR 81 M G HARRISON; C M BUTLER

F/O 20/3

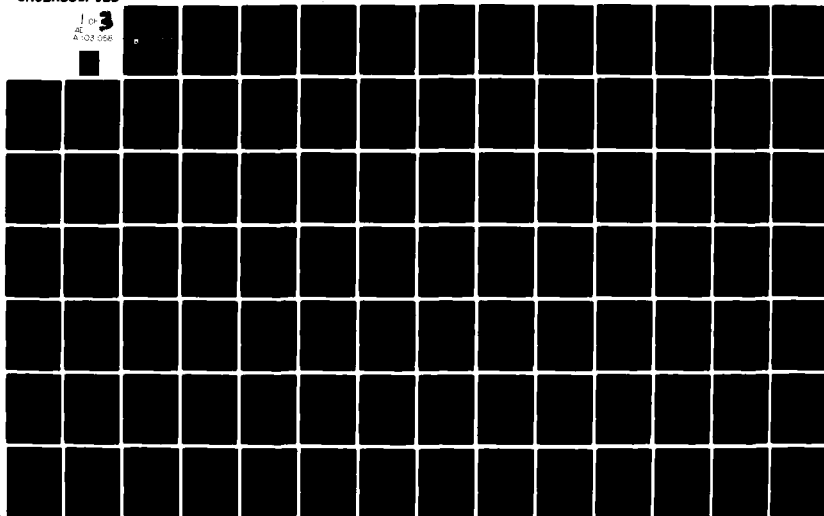
AFOSR-77-3464

UNCLASSIFIED

AFWL-TR-79-187

NL

1 of 3
AD-A103 058



① LEVEL II

AFWL-TR-79-187

AFWL-TR-
79-187

AD A103058



AN ANALYTICAL AND EXPERIMENTAL INVESTIGATION OF PLANAR DISCONTINUITIES IN COAXIAL WAVEGUIDES

Michael G. Harrison, PhD
Chalmers M. Butler, PhD

University of Mississippi
University, Mississippi 38677

March 1981

Final Report

DTIC
ELECTE
AUG 19 1981
S B D

Approved for public release; distribution unlimited.

AIR FORCE WEAPONS LABORATORY
Air Force Systems Command
Kirtland Air Force Base, NM 87117

81 8 18 078

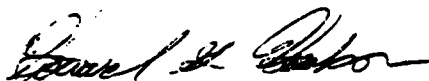
This final report was prepared by the University of Mississippi under Contract AFOSR Grant 77-3464, Job Order 37630128 with the Air Force Weapons Laboratory, Kirtland Air Force Base, New Mexico. Captain Howard G. Hudson (NTYEI) was the Laboratory Project Officer-in-Charge.

When US Government drawings, specifications, or other data are used for any purpose other than a definitely related Government procurement operation, the Government thereby incurs no responsibility nor any obligation whatsoever, and the fact that the Government may have formulated, furnished, or in any way supplied the said drawings, specifications, or other data, is not to be regarded by implication or otherwise, as in any manner licensing the holder or any other person or corporation, or conveying any rights or permission to manufacture, use, or sell any patented invention that may in any way be related thereto.

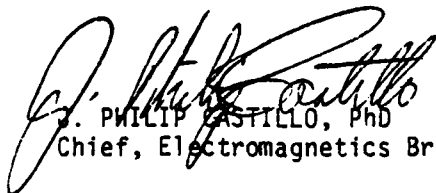
This report has been authored by a contractor of the United States Government. Accordingly, the United States Government retains a nonexclusive, royalty-free license to publish or reproduce the material contained herein, or allow others to do so, for the United States Government purposes.

This report has been reviewed by the Public Affairs Office and is releasable to the National Technical Information Service (NTIS). At NTIS, it will be available to the general public, including foreign nations.

This technical report has been reviewed and is approved for publication.




HOWARD G. HUDSON
Captain, USAF
Project Officer



P. PHILIP CASTILLO, PhD
Chief, Electromagnetics Branch

FOR THE COMMANDER



NORMAN K. BLOCKER
Colonel, USAF
Chief, Applied Physics Division

DO NOT RETURN THIS COPY. RETAIN OR DESTROY.

UNCLASSIFIED

SECURITY CLASSIFICATION OF THIS PAGE (When Data Entered)

19 REPORT DOCUMENTATION PAGE		READ INSTRUCTIONS BEFORE COMPLETING FORM
1. REPORT NUMBER AFWL TR-79-187	2. GOVT ACCESSION NO. AD-A103058	3. RECIPIENT'S CATALOG NUMBER
4. TITLE (and Subtitle) AN ANALYTICAL AND EXPERIMENTAL INVESTIGATION OF PLANAR DISCONTINUITIES IN COAXIAL WAVEGUIDES		5. TYPE OF REPORT & PERIOD COVERED Final Report
7. AUTHOR(s) Michael G. Harrison, PhD Chalmers M. Butler, PhD		6. PERFORMING ORG. REPORT NUMBER
9. PERFORMING ORGANIZATION NAME AND ADDRESS University of Mississippi University, Mississippi 38677		8. CONTRACT OR GRANT NUMBER(s) AFOSR Grant 77-3464
11. CONTROLLING OFFICE NAME AND ADDRESS Air Force Weapons Laboratory (NTYE) Kirtland Air Force Base, NM 87117		10. PROGRAM ELEMENT, PROJECT, TASK AREA & WORK UNIT NUMBERS 64711F/3763D128
14. MONITORING AGENCY NAME & ADDRESS (if different from Controlling Office)		12. REPORT DATE March 1981
15. SECURITY CLASS. (of this report) Unclassified		13. NUMBER OF PAGES 228
16. DISTRIBUTION STATEMENT (of this Report) Approved for public release; distribution unlimited.		15a. DECLASSIFICATION/DOWNGRADING SCHEDULE
17. DISTRIBUTION STATEMENT (of the abstract entered in Block 20, if different from Report)		
18. SUPPLEMENTARY NOTES		
19. KEY WORDS (Continue on reverse side if necessary and identify by block number) Electromagnetic Fields and Waves Microwave Networks Transmission Line Theory Coaxial Transmission Lines		
20. ABSTRACT (Continue on reverse side if necessary and identify by block number) An integral equation approach has been developed for treating a large class of planar discontinuities in coaxial waveguides. The technique can effectively treat single and multiple discontinuities with no constraints on frequency or relative location. The integral equations are formulated with the transverse component of electric field in the aperture of each discontinuity as the unknown quantity. A numerical solution procedure is described which allows a choice of both the number of subsectional expansion pulses employed in each aperture and		

DD FORM 1 JAN 73 1473

UNCLASSIFIED

SECURITY CLASSIFICATION OF THIS PAGE (When Data Entered)

134450

UNCLASSIFIED

SECURITY CLASSIFICATION OF THIS PAGE(When Data Entered)

Block No. 20 (Continued)

the number of terms evaluated in the modified higher-order-mode series. Once a solution for the electric field in each aperture is obtained, straightforward procedures may be used to compute the admittance of any discontinuity or the field anywhere in the waveguide.

Two sets of coaxial waveguide/cavity structures have been constructed and an extensive program of experimental measurements of cavity admittance and field components at cavity walls has been pursued. The measured results have been compared to integral equation calculations of the same quantities to verify the accuracy of the approach.

The integral equation approach has demonstrated a capability for extreme accuracy when sufficient expansion pulses and series terms are used and offers the opportunity for computing the transient response of waveguide discontinuities by means of a transform technique.

Accession For	
NTIS GRA&I	<input checked="checked" type="checkbox"/>
DTIC TAB	<input type="checkbox"/>
Unannounced	<input type="checkbox"/>
Justification	
By	
Distribution/	
Availability Codes	
Avail and/or	
Dist	Special
A	

UNCLASSIFIED

SECURITY CLASSIFICATION OF THIS PAGE(When Data Entered)

TABLE OF CONTENTS

Chapter	Page
I. INTRODUCTION	1
II. ROTATIONALL SYMMETRIC JUNCTION OF TWO DISSIMILAR COAXIAL WAVEGUIDES	10
A. Introduction	10
B. Derivation of Expressions for Field Components	12
C. Field Expressions for Two Dissimilar Coaxial Regions	18
D. Evaluation of Constants in the $z < s$ Region	20
E. Evaluation of Constants in the $z > s$ Region	25
F. Enforce Continuity of Transverse Field in the Aperture	26
G. Application to Simpler Geometries	27
H. Integral Equation for a One-Port Cavity . .	32
I. Microwave Circuit Concepts	36
III. NUMERICAL SOLUTION TECHNIQUE	40
A. Introduction	40
B. Selection of Basis and Testing Functions . .	40
C. Numerical Results for Single Discontinuities	45
IV. INTEGRAL EQUATION FOR A TWO-PORT COAXIAL CAVITY	63

Chapter	Page
A. Introduction	63
B. Expressions for Field Components	63
C. Evaluation of Constants in Field Expressions	66
D. Enforcing Continuity of Transverse Fields in the Apertures	69
V. INTEGRAL EQUATIONS FOR PARTITIONED CAVITIES	76
A. Introduction	76
B. Field Components for a Partitioned, One-Port Cavity	76
C. Integral Equations for the Aperture Fields .	79
D. Field Components for a Partitioned, Two-Port Cavity	82
E. Integral Equations for the Aperture Fields .	86
VI. INTEGRAL EQUATION FOR A TRUNCATED COAXIAL INNER CONDUCTOR	93
A. Introduction	93
B. Expressions for Field Components	94
C. Definitions of Constants in Field Expressions	97
D. Enforce Continuity of Transverse Fields in the Aperture	99
E. Application to a One-Port Cavity	100
F. Numerical Solution Considerations	103
G. Susceptance of a Truncated Center Conductor	104
VII. ADMITTANCE MEASUREMENTS FOR TWO-PORT, COAXIAL CAVITIES	110
A. Introduction	110

Chapter	Page
B. Measurement Procedure and Cavity Configuration	110
C. Presentation of Results	113
VIII. INTERNAL FIELD MEASUREMENTS IN COAXIAL CAVITIES	128
A. Introduction	128
B. Procedures for Measurements Inside Cavity End Plates	129
C. Field Interior to Simple One-Port Cavity . .	133
D. Field Interior to Simple Two-Port Cavity . .	134
E. Field Interior to Partitioned, One-Port Cavity	135
F. Field Interior to Partitioned, Two-Port Cavity	135
G. Measurements Along Center Conductor of One-Port Cavity	136
H. Evaluation of Measured and Calculated Results	136
IX. CONCLUSIONS	159
APPENDIX A. COMPLETENESS OF FIELD DERIVED FROM A MAGNETIC VECTOR POTENTIAL FOR A ROTATIONALLY SYMMETRIC WAVEGUIDE	164
APPENDIX B. PROCEDURE TO IMPROVE CONVERGENCE RATE OF BESSEL FUNCTION SERIES	167
APPENDIX C. ASYMPTOTIC FORMS FOR EIGENFUNCTION EXPANSIONS OF FIELD COMPONENTS IN COAXIAL AND CIRCULAR WAVEGUIDES	169
APPENDIX D. PROPERTIES OF SOLUTIONS TO BESSEL'S EQUATION	185
APPENDIX E. DETAILS OF COAXIAL CAVITY CONSTRUCTION . .	196

Chapter	Page
APPENDIX F. DESCRIPTIONS OF ELECTRIC AND MAGNETIC FIELD PROBES	207
BIBLIOGRAPHY	214

LIST OF FIGURES

Figure	Page
1. Examples of Cavities Formed by placing Planar Discontinuities in Coaxial Waveguides	9
2. Cross-Sectional View of a Generalized Planar Discontinuity in a Coaxial Waveguide	11
3a Annular Disk Attached to the Outer Conductor of a Coaxial Waveguide	30
3b Annular Disk Attached to the Inner Conductor of a Coaxial Waveguide	30
4a Step Discontinuity in the Outer Conductor of a Coaxial Waveguide	31
4b Step Discontinuity in the Inner Conductor of a Coaxial Waveguide	31
5. One-Port Cavity Formed from a Coaxial Waveguide with a Step Discontinuity in the Outer Radius .	33
6. Junction of Two Transmission Lines of Different Characteristic Impedance with a Lumped Susceptance at the Junction	37
7. Illustration of Numerical Solution Technique Expansion and Testing Functions	42
8. Calculated Distributions of Aperture Electric Field for Annular Disk on Outer Conductor . . .	52
9. Calculated Distributions of Aperture Electric Field for Annular Disk on Inner Conductor . . .	52
10. Calculated Distributions of Aperture Electric Field for Step in Outer Radius	53
11. Calculated Distributions of Aperture Electric Field for Step in Inner Radius	53

Figure	Page
12. Calculated Distributions of Aperture Electric Field for a One-Port, Coaxial Cavity	54
13. Calculated Distributions of Aperture Electric Field as the Number of Expansion Pulses is Varied	54
14. Two-Port, Coaxial Cavity Formed from Two Step Discontinuities in the Outer Conductor of a Coaxial Waveguide	64
15. Calculated Distributions of Aperture Electric Field for Both Apertures of a Two-Port Cavity	74
16. Calculated Distributions of Aperture Electric Field for Both Apertures of a Two-Port Cavity	74
17. Partitioned, One-Port, Coaxial Cavity	77
18. Calculated Distributions of Aperture Electric Field for the Apertures of a One-Port Partitioned Cavity	83
19. Calculated Distributions of Aperture Electric Field for the Apertures of a One-Port Partitioned Cavity	83
20. Partitioned, Two-Port, Coaxial Cavity	85
21. Calculated Distributions of Aperture Electric Field for the Apertures of a Two-Port Partitioned Cavity	91
22. Calculated Distributions of Aperture Electric Field for the Apertures of a Two-Port Partitioned Cavity	91
23. Discontinuity Formed in Coaxial Waveguide by Truncating Center Conductor	95
24. One-Port, Coaxial Cavity with the Coaxial Center Conductor Truncated	101
25. Calculated Distributions of Aperture Electric Field for Truncated Inner Conductor	108
26. Calculated Distributions of Aperture Electric Field for the Apertures of a Coaxial-to-Circular Cavity	108

Figure	Page
27. Schematic Representation of Instrumentation for Admittance Measurements for Two-Port Coaxial Cavity	111
28. Measured and Calculated Admittance for a Two-Port Coaxial Cavity	117
29. Measured and Calculated Admittance for a Two-Port Coaxial Cavity with Partition - Small Aperture	118
30. Measured and Calculated Admittance for a Two-Port Coaxial Cavity with Partition - Large Aperture	119
31. Measured and Calculated Admittance for a Two-Port Coaxial Cavity - With <u>Waveguide Handbook</u> Results	120
32. Measured and Calculated Admittance for a Two-Port Coaxial Cavity - Small Aperture - With <u>Waveguide Handbook</u> Results	121
33. Measured and Calculated Admittance for a Two-Port Coaxial Cavity - Large Aperture - With <u>Waveguide Handbook</u> Results	122
34. Measured and Calculated Admittance for a Two-Port Coaxial Cavity of Same Length as Partitioned Cavities	123
35. Measured and Calculated Admittance for a Two-Port Coaxial Cavity with Partition - Both Apertures	124
36. Schematic Diagram of Instrumentation for Interior Field Measurements	132
37. Measured and Calculated Z Component of Electric Field 900 MHz	138
38. Measured and Calculated Z Component of Electric Field 800 MHz	138
39. Measured and Calculated ϕ Component of Magnetic Field 800 MHz	139
40. Measured and Calculated ϕ Component of Magnetic Field 900 MHz	139

Figure		Page
41.	Measured and Calculated Z Component of Electric Field 1500 MHz	140
42.	Measured and Calculated Z Component of Electric Field 700 MHz	140
43.	Measured and Calculated ϕ Component of Magnetic Field 1400 MHz	141
44.	Measured and Calculated ϕ Component of Magnetic Field 1600 MHz	141
45.	Measured and Calculated Z Component of Electric Field 1700 MHz	142
46.	Measured and Calculated Z Component of Electric Field 900 MHz	142
47.	Measured and Calculated Z Component of Electric Field 2000 MHz	143
48.	Measured and Calculated Z Component of Electric Field 900 MHz	143
49.	Measured and Calculated ϕ Component of Magnetic Field 1300 MHz	144
50.	Measured and Calculated ϕ Component of Magnetic Field 900 MHz	144
51.	Measured and Calculated ϕ Component of Magnetic Field 800 MHz	145
52.	Measured and Calculated ϕ Component of Magnetic Field 600 MHz	145
53.	Measured and Calculated Z Component of Electric Field 1400 MHz	146
54.	Measured and Calculated Z Component of Electric Field 1700 MHz	146
55.	Measured and Calculated Z Component of Electric Field 1000 MHz	147
56.	Measured and Calculated Z Component of Electric Field 1800 MHz	147

Figure	Page
57. Measured and Calculated Z Component of Electric Field 1200 MHz	148
58. Measured and Calculated Z Component of Electric Field 1300 MHz	148
59. Measured and Calculated Z Component of Electric Field 1200 MHz	149
60. Measured and Calculated Z Component of Electric Field 1700 MHz	149
61. Measured and Calculated ϕ Component of Magnetic Field 1100 MHz	150
62. Measured and Calculated ϕ Component of Magnetic Field 1400 MHz	150
63. Measured and Calculated ϕ Component of Magnetic Field 900 MHz	151
64. Measured and Calculated ϕ Component of Magnetic Field 1400 MHz	151
65. Measured and Calculated ϕ Component of Magnetic Field 1300 MHz	152
66. Measured and Calculated ϕ Component of Magnetic Field 1400 MHz	152
67. Measured and Calculated ϕ Component of Magnetic Field 1300 MHz	153
68. Measured and Calculated ϕ Component of Magnetic Field 1400 MHz	153
69. Measured and Calculated ϕ Component of Electric Field 1200 MHz	154
70. Measured and Calculated ρ Component of Electric Field 900 MHz	154
71. Measured and Calculated ρ Component of Electric Field 1100 MHz	155
72. Measured and Calculated ρ Component of Electric Field 800 MHz	155

Figure	Page
73. Measured and Calculated ρ Component of Electric Field 1200 MHz	156
74. Measured and Calculated ϕ Component of Magnetic Field 1200 MHz	156
75. Measured and Calculated ϕ Component of Magnetic Field 900 MHz	157
76. Measured and Calculated ϕ Component of Magnetic Field 1100 MHz	157
77. Measured and Calculated ϕ Component Of Magnetic Field 800 MHz	158
78. Measured and Calculated ϕ Component of Magnetic Field 1200 MHz	158
E-1. Illustration of Components of Smaller Cavity Set	198
E-2. Photographs of Small and Large Coaxial Cavity Sets	203
E-3. Illustration of Components of Larger Cavity Set .	204
F-1a Orthogonal Views of Electric Field Probe for End Plates	209
F-1b Orthogonal Views of Magnetic Field Probe for End Plates	209
F-2. Photographs of Electric and Magnetic Field Probes	211
F-3a Orthogonal Views of Electric Field Probe for Coaxial Center Conductor	212
F-3b Orthogonal Views of Magnetic Field Probe for Coaxial Center Conductor	212

LIST OF TABLES

Table	Page
1. Calculated Susceptance of an Annular Disk Attached to the Outer Conductor of a Coaxial Waveguide (Normalized)	55
2. Calculated Susceptance of an Annular Disk Attached to the Inner Conductor of a Coaxial Waveguide (Normalized)	56
3. Calculated Susceptance of a Step in the Outer Radius of a Coaxial Waveguide (Normalized by the Left-Hand Waveguide)	57
4. Calculated Susceptance of a Step in the Inner Radius of a Coaxial Waveguide (Normalized by the Left-Hand Waveguide)	58
5. Calculated Susceptance of a One-Port, Coaxial Cavity (Normalized by the Input Waveguide) . . .	59
6. Calculated Susceptance of an Annular Disk on the Outer Conductor of a Coaxial Waveguide as the Number of Expansion Pulses in the Aperture is Varied (Normalized)	60
7. Calculated Susceptance of an Annular Disk Attached to the Outer Conductor of a Coaxial Waveguide as the Number of Terms in the Higher- Order Mode Series is Varied (Normalized) Aperture Field Expanded in 20 Pulses	61
8. Calculated Susceptance of an Annular Disk Attached to the Outer Conductor of a Coaxial Waveguide as the Number of Terms in the Higher- Order Mode Series is Varied (Normalized) Aperture Field Expanded in 50 Pulses	61
9. Comparisons of Calculated Capacitance of Coaxial Step Discontinuities with Results of A. Jurkus .	62

Table	Page
10. Calculated Admittance of a Two-Port, Coaxial Cavity (Normalized by the Input Waveguide) . . .	75
11. Calculated Admittance of a Partitioned, One-Port, Coaxial Cavity (Normalized by the Input Waveguide)	84
12. Calculated Admittance of a Partitioned, Two-Port, Coaxial Cavity (Normalized by the Input Waveguide)	92
13. Calculated Admittance of Coaxial-to-Circular Waveguide Junctions (Normalized by the Coaxial Waveguide)	107
14. Comparisons of Calculated and Measured Capacitance for a Coaxial-to-Circular Waveguide Junction . .	109
15. Calculated and Measured Admittance of a Two-Port, Coaxial Cavity	125
16. Calculated and Measured Admittance of a Partitioned, Two-Port Cavity - Small Aperture .	126
17. Calculated and Measured Admittance of a Partitioned, Two-Port Cavity - Large Aperture .	127

CHAPTER I

INTRODUCTION

Enclosed waveguiding structures have long been of great importance in the transmission of high-frequency electromagnetic energy. The electromagnetic properties of uniform, axial waveguides are generally well understood, but practical applications introduce discontinuities and transition regions into waveguides which often significantly affect their response. In the particular case of discontinuities which are limited to the plane transverse to the direction of propagation, an impedance mismatch and a region of reactive energy storage are normally introduced into the waveguide. Such effects are usually undesirable, but properly designed discontinuities can provide very desirable impedance-matching devices and resonating cavities.

Analyses of planar waveguide discontinuities quickly followed the beginning of efforts to develop useful radio-frequency and microwave devices utilizing waveguiding structures. Low-frequency techniques such as field mapping yielded useful results for transverse electromagnetic (TEM) mode propagation in coaxial and parallel-plate waveguides. The effective

treatment of discontinuities when higher-order modes exist in coaxial lines and for waveguides supporting transverse electric (TE) and transverse magnetic (TM) modes was much more difficult. A discontinuity requires the local contributions of an infinite set of modes to satisfy the electromagnetic boundary conditions. Mathematical complexity prevented early analytical treatments from considering more than one or two of the higher-order modes. The most accurate of the early treatments was based upon variational solutions to susceptance expressions which had been developed from integral equations. Very useful expressions for the susceptances of a large variety of waveguide discontinuities were derived by Julian Schwinger and a capable group of associates in the 1940s. Many of the results of this work were compiled by Nathan Marcuvitz into the well-known Waveguide Handbook, Ref.[1]. This work is of such quality that even today it remains the treatment of choice for most applications. Very good descriptions of the techniques employed to derive these expressions have been presented in books by Schwinger and Saxon, Ref.[2], Collin, Ref.[3], and Lewin, Refs.[4], [5], and [6]. The earliest published work on discontinuities in coaxial waveguides was by J. R. Whinnery and H. W. Jamieson, Ref.[7], and Whinnery, Jamieson, and Robbins, Ref.[8]. These investigators used an approach suggested by W. C. Hahn in 1941 which involved com-

putation of the terms of a Fourier expansion of the field in the discontinuity to calculate the capacitance of coaxial discontinuities. Computation of the terms of the series was sufficiently difficult that Whinnery, et al., used only the first four higher-order modes to obtain results that were later shown to be accurate to within five per cent.

The variational technique employed by the above authors is included in the collection of mathematical solution procedures which R. F. Harrington has identified in his Field Computation by Moment Methods, Ref.[9]. This variational approach is identical to a one-term Galerkin's solution, Ref.[9], where the assumed value of the unknown field distribution in the discontinuity serves as both the basis and testing function. As indicated earlier, this approach is very effective for dominant mode operation of waveguides when frequencies are low enough to prevent propagation of higher-order modes. Under this frequency constraint, susceptance results obtained from both analyses and experimental measurements during the course of this investigation have shown remarkable agreement with values calculated from expressions in the Waveguide Handbook. These latter calculations benefit from the characteristic of such variational solutions in that a first-order change in the assumed field distribution in the discontinuity produces only a second-order variation in the calculated susceptance. The field in the vicinity of the dis-

continuity can be calculated from the same assumed field distribution, but the field expressions are not variational and thus, do not share the property whereby a first-order error in the assumed field distribution produces a second-order error in the calculated result.

The treatments of waveguide discontinuity problems which employed variational techniques required a liberal amount of ingenuity because such problems yielded solutions very grudgingly. The increasing capability of the digital computer opened new avenues of approach and investigators began to develop techniques which took advantage of this tool. P. I. Somlo used the computer to calculate more terms in the Hahn series approach used by Whinnery, et al., Refs.[10] and [11]. D. Woods, Ref.[12], used interpolation on Somlo's results to obtain a further improvement in accuracy and A. Jurkus provided improvements to Somlo's code, Ref.[13]. E. W. Risley, Refs.[14] and [15], adapted the Rayleigh-Ritz procedure used by Schwinger, et al., to solution by a computer and obtained both upper- and lower-bound solutions for the capacitance of the coaxial-to-circular waveguide junction.

A number of more recent investigations has employed least-squares techniques to minimize the error in satisfying boundary-conditions at the discontinuities. The error results from the fact that only a finite number of higher-order modes is used in the field expansions at the discontinuities.

Investigations using such methods have been reported by J. B. Davies, Ref.[16], Davies and M. Razaz, Ref.[17], H. Oraizi and J. Perini, Ref.[18], R. Jansen, Ref.[19], and H. J. A. LaRiviere and Davies, Ref.[20]. The results reported in Refs. [16] - [20] are largely for general waveguide discontinuities with occasional specialization of the technique to coaxial waveguides as in Ref.[17].

All of the investigations mentioned thus far were directed toward the computation of discontinuity capacitance and some have obtained very good levels of accuracy. Razaz and Davies claim an error of ± 0.1 femtofarads in their calculations for the capacitance of a coaxial-to-circular waveguide junction, Ref.[21]. None of these approaches is suitable for treating situations where higher-order modes may propagate. Alvin Wexler, Ref.[22], has developed a modal analysis technique for treating waveguide discontinuities which involves selecting the amplitudes of normal modes so as to satisfy boundary conditions at the discontinuity. The method is elegantly developed and allows the treatment of as many modes as desired. It has the computational disadvantage of requiring the solution of a set of $N+1$ linear equations to treat N modes. The method can also treat coupled discontinuities, however, each discontinuity must be treated individually and the procedure must begin with the discontinuity most distant from the excitation.

All the solution techniques mentioned thus far begin with the same expressions for the field in the waveguide. It is the approach to approximating or obtaining solutions for the transverse field in the apertures of the discontinuities that provides the differences among the methods. The primary objective of this investigation is the development and validation of a frequency-independent capability of calculating the electromagnetic properties of coaxial waveguide discontinuities which is both computationally efficient and accurate. Such a method necessarily includes the treatment of higher-order modes, but it is done in such a way that it allows for general excitation of the waveguides. The method presented possesses a significant advantage over earlier approaches in that a series-convergence technique is employed which allows the recovery of essentially all the higher-order mode contributions at a given discontinuity even though a finite number of series terms is computed. The accuracy of the method can be controlled (within computational errors) by the number of basis expansion pulses and higher-order mode terms considered in the solution. A very useful aspect of this approach is the capability of combining two or more discontinuities into simple or complex, one- or two-port cavities as illustrated in Figure 1.

The formation and analytical treatment of simple and partitioned cavities are considered extensively in the body

of this report. Also presented are the results of a substantial experimental program designed to provide validation for the analysis. Two sets of coaxial cavities with differing dimensions were constructed and the internal field was measured for one- and two-port cavities of simple and partitioned configurations. The input admittance of the two-port cavity was measured. Extensive comparisons of measured data with analytical results are presented which, in conjunction with a discussion of possible experimental error, lead to quantitative evaluations of the accuracy and usefulness of the analytical approach.

Analytic formulations for the field or electromagnetic potentials within a cavity frequently include expressions that contain three infinite series. For coaxial cavities considered in this effort, the original excitation is always assumed to consist of TEM or TM_{0n} modes only. This constraint eliminates any variation in the azimuthal coordinate and simplifies the appropriate expressions to two infinite series. It is mathematically (and computationally) expedient to treat these cavities from a waveguide, i.e., traveling wave, point of view and to consider the front and rear boundaries of the cavities as planar waveguide discontinuities. The axial and radial eigenvalues in this approach are related in such a manner that the formulation requires only one infinite series for a complete set of eigenfunctions. The derivation of the

magnetic vector potential and the resulting field expressions is presented in Chapter II.

If the waveguide approach is used, it is very effective to think of the traveling waves as penetrating apertures in the discontinuities. This concept allows utilization of existing techniques for calculating aperture penetration, in particular, treating the aperture field as the unknown quantity of interest since it is common to the adjoining regions. All formulations in this report treat the transverse electric field in the aperture as the unknown quantity. It is the objective, therefore, to obtain solutions for the aperture field for each discontinuity or partition used to form a cavity structure. When this approach is used, it is imperative to recognize any singular behavior of the aperture field and then to develop a numerical solution technique accordingly. In the following chapters integral equations are developed for progressively more complex configurations of discontinuities and details are given for appropriate numerical solution techniques. The results of the complementary experimental measurements program serve to corroborate the analytical results.

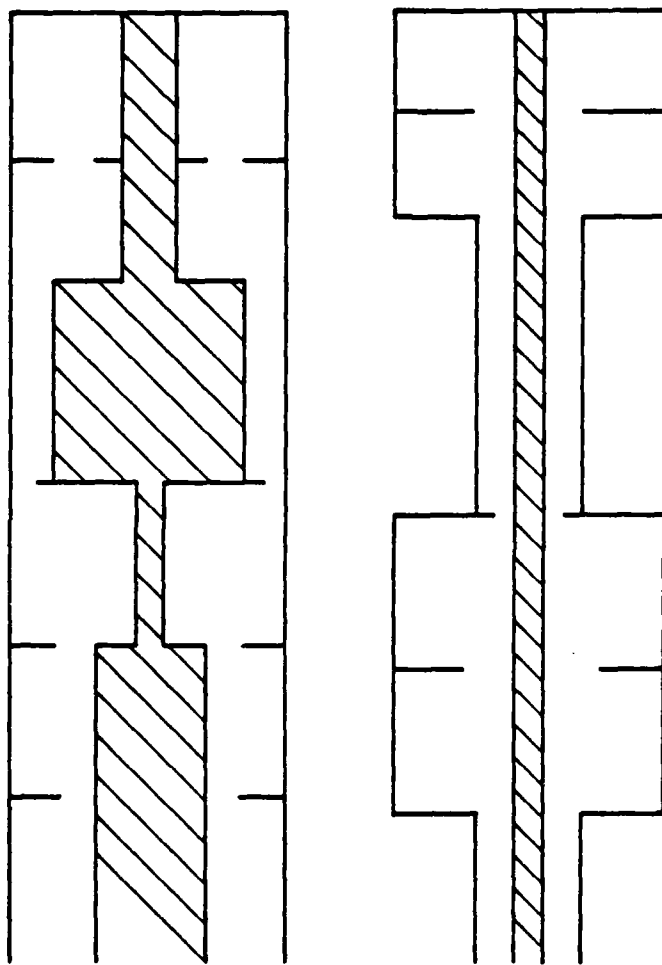


Figure 1. Examples of Cavities Formed by Placing Planar Discontinuities in Coaxial Waveguides

CHAPTER II

ROTATIONALLY SYMMETRIC JUNCTION OF TWO DISSIMILAR COAXIAL WAVEGUIDES

A. Introduction

The effects on the propagating modes produced by a discontinuity in a coaxial waveguide are a function of the resulting field distribution in the vicinity of the discontinuity. The local field distribution is a modification of the propagating modes and, in general, an infinite number of higher-order modes is required to satisfy boundary conditions at such a discontinuity. For a discontinuity confined to a two-dimensional plane, a knowledge of the field in this "aperture plane" is sufficient for determining the field everywhere. From the knowledge of the aperture field, the resulting effects on any propagating modes can be determined and, if desired, microwave circuit representations of the discontinuity can be derived. In this chapter, an integral equation is formulated for the aperture electric field of the generalized geometry depicted in Figure 2. This integral equation is then specialized to the simpler geometries of Figures 3 and 4 and is subsequently applied to a one-port

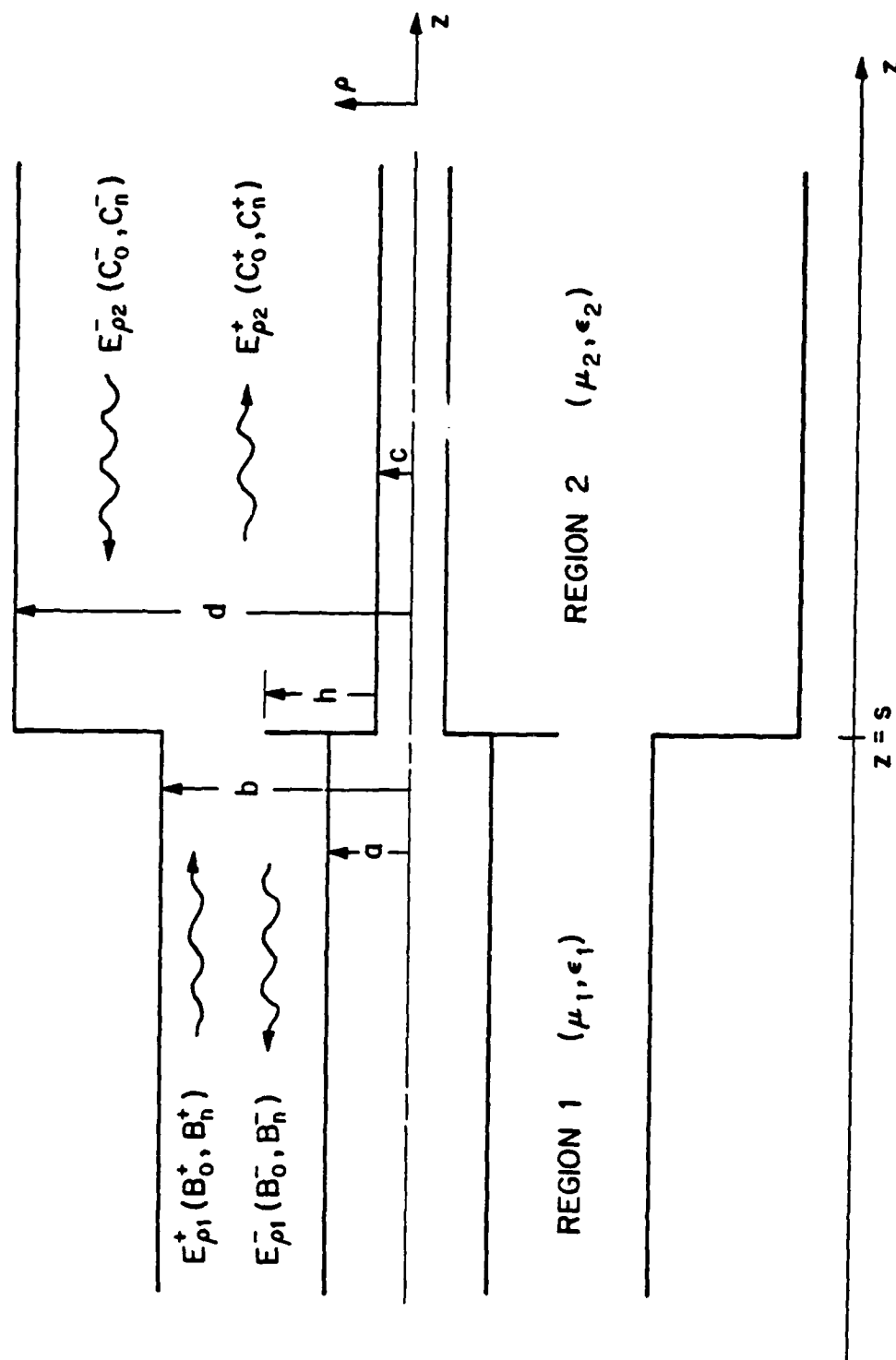


Figure 2. Cross-Sectional View of a Generalized Planar Discontinuity in a Coaxial Waveguide

coaxial cavity.

B. Derivation of Expressions for Field Components

An integral equation suitable for numerical solution is obtained by developing expressions for each of the field components in the regions either side of the discontinuity and then enforcing continuity of the transverse field components across the aperture in the discontinuity. These expressions are derived from the appropriate operations on a vector potential of the magnetic and/or electric type. The geometry under consideration is azimuthally symmetric and, with the assumption of similar symmetry of the excitation, all magnetic field components are transverse to the axial coordinate and, therefore, the magnetic vector potential suffices for the complete description of the field. This potential is the solution to the vector wave equation

$$(\nabla^2 + k^2) \vec{A} = \vec{0}, \quad (1)$$

subject to the appropriate boundary conditions and where k is the wave number of the medium. A coaxial geometry with azimuthally-symmetric excitation has only axially-directed currents and, therefore, only the axial component of the magnetic vector potential is necessary to derive the complete field. The geometries treated in this investigation have many surfaces that support ρ -directed currents; however, it is shown in

Appendix A that, for azimuthally-symmetric excitation, the field derived from the z-directed vector potential is still complete. The vector potential equation is reduced to the scalar equation

$$(\nabla^2 + k^2) A_z(\rho, \phi, z) = 0.$$

Since the axial component of vector potential is independent of ϕ , A_z may be represented by

$$A_z(\rho, z) = R(\rho)Z(z).$$

The axial function $Z(z)$ satisfies the harmonic equation

$$\frac{d^2 Z}{dz^2} + k_z^2 = 0 \quad (2)$$

which has the solution

$$Z(z) = A e^{-jk_z z} + B e^{jk_z z}$$

where A and B are arbitrary constants. The radial function $R(\rho)$ is a solution of

$$\rho^2 \frac{d^2 R}{d\rho^2} + \rho \frac{dR}{d\rho} + k_\rho^2 \rho^2 R = 0. \quad (3)$$

The parameters k_z and k_ρ are related by

$$k_z^2 = k^2 - k_\rho^2. \quad (4)$$

Equation (3) is a zero-order Bessel's equation with the solution

$$R(\rho) = C J_0(k_\rho \rho) + D N_0(k_\rho \rho)$$

where J_0 is the zero-order Bessel function of the first kind, N_0 is the zero-order Neumann function and C and D are arbitrary constants. Enforcement of the boundary condition that the tangential (or z) component of electric field be zero at the surface of the inner conductor yields the function

$$R(\rho) = E [N_0(k_\rho a)J_0(k_\rho \rho) - J_0(k_\rho a)N_0(k_\rho \rho)]$$

where a is the radius of the inner conductor and E is an arbitrary constant. The second boundary condition requires the z component of the electric field to be zero at the surface of the outer conductor and results in the expression

$$R(\rho) = \phi_n(\rho) = N_0(\gamma_n a)J_0(\gamma_n \rho) - J_0(\gamma_n a)N_0(\gamma_n \rho) \quad (5)$$

where the γ_n are the infinite set of k_ρ which satisfy

$$\phi_n(b) = N_0(\gamma_n a)J_0(\gamma_n b) - J_0(\gamma_n a)N_0(\gamma_n b) = 0, \quad n=1,2,\dots \quad (6)$$

where b is the radius of the outer conductor. The new representation for k_z is α_n where

$$\alpha_n^2 = k^2 - \gamma_n^2. \quad (7)$$

For the special case $k_0 = 0$, the solution to Eq.(3) is

$$R(\rho) = B' \ln \rho + C'$$

where the constant C' can be discarded. In this case, $k_z = k$ which yields the special case

$$A_z^{\text{TEM}}(\rho, z) = b^+ \ln \rho e^{-jkz} + b^- \ln \rho e^{jkz} \quad (8)$$

where, as indicated, A_z^{TEM} is the vector potential for the TEM mode. The complete expression for the vector potential is given by

$$A_z(\rho, z) = b_0^+ \ln \rho e^{-jkz} + b_0^- \ln \rho e^{jkz} + \sum_{n=1}^{\infty} (b_n^+ e^{-j\alpha_n z} + b_n^- e^{j\alpha_n z}) \phi_n(\rho) \quad (9)$$

The wave number α_n for the higher-order modes may be either real or imaginary depending on the relative magnitudes of k and γ_n . For the former condition, the mode would propagate and, for the latter, it would be cutoff. Proper root selection is required for each case to assure conservation of energy. The following selections are made

$$\alpha_n = \sqrt{k^2 - \gamma_n^2}, \quad k^2 > \gamma_n^2 \quad (10a)$$

$$\alpha_n = -j \sqrt{\gamma_n^2 - k^2}, \quad \gamma_n^2 > k^2 \quad (10b)$$

In Eqs.(10a&b), k is assumed to be a real number.

The electric field is calculated from the expression

$$\vec{E} = -j \frac{\omega}{k^2} [k^2 2A_z + \nabla \nabla \cdot (2A_z)] .$$

The radial component of the electric field is given by

$$\begin{aligned} E_\rho &= -j \frac{\omega}{k^2} \frac{\partial^2 A_z}{\partial \rho \partial z} , \\ E_\rho &= - \frac{\omega}{k} b_0^+ \frac{e^{-jkz}}{\rho} + \frac{\omega}{k} b_0^- \frac{e^{jkz}}{\rho} \\ &\quad + \frac{\omega}{k^2} \sum_{n=1}^{\infty} \alpha_n (-b_n^+ e^{-j\alpha_n z} + b_n^- e^{j\alpha_n z}) \frac{d\phi_n(\rho)}{d\rho} . \end{aligned} \quad (11)$$

The axial component of the electric field is given by

$$\begin{aligned} E_z &= -j \frac{\omega}{k^2} \left(k^2 + \frac{\partial^2}{\partial z^2} \right) A_z , \\ E_z &= -j \frac{\omega}{k^2} \sum_{n=1}^{\infty} (k^2 - \alpha_n^2) (b_n^+ e^{-j\alpha_n z} + b_n^- e^{j\alpha_n z}) \phi_n(\rho) . \end{aligned} \quad (12)$$

The magnetic field is calculated from

$$\vec{H} = \frac{1}{\mu} \nabla \times (2A_z)$$

where μ is the permeability of the dielectric medium. The azimuthal component of magnetic field is given by

$$H_\phi = - \frac{1}{\mu} \frac{\partial A_z}{\partial \rho} ,$$

$$\begin{aligned}
H_{\phi} = & -\frac{1}{\mu} b_0^+ \frac{e^{-jkz}}{\rho} - \frac{1}{\mu} b_0^- \frac{e^{jkz}}{\rho} \\
& - \frac{1}{\mu} \sum_{n=1}^{\infty} (b_n^+ e^{-j\alpha_n z} + b_n^- e^{j\alpha_n z}) \frac{d\phi_n(\rho)}{d\rho}
\end{aligned} \quad (13)$$

At this point, the constants used in defining the field components are redefined to make the TEM terms agree with physical concepts so that the sign conventions on the TEM and the higher-order mode terms agree, e.g.,

$$b_0^+ = -\frac{k}{\omega} B_0^+ , \quad (14a)$$

$$b_0^- = \frac{k}{\omega} B_0^- , \quad (14b)$$

$$b_n^+ = -\frac{k^2}{\omega\alpha_n} B_n^+ , \quad (14c)$$

$$b_n^- = \frac{k^2}{\omega\alpha_n} B_n^- . \quad (14d)$$

The field components are now given by

$$E_{\rho} = B_0^+ \frac{e^{-jkz}}{\rho} + B_0^- \frac{e^{jkz}}{\rho} + \sum_{n=1}^{\infty} (B_n^+ e^{-j\alpha_n z} + B_n^- e^{j\alpha_n z}) \frac{d\phi_n}{d\rho} ,$$

$$E_z = j \sum_{n=1}^{\infty} \left(\frac{k^2 - \alpha_n^2}{\alpha_n} \right) (B_n^+ e^{-j\alpha_n z} - B_n^- e^{j\alpha_n z}) \phi_n ,$$

and

$$H_{\phi} = B_0^+ \frac{e^{-jkz}}{\eta\rho} - B_0^- \frac{e^{jkz}}{\eta\rho} + \frac{k}{\eta} \sum_{n=1}^{\infty} \frac{1}{\alpha_n} (B_n^+ e^{-j\alpha_n z} - B_n^- e^{j\alpha_n z}) \frac{d\phi_n}{d\rho} ,$$

where η is the characteristic impedance of the dielectric medium,

$$\eta = \sqrt{\frac{\mu}{\epsilon}} . \quad (15)$$

C. Field Expressions for Two Dissimilar Coaxial Regions

The analysis of the junction of two coaxial regions with differing inner and/or outer radii and/or dielectric media requires separate field expressions for each region. Such a junction is shown in Figure 2 which also displays schematic representations of the incident and reflected waves in each region. In this figure and others in the report, the assumption is made that the truncated sections of waveguide have matched terminations (or equivalently, extend to \pm infinity). Under such an assumption, all incident waves represent known sources with no reflected components. The junction in Figure 2 is arbitrarily located at $z = s$ in order to retain generality in the field expressions. For single discontinuities, specifying $z = 0$ in the resulting equations will simplify the mathematics somewhat.

For the region $z < s$, with media characteristics

$$k_- = \omega \sqrt{\mu_- \epsilon_-} \quad (16a)$$

and

$$\eta_- = \sqrt{\frac{\mu_-}{\epsilon_-}} , \quad (16b)$$

the field components are

$$E_{\rho}^{-} = B_0^{+} \frac{e^{-jk_{-}z}}{\rho} + B_0^{-} \frac{e^{jk_{-}z}}{\rho} + \sum_{n=1}^{\infty} (B_n^{+} e^{-j\alpha_n z} + B_n^{-} e^{j\alpha_n z}) \frac{d\phi_n}{d\rho}, \quad (17)$$

$$E_z^{-} = j \sum_{n=1}^{\infty} \frac{\gamma_n^2}{\alpha_n} (B_n^{+} e^{-j\alpha_n z} - B_n^{-} e^{j\alpha_n z}) \phi_n, \quad (18)$$

and

$$H_{\phi}^{-} = B_0^{+} \frac{e^{-jk_{-}z}}{\eta_{-}\rho} - B_0^{-} \frac{e^{jk_{-}z}}{\eta_{-}\rho} + \frac{k_{-}}{\eta_{-}} \sum_{n=1}^{\infty} \frac{1}{\alpha_n} (B_n^{+} e^{-j\alpha_n z} - B_n^{-} e^{j\alpha_n z}) \frac{d\phi_n}{d\rho} \quad (19)$$

where

$$\phi_n(\rho) = N_0(\gamma_n a) J_0(\gamma_n \rho) - J_0(\gamma_n a) N_0(\gamma_n \rho) \quad (20)$$

and

$$\alpha_n^2 = k_{-}^2 - \gamma_n^2. \quad (21)$$

The γ_n are the roots of the transcendental equation

$$\phi_n(b) = N_0(\gamma_n a) J_0(\gamma_n b) - J_0(\gamma_n a) N_0(\gamma_n b) = 0, \quad (22)$$

where a and b are the inner and outer radii of the coaxial region for $z < s$.

For the region $z > s$, with the dielectric media characteristics

$$k_{+} = \omega \sqrt{\mu_{+} \epsilon_{+}} \quad (23a)$$

and

$$\eta_{+} = \sqrt{\frac{\mu_{+}}{\epsilon_{+}}}, \quad (23b)$$

the field components are

$$E_{\rho}^{+} = C_0^{+} \frac{e^{-jk_{+}z}}{\rho} + C_0^{-} \frac{e^{jk_{+}z}}{\rho} + \sum_{n=1}^{\infty} (C_n^{+} e^{-j\beta_n z} + C_n^{-} e^{j\beta_n z}) \frac{d\psi_n}{d\rho}, \quad (24)$$

$$E_z^{+} = j \sum_{n=1}^{\infty} \frac{\lambda_n^2}{\beta_n} (C_n^{+} e^{-j\beta_n z} - C_n^{-} e^{j\beta_n z}) \psi_n, \quad (25)$$

and

$$H_{\phi}^{+} = C_0^{+} \frac{e^{-jk_{+}z}}{\eta_{+}\rho} - C_0^{-} \frac{e^{jk_{+}z}}{\eta_{+}\rho} + \frac{k_{+}}{\eta_{+}} \sum_{n=1}^{\infty} \frac{1}{\beta_n} (C_n^{+} e^{-j\beta_n z} - C_n^{-} e^{j\beta_n z}) \frac{d\psi_n}{d\rho} \quad (26)$$

where

$$\psi_n(\rho) = N_0(\lambda_n c) J_0(\lambda_n \rho) - J_0(\lambda_n c) N_0(\lambda_n \rho) \quad (27)$$

and

$$\beta_n^2 = k_{+}^2 - \lambda_n^2. \quad (28)$$

The λ_n are the roots of the transcendental equation

$$\psi_n(d) = N_0(\lambda_n c) J_0(\lambda_n d) - J_0(\lambda_n c) N_0(\lambda_n d) = 0, \quad (29)$$

where c and d are the inner and outer radii of the coaxial region for $z > s$. Note that the annular disk attached to the inner conductor has no effect on the field definitions. The disk merely imposes a boundary condition to be enforced in the plane of the aperture.

D. Evaluation of Constants in the $z < s$ Region

The unknown constants of Eqs. (17)-(19) are evaluated in terms of integrals over the unknown aperture electric field by application of Fourier series techniques. The first step

in evaluating B_0^+ and B_0^- is to integrate both sides of Eq.(17) over the $z = s$ plane (illustrated in Figure 2) with respect to ρ which yields

$$\int_a^b E_\rho^- d\rho = B_0^+ e^{-jk_-s} \int_a^b \frac{d\rho}{\rho} + B_0^- e^{jk_-s} \int_a^b \frac{d\rho}{\rho} + \int_a^b \sum_{n=1}^{\infty} (B_n^+ e^{-j\alpha_n s} + B_n^- e^{j\alpha_n s}) \frac{d\phi_n}{d\rho} d\rho$$

After evaluation of the integrals on the right-hand side of the equation, one obtains

$$\int_a^b E_\rho^- d\rho = (B_0^+ e^{-jk_-s} + B_0^- e^{jk_-s}) \ln \rho \Big|_a^b + \sum_{n=1}^{\infty} (B_n^+ e^{-j\alpha_n s} + B_n^- e^{j\alpha_n s}) \phi_n(\rho) \Big|_a^b.$$

Note that $\phi_n(b) = 0$ from Eq.(22) and that $\phi_n(a) = 0$ from the definition in Eq.(20); therefore

$$B_0^+ e^{-jk_-s} + B_0^- e^{jk_-s} = \frac{1}{\ln \frac{b}{a}} \int_a^b E_\rho^- d\rho. \quad (30)$$

The presence of the perfectly conducting disk in the aperture affects the value of E^- over the aperture.

$$E_\rho^- = \begin{cases} 0, & \rho \in (a, h) \\ E_\rho^0, & \rho \in (h, b) \end{cases} \quad (31)$$

With the constraint of Eq.(31), Eq.(30) becomes

$$B_0^+ e^{-jk_-s} + B_0^- e^{jk_-s} = \frac{1}{\ln \frac{b}{a}} \int_h^b E_\rho^0 d\rho . \quad (32)$$

The $B_0^+ \frac{e^{-jk_-z}}{\rho}$ term in Eq.(17) represents a TEM wave traveling in the +z direction. This wave is the only such positive traveling TEM wave for $z < s$ and, hence, is identified as the known excitation. The subject term may be expressed as

$$B_0^+ \frac{e^{-jk_-z}}{\rho} = \frac{V^+}{\ln \frac{b}{a}} \frac{e^{-jk_-z}}{\rho} .$$

The quantity V^+ is the voltage (complex in general) of the excitation applied to the coaxial waveguide in the $z < s$ region and is defined by

$$V^+ = - \int_a^b E_\rho^- d\rho . \quad (33)$$

The value of V^+ is normally a specified parameter of the problem. The following definitions may now be obtained:

$$B_0^+ = \frac{V^+}{\ln \frac{b}{a}} \quad (34a)$$

and

$$B_0^- = \frac{e^{-jk_-s}}{\ln \frac{b}{a}} \left(\int_h^b E_\rho^0 d\rho - V^+ e^{-jk_-s} \right) . \quad (34b)$$

The higher-order mode coefficients are determined in a similar manner. The first step is to multiply Eq.(17) by $\rho \frac{d\phi_m}{d\rho}$ and integrate with respect to ρ over the $z = s$ plane.

$$\int_a^b E_\rho^- \rho \frac{d\phi_m}{d\rho} d\rho = B_0^+ e^{-jk_-s} \int_a^b \frac{d\phi_m}{d\rho} d\rho + B_0^- e^{jk_-s} \int_a^b \frac{d\phi_m}{d\rho} d\rho$$

$$+ \int_a^b \rho \sum_{n=1}^{\infty} (B_n^+ e^{-j\alpha_n s} + B_n^- e^{j\alpha_n s}) \frac{d\phi_m}{d\rho} \frac{d\phi_n}{d\rho} d\rho, \quad m=1,2,\dots$$

The integrals multiplied by B_0^+ and B_0^- have zero value since $\phi_m(b) = \phi_m(a) = 0$. From orthogonality relations described in Appendix D, the last integral has zero value except when $m = n$:

$$\int_h^b E_\rho^o \rho \frac{d\phi_m}{d\rho} d\rho = \begin{cases} 0, & m \neq n \\ \int_a^b (B_n^+ e^{-j\alpha_n s} + B_n^- e^{j\alpha_n s}) \rho \left(\frac{d\phi_n}{d\rho} \right)^2 d\rho, & m = n \end{cases}$$

This yields:

$$B_n^+ e^{-j\alpha_n s} + B_n^- e^{j\alpha_n s} = \frac{1}{\int_a^b \rho \left(\frac{d\phi_n}{d\rho} \right)^2 d\rho} \int_h^b E_\rho^o \rho \frac{d\phi_n}{d\rho} d\rho. \quad (35)$$

The integral in the denominator of the right-hand side is the normalization integral for the particular Fourier-Bessel series used in these field expansions. The integral is represented by M_n^2 and has the value (from Appendix D):

$$M_n^2 = \frac{b^2 \gamma_n^2}{2} \left[N_0(\gamma_n a) J_1(\gamma_n b) - J_0(\gamma_n a) N_1(\gamma_n b) \right]^2 - \frac{2}{\pi^2}. \quad (36)$$

Eq.(35) can now be written in a more compact form:

$$B_n^+ e^{-j\alpha_n s} + B_n^- e^{j\alpha_n s} = \frac{1}{M_n^2} \int_h^b E_\rho^o \rho \frac{d\phi_n}{d\rho} d\rho . \quad (37)$$

As indicated earlier, B_0^+ and B_0^- are the complex coefficients of the TEM waves in Region 1 which are traveling in the positive and negative z directions, respectively. Under the assumption of a matched waveguide in the negative z direction, B_0^+ will be non-zero only in the case of an externally excited wave traveling in the positive z direction. The TEM wave traveling in the negative z direction represents the reflected component of the incident TEM wave and/or the TEM component of a transmitted wave incident on the aperture from Region 2. The same definitions apply for B_n^+ and B_n^- which are the complex coefficients for the higher-order modes in Region 1. In order for the solutions to the problems considered in the present investigation to be tractable, the B_0^+ and the B_n^+ must be either zero or known quantities. In theory, there is no limit to the number of incident waves which can be treated as long as the values of the coefficients are specified. Satisfaction of the boundary conditions at a perfect discontinuity would require the excitation of an infinite number of higher-order modes and, thus, all B_n^- should be non-zero. The procedure for accurately evaluating an infinite series of Bessel functions which is introduced in Appendix B allows the solution of such problems

with a relatively small number of terms of the resulting series (normally less than 20).

E. Evaluation of Constants in the $z > s$ Region

The procedures for evaluating the constants in the field expressions for the $z > s$ region are the same as for the $z < s$ region. For a single discontinuity, C_0^- and C_n^- are the complex coefficients of waves incident from the negative z direction and, if non-zero, are assumed to be known quantities for the single-discontinuity case under discussion. The C_0^+ and C_n^+ are the coefficients of TEM and higher-order mode waves traveling in the positive z direction in Region 2. The expressions for these constants are

$$C_0^+ e^{-jk_+s} + C_0^- e^{jk_+s} = \frac{1}{\ln \frac{d}{c}} \int_h^b E_\rho^o d\rho \quad (38)$$

$$\begin{aligned} C_n^+ e^{-j\beta_n s} + C_n^- e^{j\beta_n s} &= \frac{1}{\int_c^d \rho \left(\frac{d\psi_n}{d\rho} \right)^2 d\rho} \int_c^d E_\rho^+ \rho \frac{d\psi_n}{d\rho} d\rho \\ &= \frac{1}{U_n^2} \int_h^b E_\rho^o \rho \frac{d\psi_n}{d\rho} d\rho . \end{aligned} \quad (39)$$

The value of the normalization integral, denoted by U_n^2 , is

$$U_n^2 = \frac{d^2 \lambda_n^2}{2} \left[N_0(\lambda_n c) J_1(\lambda_n d) - J_0(\lambda_n c) N_1(\lambda_n d) \right]^2 - \frac{2}{\pi^2} . \quad (40)$$

F. Enforce Continuity of Transverse Fields in Aperture

The unknown constants in the field component expressions for the regions on both sides of the discontinuity are now defined in terms of weighted integrals over the unknown aperture electric field. Fundamental boundary conditions require that the transverse components of the electromagnetic field be continuous across the aperture. This constraint has already been applied to the electric field component since

$$E_{\rho}^{-}(\rho, s) = E_{\rho}^{+}(\rho, s) = E_{\rho}^0, \quad \rho \in (h, b).$$

Enforcing continuity of the transverse magnetic field is accomplished by equating Eqs. (19) and (27) at the $z = s$ plane, i.e.,

$$H_{\phi}^{-}(\rho, s) = H_{\phi}^{+}(\rho, s), \quad \rho \in (h, b).$$

After the evaluation of B_0^{-} , B_n^{-} , C_0^{+} , and C_n^{+} through the use of Eqs. (32), (37), (38), and (39), this equation becomes

$$\begin{aligned} & 2B_0^{+} \frac{e^{-jk_{-}s}}{\eta_{-}\rho} - \frac{1}{\eta_{-}\rho \ln \frac{b}{a}} \int_h^b E_{\rho}^0 d\rho \\ & + \frac{k_{-}}{\eta_{-}} \sum_{n=1}^{\infty} \frac{1}{\alpha_n} \left(2B_n^{+} e^{-j\alpha_n s} - \frac{1}{M_n^2} \int_h^b E_{\rho}^0 \rho \frac{d\phi_n}{d\rho} d\rho \right) \frac{d\phi_n}{d\rho} \\ & = -2C_0^{-} \frac{e^{jk_{+}s}}{\eta_{+}\rho} + \frac{1}{\eta_{+}\rho \ln \frac{d}{c}} \int_h^b E_{\rho}^0 d\rho \\ & + \frac{k_{+}}{\eta_{+}} \sum_{n=1}^{\infty} \frac{1}{\beta_n} \left(-2C_n^{-} e^{j\beta_n s} + \frac{1}{U_n^2} \int_h^b E_{\rho}^0 \rho \frac{d\psi_n}{d\rho} d\rho \right) \frac{d\psi_n}{d\rho} \end{aligned} \quad (41)$$

The terms involving unknown constants are placed on the left-hand side of the equation to obtain

$$\begin{aligned}
& 2B_0^+ \frac{e^{-jk_-s}}{\eta_- \rho} + 2C_0^- \frac{e^{jk_+s}}{\eta_+ \rho} + \frac{2k_-}{\eta_-} \sum_{n=1}^{\infty} \frac{1}{\alpha_n} B_n^+ e^{-j\alpha_n s} \frac{d\phi_n}{d\rho} \\
& + \frac{2k_+}{\eta_+} \sum_{n=1}^{\infty} \frac{1}{\beta_n} C_n^- e^{j\beta_n s} \frac{d\psi_n}{d\rho} = \left(\frac{1}{\eta_- \ln \frac{b}{a}} + \frac{1}{\eta_+ \ln \frac{d}{c}} \right) \frac{1}{\rho} \int_h^b E_\rho^o d\rho \\
& + \frac{k_-}{\eta_-} \sum_{n=1}^{\infty} \left(\frac{1}{\alpha_n^2 M_n^2} \int_h^b E_\rho^o \rho \frac{d\phi_n}{d\rho} d\rho \right) \frac{d\phi_n}{d\rho} \\
& + \frac{k_+}{\eta_+} \sum_{n=1}^{\infty} \left(\frac{1}{\beta_n^2 U_n^2} \int_h^b E_\rho^o \rho \frac{d\psi_n}{d\rho} d\rho \right) \frac{d\psi_n}{d\rho}
\end{aligned}$$

A proper integral equation (i.e., one equation, one unknown) may be obtained from Eq.(41) by the application of sufficient constraints to evaluate the unknown constants. A commonly encountered situation is TEM excitation only and from only one direction. For an incident TEM wave in Region 1 traveling in the positive z direction, B_n^+ , C_0^- and C_n^- would be zero. The constant B_0^+ would then be evaluated from Eq.(34a).

G. Application to Simpler Geometries

The expression presented in Eq.(41) pertains to the geometry depicted in Figure 2 which is a coaxial waveguide junction which includes both an annular disk on one conductor and steps in the radii of both conductors. Most coaxial waveguide

discontinuities are not this complex and the appropriate integral equations are special cases of Eq.(41). It should be noted that the presence of an annular disk on one or both coaxial conductors affects only the limits of integration of the three integrals in Eq.(41); consequently, this type of geometry variation is easily treated. For a discontinuity consisting of a step in the inner or outer radius only, Eq.(41) is applicable with suitable adjustments of radii values used in defining ϕ_n , α_n , M_n^2 , ψ_n , β_n and U_n^2 . In addition, the proper changes must be made in the limits of integration. For the case of a discontinuity consisting solely of an annular disk attached to the inner or outer coaxial conductor, as shown in Figure 3, or both conductors, as shown in Figure 1, Eq.(41) is simplified considerably. Since the coaxial regions on both sides of the discontinuity are now the same, the ϕ_n of Eq.(20) and the ψ_n of Eq.(27) are now the same. An important and common simplification occurs when the dielectric media in the two regions are the same, i.e.,

$$\epsilon_+ = \epsilon_- = \epsilon \quad (42a)$$

and

$$\mu_+ = \mu_- = \mu \quad (42b)$$

The constraints of Eq.(42) result in $k_+ = k_-$, $\alpha_n = \beta_n$, and $\eta_+ = \eta_-$.

An integral equation appropriate for the geometry of

Figure 3a under the assumption that the excitation consists only of a TEM wave traveling in the positive z direction is given by

$$\begin{aligned}
 \frac{2V^+ e^{-jk_-s}}{\eta_- \rho \ln \frac{b}{a}} &= \left(\frac{1}{\eta_- \rho} + \frac{1}{\eta_+ \rho} \right) \frac{1}{\ln \frac{b}{a}} \int_a^g E_\rho^o d\rho \\
 &+ \frac{k_-}{\eta_-} \sum_{n=1}^{\infty} \left(\frac{1}{\alpha_n^- M_n^2} \int_a^g E_\rho^o \rho \frac{d\phi_n}{d\rho} d\rho \right) \frac{d\phi_n}{d\rho} \\
 &+ \frac{k_+}{\eta_+} \sum_{n=1}^{\infty} \left(\frac{1}{\alpha_n^+ M_n^2} \int_a^g E_\rho^o \rho \frac{d\phi_n}{d\rho} d\rho \right) \frac{d\phi_n}{d\rho} , \quad (43)
 \end{aligned}$$

where α_n^- and α_n^+ pertain to the negative and positive z regions respectively. If the constraints of Eq.(42) are applied to Eq.(43) a factor of $\frac{2}{\eta}$ may be divided from each term in the equation (noting that the two series would now be identical). It is possible to change Eq.(43) into an equation appropriate for the geometry of Figure 3b by changing the limits of integration for all integrals from (a,g) to (h,b).

An integral equation appropriate for the geometry of Figure 4a with the same excitation employed in Eq.(43) and with the parameters ψ_n , β_n and U_n^2 properly defined is given by

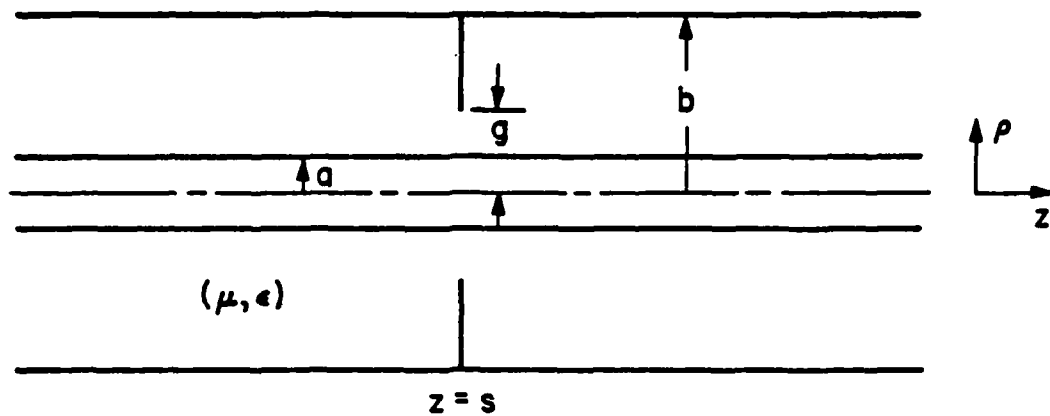


Figure 3a. Annular Disk Attached to the Outer Conductor of a Coaxial Waveguide

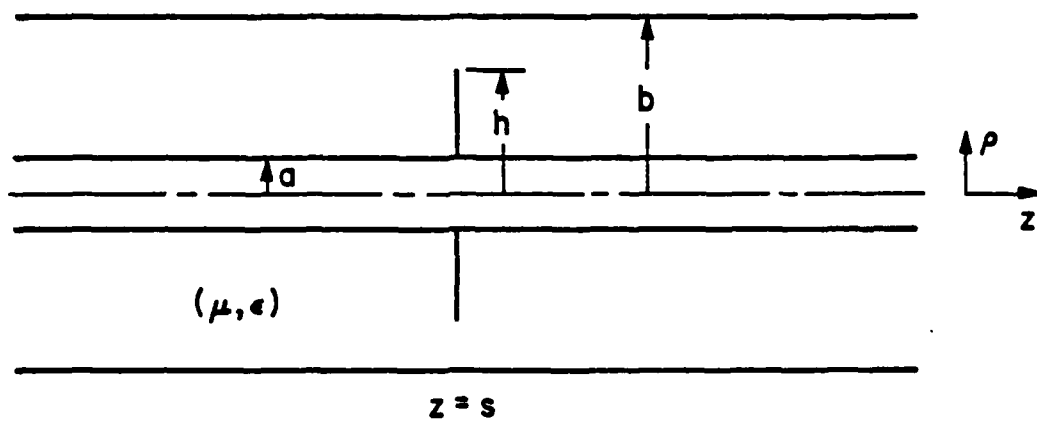


Figure 3b. Annular Disk Attached to the Inner Conductor of a Coaxial Waveguide

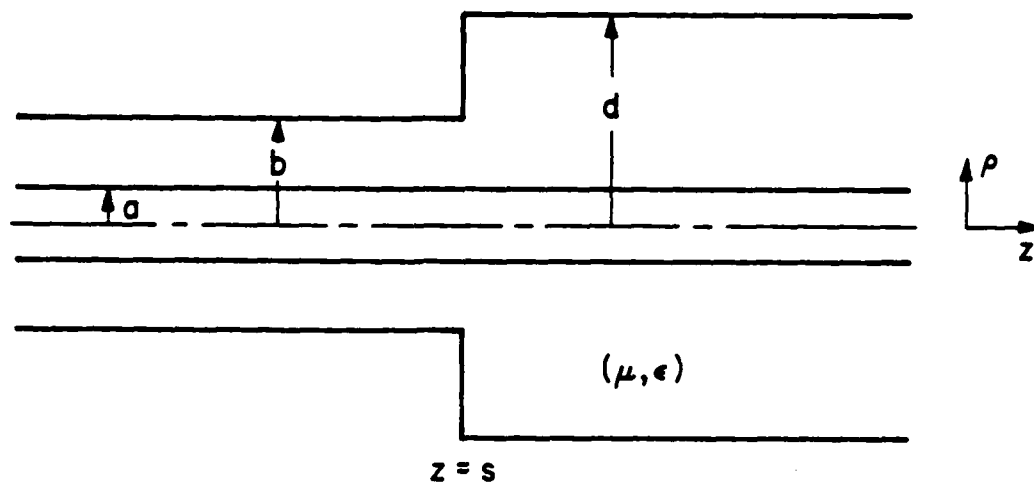


Figure 4a. Step Discontinuity in the Outer Conductor of a Coaxial Waveguide

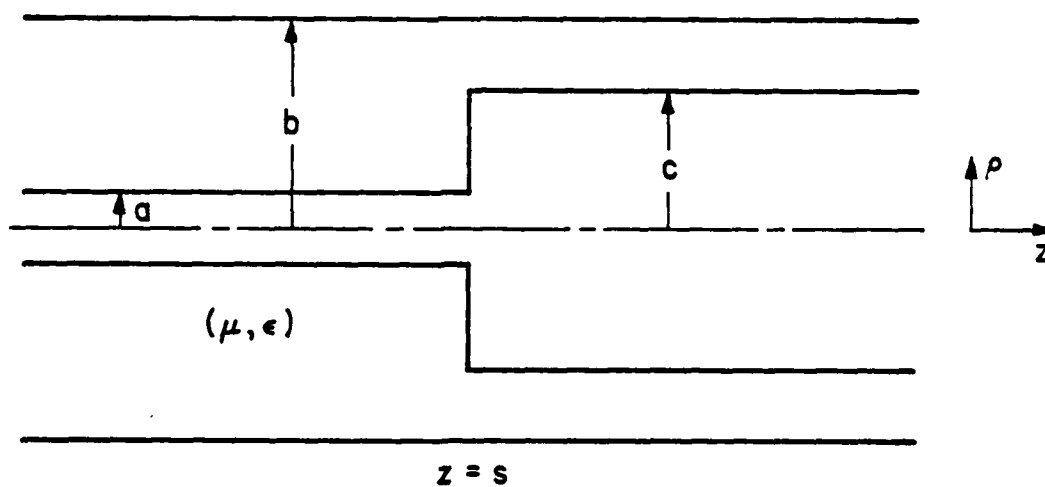


Figure 4b. Step Discontinuity in the Inner Conductor of a Coaxial Waveguide

$$\begin{aligned}
\frac{2V^+ e^{-jk_-s}}{\eta_- \rho \ln \frac{b}{a}} &= \left(\frac{1}{\eta_- \rho \ln \frac{b}{a}} + \frac{1}{\eta_+ \rho \ln \frac{d}{a}} \right) \int_a^b E_\rho^0 d\rho \\
&+ \frac{k_-}{\eta_-} \sum_{n=1}^{\infty} \left(\frac{1}{\alpha_n M_n^2} \int_a^b E_\rho^0 \rho \frac{d\phi_n}{d\rho} d\rho \right) \frac{d\phi_n}{d\rho} \\
&+ \frac{k_+}{\eta_+} \sum_{n=1}^{\infty} \left(\frac{1}{\beta_n U_n^2} \int_a^b E_\rho^0 \rho \frac{d\psi_n}{d\rho} d\rho \right) \frac{d\psi_n}{d\rho} . \quad (44)
\end{aligned}$$

This equation may be changed to one appropriate for Figure 4b by changing the limits of integration from (a,b) to (c,b) and by making the appropriate changes to the definitions of β_n , ψ_n and U_n^2 .

H. Integral Equation for a One-Port Coaxial Cavity

An effective way to create a one-port coaxial cavity is to place a perfectly conducting, transverse plate across the coaxial waveguide at a point on the positive z side of any of the discontinuities depicted in Figures 3 and 4. The cavity treated in this section is created from Figure 4a and is shown in Figure 5. The expressions for the field components in the coaxial regions are those given by Eqs. (17)-(19) and (24)-(26) with the accompanying definitions. Note that, for the subject geometry, the radii a and c are equal.

The constants in Eqs. (17)-(19) are defined by Eqs. (34) and (37) with the assumption that the only excitation is a

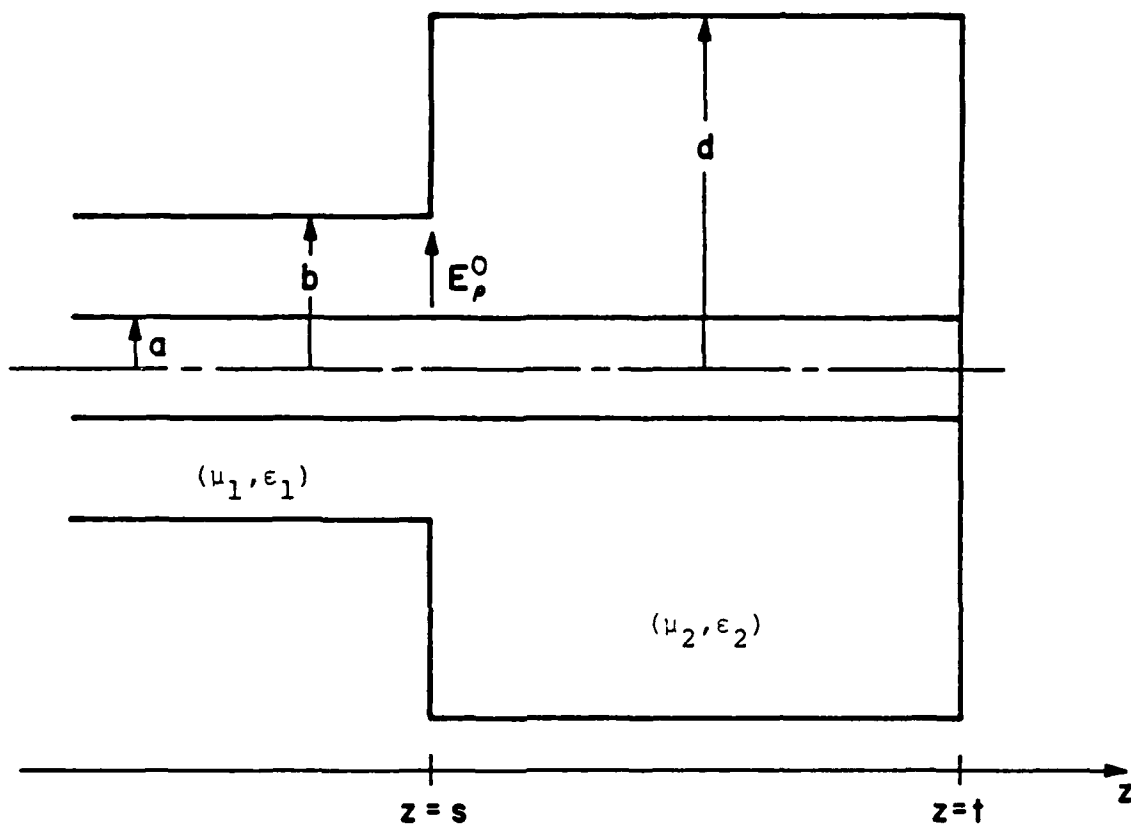


Figure 5. One-Port Cavity Formed from a Coaxial Waveguide with a Step Discontinuity in the Outer Radius

TEM wave traveling in the positive z direction in the region $z < s$. Because of the perfectly conducting plate at $z = t$, the following boundary condition is imposed:

$$E_{\rho}^{+}(\rho, t) = 0.$$

An inspection of Eq.(24) reveals that this condition is enforced by requiring

$$C_0^{+} e^{-jk_+ t} + C_0^{-} e^{jk_+ t} = 0$$

and

$$C_n^{+} e^{-j\beta_n t} + C_n^{-} e^{j\beta_n t} = 0$$

The resulting relationships between constants are

$$C_0^{-} = -C_0^{+} e^{-j2k_+ t} \quad (45a)$$

and

$$C_n^{-} = -C_n^{+} e^{-j2\beta_n t} \quad (45b)$$

Substitution of Eq.(45a) into Eq.(38) and Eq.(45b) into Eq.(39) yields the following expressions for the constants:

$$C_0^{\pm} = \frac{\pm e^{\pm jk_+ t}}{j2\sin k_+(t-s) \ln \frac{d}{a}} \int_a^b E_{\rho}^0 d\rho \quad (46)$$

and

$$C_n^{\pm} = \frac{\pm e^{\pm j\beta_n t}}{j2\sin \beta_n(t-s) U_n^2} \int_a^b E_{\rho}^0 \rho \frac{d\psi_n}{d\rho} d\rho \quad (47)$$

An integral equation for the unknown aperture electric field is again obtained by constraining the transverse mag-

netic field to be continuous across the aperture. The following expression is obtained by equating Eqs. (19) and (26) with the constants defined by Eqs. (46) and (47):

$$\begin{aligned}
& \frac{v^+ e^{-jk_-s}}{\eta_- \rho \ln \frac{b}{a}} - \frac{1}{\eta_- \rho \ln \frac{b}{a}} \left(\int_a^b E_\rho^0 d\rho - v^+ e^{-jk_-s} \right) \\
& - \frac{k_-}{\eta_-} \sum_{n=1}^{\infty} \left[\frac{1}{\alpha_n M_n^2} \int_a^b E_\rho^0 \rho \frac{d\phi_n}{d\rho} d\rho \right] \frac{d\phi_n}{d\rho} \\
& = \frac{e^{jk_+(t-s)} + e^{-jk_+(t-s)}}{j2\sin k_+(t-s) \ln \frac{d}{a} \eta_+ \rho} \int_a^b E_\rho^0 d\rho \\
& + \frac{k_+}{\eta_+} \sum_{n=1}^{\infty} \left[\frac{e^{j\beta_n(t-s)} + e^{-j\beta_n(t-s)}}{j2\sin \beta_n(t-s) \beta_n U_n^2} \int_a^b E_\rho^0 \rho \frac{d\psi_n}{d\rho} d\rho \right] \frac{d\psi_n}{d\rho} .
\end{aligned}$$

Collecting terms yields the equation:

$$\begin{aligned}
\frac{2v^+ e^{-jk_-s}}{\eta_- \rho \ln \frac{b}{a}} & = \left(\frac{1}{\eta_- \rho \ln \frac{b}{a}} - \frac{j\cot k_+(t-s)}{\eta_+ \rho \ln \frac{d}{a}} \right) \int_a^b E_\rho^0 d\rho \\
& + \frac{k_-}{\eta_-} \sum_{n=1}^{\infty} \left[\frac{1}{\alpha_n M_n^2} \int_a^b E_\rho^0 \rho \frac{d\phi_n}{d\rho} d\rho \right] \frac{d\phi_n}{d\rho} \\
& - \frac{k_+}{\eta_+} \sum_{n=1}^{\infty} \left[\frac{j\cot \beta_n(t-s)}{\beta_n U_n^2} \int_a^b E_\rho^0 \rho \frac{d\psi_n}{d\rho} d\rho \right] \frac{d\psi_n}{d\rho} . \quad (48)
\end{aligned}$$

I. Microwave Circuit Concepts

As described in Chapter I, essentially all early treatments of waveguide discontinuities were directed toward calculating the resulting change in admittance of the waveguide. With the assumption of lossless waveguide walls and dielectrics, these admittance changes are purely reactive in nature. The susceptance expressions found in the Waveguide Handbook provide excellent data for comparison with results obtained from solutions to the previously derived integral equations. Since such solutions yield only the radial component of electric field in the aperture, a small amount of additional analysis is required to compute values of susceptance due to the discontinuities.

Consider a uniform transmission line extending to $z = \pm\infty$ which has a single discontinuity at $z = s$. Such a transmission line is depicted in Figure 6. The admittance at $z = s$ looking in the positive z direction is given by

$$Y_L = Y_0^+ + jB$$

where Y_0^+ is the transmission line TEM characteristic admittance for $z > s$ and B is the TEM susceptance of the discontinuity. The characteristic admittance of the line for $z < s$ is designated Y_0^- . The complex TEM (voltage) reflection coefficient in the region $z < s$ is defined by

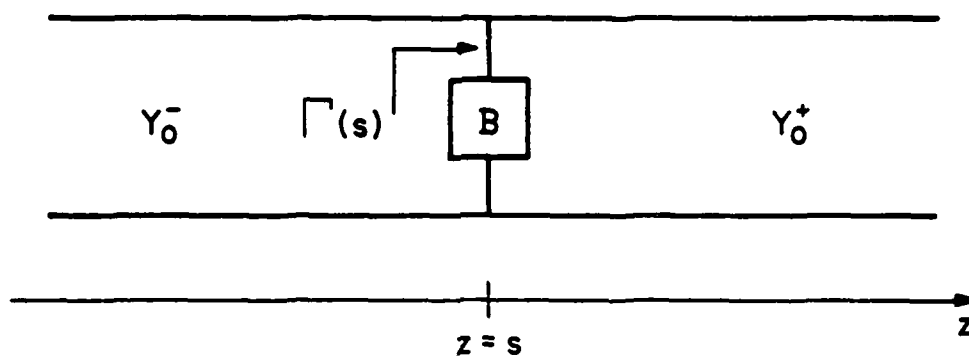


Figure 6. Junction of Two Transmission Lines of Different Characteristic Impedance with a Lumped Susceptance at the Junction

$$\Gamma(z) = \frac{Y_0^- - Y_L}{Y_0^- + Y_L} e^{j2k_-(z-s)}$$

or

$$\Gamma(z) = \frac{Y_0^- - (Y_0^+ + jB)}{Y_0^- + (Y_0^+ + jB)} e^{j2k_-(z-s)} \quad (49)$$

From Eq.(49), an expression for the normalized susceptance at $z = s$ is obtained

$$\frac{jB}{Y_0^-} = \frac{1 - Y_0^+/Y_0^- - \Gamma(s)(1 + Y_0^+/Y_0^-)}{1 + \Gamma(s)} \quad (50)$$

For transmission lines where $Y_0^+ = Y_0^-$, Eq.(50) becomes

$$\frac{jB}{Y_0^-} = \frac{-2\Gamma(s)}{1 + \Gamma(s)} \quad (51)$$

In the transmission line (or waveguide) region $z < s$, the TEM voltage reflection coefficient is the ratio of the reflected TEM voltage (or electric field) wave to the incident TEM voltage wave. As noted in Section D of this chapter, B_0^+ and B_0^- are the complex coefficients of the positive and negatively traveling TEM waves for Eqs.(17)-(19) which are defined for the $z < s$ region. The reflection coefficient can now be represented by

$$\Gamma(z) = \Gamma(s) e^{j2k_-(z-s)} = \frac{B_0^- e^{jk_-s}}{B_0^+ e^{-jk_-s}} e^{j2k_-(z-s)} = \frac{B_0^-}{B_0^+} e^{j2k_-z} \quad (52)$$

The reflection coefficient can be defined in terms of the aperture electric field through the use of Eqs.(34a&b)

$$\Gamma(s) = \frac{e^{jk_{-s}}}{V^+} \left(\int_h^b E_{\rho}^o d\rho - V^+ e^{-jk_{-s}} \right) . \quad (53)$$

The susceptance of the discontinuity may then be calculated through use of Eq.(50) or Eq.(51). It should be noted that Eq.(53) is a normalized expression since E_{ρ}^o is linearly related to V^+ .

CHAPTER III

NUMERICAL SOLUTION TECHNIQUE

A. Introduction

A solution for the unknown aperture electric field distribution in Eq.(43) may be obtained through use of the method of moments, Ref.[9]. Application of such a method requires intelligent choices of a set of expansion or basis functions. For the waveguide discontinuities being treated in this investigation, once a solution for the aperture field distribution is obtained, all other quantities of interest can be calculated. The desired field and susceptance values are calculated from integrals of the aperture electric field and weight functions over the aperture. The sample solution technique illustrated in this chapter is applicable to all single-aperture equations.

B. Selection of Basis and Testing Functions

An inspection of the integral under the summation sign in Eq.(43) reveals that the integral is easily evaluated if the value of ρE_{ρ}^0 is constant over the range of integration. This may be effected by the choice of the following subsectional, constant-value pulse expansion for the unknown

aperture field. The expansion is illustrated in Figure 7.

$$\rho E_{\rho}^0(\rho) = \sum_{q=1}^N E_q P_q(\rho) \quad (54)$$

where

$$P_q(\rho) = \begin{cases} 1, & \rho \in (r_q - \Delta/2, r_q + \Delta/2) \\ 0, & \text{otherwise} \end{cases} \quad (55)$$

and $r_q = a + (q-1)\Delta$ where $\Delta = (g-a)/N$ is the pulse width.

Substituting Eq. (54) into Eq. (43) yields

$$\begin{aligned} \frac{2V^+ e^{-jk_-s}}{\eta_{-}\rho \ln \frac{b}{a}} &= \left(\frac{1}{\eta_{-}\rho} + \frac{1}{\eta_{+}\rho} \right) \frac{1}{\ln \frac{b}{a}} \int_a^g \sum_{q=1}^N E_q P_q(\rho) \frac{1}{\rho} d\rho \\ &+ \frac{k_-}{\eta_-} \sum_{n=1}^{\infty} \left(\frac{1}{\alpha_n^2 M_n^2} \int_a^g \sum_{q=1}^N E_q P_q(\rho) \frac{d\phi_n}{d\rho} d\rho \right) \frac{d\phi_n}{d\rho} \\ &+ \frac{k_+}{\eta_+} \sum_{n=1}^{\infty} \left(\frac{1}{\alpha_n^2 M_n^2} \int_a^g \sum_{q=1}^N E_q P_q(\rho) \frac{d\phi_n}{d\rho} d\rho \right) \frac{d\phi_n}{d\rho}. \end{aligned} \quad (56)$$

The first integral is easily evaluated:

$$\begin{aligned} \int_a^g \sum_{q=1}^N E_q P_q(\rho) \frac{1}{\rho} d\rho &= \sum_{q=1}^N E_q \int_{r_q - \Delta/2}^{r_q + \Delta/2} \frac{1}{\rho} d\rho \\ &= \sum_{q=1}^N E_q \ln \{ (r_q + \Delta/2) / (r_q - \Delta/2) \}. \end{aligned} \quad (57)$$

The last two integrals have the same value which is given by

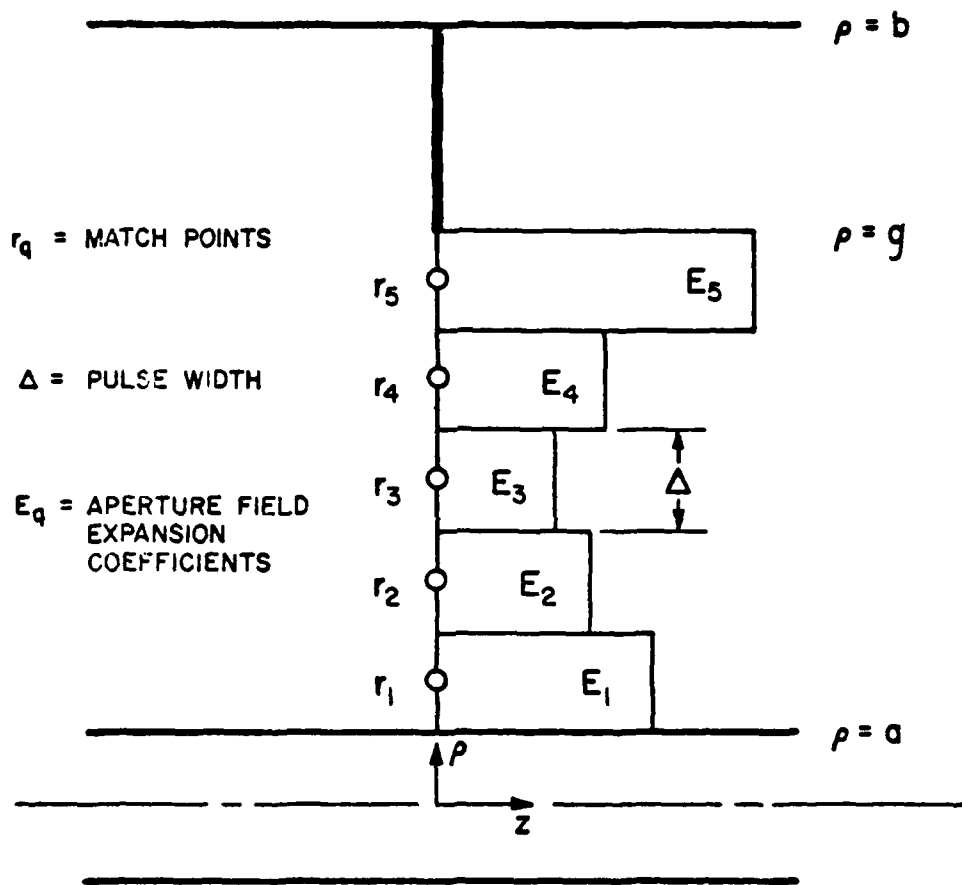


Figure 7. Illustration of Numerical Solution Technique
Expansion and Testing Functions

$$\begin{aligned}
\int_a^q \sum_{q=1}^N E_q P_q(\rho) d\phi_n &= \sum_{q=1}^N E_q \int_{r_q-\Delta/2}^{r_q+\Delta/2} d\phi_n \\
&= \sum_{q=1}^N E_q [\phi_n(r_q+\Delta/2) - \phi_n(r_q-\Delta/2)] . \quad (58)
\end{aligned}$$

After the substitution of the integral values of Eqs. (57) and (58) into Eq. (56), the following equation is obtained

$$\begin{aligned}
\frac{2V^+ e^{-jk_-s}}{\eta_- \rho \ln \frac{b}{a}} &= \left(\frac{1}{\eta_- \rho} + \frac{1}{\eta_+ \rho} \right) \frac{1}{\ln \frac{b}{a}} \sum_{q=1}^N E_q \ln \{ (r_q+\Delta/2) / (r_q-\Delta/2) \} \\
&+ \frac{k_-}{\eta_-} \sum_{n=1}^{\infty} \left[\frac{1}{\alpha_n^2 M_n^2} \sum_{q=1}^N E_q [\phi_n(r_q+\Delta/2) - \phi_n(r_q-\Delta/2)] \right] \frac{d\phi_n}{d\rho} \\
&+ \frac{k_+}{\eta_+} \sum_{n=1}^{\infty} \left[\frac{1}{\alpha_n^2 M_n^2} \sum_{q=1}^N E_q [\phi_n(r_q+\Delta/2) - \phi_n(r_q-\Delta/2)] \right] \frac{d\phi_n}{d\rho} . \quad (59)
\end{aligned}$$

An important consideration in the selection of a set of testing functions is the avoidance of "sampling" the integral equation at a point where the aperture field has a singularity. All planar discontinuities discussed in the report possess 90 degree or 180 degree exterior corners at which points the normal component of electric field is singular. The integral equation for the aperture field of a planar coaxial waveguide discontinuity such as given by Eq. (43) possesses the same important features as does the integral equation for the two-dimensional, conducting strip illuminated by

a TM wave (and the infinite slot illuminated by a TE wave). The experiences of Butler, et al., Refs.[23] and [24], support the selection of constant-value, pulse basis functions with the testing functions consisting of Dirac delta functions at the pulse centers. Delta functions used in this manner are commonly called "match points." The set of R match points, which is illustrated in Figure 7, may be expressed mathematically by

$$T(\rho) = (\delta(\rho-r_1), \dots, \delta(\rho-r_p), \dots, \delta(\rho-r_R)). \quad (60)$$

The testing functions force the subject equation to be valid at each point

$$\rho = r_p = a + (p-\frac{1}{2})\Delta, \quad p = 1, 2, \dots, R.$$

Substitution of the expressions

$$r_q + \Delta/2 = a + q\Delta = r_q^+ \quad (61a)$$

and

$$r_q - \Delta/2 = a + (q-1)\Delta = r_q^- \quad (61b)$$

for the pulse limits in Eq.(59) simplifies the notation somewhat. By sampling Eq.(59) at a set of $R = N$ match points, a set of N algebraic equations for N unknown Pulse amplitudes is obtained which can be solved for the unknown electric field in the aperture. This set of equations is

represented by

$$\begin{aligned} \frac{2V^+ e^{-jk_-s}}{\eta_- r_p \ln \frac{b}{a}} = & \left(\frac{1}{\eta_- r_p} + \frac{1}{\eta_+ r_p} \right) \frac{1}{\ln \frac{b}{a}} \sum_{q=1}^N E_q \ln(r_q^+/r_q^-) \\ & + \frac{k_-}{\eta_-} \sum_{q=1}^N E_q \left(\sum_{n=1}^{\infty} \frac{1}{\alpha_n^2 M_n^2} [\phi_n(r_q^+) - \phi_n(r_q^-)] \frac{d\phi_n(r_p)}{d\rho} \right) \\ & + \frac{k_+}{\eta_+} \sum_{q=1}^N E_q \left(\sum_{n=1}^{\infty} \frac{1}{\alpha_n^2 M_n^2} [\phi_n(r_q^+) - \phi_n(r_q^-)] \frac{d\phi_n(r_p)}{d\rho} \right), \\ & p = 1, 2, \dots, N \end{aligned} \quad (62)$$

The final expression given by Eq. (62) is now in a desirable form for numerical determination of E_q . Special attention must be paid to the convergence of the infinite series of Bessel functions. In general, such series have poor convergence properties and operations on the series to improve the rate of convergence are warranted. A very effective procedure for improving the convergence of series such as that in Eq. (62) is described in Appendices B and C. Application of the procedure does not affect the form of the equation since the operations are only upon the series, but the additional step of determining the asymptotic form of the series elements is required.

C. Numerical Results for Single Discontinuities

A digital computer has been employed to obtain solutions to Eq. (62) with constant ratios of a , b and c at five

different frequencies. The real and imaginary parts of the aperture electric field are plotted for a frequency range that extends from below to above the cutoff frequency for the first higher-order mode in the waveguide. The first three frequencies are below and the last two are above cutoff. All plotted field distributions display a $\frac{1}{\rho}$ variation near the center conductor and a singular behavior as the edge of the disk is approached. For frequencies above the cutoff, the imaginary part normally exhibits one or more zero crossings. The aperture field distributions for an annular disk attached to the center conductor of a coaxial guide (Figure 3b) are shown in Figure 9. In this set of curves, the singular behavior is again displayed near the edge of the disk, and the $\frac{1}{\rho}$ variation becomes apparent near the outer conductor.

Similar results for the steps in outer and inner radii of the coaxial guides illustrated in Figures 4a and 4b are presented in Figures 10 and 11. The behavior of the aperture field distributions is analogous to that shown in Figures 8 and 9 with the singular behavior being less pronounced near the 90 degree edges than for the 180 degree ones. In Figure 12 are shown the aperture field distributions obtained when a shorting plate is added to the geometry of Figure 10 to create a one-port cavity.

In Figure 13, the effect of varying the number of basis function pulses across the aperture is presented for the geometry of Figure 3a. The plotted curves show that the correct $\frac{1}{\rho}$ behavior is captured by even a few pulses across the aperture. The nature of the field singularity becomes much more evident as the number of pulses is increased. Because most of the quantities of interest in this investigation are calculated from an integral of the aperture field, the effect of missing the fine detail of the singularity is substantially reduced, a fact that is demonstrated in Table 6.

In Tables 1 through 5 are presented values of susceptance computed from expressions in the Waveguide Handbook for the discontinuities depicted in Figures 3a, 3b, 4a, 4b and 5. Also in each table are the corresponding susceptance values calculated from Eq.(50) and (51) with the aperture field approximated by means of solutions to integral equations. The use of Eqs.(50 and (51) requires evaluation of the aperture field integral in Eq.(53). The value of this integral is obtained by evaluating the right-hand side of Eq.(57) with the known values of E_q .

The variational approach used in the derivation of the susceptance expressions in the Waveguide Handbook also involves determining an approximation for the aperture field. For assumed aperture electric field distributions that dif-

fer from the true distribution by a small amount, the resulting susceptance computations are only slightly larger than those that would be computed from the true distribution. It should be recalled from Chapter I that, with the variational approach, a first-order error in the aperture distribution results in only a second-order error in the calculated susceptance. This discussion tends to indicate that the smaller of two calculated susceptance values is the more accurate; however, caution must be exercised since the exact answer is not known. The concept of the true susceptance value being a local minimum is supported by the results presented in Table 6 where complex admittance calculations are given for three variations of the discontinuity in Figure 3a as the number of basis function pulses is increased. Both the real and imaginary parts of the admittance appear to be converging to lower bounds. For the two cases where the frequency is below cutoff, the real part rapidly tends toward zero as the number of pulses is increased. As the number of pulse functions is increased, there is a requirement for a larger number of terms in the Bessel function series to maintain accuracy because representing a narrow pulse with a Fourier-Bessel series requires a greater number of terms than does a wider pulse. It is probable that at some point numerical error will become significant, but, even with this

caveat, the concept of the lower bound on calculated susceptibility being the correct value is supported.

In Tables 7 and 8, the effects of increasing the number of terms in the modified higher-order mode series are demonstrated for two different size pulse expansions in three different apertures. The convergence behavior shown in Table 6 is not present. After a relatively few terms in the series have been computed, an oscillatory behavior is observed which appears to converge toward an ultimate correct value. It is expected that numerical error becomes a factor before the final limit is identified, but, because this convergence behavior manifests itself in relatively few terms, the magnitude of such error appears to be small.

The calculated integral equation data presented in Tables 1 through 5 contain calculations made at the cutoff frequency for the TM_{01} mode in the larger section of waveguide. These calculations are actually made in the limit as the frequency approaches the cutoff point and are courtesy of the small inaccuracies introduced by the computer. The integral equations have terms which are undefined at these transverse resonance frequencies. This attempt to sidestep the singular nature of the equations is rewarded by negative real parts for the admittance in three of the tables. The relatively large real parts (although very small when compared to the imaginary parts) of the admittances calculated

at the cutoff frequencies in Table 5 are also a product of computer error.

It is not possible to draw conclusions on the relative accuracies of the integral equation and Waveguide Handbook approaches without establishing parameters. It appears to be always possible to take sufficient expansion pulses and series terms to calculate an admittance correction which is smaller than the corresponding Waveguide Handbook figure. All calculations made for Tables 1 through 5 and for Tables 10, 11, 12, and 13 used 20 pulses and 30 series terms. This pulse-series combination gives very acceptable results with minimal computer time expenditure.

It is possible to compare integral equation results with more accurate calculations of coaxial discontinuity susceptance. A. Jurkus, Ref.[13], has produced a refinement of P. I. Somlo's computer code, Ref.[10], which employs the Hahn series approach developed by Whinnery, et al., Ref.[8]. Jurkus presents results for the capacitance of a coaxial waveguide with a step in the inner conductor. His calculations contain 10 digits and the numerical precision is claimed to be ± 1 in the fifth digit. In Table 9, comparisons are presented for the results obtained for the Jurkus, integral equation, and Waveguide Handbook approaches. The integral equation calculations were made with 50 pulses and 50 series terms. Jurkus' results, which employed 1000 series terms

compared to Somlo's 40, are uniformly slightly less than 0.3% below the integral equation results. The approach employed by Jurkus, et al., does not involve the solution of a set of simultaneous linear equations, so there can be no straightforward comparison of numerical computation expense. Experience gained during this effort strongly indicates that the magnitude of the computed integral equation capacitance could be reduced below that of Jurkus by using a sufficient number of expansion pulses. It should be noted that the agreement of the integral equation capacitance for both geometries was obtained by different calculations. In Chapter IX, Table 14 presents a number of comparisons of the capacitance of a coaxial-to-circular waveguide junction in which the integral equation results are shown to be very accurate.

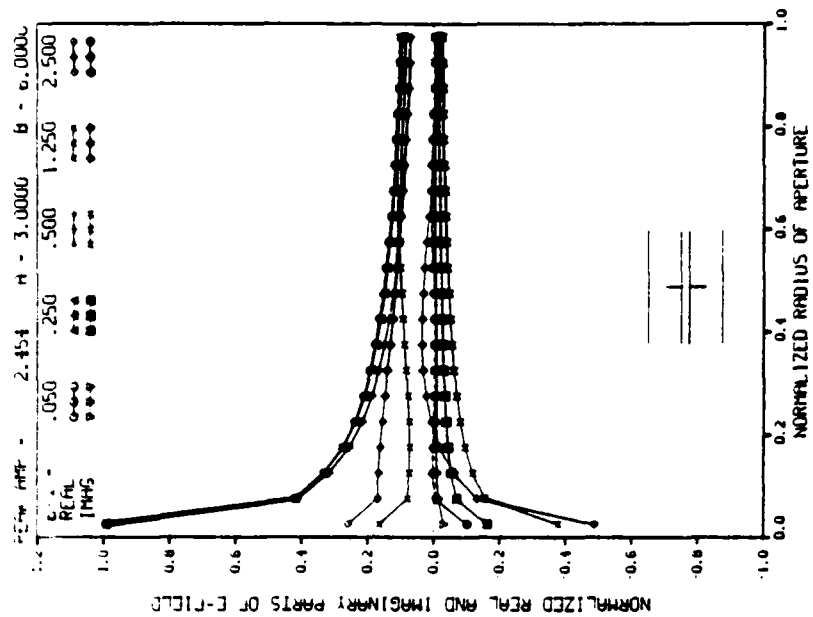


FIGURE 8 CALCULATED DISTRIBUTIONS OF APERTURE ELECTRIC FIELD FOR ANNULAR DISK ON OUTER CONDUCTOR

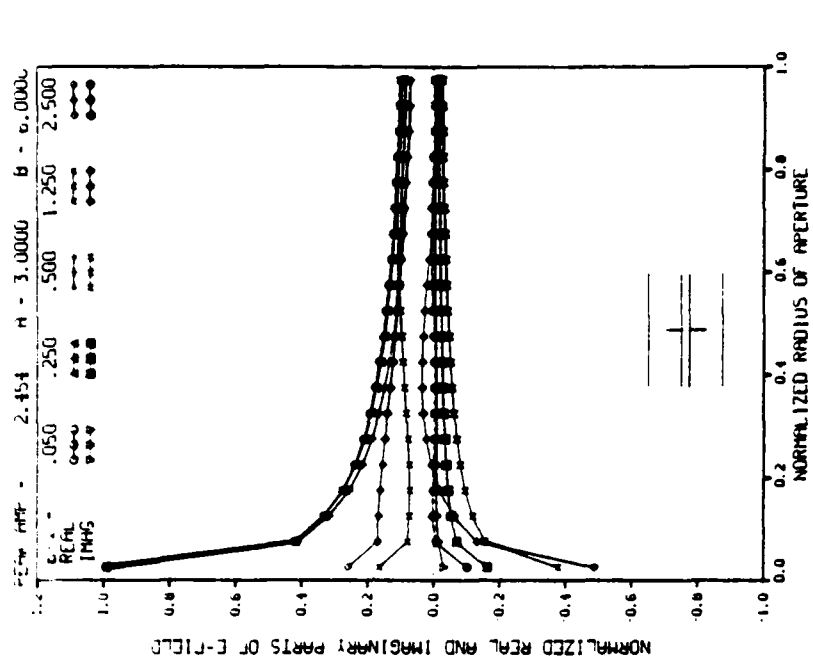


FIGURE 9 CALCULATED DISTRIBUTIONS OF APERTURE ELECTRIC FIELD FOR ANNULAR DISK ON INNER CONDUCTOR

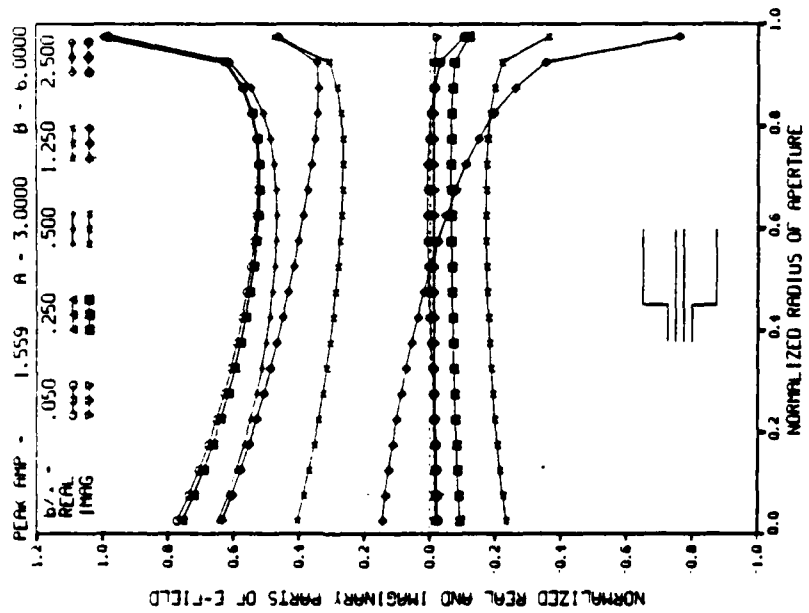


FIGURE 10 CALCULATED DISTRIBUTIONS OF APERTURE ELECTRIC FIELD FOR STEP IN OUTER RADIUS

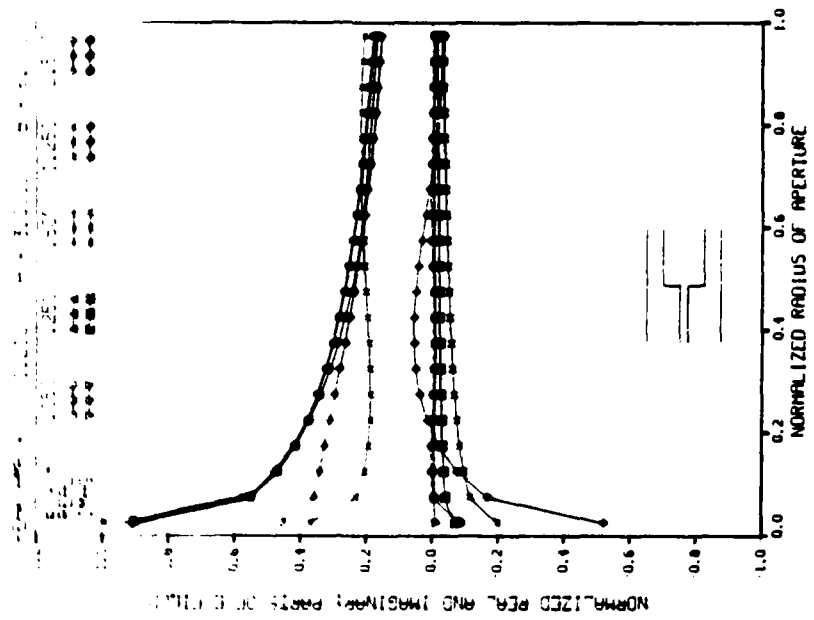


FIGURE 11 CALCULATED DISTRIBUTIONS OF APERTURE ELECTRIC FIELD FOR STEP IN INNER RADIUS

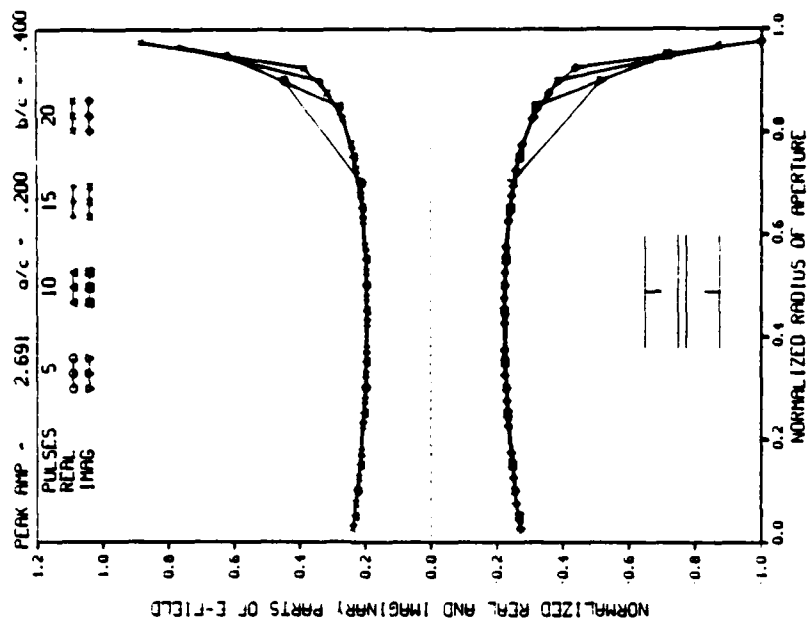


FIGURE 12 CALCULATED DISTRIBUTIONS OF APERTURE ELECTRIC FIELD FOR ONE PORT CAVITY

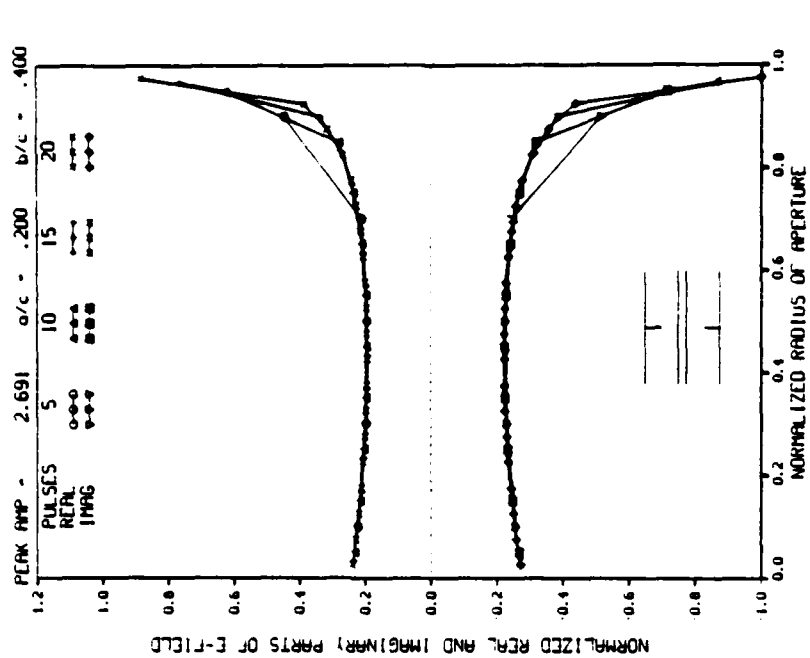


FIGURE 13 CALCULATED DISTRIBUTIONS OF APERTURE ELECTRIC FIELD AS THE NUMBER OF EXPANSION PULSES IS VARIED

TABLE 1. CALCULATED SUSCEPTANCE OF AN ANNULAR DISK ATTACHED TO THE OUTER CONDUCTOR OF A COAXIAL WAVEGUIDE (NORMALIZED)

	a = c/6	b = c/2
c/λ	<u>Waveguide Handbook</u>	<u>Integral Equation</u>
0.0010	0.0 + j0.00156520	0.00058660 + j0.00157331
0.0100	0.0 + j0.01565200	0.00058659 + j0.01565393
0.0500	0.0 + j0.07850436	0.00058634 + j0.07890602
0.1000	0.0 + j0.15850730	0.00058555 + j0.15928538
0.2000	0.0 + j0.33006177	0.00058209 + j0.33135521
0.3000	0.0 + j0.53492015	0.00057511 + j0.53571828
0.4000	0.0 + j0.82068523	0.00056125 + j0.81659679
0.5000	0.0 + j1.38924230	0.00052592 + j1.34509956
0.5600	0.0 + j2.82512207	0.00043400 + j2.38070170
0.5817	Cutoff Freq	-0.00005884 + j7.67352323
0.6000	Above Cutoff	3.11703197 + j1.61050941
0.7000	Above Cutoff	1.64418242 + j0.38996023

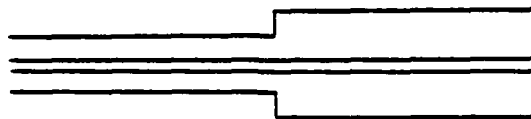
	$a = c/2$	$b = 2c/3$
c/λ	<u>Waveguide Handbook</u>	<u>Integral Equation</u>
0.0010	0.0 + j0.00197451	0.00003314 + j0.00199170
0.0100	0.0 + j0.01974593	0.00003314 + j0.01991780
0.0500	0.0 + j0.09882843	0.00003314 + j0.09968915
0.1000	0.0 + j0.19827879	0.00003313 + j0.20000873
0.2000	0.0 + j0.40167294	0.00003311 + j0.40520104
0.4000	0.0 + j0.84941823	0.00003302 + j0.85702615
0.5000	0.0 + j1.11344261	0.00003293 + j1.12347096
0.6000	0.0 + j1.42841388	0.00003280 + j1.44118492
0.8000	0.0 + j2.43356469	0.00003227 + j2.45173828
0.9000	0.0 + j3.61737121	0.00003151 + j3.62722902
0.9945	Cutoff Freq	0.00001057 + j30.33650604
1.1000	Above Cutoff	4.15095650 + j0.85150308

TABLE 2. CALCULATED SUSCEPTANCE OF AN ANNULAR DISK ATTACHED TO THE
INNER CONDUCTOR OF A COAXIAL WAVEGUIDE (NORMALIZED)

	$a = c/6$	$b = c/2$
c/λ	Waveguide Handbook	Integral Equation
0.0010	$0.0 + j0.00362468$	$0.00027253 + j0.00365967$
0.0100	$0.0 + j0.03625057$	$0.00027254 + j0.03660017$
0.0500	$0.0 + j0.18170876$	$0.00027267 + j0.18342761$
0.1000	$0.0 + j0.36631767$	$0.00027309 + j0.36956776$
0.2000	$0.0 + j0.75753951$	$0.00027487 + j0.76232629$
0.3000	$0.0 + j1.21013329$	$0.00027839 + j1.21116118$
0.4000	$0.0 + j1.80461695$	$0.00028501 + j1.78144529$
0.5000	$0.0 + j2.88524378$	$0.00029977 + j2.67602259$
0.5600	$0.0 + j5.72519939$	$0.00032587 + j3.85053889$
0.5817	Cutoff Freq	$0.00038165 + j5.81638213$
0.6000	Above Cutoff	$2.15903638 + j5.12827991$
0.7000	Above Cutoff	$3.62498168 + j4.91082115$

	$a = c/2$	$b = 2c/3$
c/λ	Waveguide Handbook	Integral Equation
0.0010	$0.0 + j0.00083319$	$0.00007785 + j0.00085388$
0.0100	$0.0 + j0.00833212$	$0.00007785 + j0.00853904$
0.0500	$0.0 + j0.04168796$	$0.00007786 + j0.04272324$
0.1000	$0.0 + j0.08354763$	$0.00007787 + j0.08562268$
0.2000	$0.0 + j0.16849223$	$0.00007795 + j0.17268213$
0.4000	$0.0 + j0.34899602$	$0.00007828 + j0.35781976$
0.5000	$0.0 + j0.44883165$	$0.00007856 + j0.46044428$
0.6000	$0.0 + j0.55951281$	$0.00007895 + j0.57451142$
0.8000	$0.0 + j0.84654291$	$0.00008040 + j0.86911853$
0.9000	$0.0 + j1.08977905$	$0.00008196 + j1.09639242$
0.9945	Cutoff Freq	$0.00008834 + j1.70338315$
1.1000	Above Cutoff	$0.71330318 + j1.61754223$

TABLE 3. CALCULATED SUSCEPTANCE OF A STEP IN THE OUTER RADIUS OF A COAXIAL WAVEGUIDE (NORMALIZED BY THE LEFT-HAND WAVEGUIDE)



c/λ	$a = c/6$		$b = c/2$	
	Waveguide Handbook		Integral Equation	
0.0010	0.0 + j0.00052259		0.00051126 + j0.00052505	
0.0100	0.0 + j0.00522663		0.00051126 + j0.00525117	
0.0500	0.0 + j0.02621644		0.00051116 + j0.02633891	
0.1000	0.0 + j0.05296478		0.00051083 + j0.05320808	
0.2000	0.0 + j0.11056802		0.00050942 + j0.11103353	
0.3000	0.0 + j0.18006588		0.00050655 + j0.18064396	
0.4000	0.0 + j0.27869199		0.00050074 + j0.27879113	
0.5000	0.0 + j0.47982823		0.00048527 + j0.47401488	
0.5600	0.0 + j0.98287410		0.00044321 + j0.90923393	
0.5817	Cutoff Freq		-0.00007031 + j5.68891810	
0.6000	Above Cutoff		1.16333598 + j0.26601990	
0.7000	Above Cutoff		0.53058243 + j0.07136124	

c/λ	$a = c/2$		$b = 2c/3$	
	Waveguide Handbook		Integral Equation	
0.0010	0.0 + j0.00044256		0.00002425 + j0.00044315	
0.0100	0.0 + j0.00442577		0.00002425 + j0.00443165	
0.0500	0.0 + j0.02215205		0.00002425 + j0.02218148	
0.1000	0.0 + j0.04445010		0.00002425 + j0.04450931	
0.2000	0.0 + j0.09010117		0.00002424 + j0.09022265	
0.4000	0.0 + j0.19102869		0.00002420 + j0.19129943	
0.5000	0.0 + j0.25094968		0.00002417 + j0.25131700	
0.6000	0.0 + j0.32292430		0.00002413 + j0.32340570	
0.8000	0.0 + j0.55683513		0.00002394 + j0.55737816	
0.9000	0.0 + j0.84136428		0.00002366 + j0.84018797	
0.9945	Cutoff Freq		0.00000713 + j14.87807544	
1.1000	Above Cutoff		0.90926887 + j0.12537772	

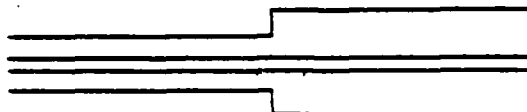
TABLE 4. CALCULATED SUSCEPTANCE OF A STEP IN THE INNER RADIUS OF A COAXIAL WAVEGUIDE (NORMALIZED BY THE LEFT-HAND WAVEGUIDE)



c/λ	$a = c/6$	$b = c/2$
	Waveguide Handbook	Integral Equation
0.0010	0.0 + j0.00209161	0.00044132 + j0.00210399
0.0100	0.0 + j0.02091867	0.00044132 + j0.02104239
0.0500	0.0 + j0.10490495	0.00044144 + j0.10551809
0.1000	0.0 + j0.21179806	0.00044182 + j0.21298804
0.2000	0.0 + j0.44086145	0.00044349 + j0.44287046
0.3000	0.0 + j0.71368241	0.00044685 + j0.71510837
0.4000	0.0 + j1.09143147	0.00045356 + j1.08610510
0.5000	0.0 + j1.82817276	0.00047050 + j1.76514962
0.5600	0.0 + j3.63777780	0.00050965 + j2.99413580
0.5817	Cutoff Freq	0.00067809 + j7.50582984
0.6000	Above Cutoff	3.70562650 + j2.80386573
0.7000	Above Cutoff	2.35142230 + j0.69252237

c/λ	$a = c/2$	$b = 2c/3$
	Waveguide Handbook	Integral Equation
0.0010	0.0 + j0.00050401	0.00010060 + j0.00050544
0.0100	0.0 + j0.00504031	0.00010060 + j0.00505455
0.0500	0.0 + j0.02522438	0.00010060 + j0.02529554
0.1000	0.0 + j0.05059232	0.00010062 + j0.05073454
0.2000	0.0 + j0.10236195	0.00010067 + j0.10264547
0.4000	0.0 + j0.21519440	0.00010092 + j0.21574369
0.5000	0.0 + j0.28051462	0.00010113 + j0.28115931
0.6000	0.0 + j0.35676104	0.00010145 + j0.35739963
0.8000	0.0 + j0.58432744	0.00010275 + j0.58288265
0.9000	0.0 + j0.82080969	0.00010446 + j0.80792331
0.9945	Cutoff Freq	0.00011939 + j2.24993063
1.1000	Above Cutoff	1.06489802 + j0.63059216

TABLE 5. CALCULATED SUSCEPTANCE OF A ONE-PORT COAXIAL CAVITY
(NORMALIZED BY THE INPUT WAVEGUIDE)



	$a = c/6$	$b = c/2$	$d = 3c$
c/λ	<u>Waveguide Handbook</u>	<u>Integral Equation</u>	
0.0010	0.0 - j32.52409365	0.00031693	- j32.53439935
0.0100	0.0 - j 3.20900351	0.00031693	- j 3.20999767
0.0500	0.0 - j 0.41926107	0.00031687	- j 0.41927976
0.1000	0.0 + j 0.25218838	0.00031667	+ j 0.25249477
0.2000	0.0 - j 0.73335669	0.00031579	- j 0.73315769
0.3000	0.0 + j 1.02399059	0.00031401	+ j 1.02483368
0.4000	0.0 + j 0.07946839	0.00031041	+ j 0.07950574
0.5000	0.0 - j 4.9826x10 ⁸	881.54673050	- j 4.9841x10 ⁸
0.5600	0.0 + j 0.69434893	0.00027447	+ j 0.62456391
0.5817	Cutoff Freq	-0.00004352	+ j 5.67004190
0.6000	Above Cutoff	0.00020467	+ j 2.26837281
0.7000	Above Cutoff	0.00035314	- j 1.12708972

	$a = c/2$	$b = 2c/3$
c/λ	<u>Waveguide Handbook</u>	<u>Integral Equation</u>
0.0010	0.0 - j22.01537281	0.00001714 - j22.01574949
0.0100	0.0 - j 2.17127699	0.00001714 - j 2.17130840
0.0500	0.0 - j 0.27939034	0.00001714 - j 0.27936609
0.1000	0.0 + j 0.17930395	0.00001713 + j 0.17936609
0.2000	0.0 - j 0.48114894	0.00001713 - j 0.48103724
0.4000	0.0 + j 0.05617483	0.00001711 + j 0.05644327
0.5000	0.0 - j 3.3727x10 ⁸	403.14432740 - j 3.3728x10 ⁸
0.6000	0.0 + j 0.45777816	0.00001705 + j 0.45826186
0.8000	0.0 + j 1.12808524	0.00001692 + j 1.12863794
0.9000	0.0 + j 0.70651042	0.00001672 + j 0.70533203
0.9945	Cutoff Freq	0.00000501 + j18.90491948
1.1000	Above Cutoff	0.00001645 + j 1.53150570

TABLE 6. CALCULATED SUSCEPTANCE OF AN ANNULAR DISK ON THE OUTER CONDUCTOR OF A COAXIAL WAVEGUIDE AS THE NUMBER OF EXPANSION PULSES IN THE APERTURE IS VARIED (NORMALIZED)

$$a = c/5 \quad b = 4c/5 \quad \lambda = 2c \quad \lambda_{\text{cutoff}} = 1.65c$$

$$\text{Waveguide Handbook Susceptance} = 0.0 + j0.16470255$$

No. of Pulses	$\frac{\Delta}{\lambda}$	Integral Equation Susceptance
5	0.0600	0.01727536 + j0.18367030
10	0.0300	0.00446745 + j0.16502277
15	0.0200	0.00199920 + j0.15899635
20	0.0150	0.00112726 + j0.15601510
25	0.0120	0.00072224 + j0.15423484
30	0.0100	0.00050185 + j0.15305148
35	0.0086	0.00036883 + j0.15220771
40	0.0075	0.00028244 + j0.15157575
50	0.0060	0.00018081 + j0.15069203

$$a = c/5 \quad b = 2c/5 \quad \lambda = 2c \quad \lambda_{\text{cutoff}} = 1.65c$$

$$\text{Waveguide Handbook Susceptance} = 0.0 + j2.27553677$$

No. of Pulses	$\frac{\Delta}{\lambda}$	Integral Equation Susceptance
5	0.0200	0.00307077 + j2.32601738
10	0.0100	0.00076432 + j2.28872639
15	0.0067	0.00033898 + j2.27678771
20	0.0050	0.00019045 + j2.27091264
25	0.0040	0.00012180 + j2.26741777
30	0.0033	0.00008454 + j2.26510059
35	0.0029	0.00006209 + j2.26345157
40	0.0025	0.00004752 + j2.26221827
50	0.0020	0.00003040 + j2.26049647

$$a = c/5 \quad b = 2c/5 \quad \lambda = c/5 \quad \lambda_{\text{cutoff}} = 1.65c$$

$$\text{Waveguide Handbook Susceptance} = \text{Above Cutoff Freq}$$

No. of Pulses	$\frac{\Delta}{\lambda}$	Integral Equation Susceptance
5	0.2000	2.63616915 + j0.18763705
10	0.1000	2.59431266 + j0.17881963
15	0.0667	2.58133988 + j0.17437867
20	0.0500	2.57510034 + j0.17181552
25	0.0400	2.57144336 + j0.17015885
30	0.0333	2.56904400 + j0.16900265
35	0.0286	2.56734976 + j0.16815072
40	0.0250	2.56609013 + j0.16749720
50	0.0200	2.56434298 + j0.16656094

Δ = Width of Pulse 30 Terms were calculated in the series

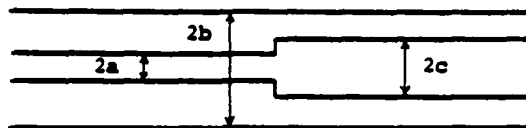
TABLE 7. CALCULATED SUSCEPTANCE OF AN ANNULAR DISK ATTACHED TO THE OUTER CONDUCTOR OF A COAXIAL WAVEGUIDE AS THE NUMBER OF TERMS IN THE HIGHER-ORDER MODE SERIES IS VARIED (NORMALIZED)
APERTURE FIELD EXPANDED IN 20 PULSES

a = c/5 b = 4c/5		a = c/5 b = 2c/5		a = c/5 b = 2c/5	
$\lambda = 20c$	$\lambda_{\text{cutoff}} = 1.65c$	$\lambda = 20c$	$\lambda_{\text{cutoff}} = 1.65c$	$\lambda = c/5$	$\lambda_{\text{cutoff}} = 1.65c$
Waveguide Handbook Susceptance		Waveguide Handbook Susceptance		Waveguide Handbook Susceptance	
0.0 + j0.01280232		0.0 + j0.14230349		Above Cutoff Frequency	
No. Terms in Series	Integral Equation Susceptance	No. Terms in Series	Integral Equation Susceptance	No. Terms in Series	Integral Equation Susceptance
1	0.00118614 + j0.01351677	1	0.00020059 + j0.15513573	1	1.37815686 + j4.44734382
5	0.00116467 + j0.01319154	5	0.00019970 + j0.14343800	5	2.43647412 + j0.37385966
10	0.00116489 + j0.01314581	10	0.00019960 + j0.14332278	10	2.57052629 + j0.16619757
15	0.00116502 + j0.01314133	15	0.00019952 + j0.14334945	15	2.57297198 + j0.17056063
20	0.00116507 + j0.01314024	20	0.00019956 + j0.14334071	20	2.57426588 + j0.17093339
25	0.00116508 + j0.01313959	25	0.00019955 + j0.14334229	25	2.57486588 + j0.17160180
30	0.00116507 + j0.01313960	30	0.00019955 + j0.14334152	30	2.57510034 + j0.17181552
40	0.00116506 + j0.01313975	40	0.00019955 + j0.14334104	40	2.57524851 + j0.17171150
50	0.00116506 + j0.01313969	50	0.00019955 + j0.14334051	50	2.57532391 + j0.17195233

TABLE 8. CALCULATED SUSCEPTANCE OF AN ANNULAR DISK ATTACHED TO THE OUTER CONDUCTOR OF A COAXIAL WAVEGUIDE AS THE NUMBER OF TERMS IN THE HIGHER-ORDER MODE SERIES IS VARIED (NORMALIZED)
APERTURE FIELD EXPANDED IN 50 PULSES

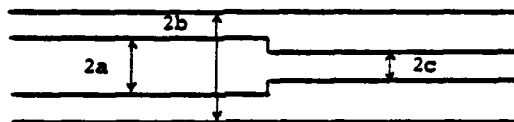
a = c/5 b = 4c/5		a = c/5 b = 2c/5		a = c/5 b = 2c/5	
$\lambda = 20c$	$\lambda_{\text{cutoff}} = 1.65c$	$\lambda = 20c$	$\lambda_{\text{cutoff}} = 1.65c$	$\lambda = c/5$	$\lambda_{\text{cutoff}} = 1.65c$
Waveguide Handbook Susceptance		Waveguide Handbook Susceptance		Waveguide Handbook Susceptance	
0.0 + j0.01280232		0.0 + j .14230349		Above Cutoff Frequency	
No. Terms in Series	Integral Equation Susceptance	No. Terms in Series	Integral Equation Susceptance	No. Terms in Series	Integral Equation Susceptance
1	0.00018993 + j0.01310735	1	0.00003203 + j0.15424329	1	1.37399736 + j4.39469120
5	0.00018667 + j0.01278999	5	0.00003189 + j0.14273483	5	2.42168653 + j0.36707202
10	0.00018669 + j0.01274783	10	0.00003188 + j0.14261662	10	2.55995962 + j0.16163260
15	0.00018671 + j0.01274350	15	0.00003186 + j0.14264501	15	2.56233020 + j0.16542236
20	0.00018671 + j0.01274270	20	0.00003187 + j0.14263675	20	2.56360487 + j0.16577117
25	0.00018672 + j0.01274224	25	0.00003187 + j0.14263748	25	2.56413201 + j0.16636831
30	0.00018672 + j0.01274206	30	0.00003187 + j0.14263699	30	2.56434298 + j0.16656094
40	0.00018671 + j0.01274218	40	0.00003187 + j0.14263666	40	2.56447746 + j0.16663587
50	0.00018671 + j0.01274213	50	0.00003187 + j0.14263606	50	2.56453807 + j0.16666803

TABLE 9. COMPARISONS OF CALCULATED CAPACITANCE OF COAXIAL STEP DISCONTINUITIES WITH RESULTS OF A. JURKUS



a = 0.209672 cm b = 0.714375 cm c = 0.310205 cm

Freq GHz	Jurkus Capacitance femtoFarads	Integral Equation Complex Capacitance femtoFarads	Waveguide Handbook Capacitance femtoFarads
0.000	18.87112905	0.0006691302 + j18.92582501 *	**
1.000	18.87742237	0.0000000008 + j18.93211996	18.96409053
2.000	18.89635437	0.0000000003 + j18.95105772	18.98333401
3.000	18.92808243	0.0000000002 + j18.98279505	19.01559548
4.000	18.97287338	0.0000000002 + j19.02759828	19.06116396



a = 0.310205 cm b = 0.714375 cm c = 0.209672 cm

Freq GHz	Jurkus Capacitance femtoFarads	Integral Equation Complex Capacitance femtoFarads	Waveguide Handbook Capacitance femtoFarads
0.000	18.87101768	0.0006691302 + j18.92582501 *	**
1.000	18.87731097	0.0000000006 + j18.93211996	18.96409053
2.000	18.89624288	0.0000000004 + j18.95105772	18.98333401
3.000	18.92797080	0.0000000002 + j18.98279505	19.01559548
4.000	18.97276154	0.0000000001 + j19.02759828	19.06116396

* Integral Equation calculation at 1000 Hz

** No Result

CHAPTER IV

INTEGRAL EQUATIONS FOR A TWO-PORT COAXIAL CAVITY

A. Introduction

In Chapter II, integral equations are derived for the transverse electric field in the apertures of the coaxial waveguide discontinuities depicted in Figures 3 and 4. Subsequently, it is demonstrated that a one-port coaxial cavity can be formed by adding a shorting plate to a waveguide containing a discontinuity, and the integral equation appropriate for such a geometry is derived. The analysis is now undertaken for the treatment of a two-port, coaxial cavity formed by placing two discontinuities in a coaxial waveguide. Such a geometry is illustrated in Figure 14 where three regions of interest are defined:

Region 1: $z < s$

Region 2: $s < z < t$

Region 3: $z > t$.

B. Expressions for Field Components

In order to describe the field in each of the three regions, three sets of expressions equivalent to those of Eqs.(17)-(22) are required. The following set of equations

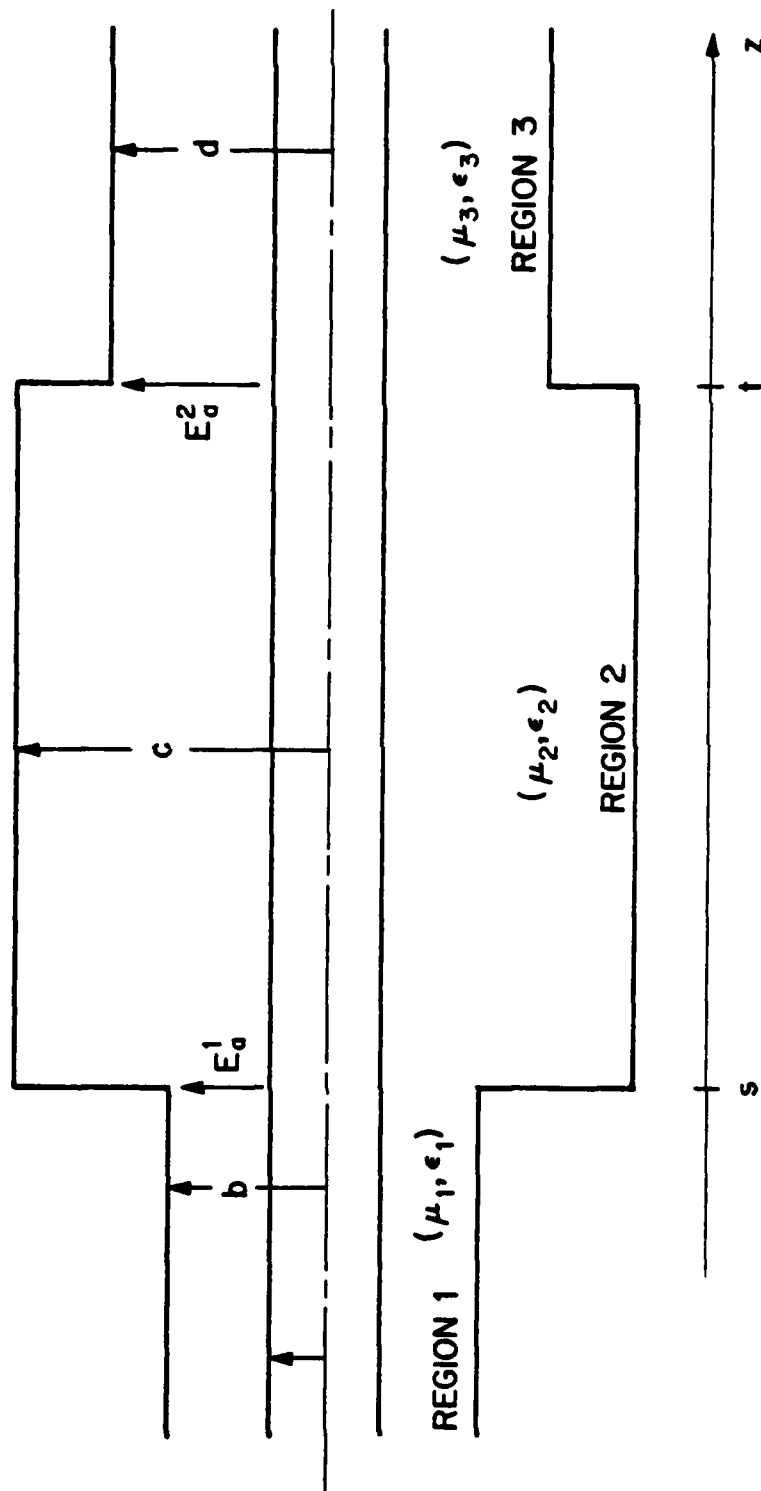


Figure 14. Two-Port, Coaxial Cavity Formed from Two Step Discontinuities in the Outer Conductor of a Coaxial Waveguide

represents the field in each of the three regions where the individual regions are specified by $i = 1, 2, \text{ or } 3$.

$$E_{\rho}^i = B_{i0}^+ \frac{e^{-jk_i z}}{\rho} + B_{i0}^- \frac{e^{jk_i z}}{\rho} + \sum_{n=1}^{\infty} (B_{in}^+ e^{-j\alpha_{in} z} + B_{in}^- e^{j\alpha_{in} z}) \frac{d\phi_{in}}{d\rho}, \quad (63)$$

$$E_z^i = j \sum_{n=1}^{\infty} \frac{\gamma_{in}^2}{\alpha_{in}} (B_{in}^+ e^{-j\alpha_{in} z} - B_{in}^- e^{j\alpha_{in} z}) \phi_{in}, \quad (64)$$

$$H_{\phi}^i = B_{i0}^+ \frac{e^{-jk_i z}}{\eta_i \rho} - B_{i0}^- \frac{e^{jk_i z}}{\eta_i \rho} + \frac{k_i}{\eta_i} \sum_{n=1}^{\infty} \frac{1}{\alpha_{in}} (B_{in}^+ e^{-j\alpha_{in} z} - B_{in}^- e^{j\alpha_{in} z}) \frac{d\phi_{in}}{d\rho}, \quad (65)$$

where

$$\phi_{in}(\rho) = N_0(\gamma_{in} a) J_0(\gamma_{in} \rho) - J_0(\gamma_{in} a) N_0(\gamma_{in} \rho) \quad (66)$$

and

$$\alpha_{in}^2 = k_{in}^2 - \gamma_{in}^2 \quad (67)$$

The ϕ_{in} are the roots of the transcendental equations:

$$\phi_{1n}(b) = N_0(\gamma_{1n} a) J_0(\gamma_{1n} b) - J_0(\gamma_{1n} a) N_0(\gamma_{1n} b) = 0, \quad (68a)$$

$$\phi_{2n}(c) = N_0(\gamma_{2n} a) J_0(\gamma_{2n} c) - J_0(\gamma_{2n} a) N_0(\gamma_{2n} c) = 0, \quad (68b)$$

$$\phi_{3n}(d) = N_0(\gamma_{3n} a) J_0(\gamma_{3n} d) - J_0(\gamma_{3n} a) N_0(\gamma_{3n} d) = 0 \quad (68c)$$

where a, b, c and d are radial dimensions defined in

Figure 14. The dielectric medium in each of the three regions is characterized by the parameters:

$$k_i = \omega \sqrt{\mu_i \epsilon_i} \quad (69a)$$

and

$$\eta = \sqrt{\frac{\mu_i}{\epsilon_i}} \quad (69b)$$

C. Evaluation of Constants in Field Expressions

The procedure for evaluating the expansion constants in Eqs. (63), (64) and (65) for $i = 1, 2$ and 3 is the same as that employed in Chapter II. The unknown aperture field in each of the two discontinuities is designated

$$E_{\rho}^1(\rho, s) = E_{\rho}^2(\rho, s) = E_a^1 \quad (70a)$$

and

$$E_{\rho}^2(\rho, t) = E_{\rho}^3(\rho, t) = E_a^2 \quad (70b)$$

The above notation allows the unknown constants in all three regions to be expressed in terms of weighted integrals over the appropriate aperture fields. A notation is adopted for representing the individual integrals which will allow the resulting equations to be written more compactly. Each integral will be denoted by I_p^i where i is the number of the aperture, $p = 0$ represents a weight function of unity, and $p = mn$ indicates the use of the proper

Bessel function weighting factor. The following expressions are obtained for the constants in each region by application of the Fourier-Bessel series techniques described in Chapter II.

Region 1:

$$B_{1,0}^{+*} e^{-jk_1 s} + B_{1,0}^{-} e^{jk_1 s} = \frac{1}{\ln \frac{b}{a}} \int_a^b E_a^1 d\rho = \frac{1}{\ln \frac{b}{a}} I_0^1 \quad (71a)$$

$$B_{1n}^{+} e^{-j\alpha_{1n} s} + B_{1n}^{-} e^{j\alpha_{1n} s} = \frac{1}{M_{1n}^2} \int_a^b E_a^1 \rho \frac{d\phi_{1n}}{d\rho} d\rho = \frac{1}{M_{1n}^2} I_{1n}^1 \quad (71b)$$

Region 2:

$$B_{2,0}^{+} e^{-jk_2 s} + B_{2,0}^{-} e^{jk_2 s} = \frac{1}{\ln \frac{c}{a}} \int_a^b E_a^1 d\rho = \frac{1}{\ln \frac{c}{a}} I_0^1 \quad (72a)$$

$$B_{2n}^{+} e^{-j\alpha_{2n} s} + B_{2n}^{-} e^{j\alpha_{2n} s} = \frac{1}{M_{2n}^2} \int_a^b E_a^1 \rho \frac{d\phi_{2n}}{d\rho} d\rho = \frac{1}{M_{2n}^2} I_{2n}^1 \quad (72b)$$

$$B_{2,0}^{+} e^{-jk_2 t} + B_{2,0}^{-} e^{jk_2 t} = \frac{1}{\ln \frac{c}{a}} \int_a^d E_a^2 d\rho = \frac{1}{\ln \frac{c}{a}} I_0^2 \quad (73a)$$

$$B_{2n}^{+} e^{-j\alpha_{2n} t} + B_{2n}^{-} e^{j\alpha_{2n} t} = \frac{1}{M_{2n}^2} \int_a^d E_a^2 \rho \frac{d\phi_{2n}}{d\rho} d\rho = \frac{1}{M_{2n}^2} I_{2n}^2 \quad (73b)$$

* The subscript notation 1,0 is used where there is a chance of misinterpretation; otherwise, the comma is omitted in the subscripts of the unknown constants and integral symbols.

Region 3:

$$B_{3,0}^+ e^{-jk_3 t} + B_{3,0}^- e^{jk_3 t} = \frac{1}{\ln \frac{d}{a}} \int_a^d E_a^2 d\rho = \frac{1}{\ln \frac{d}{a}} I_0^2 \quad (74a)$$

$$B_{3n}^+ e^{-j\alpha_{3n} t} + B_{3n}^- e^{j\alpha_{3n} t} = \frac{1}{M_{3n}^2} \int_a^d E_a^2 \rho \frac{d\phi_{3n}}{d\rho} d\rho = \frac{1}{M_{3n}^2} I_{3n}^2 \quad (74b)$$

In Region 1, the constants for the waves traveling in the negative z direction may be expressed in terms of the constants for the positive-traveling waves:

$$B_{1,0}^- = e^{-jk_1 s} \left(\frac{1}{\ln \frac{b}{a}} I_0^1 - B_{1,0}^+ e^{-jk_1 s} \right) \quad (75a)$$

$$B_{1n}^- = e^{-j\alpha_{1n} s} \left(\frac{1}{M_{1n}^2} I_{1n}^1 - B_{1n}^+ e^{-j\alpha_{1n} s} \right) \quad (75b)$$

In Region 2 there are four unknown constants and also four equations given by Eqs. (69) and (70). It is therefore possible to express each constant in terms of aperture-field integrals:

$$B_{2,0}^+ = \frac{1}{j2\sin k_2(t-s) \ln \frac{c}{a}} \left(\pm I_0^1 e^{\pm jk_2 t} \mp I_0^2 e^{\pm jk_2 s} \right) \quad (76a)$$

$$B_{2n}^+ = \frac{1}{j2\sin \alpha_{2n}(t-s) M_{2n}^2} \left(\pm I_{2n}^1 e^{\pm j\alpha_{2n} t} \mp I_{2n}^2 e^{\pm j\alpha_{2n} s} \right) \quad (76b)$$

In Region 3, the constants for the waves traveling in the positive z direction are expressed in terms of the constants

for the negative-traveling waves:

$$B_{3,0}^+ = e^{jk_3 t} \left(\frac{1}{\ln \frac{d}{a}} I_0^2 - B_{3,0}^- e^{jk_3 t} \right) \quad (77a)$$

$$B_{3n}^+ = e^{j\alpha_{3n} t} \left(\frac{1}{M_{3n}^2} I_{3n}^2 - B_{3n}^- e^{j\alpha_{3n} t} \right) . \quad (77b)$$

D. Enforcing Continuity of Transverse Fields in Apertures

The next step in formulating an integral equation for the transverse electric field in each of the two apertures is to require that the transverse component of the magnetic field be continuous across each aperture. The continuity requirement on the transverse electric field already is enforced by Eqs. (70a&b). An equation is now obtained by requiring that $H_\phi^1(\rho, s) = H_\phi^2(\rho, s)$:

$$\begin{aligned} & \frac{2B_{1,0}^+ e^{-jk_1 s}}{\eta_1 \rho} - \frac{1}{\eta_1 \rho \ln \frac{b}{a}} I_0^1 \\ & + \frac{k_1}{\eta_1} \sum_{n=1}^{\infty} \frac{1}{\alpha_{1n}} \left(2B_{1n}^+ e^{-j\alpha_{1n} s} - \frac{1}{M_{1n}^2} I_{1n}^1 \right) \frac{d\phi_{1n}}{d\rho} \\ & = \frac{1}{j2s \ln k_2(t-s) \eta_2 \rho \ln \frac{c}{a}} \left(I_0^1 e^{jk_2(t-s)} - 2I_0^2 + I_0^1 e^{-jk_2(t-s)} \right) \\ & + \frac{k_2}{\eta_2} \sum_{n=1}^{\infty} \frac{1}{j2s \ln \alpha_{2n}(t-s) \alpha_{2n} M_{2n}^2} \left(I_{2n}^1 e^{j\alpha_{2n}(t-s)} - 2I_{2n}^2 \right. \\ & \quad \left. + I_{2n}^1 e^{-j\alpha_{2n}(t-s)} \right) \frac{d\phi_{2n}}{d\rho} \end{aligned}$$

Collecting the terms with unknown constants on the left-hand side yields the equation

$$\begin{aligned}
 & \frac{2B_{1,0}^+ e^{-jk_1 s}}{\eta_1 \rho} + \frac{k_1}{\eta_1} \sum_{n=1}^{\infty} \frac{2}{\alpha_{1n}} B_{1n}^+ e^{-j\alpha_{1n} s} \frac{d\phi_{1n}}{d\rho} \\
 & = \frac{1}{\eta_1 \rho \ln \frac{b}{a}} + \frac{k_1}{\eta_1} \sum_{n=1}^{\infty} \frac{1}{\alpha_{1n} M_{1n}^2} I_{1n}^1 \frac{d\phi_{1n}}{d\rho} \\
 & + \frac{1}{jsink_2(t-s) \eta_2 \rho \ln \frac{c}{a}} \left(I_0^1 \cos k_2(t-s) - I_0^2 \right) \\
 & + \frac{k_2}{\eta_2} \sum_{n=1}^{\infty} \frac{1}{jsin\alpha_{2n}(t-s) \alpha_{2n} M_{2n}^2} \left(I_{2n}^1 \cos\alpha_{2n}(t-s) - I_{2n}^2 \right) \frac{d\phi_{2n}}{d\rho} .
 \end{aligned} \tag{78}$$

Inspection of Eq.(78) reveals that this equation would be identical in form to Eq.(48) if all the constants B_{1n}^+ and the integrals I_0^2 and I_{2n}^2 were equal to zero. The reason for this similarity is that Eq.(78) is the general form of the coupled integral equations obtained when two planar discontinuities are placed in a coaxial waveguide. A shorting plate is a special case of a planar discontinuity and, therefore, Eq.(48) is representative of a two-discontinuity geometry. It follows that the integral equation obtained from constraining $H_\phi^2(\rho, t)$ to be equal to $H_\phi^3(\rho, t)$ has the same form as Eq.(78) and can be written as

$$\begin{aligned}
& \frac{2B_{3,0}^- e^{jk_3 t}}{\eta_3 \rho} + \frac{k_3}{\eta_3} \sum_{n=1}^{\infty} \frac{2}{\alpha_{3n}} B_{3n}^- e^{ja_{3n} t} \frac{d\phi_{3n}}{d\rho} \\
& = \frac{1}{\eta_3 \rho \ln \frac{d}{a}} I_0^2 + \frac{k_3}{\eta_3} \sum_{n=1}^{\infty} \frac{1}{\alpha_{3n} M_{3n}^2} I_{3n}^2 \frac{d\phi_{3n}}{d\rho} \\
& + \frac{1}{jsink_2(t-s) \eta_2 \rho \ln \frac{c}{a}} \left[I_0^2 \cos k_2(t-s) - I_0^1 \right] \\
& + \frac{k_2}{\eta_2} \sum_{n=1}^{\infty} \frac{1}{jsina_{2n}(t-s) \alpha_{2n} M_{2n}^2} \left[I_{2n}^2 \cos \alpha_{2n}(t-s) - I_{2n}^1 \right] \frac{d\phi_{2n}}{d\rho} .
\end{aligned} \tag{79}$$

If the constants $B_{1,0}^+$, B_{1n}^+ , $B_{3,0}^-$ and B_{3n}^- are known, Eqs. (78) and (79) represent two integral equations for the two unknown aperture field distributions. If the output waveguide is matched and there is no excitation incident from the negative z direction, $B_{3,0}^-$ and all B_{3n}^- will be zero. The numerical solution technique described in Chapter III may be applied to each equation in order to obtain expansions of the form of Eq. (54) for each aperture electric field.

Aperture electric field distributions have been calculated for two different size two-port cavities at two frequencies for each cavity and the results are presented in Figures 15 and 16. The two cavities that are treated are symmetric in that the radii b and d as depicted in Figure 14

are equal. The two frequencies are chosen such that one is below and the other is above the cutoff frequency for the first higher-order mode in the larger section of waveguide. The curves in Figures 15 and 16 display more variety than the aperture distributions shown in Figures 11 and 12 which are for similar-size step discontinuities. The distributions in Figures 15 and 16 do, however, possess the same characteristics of decreasing in magnitude as $\frac{1}{\rho}$ at points near the center conductor and then increasing without bound as the discontinuity is approached. In contrast to the aperture distributions for the one-port cavity, there are examples of real and imaginary components crossing the zero axis.

The approximation for the aperture field at $z = s$ allows the calculation of the input admittance of the cavity at that point through the use of Eqs.(50) and (53). A similar expression may be obtained for the input admittance looking into the cavity at $z = t$ by accounting for the directions of wave propagation. Calculated values of input admittance are presented in Table 10 for two different size cavities as a function of frequency. The admittances are computed both from solutions to Eqs.(78) and (79) and from transmission line theory with susceptance corrections from an expression in the Waveguide Handbook. The latter calculations are valid only for frequencies below the cutoff

frequency of the first higher-order mode in the larger cavity. Comparisons between calculated admittance values and measured ones for a two-port coaxial cavity are presented in Chapter VII where the experimental procedures are also described.

The approximations for the aperture fields may be used to calculate the field anywhere in the three regions by using the appropriate form of Eq. (63), (64) or (65) with the corresponding expressions for the constants in these equations. In Chapter VIII, calculated and measured internal field components at the inner surfaces of the end plates of a two-port coaxial cavity are presented. Comparisons between calculated and measured impedance and field data make possible quantitative assessments of the accuracy obtained with integrals of the aperture field solutions. A more direct validation of the accuracy of the aperture field solutions is not within the scope of this effort. Calculated values of the impedance and distributions of field components do provide a definitive estimate of the usefulness of the integral equation solutions since these quantities are of particular interest when characterizing a waveguide section or cavity.

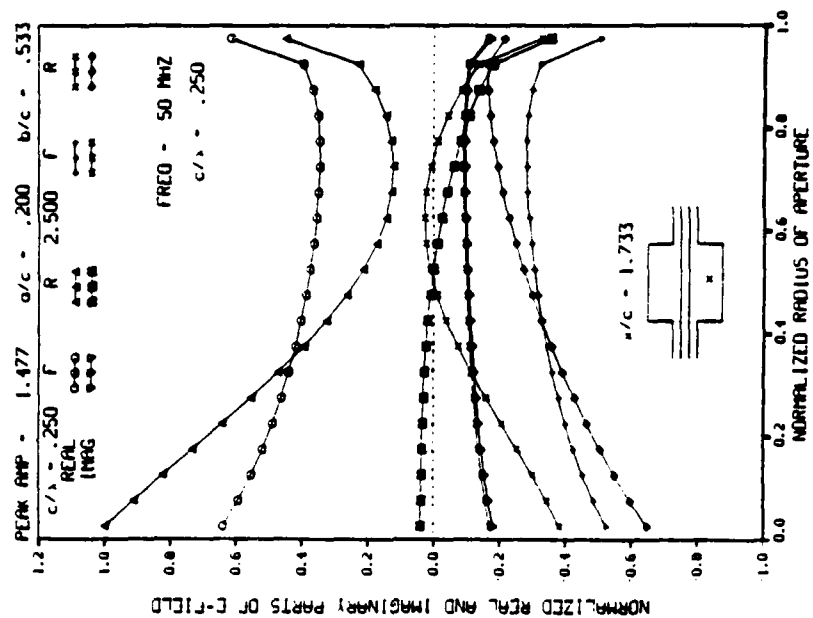


FIGURE 16 CALCULATED DISTRIBUTIONS OF APERTURE ELECTRIC FIELD FOR BOTH APERTURES OF A TWO-PORT CAVITY

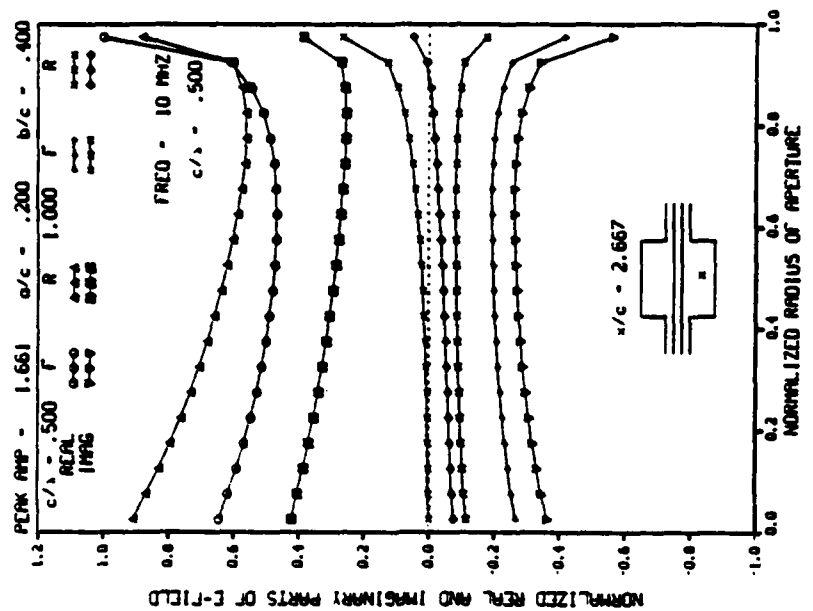
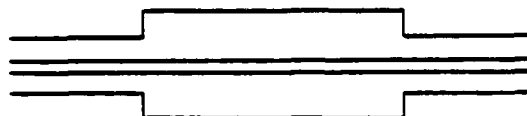


FIGURE 15 CALCULATED DISTRIBUTIONS OF APERTURE ELECTRIC FIELD FOR BOTH APERTURES OF A TWO-PORT CAVITY

TABLE 10. CALCULATED ADMITTANCE OF A TWO-PORT COAXIAL CAVITY
(NORMALIZED BY THE INPUT WAVEGUIDE)



c/λ	$a = c/6$ <u>Waveguide Handbook</u>	$b = c/2$ <u>Waveguide Handbook</u>	$d = 3c$ <u>Integral Equation</u>
0.0010	0.99944272 - j0.01812500		1.00196814 - j0.01813840
0.0100	0.94773463 - j0.16771975		0.95022001 - j0.16784703
0.0500	0.48852657 - j0.21444090		0.49048806 - j0.21455535
0.1000	0.39078594 + j0.15363671		0.39245002 + j0.15414453
0.2000	0.70760169 - j0.21443225		0.71040425 - j0.21394403
0.3000	0.53118295 + j0.48006425		0.53239471 + j0.48203314
0.4000	0.41303114 + j0.04664547		0.41447072 + j0.04752152
0.5000	1.00000000 + j0.95965646		1.00239613 + j0.95982762
0.5600	0.30982384 + j0.47922307		0.40973071 + j0.37257491
0.5817	Cutoff Freq		0.62882691 + j1.31400852
0.6000	Above Cutoff		0.28442809 + j1.19896375
0.7000	Above Cutoff		1.22676713 + j0.26613012

c/λ	$a = c/2$ <u>Waveguide Handbook</u>	$b = 2c/3$ <u>Waveguide Handbook</u>	$d = 3c$ <u>Integral Equation</u>
0.0010	0.99833581 - j0.03663773		0.99847306 - j0.03663551
0.0100	0.85851552 - j0.30720201		0.85865845 - j0.30718608
0.0500	0.24412759 - j0.21118345		0.24422795 - j0.21110388
0.1000	0.18450972 + j0.14622063		0.18457563 + j0.14642800
0.2000	0.40485674 - j0.28635255		0.40510632 - j0.28601009
0.4000	0.18984262 + j0.04551056		0.18990183 + j0.04635422
0.5000	1.00000000 + j0.50189935		1.00013674 + j0.50467629
0.6000	0.15744697 + j0.38570238		0.15731578 + j0.38731123
0.8000	0.21939101 + j0.88059348		0.21886714 + j0.88348416
0.9000	0.12703252 + j0.61676062		0.12713311 + j0.61875045
0.9945	Cutoff Freq		0.60087728 + j5.25158940
1.1000	Above Cutoff		1.21393128 - j0.29987103

CHAPTER V

INTEGRAL EQUATIONS FOR PARTITIONED CAVITIES

A. Introduction

In the preceding chapter, it is demonstrated that the same general form applies for both of the coupled integral equations for the aperture electric fields which are present when two planar discontinuities are placed in a coaxial waveguide. This general form can be used to formulate the appropriate coupled integral equations for any combination of two of the discontinuities depicted in Figures 3 and 4. In this chapter, it is shown that with one additional general form of an integral equation, it is possible to treat any combination of planar discontinuities with no limit on the number. The use of such a procedure is demonstrated by placing annular disks within the geometries depicted in Figures 5 and 14 such that the cavities are further partitioned into two regions which are coupled through the aperture in the partition.

B. Field Components for a Partitioned One-Port Cavity

The one-port, partitioned cavity depicted in Figure 17

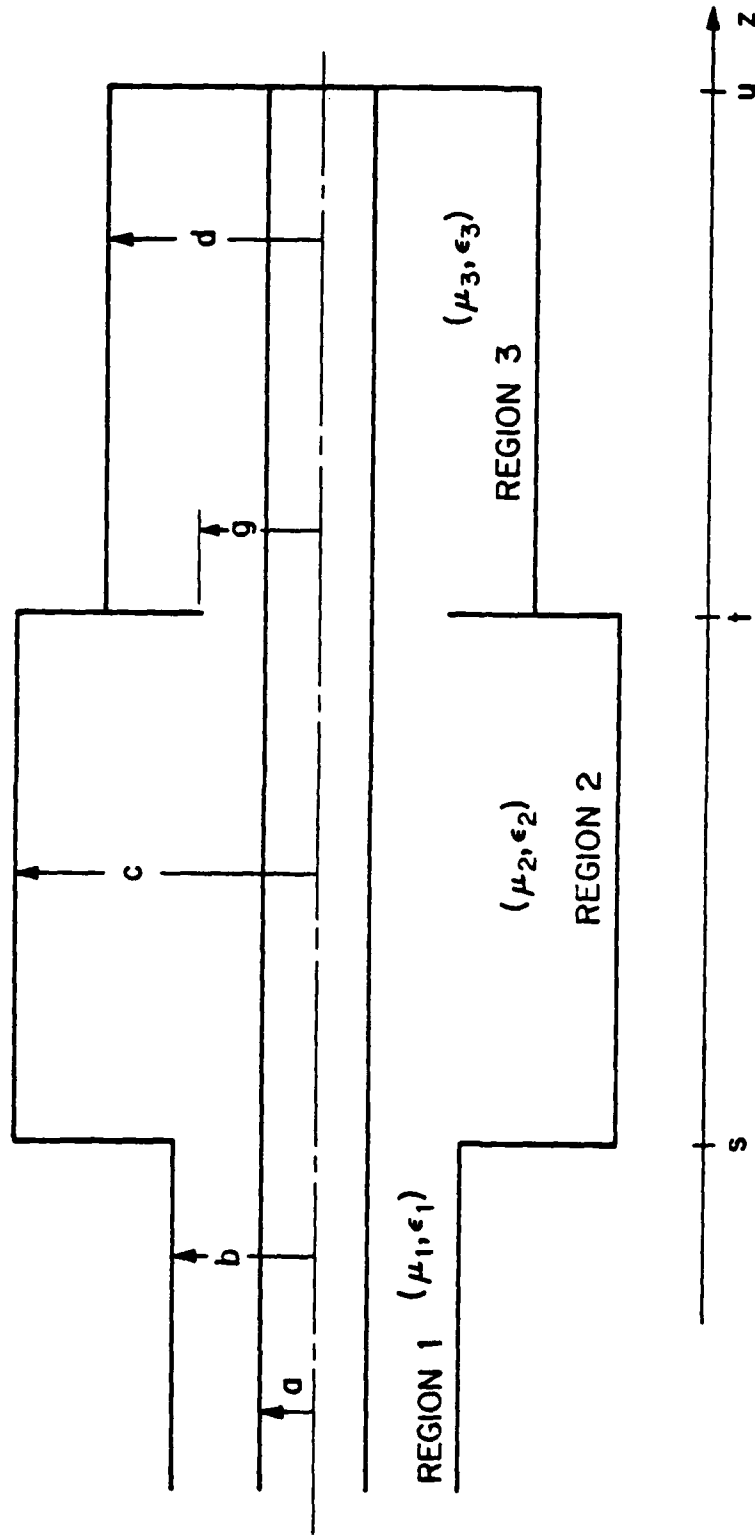


Figure 17. Partitioned, One-Port Coaxial Cavity

is formed by placing a shorting plate across Region 3 of the two-port cavity of Figure 14. An annular disk is attached to the outer conductor at the junction of Regions 2 and 3 to make the problem more general. The field components in the three regions are described by Eqs.(63)-(65) with the accompanying definitions in Eqs.(66)-(69). The unknown aperture electric fields in each of the two discontinuities are designated E_a^1 and E_a^2 with the same definitions as given by Eqs.(70a&b). The expressions for the unknown constants in the field expansion for Region 1 are given by Eqs.(75a&b). The expressions in Eqs.(76a-d) are applicable to Region 2 if the limits of integration for I_0^2 and I_{2n}^2 are changed from (a,d) to (a,g) to reflect the presence of the annular disk. The constants for the field components in Region 3 are derived in the same manner as for the interior region of the one-port cavity in Chapter II. The constants have the same form as those defined in Eqs.(47) and (48) and are given by the following expressions:

$$B_{3,0}^{\pm} = \frac{\pm e^{\pm jk_3 u}}{j2\sin k_3(u-t) \ln \frac{d}{a}} I_0^2 \quad (80a)$$

$$B_{3n}^{\pm} = \frac{\pm e^{\pm j\alpha_{3n} u}}{j2\sin \alpha_{3n}(u-t) M_{3n}^2} I_{3n}^2 \quad (80b)$$

C. Integral Equations for the Aperture Fields

Two coupled integral equations for the transverse electric field components in the two apertures of the geometry depicted in Figure 17 are obtained by constraining the transverse component of magnetic field to be continuous across both apertures. The first integral equation, which is obtained for the aperture connecting Regions 1 and 2, is given by Eq.(78) with the previously mentioned changes to the limits of the integrals I_0^2 and I_{2n}^2 . This is the appropriate form of the integral equation for an aperture which faces another discontinuity in one axial direction and an infinite waveguide in the other direction. The aperture connecting Regions 2 and 3 faces discontinuities in both axial directions, thus a slightly different general form is required for the integral equation. This equation is obtained by requiring $H_\phi^2(\rho, t) = H_\phi^3(\rho, t)$.

$$\begin{aligned} & \frac{1}{j2\sin k_2(t-s) \eta_2 \rho \ln \frac{c}{a}} \left(I_0^1 - e^{-jk_2(t-s)} I_0^2 - e^{jk_2(t-s)} I_0^2 + I_0^1 \right) \\ & + \frac{k_2}{\eta_2} \sum_{n=1}^{\infty} \frac{1}{j2\sin \alpha_{2n}(t-s) \alpha_{2n} M_{2n}^2} \left(I_{2n}^1 - e^{-j\alpha_{2n}(t-s)} I_{2n}^2 \right. \\ & \quad \left. - e^{j\alpha_{2n}(t-s)} I_{2n}^2 + I_{2n}^1 \right) \frac{d\phi_{2n}}{d\rho} \end{aligned}$$

$$\begin{aligned}
&= \frac{I_0^2}{j2\text{sink}_3(u-t) \eta_3 \rho \ln \frac{d}{a}} \left(e^{jk_3(u-t)} + e^{-jk_3(u-t)} \right) \\
&+ \frac{k_3}{\eta_3} \sum_{n=1}^{\infty} \frac{I_{3n}^2}{j2\text{sin}\alpha_{3n}(u-t) \alpha_{3n} M_{3n}^2} \left(e^{j\alpha_{3n}(u-t)} + e^{-j\alpha_{3n}(u-t)} \right) \frac{d\phi_{3n}}{d\rho} .
\end{aligned}$$

As can be seen, this equation contains no unknown constants. Collecting terms yields

$$\begin{aligned}
0 &= \frac{1}{j\text{sink}_2(t-s) \eta_2 \rho \ln \frac{c}{a}} \left(I_0^2 \cos k_2(t-s) - I_0^1 \right) \\
&+ \frac{k_2}{\eta_2} \sum_{n=1}^{\infty} \frac{1}{j\text{sin}\alpha_{2n}(t-s) \alpha_{2n} M_{2n}^2} \left(I_{2n}^2 \cos \alpha_{2n}(t-s) - I_{2n}^1 \right) \frac{d\phi_{2n}}{d\rho} \\
&+ \frac{I_0^2 \cos k_3(u-t)}{j\text{sink}_3(u-t) \eta_3 \rho \ln \frac{d}{a}} + \frac{k_3}{\eta_3} \sum_{n=1}^{\infty} \frac{I_{3n}^2 \cos \alpha_{3n}(u-t)}{j\text{sin}\alpha_{3n}(u-t) \alpha_{3n} M_{3n}^2} \frac{d\phi_{3n}}{d\rho}. \quad (81)
\end{aligned}$$

Because the discontinuity at $z = u$ has no aperture, Eq. (81) does not represent the most general form of the integral equation for an aperture which faces discontinuities in both axial directions. The most general form will be derived in the next section where a partitioned, two-port cavity is treated.

If the constants $B_{1,0}^+$ and B_{1n}^+ are known quantities, Eqs. (78) and (81) represent two integral equations for the two unknown aperture field distributions. Solutions for the aperture fields may be obtained by application of the numer-

AD-A103 058

MISSISSIPPI UNIV UNIVERSITY
AN ANALYTICAL AND EXPERIMENTAL INVESTIGATION OF PLANAR DISCONTI--ETC(U)
MAR 81 M G HARRISON; C M BUTLER AFOSR-77-3464

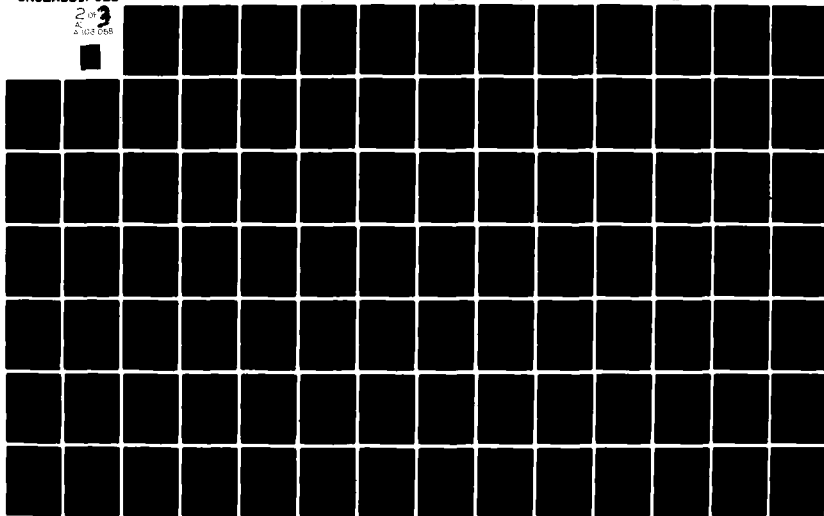
F/O 20/3

UNCLASSIFIED

AFWL-TR-79-187

NL

2 of 3
AD-A103 058



ical procedure described in Chapter III. Aperture electric field distributions which have been calculated for two different size partitioned, one-port cavities at two frequencies each are presented in Figures 18 and 19. The two radii c and d in Figure 17 are equal for each of the cavities but the apertures are of different size. One of the frequencies is above and the other is below the cutoff frequency or the first higher-order mode in the larger section of waveguide. The aperture distributions are very similar in form to those shown in Figure 8 for the annular disk and in Figure 12 for the simple one-port cavity. The singular behavior of the distributions differs in the two apertures because of the different geometry of the discontinuities. No zero crossing of the real or imaginary parts is observed, as was the case in Figure 12 for the simple one-port cavity.

The input admittance of the cavity can be computed from the approximate solution for the aperture electric field at $z = s$. Calculated values of input admittance are presented in Table 11 for two different size cavities as a function of frequency. As in previous examples, the admittance values are computed both from solutions to integral equations and from transmission line theory with susceptance corrections from the Waveguide Handbook. The admittance data appear to support earlier observations that the transmission line theory with corrections is more accurate than the integral

equation approach for geometries where the aperture is a significant percentage of the radius of the larger section of waveguide. The integral equation solutions appear to give better results than the transmission line theory when the aperture is a comparatively small part of the waveguide radius. There is a pronounced peak in the input admittance at frequencies where there is an axial resonance. The calculated admittance at these frequencies has a real part that is much greater than zero but is still many orders of magnitude smaller than the imaginary part. These calculations actually give only a qualitative description of the admittance at axial resonance because the value actually approaches infinity. The numerical error introduced by the digital computer allows a calculation to be made.

D. Field Components for a Partitioned Two-Port Cavity

A two-port partitioned cavity may be created from the geometry depicted in Figure 17 by removing the shorting plate at $z = u$ and connecting Region 3 to an infinitely-long section of waveguide of a different size. Such a cavity is illustrated in Figure 20. The field components in the four regions are described by Eqs.(63)-(65) with i now equal to 1, 2, 3 and 4. The unknown aperture electric field at $z = u$ is defined

$$E_{\rho}^3(\rho, u) = E_{\rho}^4(\rho, u) = E_a^3 \quad . \quad (82)$$

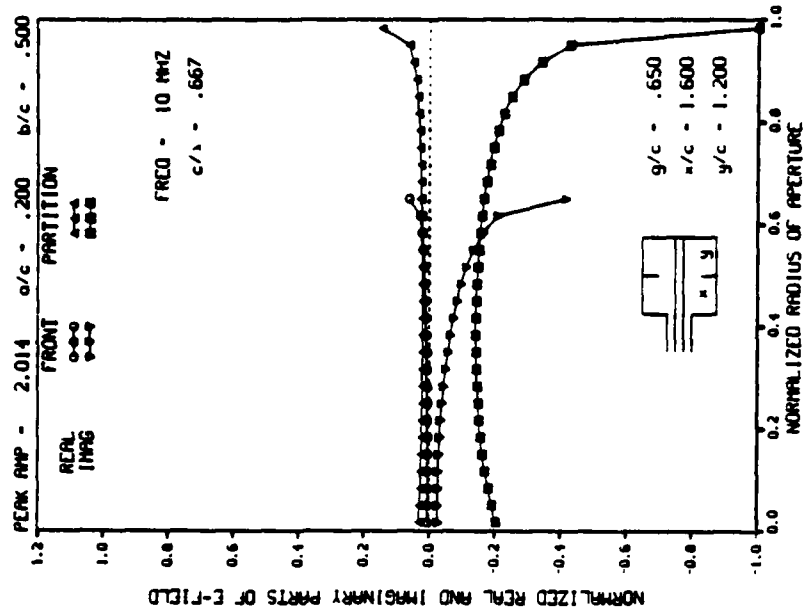


FIGURE 18 CALCULATED DISTRIBUTIONS OF APERTURE ELECTRIC FIELD FOR THE APERTURES OF A ONE-PORT PARTITIONED CAVITY

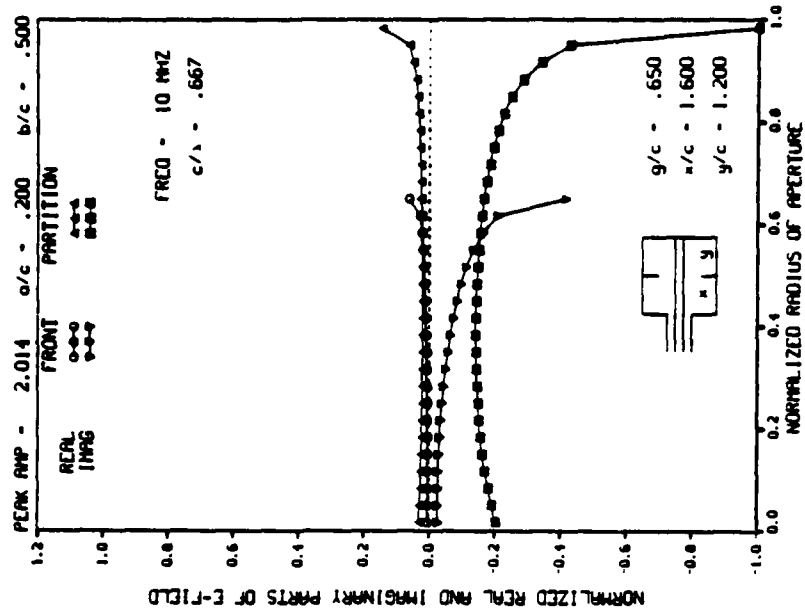


FIGURE 19 CALCULATED DISTRIBUTIONS OF APERTURE ELECTRIC FIELD FOR THE APERTURES OF A ONE-PORT PARTITIONED CAVITY

TABLE 11. CALCULATED ADMITTANCE OF A PARTITIONED, ONE-PORT
COAXIAL CAVITY (NORMALIZED BY THE INPUT WAVEGUIDE)



$a = c/2$	$b = 2c/3$	$d = 5c/6$	$x = 3c/2$	$y = 3c/2$
c/λ	<u>Waveguide Handbook</u>	<u>Integral Equation</u>		
0.0010	0.0 + j 0.04542289	0.00000014 + j 0.04541979		
0.0100	0.0 + j 0.46065099	0.00001455 + j 0.46062760		
0.0500	0.0 + j 3.61464770	0.00089707 + j 3.61712020		
0.1000	0.0 - j 5.20242693	0.00184342 - j 5.18534685		
0.2000	0.0 + j 2.49915937	0.00043327 + j 2.51429549		
0.4000	0.0 - j 11.66961875	0.00889162 - j 11.39779337		
0.5000	0.0 + j 0.62501141	0.00002848 + j 0.64550426		
0.6000	0.0 - j 2.00806112	0.00027188 - j 1.99606828		
0.8000	0.0 - j 0.41045183	0.00001040 - j 0.39189766		
0.9000	0.0 - j 1.21202495	0.00009623 - j 1.19927743		
0.9945	Cutoff Freq	0.00000000 + j 0.00008060		
1.1000	Above Cutoff	0.00022378 - j 1.81561836		

$a = c/2$	$b = 2c/3$	$d = 5c/6$	$x = 2c$	$x = c$
c/λ	<u>Waveguide Handbook</u>	<u>Integral Equation</u>		
0.0010	0.0 + j 0.04542285	0.00000014 + j 0.04541974		
0.0100	0.0 + j 0.46059965	0.00001454 + j 0.46057495		
0.0500	0.0 + j 3.59553783	0.00088736 + j 3.59749163		
0.1000	0.0 - j 5.37370058	0.00196982 - j 5.36018579		
0.2000	0.0 + j 2.52256821	0.00044187 + j 2.53908775		
0.4000	0.0 - j 12.30740830	0.00992517 - j 12.04200640		
0.5000	0.0 + j 0.00000000	0.00000000 + j 0.00000000		
0.6000	0.0 - j 1.95779087	0.00025766 - j 1.94321006		
0.8000	0.0 - j 0.52793367	0.00001805 - j 0.51626468		
0.9000	0.0 - j 1.29588364	0.00011173 - j 1.29207960		
0.9945	Cutoff Freq	0.00000000 - j 0.00020133		
1.1000	Above Cutoff	0.00001291 - j 0.45044112		

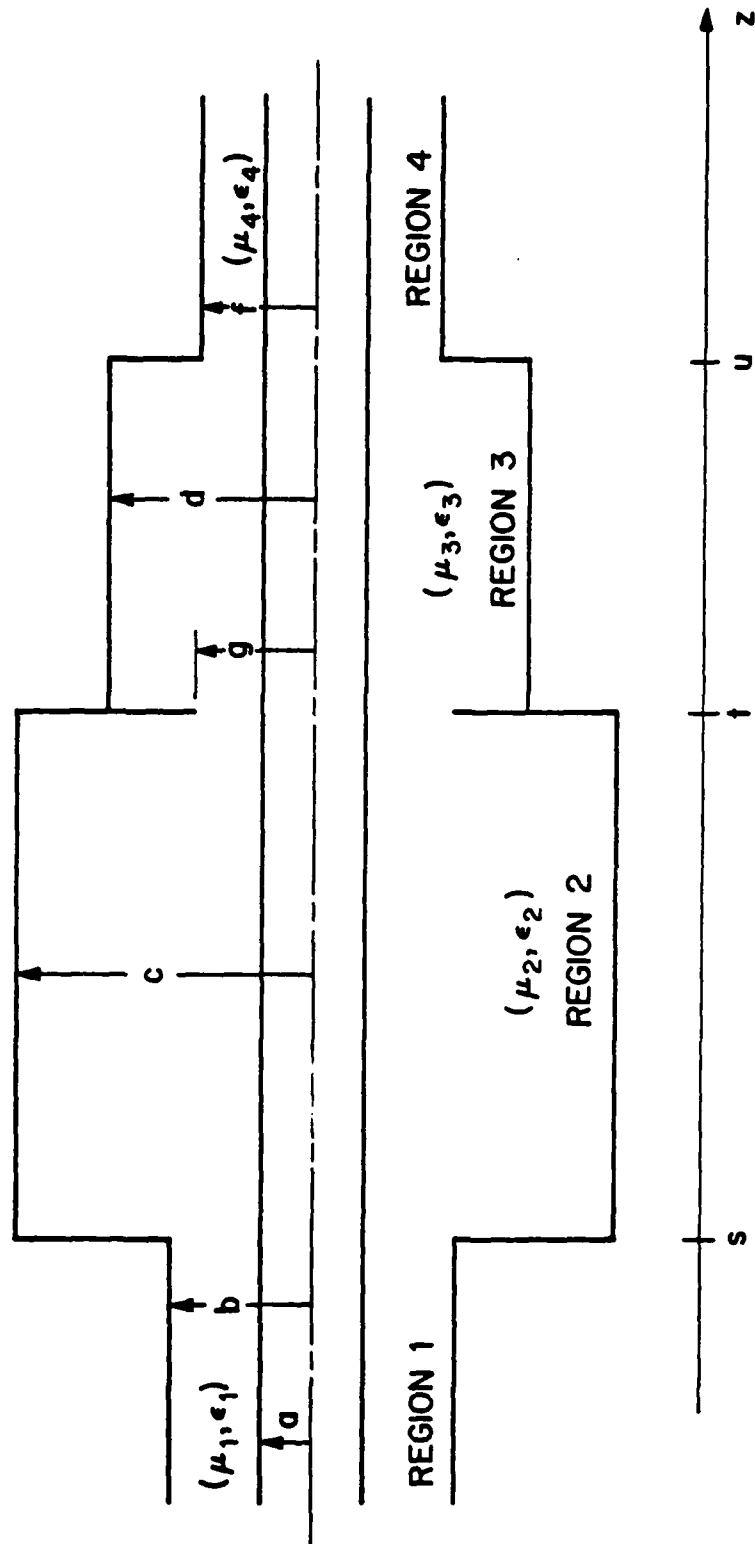


Figure 20 Partitioned, Two-Port, Coaxial Cavity

The expressions for the unknown constants in the field expansions for Regions 1 and 2 are the same as for the one-port, partitioned cavity. The constants for Region 3 are defined similarly to those of Region 2 since the region is bounded on both ends by apertures.

$$B_{3,0}^{\pm} = \frac{1}{j2\sin k_3(u-t) \ln \frac{d}{a}} \left(\pm I_0^2 e^{\pm jk_3 u} \mp I_0^3 e^{\pm jk_3 t} \right) \quad (83a)$$

$$B_{3n}^{\pm} = \frac{1}{j2\sin \alpha_{3n}(u-t) M_{3n}^2} \left(\pm I_{3n}^2 e^{\pm j\alpha_{3n} u} \mp I_{3n}^3 e^{\pm j\alpha_{3n} t} \right). \quad (83b)$$

The expressions for the constants in Region 4 are similar to those defined in Eq.(74):

$$B_{4,0}^{+} = e^{jk_4 u} \left(\frac{1}{\ln \frac{f}{a}} I_0^3 - B_{4,0}^{-} e^{jk_4 u} \right) \quad (84a)$$

$$B_{4n}^{+} = e^{j\alpha_{4n} u} \left(\frac{1}{M_{4n}^2} I_{4n}^3 - B_{4n}^{-} e^{j\alpha_{4n} u} \right). \quad (84b)$$

E. Integral Equations for the Aperture Fields

The structure depicted in Figure 20 has three apertures with unknown fields, and, by following previously established procedures, one can derive three coupled integral equations for these unknown fields. The equation for the aperture at $z = s$ is again given by Eq.(78). It is apparent at this point that the form of Eq.(78) is not influenced by any

geometrical features beyond the discontinuity at $z = t$, although the final solutions for the aperture fields certainly are. The aperture at $z = t$ faces discontinuities containing apertures in both axial directions. The integral equation appropriate for this aperture is the most general of the equations to be developed for treatment of such apertures in discontinuities. The equation is obtained by requiring that $H_{\phi}^2(\rho, t) = H_{\phi}^3(\rho, t)$:

$$\begin{aligned}
0 = & \frac{1}{jsink_2(t-s) \eta_2 \rho \ln \frac{c}{a}} \left(I_0^2 \cos k_2(t-s) - I_0^1 \right) \\
& + \frac{k_2}{\eta_2} \sum_{n=1}^{\infty} \frac{1}{jsina_{2n}(t-s) \alpha_{2n} M_{2n}^2} \left(I_{2n}^2 \cos \alpha_{2n}(t-s) - I_{2n}^1 \right) \frac{d\phi_{2n}}{d\rho} \\
& + \frac{1}{jsink_3(u-t) \eta_3 \rho \ln \frac{d}{a}} \left(I_0^3 \cos k_3(u-t) - I_0^2 \right) \\
& + \frac{k_3}{\eta_3} \sum_{n=1}^{\infty} \frac{1}{jsina_{3n}(u-t) \alpha_{3n} M_{3n}^2} \left(I_{3n}^3 \cos \alpha_{3n}(u-t) - I_{3n}^2 \right) \frac{d\phi_{3n}}{d\rho}. \quad (85)
\end{aligned}$$

The fact that weighted integrals of all three aperture fields appear in Eq.(85) clearly demonstrates the interdependence of these fields. If more apertures were added, the interdependence would still be present although integrals of all aperture fields would not appear in the same equation. The integral equation obtained by constraining continuity of

the transverse magnetic field across the aperture at $z = u$ is of the same form as Eq.(79) and is given by

$$\begin{aligned}
& \frac{2B_{4,0}^- e^{jk_4 u}}{\eta_4 \rho} + \frac{k_4}{\eta_4} \sum_{n=1}^{\infty} \frac{2B_{4n}^-}{\alpha_{4n}} e^{j\alpha_{4n} u} \frac{d\phi_{4n}}{d\rho} \\
&= \frac{1}{\eta_4 \rho \ln \frac{f}{a}} I_0^3 + \frac{k_4}{\eta_4} \sum_{n=1}^{\infty} \frac{1}{\alpha_{4n} M_{4n}^2} I_{4n}^3 \frac{d\phi_{4n}}{d\rho} \\
&+ \frac{1}{j \sin k_3 (u-t) \eta_3 \rho \ln \frac{d}{a}} \left(I_0^3 \cos k_3 (u-t) - I_0^2 \right) \\
&+ \frac{k_3}{\eta_3} \sum_{n=1}^{\infty} \frac{1}{j \sin \alpha_{3n} (u-t) \alpha_{3n} M_{3n}^2} \left(I_{3n}^3 \cos \alpha_{3n} (u-t) - I_{3n}^2 \right) \frac{d\phi_{3n}}{d\rho}. \quad (86)
\end{aligned}$$

With the assumption that the constants $B_{1,0}^+$, B_{1n}^+ , $B_{4,0}^-$ and B_{4n}^- are known quantities, Eq.(78), (85) and (86) form the set of equations necessary to obtain solutions for the three unknown aperture fields. The numerical technique of Chapter III is again suitable for obtaining solutions. There is no additional difficulty involved with treating three simultaneous equations beyond the "bookkeeping" problems. Simple logic advises that the optimum solutions for a given total number of expansion pulses would be obtained by dividing each of the apertures into pulses that are of approximately equal width. This effect actually is diminished significantly because the equations involve integrals of the aperture

fields. It has been demonstrated in earlier tables of admittance values that the integrals of the aperture fields are not very sensitive to the number of expansion pulses (above a usually small minimum number). The result of this situation is that very good solutions can be obtained with pulse distributions that vary widely for different apertures of the same cavity configuration. If there were reason to concentrate attention on one cavity region, the non-adjointing aperture could be adequately treated with comparatively few expansion pulses.

Aperture electric field distributions which have been calculated for two different size, partitioned, two-port cavities are presented in Figures 21 and 22. These cavities have been created by adding annular disks to the outer conductors of the two-port cavities of Figures 15 and 16 so that the effects of partitioning such cavities can be observed. The resulting aperture distributions are very frequency dependent as the first transverse resonance frequency is approached and for frequencies beyond. A qualitative idea of the aperture field variation with frequency can be interpreted from the comparisons of measured and calculated field components in Chapter VIII which are given for a number of frequencies.

The input admittance at either port can be computed from the approximation to the aperture electric field at that port.

In Table 12 comparisons are presented for admittance values calculated from solutions to integral equations and computed from transmission line theory with susceptance corrections from the Waveguide Handbook. This data again appears to demonstrate that the integral equation approach is superior to the transmission line approach when the aperture is small enough that the singular behavior of the aperture field caused by the discontinuity is seen over most of the aperture.

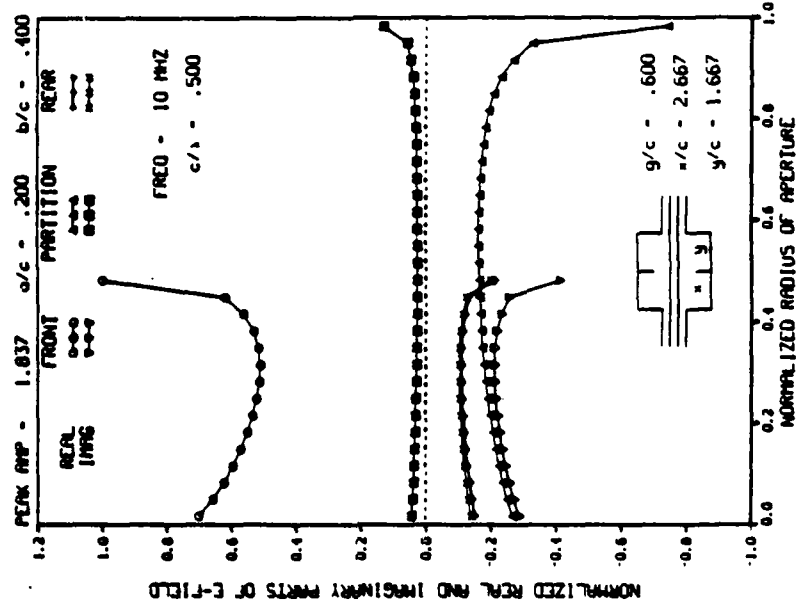


FIGURE 21 CALCULATED DISTRIBUTIONS OF APERTURE ELECTRIC FIELD FOR THE APERTURES OF A TWO-PORT PARTITIONED CAVITY

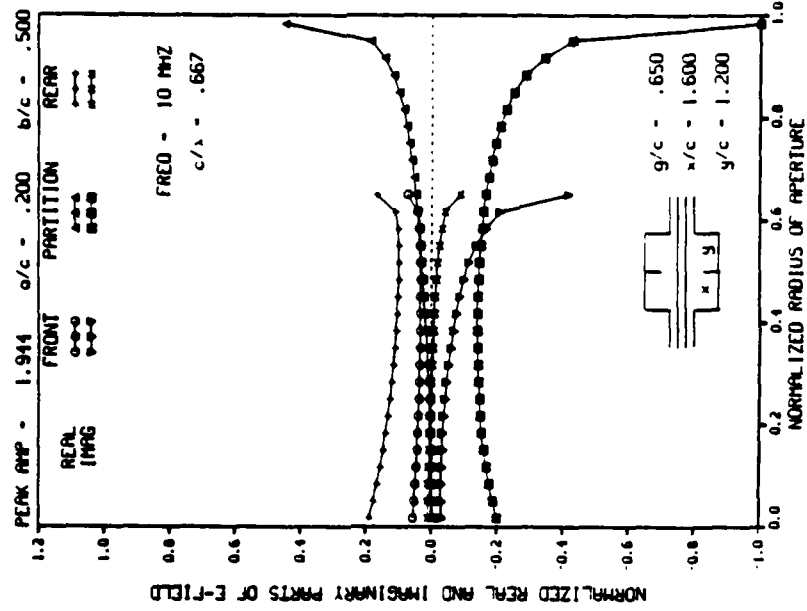
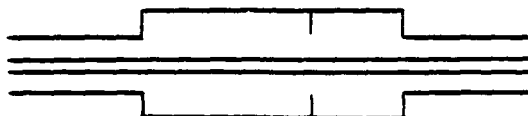


FIGURE 22 CALCULATED DISTRIBUTIONS OF APERTURE ELECTRIC FIELD FOR THE APERTURES OF A TWO-PORT PARTITIONED CAVITY

TABLE 12. CALCULATED ADMITTANCE OF A PARTITIONED, TWO-PART COAXIAL CAVITY (NORMALIZED BY THE INPUT WAVEGUIDE)



$a = c/2$	$b = 2c/3$	$d = 5c/6$	$x = 3c/2$	$y = 3c/2$
c/λ	<u>Waveguide Handbook</u>	<u>Integral Equation</u>		
0.0010	0.99834364 - j0.03646526	0.99889305 - j0.03645737		
0.0100	0.85913835 - j0.30578823	0.85970885 - j0.30573056		
0.0500	0.24708957 - j0.20829428	0.24755160 - j0.20801032		
0.1000	0.19468650 + j0.15497574	0.19523825 + j0.15561873		
0.2000	0.33681097 - j0.26536484	0.33590023 - j0.26378041		
0.4000	0.21549346 + j0.06722641	0.21648982 + j0.07016078		
0.5000	0.96235858 - j0.06022518	0.95726980 - j0.06694721		
0.6000	0.12576944 + j0.43536054	0.12489168 + j0.44122015		
0.8000	0.58503247 + j1.01100177	0.59984037 + j1.02307863		
0.9000	0.06010651 + j0.77547372	0.05651798 + j0.79681264		
0.9945	Cutoff Freq	0.52758674 + j6.67688686		
1.1000	Above Cutoff	0.94391508 + j0.03856458		
$a = c/2$	$b = 2c/3$	$d = 5c/6$	$x = 2c$	$x = c$
c/λ	<u>Waveguide Handbook</u>	<u>Integral Equation</u>		
0.0010	0.99834625 - j0.03646544	0.99889565 - j0.03645841		
0.0100	0.85932100 - j0.30592364	0.85989129 - j0.30587505		
0.0500	0.24701063 - j0.21024318	0.24745830 - j0.21000502		
0.1000	0.19266498 + j0.14812225	0.19314166 + j0.14879100		
0.2000	0.35572846 - j0.23677548	0.35517085 - j0.23466776		
0.4000	0.15438273 + j0.06244383	0.15359618 + j0.06533893		
0.5000	1.00000000 + j0.59496446	1.00054745 + j0.60669547		
0.6000	0.20108709 + j0.39082365	0.20211057 + j0.39476634		
0.8000	0.46097070 + j1.23927333	0.47402267 + j1.24904843		
0.9000	0.06190716 + j0.71737474	0.06739482 + j0.72441466		
0.9945	Cutoff Freq	0.60245035 + j5.48157554		
1.1000	Above Cutoff	0.23160684 + j0.48464206		

CHAPTER VI

INTEGRAL EQUATION FOR A TRUNCATED COAXIAL INNER CONDUCTOR

A. Introduction

The discontinuities which are the subjects of the analyses in the preceding chapters are all coaxial in nature. It is demonstrated that, in theory, any combination of planar, coaxial discontinuities can be treated by proper application of one or more of the general equation forms developed in Chapters II, IV and V. An additional type of discontinuity is formed by truncating the center conductor of a coaxial waveguide and it can be treated by a similar approach to that used for the coaxial discontinuities. The analysis for such a structure is presented in this chapter, and it is subsequently demonstrated that the expressions which are derived for the circular waveguide region are analogous to those derived for the coaxial regions, noting that there are no corresponding TEM terms. This fact facilitates the derivation of integral equations for waveguides where the previously-treated discontinuities and the truncated center conductor are mixed.

B. Expressions for Field Components

A coaxial waveguide with a truncated inner conductor is depicted in Figure 23. The outer radius of the waveguide is also reduced in the plane of the truncation to demonstrate that other discontinuities can be treated simultaneously. For Region 1 ($z < s$), the field component definitions of Eqs. (17)-(22) are appropriate. For the circular waveguide region, ($z > s$), the field components must be derived from an appropriate magnetic vector potential which is a solution to Eq. (1). The axial component of magnetic vector potential is sufficient to provide a complete field definition, as is demonstrated for the coaxial case in Appendix A. The magnetic vector potential component is defined as the product (no variation with ϕ):

$$A_z^C(\rho, z) = R^C(\rho) Z(z) \quad (87)$$

where the axial function, $Z(z)$, which satisfies Eq. (2), has the form

$$Z(z) = c_1 e^{-jk_z z} + c_2 e^{jk_z z} \quad (88)$$

and the radial function, $R^C(\rho)$, is a solution of Eq. (3) and has the form

$$R^C(\rho) = c_3 J_0(k_\rho \rho) + c_4 N_0(k_\rho \rho) \quad (89)$$

The boundary condition that the field have a finite value at $\rho = 0$ eliminates $N_0(k_\rho \rho)$ as a possible solution.

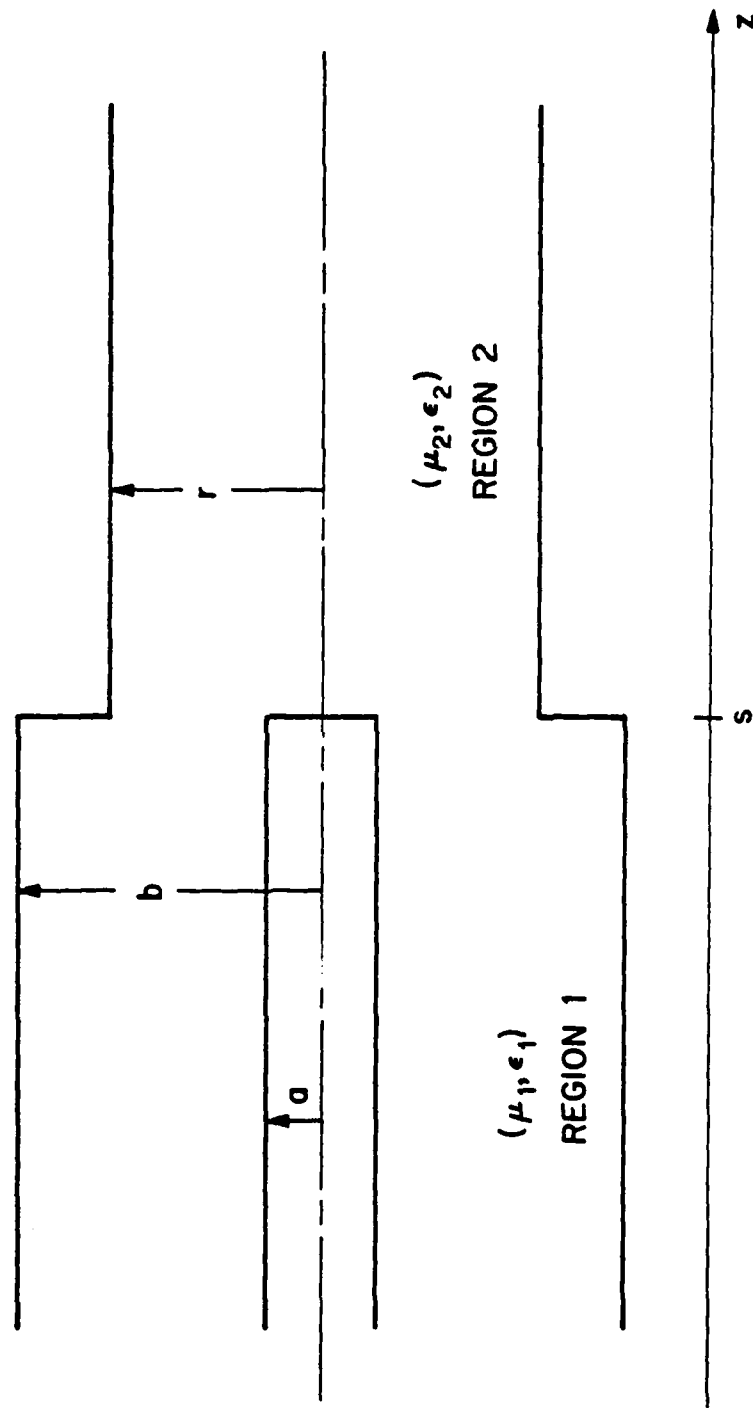


Figure 23. Discontinuity Formed in Coaxial Waveguide by Truncating Center Conductor

A second boundary condition requires that the tangential component (in this case, E_z) of the electric field be zero at the inner surface of the waveguide (at $\rho = c$). The resulting function is

$$R^C(\rho) = c_3 J_0(\lambda_n \rho) \quad (90)$$

where the λ_n are the infinite set of k_ρ which satisfy

$$J_0(\lambda_n c) = 0, \quad n = 1, 2, \dots \quad (91)$$

The eigenvalue representation for k_z is now given by

$$k_z^2 = \beta_n^2 = k^2 - \lambda_n^2.$$

The following definitions for β_n are used

$$\beta_n = \sqrt{k_2^2 - \lambda_n^2}, \quad k_2^2 > \lambda_n^2 \quad (92a)$$

$$\beta_n = -j \sqrt{\lambda_n^2 - k_2^2}, \quad \lambda_n^2 > k_2^2. \quad (92b)$$

The resulting expression for the magnetic vector potential is

$$A_z^C(\rho, z) = \sum_{n=1}^{\infty} (c_n^+ e^{-j\beta_n z} + c_n^- e^{j\beta_n z}) J_0(\lambda_n \rho). \quad (93)$$

The field components for Region 2 can now be computed from Eqs.(11), (12), and (13) operating on Eq.(93). The resulting expressions are

$$E_{\rho}^2 = \frac{\omega}{k_2^2} \sum_{n=1}^{\infty} \beta_n (-c_n^+ e^{-j\beta_n z} + c_n^- e^{j\beta_n z}) \{-\lambda_n J_1(\lambda_n \rho)\}$$

$$E_z^2 = -\frac{j\omega}{k_2^2} \sum_{n=1}^{\infty} (k_2^2 - \beta_n^2) (c_n^+ e^{-j\beta_n z} + c_n^- e^{j\beta_n z}) J_0(\lambda_n \rho)$$

$$H_{\phi}^2 = -\frac{1}{\mu_2} \sum_{n=1}^{\infty} (c_n^+ e^{-j\beta_n z} + c_n^- e^{j\beta_n z}) \{-\lambda_n J_1(\lambda_n \rho)\} .$$

The constants c_n^+ and c_n^- are now redefined to give the field expressions a more standard form:

$$c_n^+ = \frac{-k_2^2}{\omega \beta_n} C_n^+ \quad (94a)$$

and

$$c_n^- = \frac{k_2^2}{\omega \beta_n} C_n^- . \quad (94b)$$

The field components are now given by

$$E_{\rho}^2 = \sum_{n=1}^{\infty} -\lambda_n (C_n^+ e^{-j\beta_n z} + C_n^- e^{j\beta_n z}) J_1(\lambda_n \rho) \quad (95)$$

$$E_z^2 = j \sum_{n=1}^{\infty} \frac{\lambda_n^2}{\beta_n} (C_n^+ e^{-j\beta_n z} - C_n^- e^{j\beta_n z}) J_0(\lambda_n \rho) \quad (96)$$

$$H_{\phi}^2 = \frac{k_2}{\eta_2} \sum_{n=1}^{\infty} \frac{-\lambda_n}{\beta_n} (C_n^+ e^{-j\beta_n z} - C_n^- e^{j\beta_n z}) J_1(\lambda_n \rho) . \quad (97)$$

C. Definitions of Constants in Field Expressions

The procedure to obtain useful definitions for the unknown constants of Eqs.(95)-(97) employs similar orthogo-

nality properties to those of the method used in Chapter II.

The first step is to multiply both sides of Eq.(95) by $\rho J_1(\lambda_m \rho)$ and then integrate both sides over the interval $(0, c)$. This yields

$$\int_0^c E_\rho^2 \rho J_1(\lambda_m \rho) d\rho = \quad (98)$$

$$\int_0^c \rho \sum_{n=1}^{\infty} -\lambda_n (C_n^+ e^{-j\beta_n s} + C_n^- e^{j\beta_n s}) J_1(\lambda_m \rho) J_1(\lambda_n \rho) d\rho, \quad m=1,2,\dots$$

Because of the orthogonality properties of the integral on the right-hand side, Eq.(98) has zero value except when $m = n$. The constants may now be defined by

$$C_n^+ e^{-j\beta_n s} + C_n^- e^{j\beta_n s} = \frac{1}{-\lambda_n \int_0^c \rho [J_1(\lambda_n \rho)]^2 d\rho} \int_a^c E_a^0 \rho J_1(\lambda_n \rho) d\rho \quad (99)$$

where the radial component of the electric field in the aperture is defined by

$$E_\rho^2(\rho) = \begin{cases} E_a^0, & a < \rho < c \\ 0, & 0 < \rho < a \end{cases} \quad (100)$$

The normalization integral in Eq.(99) has the value:

$$-\lambda_n \int_0^c \rho [J_1(\lambda_n \rho)]^2 d\rho = -\lambda_n \frac{c^2}{2} J_1^2(\lambda_n c) \quad (101)$$

D. Enforce Continuity of Transverse Fields in the Aperture

An equation containing the integral of the unknown aperture electric field is obtained by constraining the transverse component of magnetic field to be continuous across the aperture, i.e., $H_{\phi}^1(\rho, s) = H_{\phi}^2(\rho, s)$. This yields

$$B_0^+ \frac{e^{-jk_1 s}}{\eta \rho} - B_0^- \frac{e^{jk_1 s}}{\eta \rho} + \frac{k_1}{\eta_1} \sum_{n=1}^{\infty} \frac{1}{\alpha_n} (B_n^+ e^{-j\alpha_n s} - B_n^- e^{j\alpha_n s}) \frac{d\phi_n}{d\rho} \\ = \frac{k_2}{\eta_2} \sum_{n=1}^{\infty} \frac{-\lambda_n}{\beta_n} (C_n^+ e^{-j\beta_n s} - C_n^- e^{j\beta_n s}) J_1(\lambda_n \rho), \quad \rho \in (a, c). \quad (102)$$

An integral equation appropriate for the geometry of Figure 23 is easily obtained from Eq.(102) if the waves incident on the aperture from both directions are fully defined. As an example, assume that the excitation traveling in the +z direction in Region 1 consists of a TEM wave with amplitude B_0^+ . The existence of only a TEM mode implies that all the $B_n^+ = 0$. It is also assumed that the waveguide on the right-hand side of the aperture is either infinitely long or terminated in a matched load, either of which implies that all the $C_n^- = 0$. The resulting integral equation for the coaxial waveguide with a truncated inner conductor is, from Eq.(99),

$$\begin{aligned}
& 2B_0^+ \frac{e^{-jk_1 s}}{\eta_1 \rho} - \frac{1}{\eta_1 \rho \ln \frac{b}{a}} \int_a^c E_a^O d\rho \\
& + \frac{k_1}{\eta_1} \sum_{n=1}^{\infty} \left(\frac{-1}{\alpha_n M_n^2} \int_a^c E_a^O \rho \frac{d\phi_n}{d\rho} d\rho \right) \frac{d\phi_n(\rho)}{d\rho} \\
& = \frac{k_2}{\eta_2} \sum_{n=1}^{\infty} \left(\frac{2}{\beta_n c^2 J_1^2(\lambda_n c)} \int_a^c E_a^O \rho J_1(\lambda_n \rho) d\rho \right) J_1(\lambda_n \rho) \quad (103)
\end{aligned}$$

E. Application to a One-Port Cavity

The geometry depicted in Figure 24 possesses two discontinuities: the first, at $z = s$, is the now-familiar step-discontinuity in the outer conductor of a coaxial waveguide; and the second, at $z = t$, is the truncated center conductor of a coaxial line. The two unknown aperture field distributions are obtained from solutions to a pair of coupled integral equations which are derived according to previously determined procedures. It is convenient to define the field components in Regions 1 and 2 with the expressions in Eqs.(63)-(65) with $i = 1$ and 2. The constants in these expressions are defined in Eqs.(71)-(73) where the notation for the weighted integrals of the aperture fields retains the same meaning. The field components for Region 3 are given by Eqs(95)-(97) where the subscripts and superscripts which denote parameters corresponding to a particular region are changed from 2 to 3. The constants in Eqs.(95)-(97) are evaluated by application of the boundary condition requiring zero tangential electric

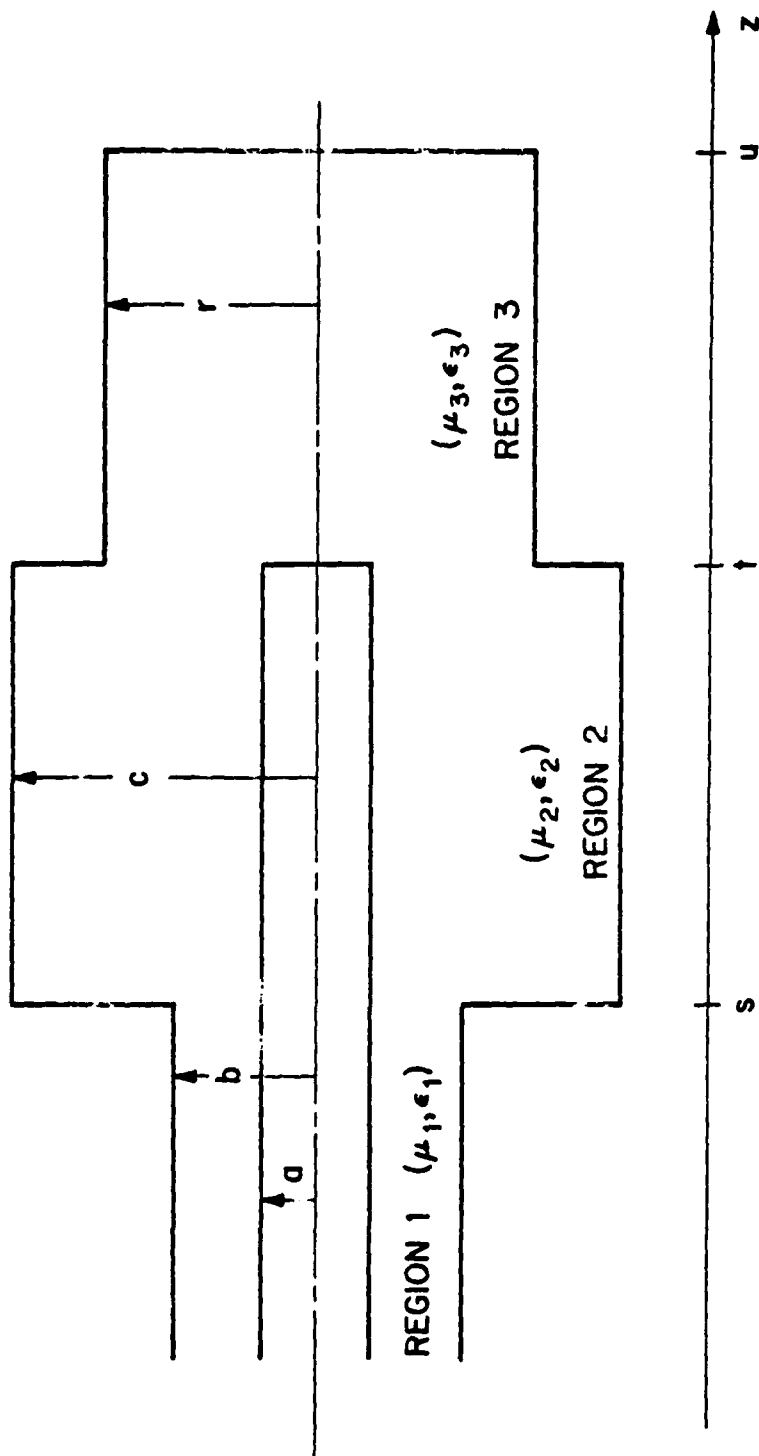


Figure 24. One-Port, Coaxial Cavity with the Coaxial Center Conductor Truncated

field on the plate at $z = u$. These constants, which are analogous in form to those defined in Eq.(48), are given by

$$C_n^{\pm} = \frac{\pm e^{\pm j\beta_n u}}{-j\lambda_n d^2 \sin\beta_n(u-t) J_1^2(\lambda_n d)} \int_a^d E_a^2 \rho J_1(\lambda_n \rho) d\rho \quad (104)$$

The first of the required pair of integral equations is given by Eq.(78) with $z = s$. The second integral equation, which results from the substitution of the proper expressions for the constants into Eq.(102) with $z = t$, is quite similar to Eq.(81):

$$\begin{aligned} 0 = & \frac{1}{jsink_2(t-s) \eta_2 \rho \ln \frac{c}{a}} \left(I_0^2 \cos k_2(t-s) - I_0^1 \right) \\ & + \frac{k_2}{\eta_2} \sum_{n=1}^{\infty} \frac{1}{jsin\alpha_{2n}(t-s) \alpha_{2n} M_{2n}^2} \left(I_{2n}^2 \cos \alpha_{2n}(t-s) - I_{2n}^1 \right) \frac{d\phi_{2n}}{d\rho} \\ & + \frac{k_3}{\eta_3} \sum_{n=1}^{\infty} \left(\frac{2\cos\beta_n(u-t)}{j\sin\beta_n(u-t) d^2 \beta_n J_1^2(\lambda_n d)} \int_a^d E_a^2 \rho J_1(\lambda_n \rho) d\rho \right) J_1(\lambda_n \rho) . \end{aligned} \quad (105)$$

where the λ_n are the solutions to

$$J_0(\lambda_n d) = 0, \quad n = 1, 2, \dots$$

and the β_n are defined by Eq.(92).

It is a straightforward procedure to combine the discontinuity depicted in Figure 23 with any or all of the coaxial discontinuities illustrated in Figures 3 and 4 to create an arbitrarily complex cavity structure. The equa-

tion for the truncated center conductor would be included where necessary to obtain a tractable set of integral equations. A similar treatment of the junction of two circular waveguides of differing radii can be accomplished with a simple extension of the material presented in this chapter. Such a configuration was not of interest during this investigation primarily because circular waveguides do not support the TEM mode.

F. Numerical Solution Considerations

The numerical procedure employed to obtain solutions to Eqs.(103) and (104) is, in principle, the same technique described in Chapter III. The expansion for the aperture electric field defined by Eqs.(55) and (56) is appropriate. The resulting integral is easily evaluated to yield

$$\begin{aligned} \int_a^d \sum_{q=1}^N E_q P_q(\rho) J_1(\lambda_n \rho) d\rho &= \sum_{q=1}^N E_q \int_{r_q - \Delta/2}^{r_q + \Delta/2} J_1(\lambda_n \rho) d\rho \\ &= \sum_{q=1}^N E_q \frac{-1}{\lambda_n} [J_0(\lambda_n r_q^+) - J_0(\lambda_n r_q^-)] \quad (106) \end{aligned}$$

where

$$r_q^+ = r_q + \Delta/2$$

$$r_q^- = r_q - \Delta/2$$

The testing function set given by Eq.(61) is used to

generate the N algebraic equations necessary to obtain a solution for the aperture field. The two sets of algebraic equations obtained from Eqs.(78) and (105) are sufficient to obtain solutions for both aperture electric fields when the constants of Eq.(78) are defined. In Figures 25 and 26 are presented calculated aperture field distributions for the coaxial-to-circular waveguide junction of Figure 23 without the step in the outer conductor and the one-port cavity of Figure 24.

G. Susceptance of a Truncated Center Conductor

The lumped TEM susceptance introduced into a transmission line when the coaxial center conductor is truncated can be calculated by following the procedure described in Chapter II. Once the aperture distribution is obtained, its integral can be used to evaluate the voltage reflection coefficient through Eq.(54) and the susceptance can then be computed with the aid of Eq.(51) where the characteristic admittance (in the TEM sense of the circular waveguide section, Y_0^+ , is equal to zero. The resulting expression is

$$\frac{jB}{Y_0^-} = \frac{1 - \Gamma(s)}{1 + \Gamma(s)} . \quad (107)$$

The expression on the right-hand side of Eq.(107) is the definition of the normalized admittance at $z = s$ expressed in terms of the voltage reflection coefficient. For frequencies

below the cutoff frequency for the first propagating mode in the circular waveguide, the TEM admittance is imaginary. At frequencies above cutoff for one or more circular waveguide modes, a portion of the incident energy is converted to a propagating mode(s) in the circular waveguide. Under the latter circumstance, the admittance is complex. Whereas previous susceptance expressions are generally applicable to TEM waves incident from either direction, the expression in Eq.(107) is only valid for a TEM wave incident from the coaxial waveguide side of a truncated center conductor discontinuity. In Table 13 are presented TEM admittance values calculated from solutions to integral equations for four different ratios of outer coaxial radius to inner radius. There is no corresponding expression in the Waveguide Handbook for comparison, although Marcuvitz does provide a susceptance expression for a coaxial-to-circular waveguide junction where the inner conductor is also a circular waveguide. The $b/\lambda = 0.3827$ frequency for each geometry is the cutoff frequency for the TM_{01} mode in the circular waveguide. As for the other planar discontinuities, the admittance has a non-zero real part when power is converted to propagating higher-order modes.

As mentioned in Chapter I, the coaxial-to-circular waveguide junction has been treated by a number of other investigators. In Table 14 comparisons of calculated capacitance

are presented for six junctions of varying size along with measured values for three of the junctions. The integral equation results are computed with 20 pulses across the aperture and 30 series terms and with 50 pulses and 50 series terms. The two calculations give a qualitative feel for the convergence of the integral equation approach. The integral equation results compare extremely well with the other values in the table and indicate that this approach would be very useful when extreme accuracy is desired.

TABLE 13. CALCULATED ADMITTANCE OF COAXIAL-TO-CIRCULAR WAVEGUIDE JUNCTIONS
(NORMALIZED BY THE COAXIAL WAVEGUIDE)

b/λ	$a = 10 \text{ m}$	$b = 60 \text{ m}$	b/λ	$a = 10 \text{ m}$	$b = 30 \text{ m}$
0.0100	0.00191089 + j0.01744352		0.0050	0.00040563 + j0.01046958	
0.0500	0.00191390 + j0.08771871		0.0250	0.00040576 + j0.05243914	
0.1000	0.00192371 + j0.17870852		0.0500	0.00040616 + j0.10543503	
0.2000	0.00197098 + j0.38887531		0.1000	0.00040787 + j0.21573702	
0.3000	0.00210462 + j0.71558373		0.2000	0.00041627 + j0.47874712	
0.3500	0.00231081 + j1.06790249		0.2500	0.00042511 + j0.65986060	
0.3600	0.00240087 + j1.20129638		0.3000	0.00044171 + j0.92837452	
0.3800	0.00291225 + j1.86998604		0.3500	0.00048546 + j1.49467353	
0.3827	0.00348897 + j2.55084881		0.3750	0.00057774 + j2.50984587	
0.4000	1.31789521 + j1.45873287		0.3800	0.00065154 + j3.27713698	
0.5000	1.09293073 + j0.44577374		0.3827	0.00090171 + j5.78165555	
0.6000	0.77851831 + j0.31616103		0.4000	2.47358062 + j1.29941802	

b/λ	$a = 0.001521$	$b = 0.0025$	b/λ	$a = 3 \text{ m}$	$b = 30 \text{ m}$
0.0058	0.00019634 + j0.01256161		0.0050	0.00514131 + j0.00738530	
0.0292	0.00019640 + j0.06296577		0.0250	0.00514312 + j0.03697297	
0.0583	0.00019660 + j0.12693355		0.0500	0.00514884 + j0.07423933	
0.1167	0.00019744 + j0.26241962		0.1000	0.00517258 + j0.15092167	
0.1750	0.00019907 + j0.41843924		0.2000	0.00528542 + j0.32521859	
0.2333	0.00020206 + j0.61781907		0.2500	0.00539763 + j0.43577291	
0.2917	0.00020806 + j0.92164639		0.3000	0.00559469 + j0.58465831	
0.3500	0.00022628 + j1.64172801		0.3500	0.00605477 + j0.84802125	
0.3617	0.00023668 + j2.00888777		0.3750	0.00682852 + j1.19680288	
0.3733	0.00025969 + j2.78448222		0.3800	0.00731500 + j1.39072306	
0.3827	0.00048351 + j9.88536282		0.3827	0.00841109 + j1.79451644	
0.4083	2.38129436 + j0.58735311		0.4000	0.89278293 + j1.22679813	

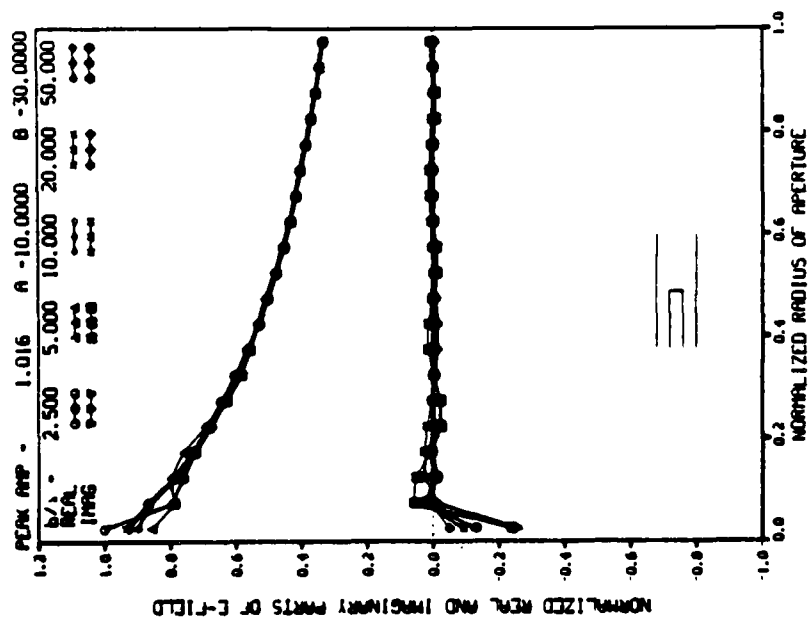


FIGURE 25 CALCULATED DISTRIBUTIONS OF APERTURE ELECTRIC FIELD FOR TRUNCATED INNER CONDUCTOR

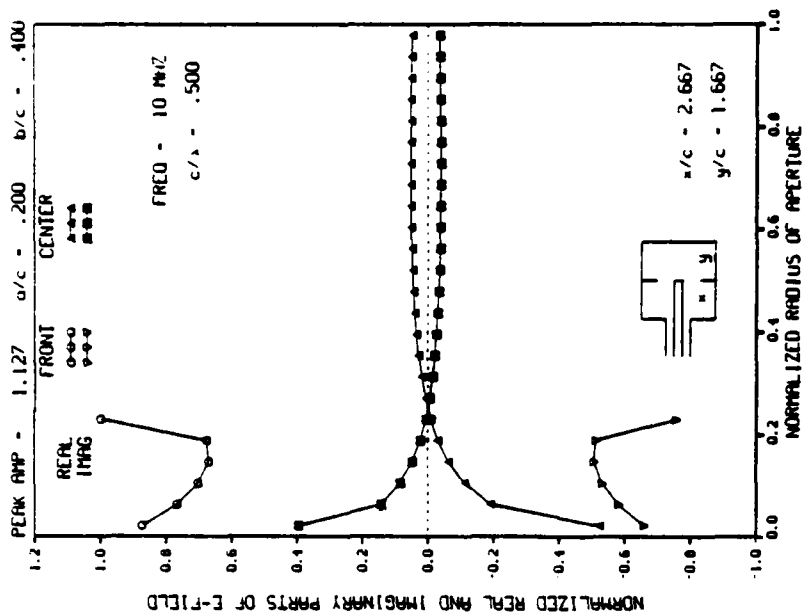


FIGURE 26 CALCULATED DISTRIBUTIONS OF APERTURE ELECTRIC FIELD FOR THE APERTURES OF A COAXIAL-TO-CIRCULAR CAVITY

TABLE 14. COMPARISONS OF CALCULATED AND MEASURED CAPACITANCE
FOR A COAXIAL-TO-CIRCULAR WAVEGUIDE JUNCTION

Waveguide Parameters	Freq Hz	Risley Upper Bound	Somlo	Woods	Razaz and Davies	Measurement	Harrison and Butler 20P×30S 50P×50S
a = 1.521 mm b = 3.500 mm Z _C = 50.0 Ω	10 ³ 10 ⁹	80.66 80.70	79.70 *	79.7 79.7	79.88 79.917		79.940 79.738 79.985 79.770
a = 3.042 mm b = 7.000 mm Z _C = 50.0 Ω	10 ³ 10 ⁹	164.56 164.85	159.40 *	159.4 *	159.76 160.039		159.896 159.474 160.172 159.741
a = 3.1047 mm b = 7.1438 mm Z _C = 50.0 Ω	10 ³ 10 ⁹	* *	162.67 *	162.7 163.0	163.04 163.336	162.4±0.5 Zorzy	163.203 162.764 163.487 163.048
a = 4.1395 mm b = 9.5250 mm Z _C = 50.0 Ω	10 ³ 10 ⁹	219.49 220.18	216.89 *	217.0 217.7	217.40 218.07		217.596 217.013 218.272 217.686
a = 4.1393 mm b = 9.5244 mm Z _C = 50.0 Ω	10 ³ 10 ⁹	217.71 *	216.88 *	216.9557 *	217.38 218.05	216.4±1 Risley	217.565 217.004 218.262 217.676
a = 6.353 mm b = 9.525 mm Z _C = 24.3 Ω	10 ³ 10 ⁹	386.51 387.68	* *	398.8 *	399.02 400.18	396±2.0 Spinney	399.135 398.585 400.328 399.776

CHAPTER VII

ADMITTANCE MEASUREMENTS FOR TWO-PORT COAXIAL CAVITIES

A. Introduction

During the course of the present investigation, two sets of coaxial cavities were constructed and a number of measurements of the electromagnetic properties of the cavities were performed. The term "sets of cavities" is used because a number of interchangeable parts were constructed for each cavity which allows it to be configured as a simple or partitioned cavity and, for one set, as either a one- or two-port cavity. Descriptions of the cavities and interesting details of their construction are given in Appendix E. It was found, as anticipated, that the voltage standing wave ratio (VSWR) on the waveguide feeding a one-port cavity was far too large to measure accurately. Consequently, the admittance measurements presented in this chapter are only for the two-port configuration with one port being excited by an RF generator and a matched load placed at the other port.

B. Measurement Procedure and Cavity Configuration

A schematic representation of the apparatus used in performing the admittance measurements is given in Figure 27.

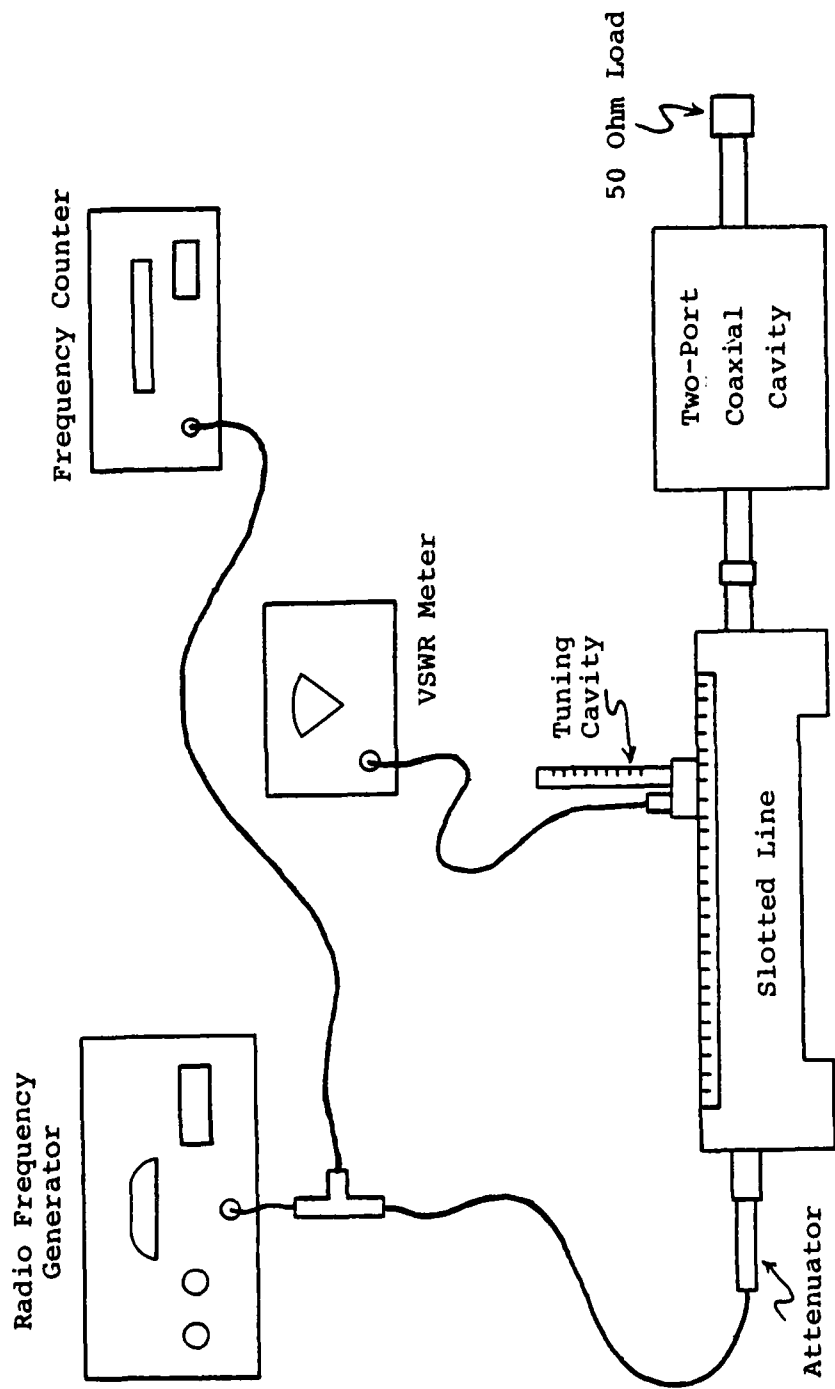


Figure 27. Schematic Representation of Instrumentation For Admittance Measurements for Two-Port Coaxial Cavities

The primary instrument used is a General Radio (now GenRad) 50 ohm precision slotted line. Three quantities were measured on the slotted line which together provided the necessary data for calculating the admittance of the cavity at the discontinuity where the input waveguide joined the cavity proper ($z = s$ in Figure 14). The first quantity was the VSWR on the transmission line between the cavity and the source generator. The second quantity was the location of a minimum of the voltage on the slotted line. The third was the location of a minimum of the voltage when an electrical short was placed at the location of the cavity input. The procedures for measuring this data and the subsequent calculations of the admittance are described very well in a number of books and in particular, Ref.[25] which was consulted during this investigation. The results presented in the next section for each frequency are the averages of calculations made using all the possible combinations of measured standing wave minima. At almost all frequencies, this total was nine separate calculations. All measured values are normalized by 20 millimhos.

The input admittance was measured for three cavity configurations:

1. Simple cavity, no partition
2. Partitioned cavity, aperture diameter = 2.540 cm
3. Partitioned cavity, aperture diameter = 8.006 cm.

The dimensions of the various cavity sections are given in Appendix E. During the measurements only an air dielectric was used in the cavities. The output waveguide, which is a section of 50-ohm air line, was terminated in a 50-ohm load at a point 13.472 cm beyond the output port of the cavity. The admittance was measured at 50 MHz intervals over a bandwidth which differed slightly for each cavity. The frequency intervals measured for each cavity configuration are given below.

Configuration No.	Frequency Range
1	300 - 1700 MHz
2	400 - 2000 MHz
3	400 - 1700 MHz

The cutoff frequency for the first higher-order mode (TM_{01}) in the larger section of waveguide is 1325 MHz, a point which is covered by all three measurement intervals.

C. Presentation of Results

The real and imaginary parts of the measured admittance for each configuration are graphically presented in Figures 28-30. Also plotted on each graph are the real and imaginary parts of the admittance calculated from solutions to the appropriate integral equations. In Figures 31-33, the admittances computed from transmission line theory with

susceptance corrections are plotted together with the previously plotted curves. The effects of the size of the aperture in the partition are illustrated in Figure 34 where the calculated values of admittance for the two cases are presented together.

The transmission line theory values agree quite well with the other results for frequencies well below the TM_{01} cutoff in the larger cavity section; however, the results of this procedure begin to display significant errors as the cutoff frequency is approached. The admittances computed from the integral equation solutions display excellent agreement with measured results at almost all sampled frequencies. It is very difficult to distinguish any differences in the two for frequencies below 1900 MHz. It is probable that measurement error was becoming significant at frequencies above 1900 MHz. This contention is supported by the results shown in Tables 15, 16 and 17 where the mean and standard deviation for the measurements at each frequency are presented along with the admittance computed from solutions to integral equations. The standard deviations of the real and imaginary parts of the admittance are calculated from the expression

$$\text{Std Dev of } y_n = \sqrt{\frac{\sum_{n=1}^N y_n^2 - N(\bar{y}^2)}{N-1}}$$

where

y_n = set of N measurement results

\bar{y} = mean of N measurement results

The standard deviations for both the real and imaginary parts of the measured values grow substantially larger as the frequency increases beyond 1900 MHz. The standard deviations for both parts of the admittance are also large near peaks in the admittance which correspond to axial resonances of the particular cavity (length equal to odd multiple of one-half wavelength). Three of the four peaks on the admittance curve for the simple two-port cavity can be identified easily. The axial length of the cavity is equal to one-half the free-space wavelength at 1000 MHz which is the location of the first peak. The second peak occurs at 1325 MHz which is the first transverse resonance frequency. The peak near 1650 MHz is also immediately identifiable, since it represents the axial resonance of the first higher-order mode. The fourth peak occurs at 2000 MHz where the axial length of the cavity is equal to one free-space wavelength. All of these resonances are characterized by a zero crossing of the imaginary part of the admittance with a steep negative slope.

The behavior of the admittance curves for the partitioned cavities becomes more difficult to interpret. The

one-half wavelength, resonance peak for the total axial length of the cavity occurs near 600 MHz for both cavities. The nature of this peak is verified by its occurrence in Figure 34 where the admittance of an unpartitioned cavity of the same length is presented. Except for the transverse resonance peak which occurs at 1325 MHz for all structures, the introduction of the partitions significantly changes the admittance response of the two-port cavity above the primary TEM axial resonance. The most prominent feature of the admittance curves for the partitioned cavities is a very large, sharp peak between 1100 and 1200 MHz. The peak appears to be directly related to the existence of the partition and its aperture. The value of the peak and its position vary as the size of the aperture is changed, while the other features of the admittance curve change very little. The exact physical origin of this resonance-like peak has not been explained but it is almost certainly an axial resonance since it is also described by the transmission line theory calculations. It is also interesting to note in Figure 35 the almost precise agreement of the admittance for the two partitioned cavities between the transverse resonance frequency (1325 MHz) and 1800 MHz. In this region, the partition has a definite effect, but the size of the aperture appears to have little influence.

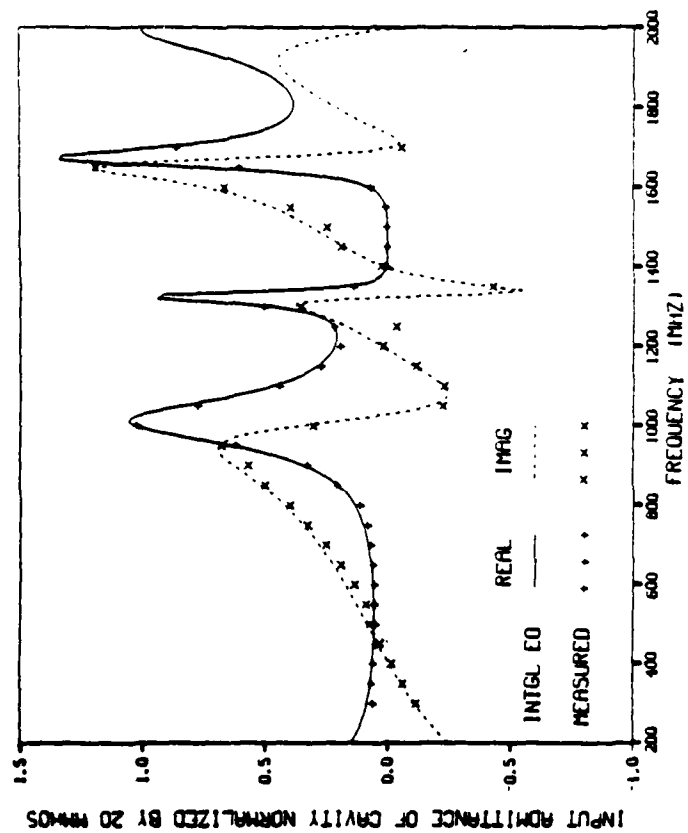


FIGURE 28 MEASURED AND CALCULATED ADMITTANCE FOR A TWO-PORT COAXIAL CAVITY

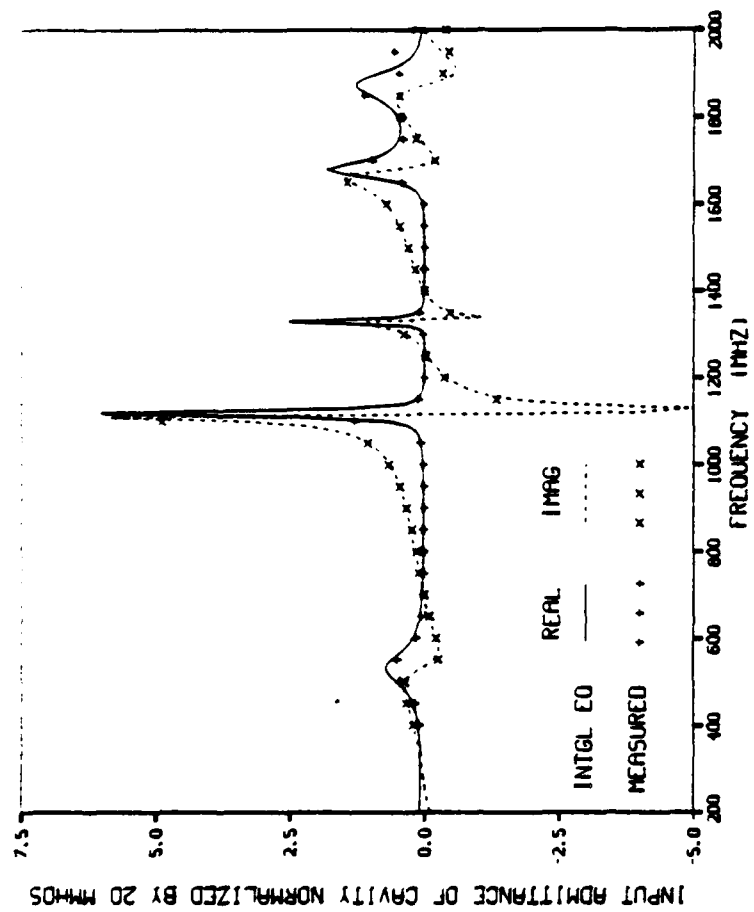


FIGURE 29 MEASURED AND CALCULATED ADMITTANCE FOR A TWO-PORT COAXIAL CAVITY WITH PARTITION - SMALL APERTURE

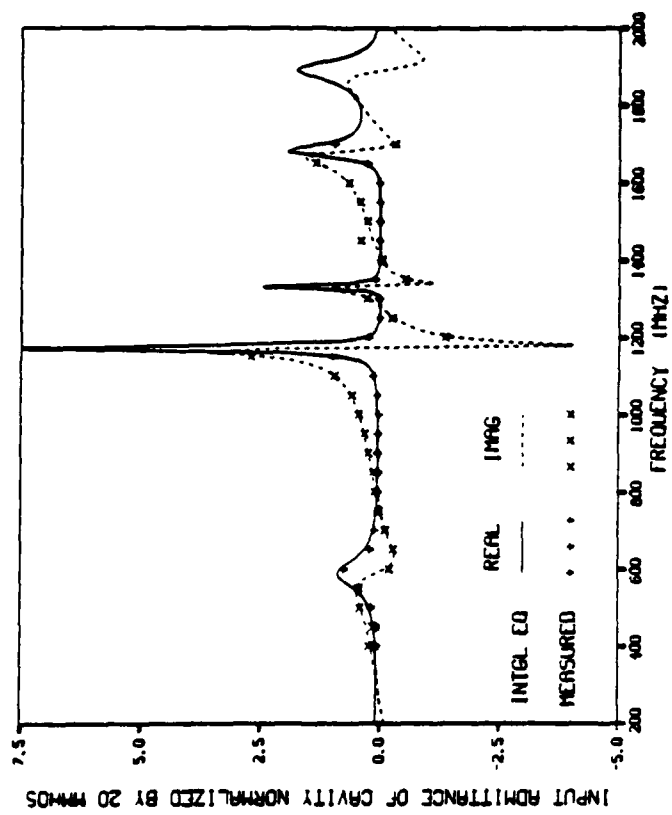


FIGURE 30 MEASURED AND CALCULATED ADMITTANCE FOR A TWO-PORT CORNICAL CAVITY
WITH PARTITION - LARGE APERTURE

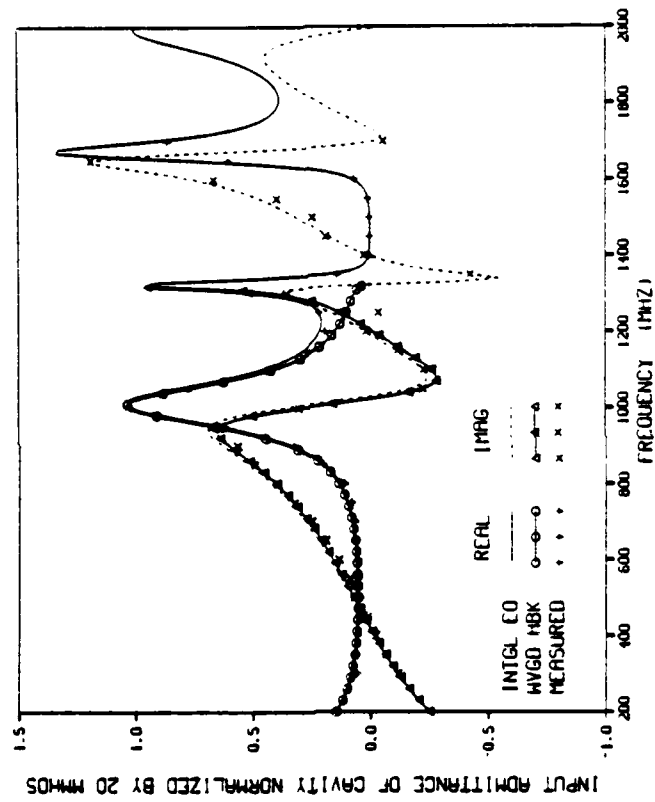


FIGURE 31 MEASURED AND CALCULATED ADMITTANCE FOR A TWO-PORT COAXIAL CAVITY

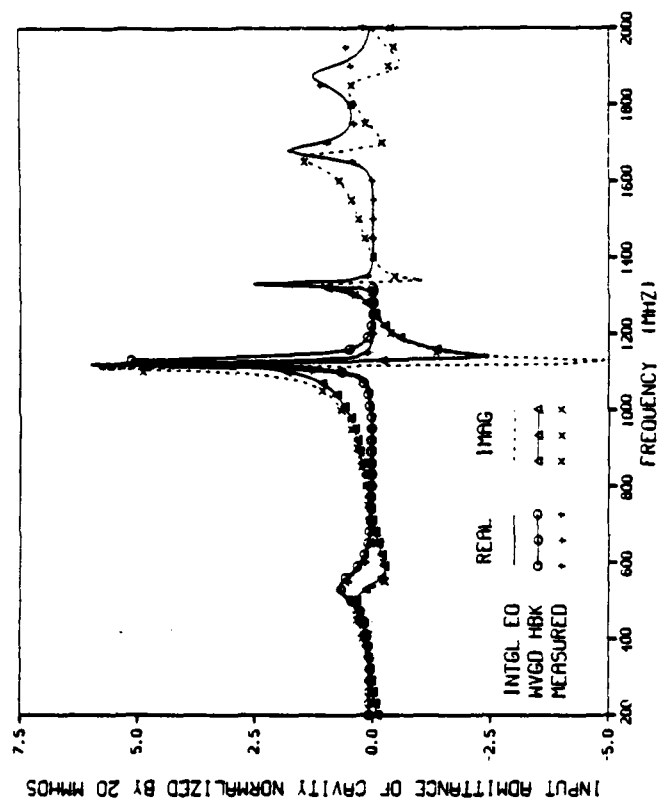


FIGURE 32 MEASURED AND CALCULATED ADMITTANCE FOR A TWO-PORT COAXIAL CAVITY WITH PARTITION - SMALL APERTURE

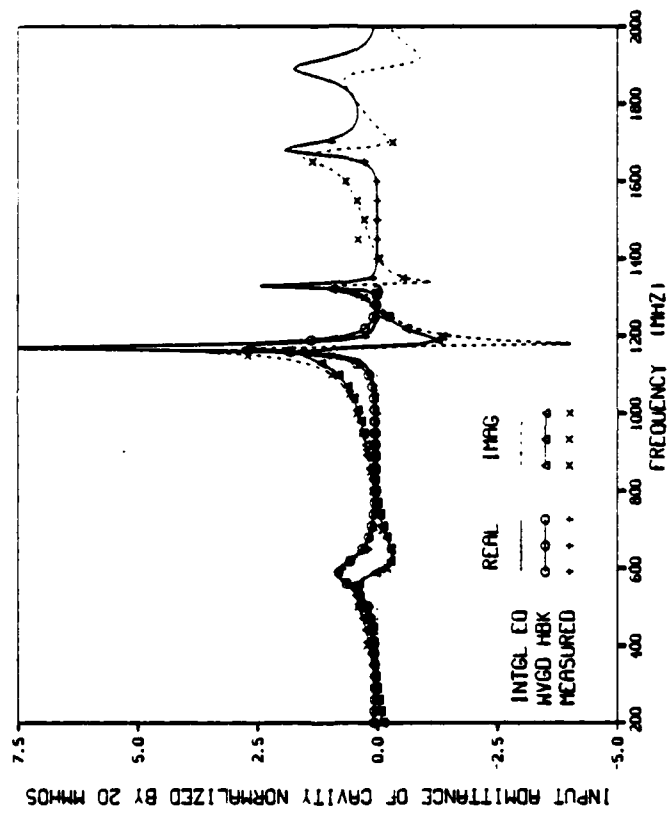


FIGURE 33 MEASURED AND CALCULATED ADMITTANCE FOR A TWO-PORT COAXIAL CAVITY WITH PARTITION - LARGE APERTURE

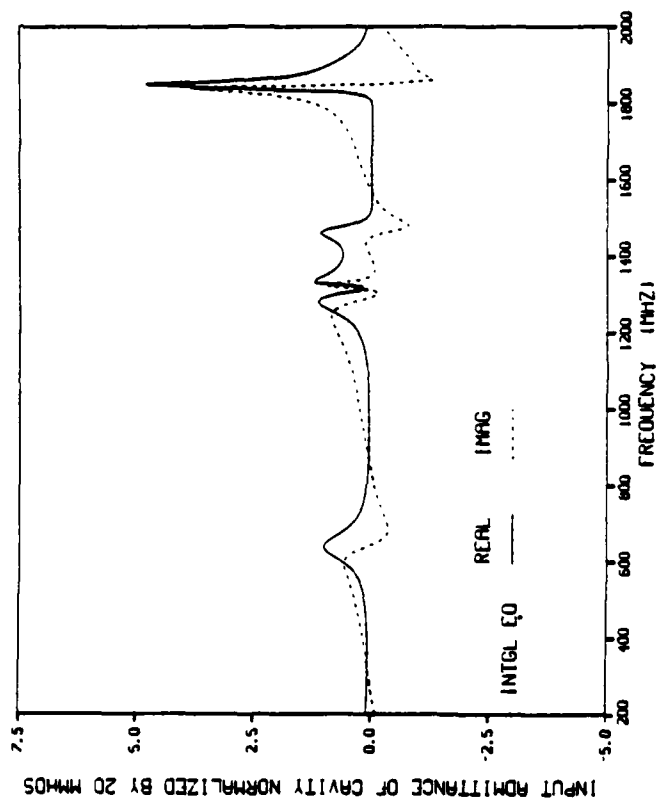


FIGURE 34 MEASURED AND CALCULATED ADMITTANCE FOR A TWO-PORT COAXIAL CAVITY OF SAME LENGTH AS PARTITIONED CAVITIES

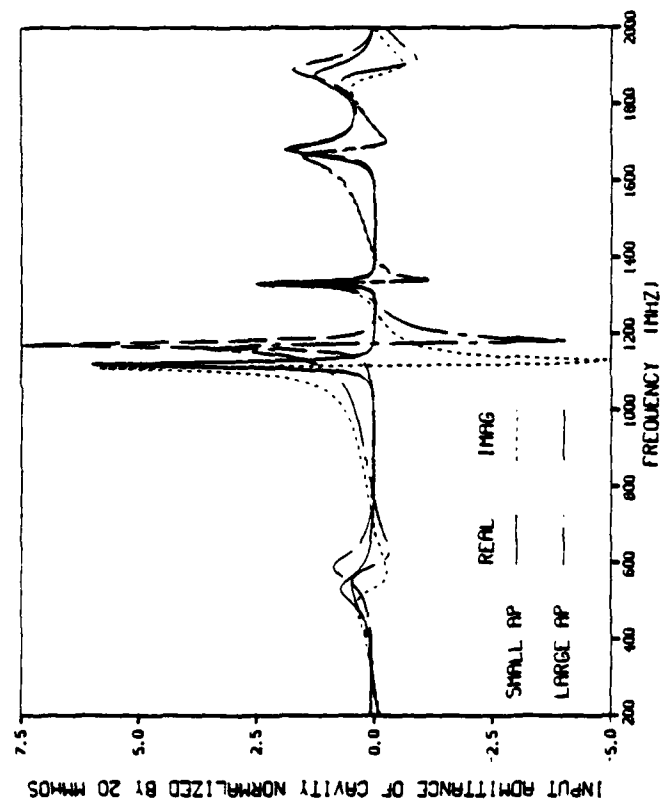


FIGURE 35 MEASURED AND CALCULATED ADMITTANCE FOR A TWO-PORT COAXIAL CAVITY
WITH PARTITION - BOTH APERTURES

TABLE 15. CALCULATED AND MEASURED ADMITTANCE OF A
TWO-PORT COAXIAL CAVITY

Freq MHz	Integral Eq. Calculation		Mean of Measured Results		Standard Deviation	
	Real	Imag	Real	Imag	Real	Imag
300	0.0835	-0.1102	0.0589	-0.1164	0.0000	0.0000
350	0.0696	-0.0563	0.0656	-0.0630	0.0000	0.0000
400	0.0614	-0.0076	0.0578	-0.0188	0.0000	0.0041
450	0.0569	0.0379	0.0513	0.0315	0.0000	0.0029
500	0.0552	0.0821	0.0497	0.0712	0.0022	0.0044
550	0.0560	0.1265	0.0546	0.0887	0.0041	0.0088
600	0.0596	0.1726	0.0550	0.1349	0.0007	0.0075
650	0.0665	0.2222	0.0628	0.1917	0.0001	0.0037
700	0.0785	0.2774	0.0677	0.2501	0.0009	0.0089
750	0.0986	0.3415	0.0816	0.3253	0.0009	0.0122
800	0.1339	0.4189	0.1133	0.3993	0.0023	0.0080
850	0.2003	0.5150	0.2047	0.4961	0.0059	0.0120
900	0.3382	0.6278	0.3266	0.5670	0.0091	0.0250
950	0.6370	0.6872	0.6197	0.6744	0.0076	0.0097
1000	1.0325	0.3635	1.0218	0.3036	0.0096	0.0065
1050	0.8430	-0.1719	0.7745	-0.2245	0.0109	0.0104
1100	0.4723	-0.2242	0.4431	-0.2276	0.0012	0.0049
1150	0.2889	-0.1084	0.2706	-0.1172	0.0004	0.0055
1200	0.2164	0.0223	0.1924	0.0186	0.0001	0.0083
1250	0.2195	0.1676	0.2201	-0.0348	0.0138	0.2584
1300	0.4694	0.3747	0.5048	0.3545	0.0029	0.0069
1350	0.2015	-0.4217	0.1410	-0.4259	0.0010	0.0097
1400	0.0069	0.0073	0.0088	0.0275	0.0009	0.0061
1450	0.0014	0.1750	0.0053	0.1892	0.0005	0.0068
1500	0.0021	0.3093	0.0065	0.2467	0.0009	0.00062
1550	0.0104	0.4704	0.0137	0.3974	0.0008	0.0070
1600	0.0747	0.7450	0.0688	0.6659	0.0005	0.0072
1650	0.7550	1.1941	0.6050	1.1892	0.0089	0.0121
1700	0.9587	-0.0166	0.8626	-0.0561	0.0021	0.0070

TABLE 16. CALCULATED AND MEASURED ADMITTANCE OF A PARTITIONED,
TWO-PORT CAVITY - SMALL APERTURE

Freq MHz	Integral Eq. Calculation		Mean of Measured Results		Standard Deviation	
	Real	Imag	Real	Imag	Real	Imag
400	0.1214	0.2097	0.1080	0.2163	0.0003	0.0061
450	0.2177	0.3186	0.1937	0.3445	0.0047	0.0384
500	0.5189	0.3565	0.4668	0.3815	0.0011	0.0120
550	0.6174	-0.1778	0.5174	-0.2553	0.0026	0.0080
600	0.2199	-0.2130	0.1608	-0.2097	0.0003	0.0052
650	0.0937	-0.0790	0.0704	-0.0833	0.0005	0.0053
700	0.0527	0.0228	0.0435	0.0173	0.0000	0.0149
750	0.0360	0.1046	0.0287	0.1186	0.0012	0.0183
800	0.0284	0.1794	0.0257	0.1559	0.0005	0.0735
850	0.0253	0.2565	0.0227	0.2346	0.0008	0.0066
900	0.0252	0.3454	0.0227	0.3387	0.0013	0.0108
950	0.0287	0.4624	0.0283	0.4648	0.0007	0.0100
1000	0.0395	0.6466	0.0422	0.6737	0.0021	0.0130
1050	0.0793	1.0451	0.0908	1.0666	0.0080	0.0855
1100	0.6530	3.2300	1.3069	4.8789	0.0729	0.2019
1150	0.1574	-1.6821	0.1239	-1.3361	0.0126	0.1010
1200	0.0111	-0.4278	0.0134	-0.3652	0.0007	0.0090
1250	0.0026	-0.0541	0.0065	-0.0148	0.0012	0.0061
1300	0.0320	0.3348	0.0408	0.3958	0.0008	0.0066
1350	0.1488	-0.5198	0.1056	-0.4640	0.0010	0.0117
1400	0.0104	0.0087	0.0111	0.0060	0.0010	0.0059
1450	0.0034	0.1760	0.0061	0.1735	0.0006	0.0067
1500	0.0038	0.3101	0.0067	0.3042	0.0005	0.0064
1550	0.0094	0.4669	0.0109	0.4602	0.0008	0.0076
1600	0.0462	0.7258	0.0308	0.7138	0.0007	0.0080
1650	0.5148	1.3673	0.4281	1.4438	0.0072	0.0169
1700	1.1483	-0.1735	0.9656	-0.2007	0.0076	0.0053
1750	0.4774	0.0913	0.3951	0.1521	0.0008	0.0060
1800	0.5003	0.3702	0.4458	0.4568	0.0052	0.0129
1850	0.9779	0.4549	1.1128	0.4568	0.0122	0.0071
1900	0.8825	-0.5633	0.4745	-0.3327	0.0095	0.0271
1950	0.1796	-0.3126	0.5640	-0.4516	0.0592	0.1067
2000	0.0407	0.0151	0.1912	-0.3896	0.0232	0.1763

TABLE 17. CALCULATED AND MEASURED ADMITTANCE OF A PARTITIONED,
TWO-PORT CAVITY - LARGE APERTURE

Freq MHz	Integral Eq. Calculation		Mean of Measured Results		Standard Deviation	
	Real	Imag	Real	Imag	Real	Imag
400	0.0828	0.1786	0.0631	0.2179	0.0002	0.0062
450	0.1194	0.2703	0.0759	0.1292	0.0007	0.0359
500	0.2178	0.3925	0.1719	0.4055	0.0006	0.0048
550	0.5350	0.4829	0.4575	0.4419	0.0057	0.0012
600	0.8247	-0.1037	0.7436	-0.2050	0.0013	0.0012
650	0.3197	-0.2802	0.2075	-0.2756	0.0011	0.0103
700	0.1348	-0.1311	0.1154	-0.1219	0.0005	0.0165
750	0.0757	-0.0148	0.0439	0.0259	0.0013	0.0225
800	0.0521	0.0753	0.0388	0.1015	0.0006	0.0770
850	0.0415	0.1542	0.0358	0.1423	0.0007	0.0064
900	0.0375	0.2326	0.0291	0.2326	0.0003	0.0126
950	0.0381	0.3199	0.0305	0.3121	0.0002	0.0091
1000	0.0444	0.4307	0.0269	0.4367	0.0010	0.0097
1050	0.0624	0.5986	0.0505	0.5757	0.0026	0.0542
1100	0.1254	0.9411	0.1503	0.9552	0.0037	0.0126
1150	0.8239	2.4444	0.9953	2.6990	0.2599	0.3148
1200	0.3237	-1.5965	0.2454	-1.3653	0.0065	0.0391
1250	0.0133	-0.3077	0.0088	-0.2577	0.0013	0.0074
1300	0.0215	0.2384	0.0206	0.2754	0.0003	0.0076
1350	0.1716	-0.5995	0.0909	-0.5370	0.0019	0.0110
1400	0.0083	-0.0344	0.0094	-0.0370	0.0002	0.0049
1450	0.0026	0.1455	0.0072	0.4004	0.0026	0.3960
1500	0.0026	0.2815	0.0055	0.2691	0.0006	0.0053
1550	0.0039	0.4244	0.0089	0.4189	0.0005	0.0084
1600	0.0241	0.6780	0.0196	0.6566	0.0004	0.0091
1650	0.3426	1.3212	0.2680	1.3458	0.0049	0.0158
1700	1.2635	-0.2282	0.9497	-0.3228	0.0153	0.0066

CHAPTER VIII

INTERNAL FIELD MEASUREMENTS IN COAXIAL CAVITIES

A. Introduction

In Chapter II it is demonstrated that the rotational symmetry of the coaxial cavities under investigation limits the number of field components excited within the cavities. With only the E_ρ , E_z and H_ϕ components present inside a cavity, it is possible to construct probes which do not couple to multiple field components and to provide access to the cavity interiors without seriously perturbing the field within the cavity. These factors have made possible an extensive program of interior field measurements on all possible configurations of the two sets of coaxial cavities described in Appendix E. The field distributions measured within the cavities are compared to distributions computed from solutions to the appropriate integral equations for the same geometries. The measured results serve, therefore, both as a direct observation of the electromagnetic response of a given cavity and as a rigorous test of the validity of the integral equation technique.

B. Procedures for Measurements Inside Cavity End Plates

It is desirable to perform field measurements in such a manner that the transmission line from the probe to the sensing instrumentation does not interact with the subject field. This may be effectively accomplished by placing the probe on the surface of a highly-conducting boundary and allowing the transmission line to exit through and be shielded by the conductor. Since the cavities under investigation were constructed entirely of brass, several options for providing shielded access to the cavity interior were available. The options were to measure at the inner surfaces of the end plates or on the walls of the inner or outer coaxial conductors. Boundary conditions constrain E_ρ to be zero on the end plate surfaces and E_z to be zero on the walls of the coaxial conductors, therefore, it was desirable to choose a combination of measurement locations which would sample all field components.

The center conductor for the smaller cavity set is less than one centimeter in diameter which renders it an impractical probe location. Difficulty of machining argued against cutting slots in the outer coaxial wall. Conversely, it was relatively simple to cut slots in the cavity end plates for probe access. These slots were required to be along a radial line in order to provide no interference with the axially-directed currents flowing through the

cavity. These radial slots allowed the measurement of both the E_z and the H_ϕ components on the front and rear end plates of the cavities with the front of the cavity being defined as the end which contains the port being excited.

Radial slots were also cut in the end plates of the larger set of coaxial cavities. In addition, the center conductor is large enough to accomodate a moveable probe, so it was possible to cut an axial slot in this conductor which extended the entire length of the cavity and beyond. The axial slot in the center conductor allowed the measurement of the E_ρ and H_ϕ components.

The field probes were designed for operation over a conducting screen and their size was chosen to achieve an acceptable balance between providing a measureable signal and imposing minimal perturbation of the field being measured. The construction of the probes is briefly described in Appendix F. The lead from the probe in use was connected to one input port (test) of a network analyzer. The reference input port of the network analyzer was connected to the RF generator which provided the excitation for the cavity. The network analyzer, configured in this manner, performed as a vector voltmeter displaying relative amplitude and phase as a function of position as the probe was moved along the slot. A schematic diagram of the measurement instrumentation is presented in Figure 36.

Field component measurements were made for six different configurations of the smaller set of cavities and for three configurations of the larger set. As indicated earlier, only two field components were measured in the smaller set of cavities while all three components were measured in the larger set. In the following sections of this chapter, graphical presentations are given for selected measured field distributions for each of the nine cavity configurations. In each graph, the field distribution calculated from an integral equation solution is given for comparison. The calculated distributions have been obtained assuming an excitation resulting from the application of a time-varying, one volt potential between the coaxial conductors (See Eq.30). The amplitude distributions in each graph have been normalized twice; the first normalization is by a factor composed of geometrical and excitation constants which cancels the units and the second is the division of all the calculated values by the largest value. The peak value of the measured amplitudes is then set equal to the corresponding calculated value at the same radial or axial location. The remainder of the measured values are then divided by this factor. The calculated phase is plotted relative to an assumed phase of zero degrees at the first point. The

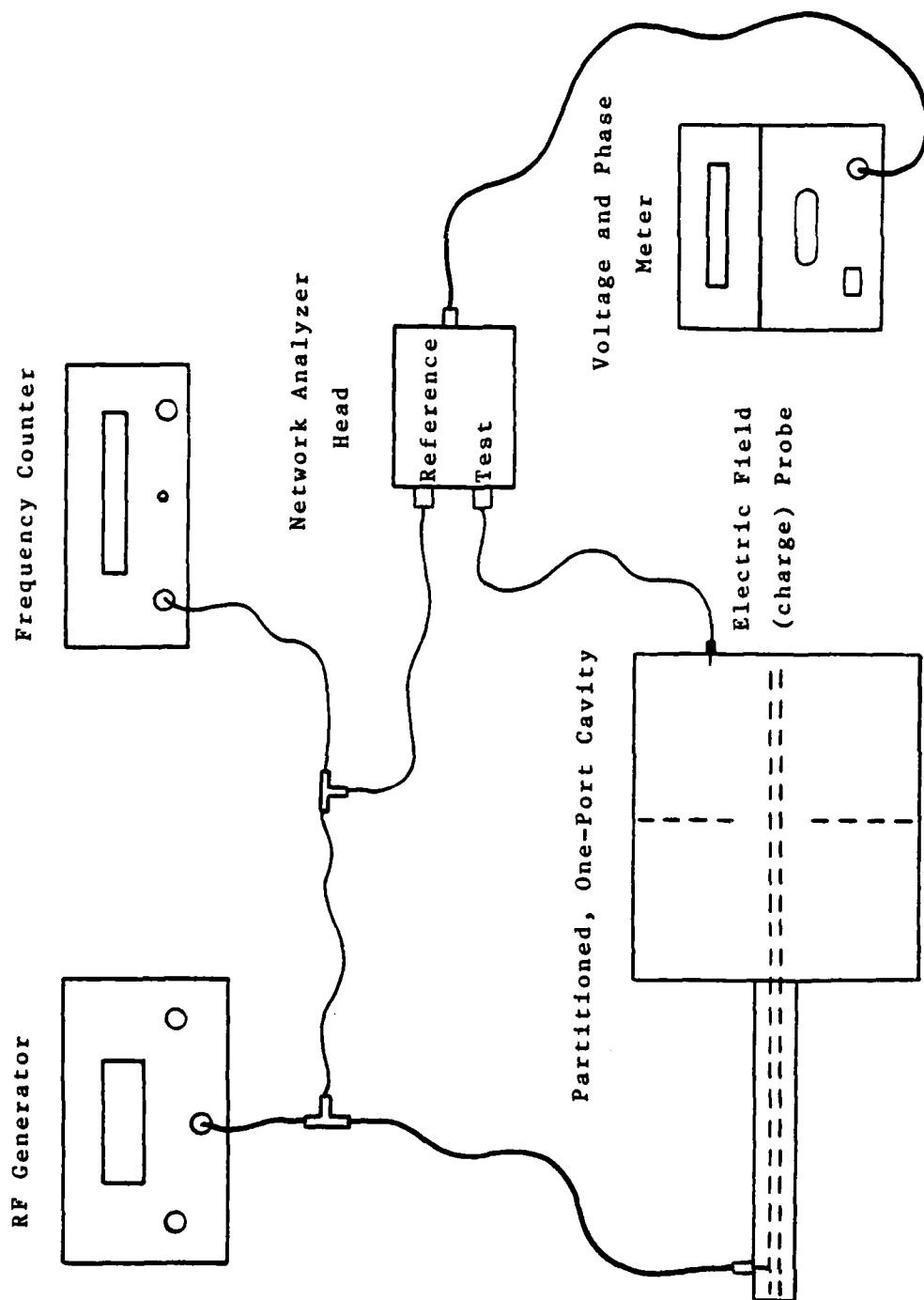


Figure 36. Schematic Diagram of Instrumentation for Interior Field Measurements

measured phase is set equal to the calculated phase at the same point where the amplitudes are made to be equal and the other measured phase points are plotted relative to this value.

C. Field Interior to Simple One-Port Cavity

Measurements of the interior field components were performed for two sizes of one-port, coaxial cavities. The E_z and H_ϕ components were measured on both cavities and the E_ρ component was also measured on the larger cavity. The measurements on the smaller cavity were performed for the frequency band 400 - 2000 MHz at 100 MHz intervals. For the larger cavity, the frequency band was 400 - 1200 MHz at 100 MHz intervals. There was great difficulty in obtaining useful measurements of E_z on the rear plate of the smaller cavity. This was the only measurement set during the entire investigation which produced such difficulty. The problem was based on the extreme mismatch between the input transmission line and the cavity. Essentially all the incident energy was reflected back toward the generator and it was not possible to safely produce enough power from the generator to yield meaningful field distributions on the rear plate. The measurements made on the front end-plates showed far more variation with frequency than the values measured on the

rear plates. The latter values were almost frequency independent. Representative distributions of E_z and H_ϕ on the front and rear end plates of a simple one-port, coaxial cavity are presented in Figures 37 - 40. The two letters, LC, under the small picture of the cavity indicate that the particular measurement was performed on the larger cavity set. Such a distinction, with SC indicating the smaller cavity set, is made for the one-port cavities. All two-port cavity measurements were made on the smaller cavity set.

D. Field Interior to Simple Two-Port Cavity

A two-port cavity configuration could only be constructed from the smaller cavity set, therefore only one set of such measurements was made. The output waveguide section was terminated with a 50-ohm load in the same manner as for the admittance measurements of Chapter VII. The frequency range of these measurements was 400 to 2000 MHz in 100 MHz steps. There was no problem in feeding energy into this cavity configuration and the measurements were made with no difficulty. Distributions of E_z and H_ϕ on the front and rear end plates of a simple, two-port coaxial cavity are presented in Figures 41 - 44. The magnetic field measurements show some interesting variations which are predicted quite accurately by the integral equation calculations

E. Field Interior to Partitioned, One-Port Cavity

Partitioned, one-port cavities were constructed from both sets of cavities. Two partitions for each set with different size apertures were made, thus it was possible to form two variations of each one-port cavity. The frequency range for the smaller set of cavities was 400 - 2000 MHz at 100 MHz intervals. The field components in the larger set were measured from 400 - 1200 MHz at 100 MHz intervals with a few additional measurements at 1300 and 1400 MHz. Distributions of E_z and H_ϕ on the front and rear end plates of several partitioned, one-port cavity structures are presented in Figures 45 - 52. The distributions do not differ markedly from those of the simple, one-port cavity.

F. Field Interior to Partitioned, Two-Port Cavity

It was only possible to construct two-port, partitioned cavities from the smaller set of cavities, but by making two partitions with different size apertures, two variations of such a cavity were formed. The frequency range of these measurements was 400 - 2000 MHz at 100 MHz intervals. Distributions of E_z and H_ϕ on the end plates of both cavity configurations are presented in Figures 53 - 68. The amplitude and phase curves in many of these figures have a wide variety of shapes that are predicted very accurately by the integral equation solutions.

G. Measurements Along Center Conductor of One-Port Cavity

The most interesting measurements in terms of variety of waveforms were made at the surface of the inner conductor of the larger cavity set. The transverse field in a coaxial waveguide has its greatest intensity at the surface of the inner conductor and this fact appeared to enhance the quality of the measurements made there. The spatial range over which the measurements were made was greater than for the end-plate measurements which added to the possibility of interesting field variations. The measurements were made for the simple, one-port cavity and the partitioned, one-port cavity with two sizes of apertures. The size of the aperture in a particular figure is designated by the letters SA for small and LA for large immediately following the LC designation for the larger cavity set. Distributions of E_0 and H_ϕ are presented in Figures 69 - 78 for all three cavity configurations. The integral equation solutions do an excellent job of predicting the amplitude and phase in all cases.

H. Evaluation of Measured and Calculated Results

The primary objective of the field-measurement program was to provide verification for the accuracy and demonstrate the utility of the integral equation approach. Sufficient measurements were made to provide a very good description of the field in the various cavities in the frequency range

which extends from below to above the cutoff frequency for the first higher-order mode in the cavity section. Space restrictions prevent the presentation of more than a representative sample of the entire body of measurements.

A small number of the measurements display evidence of excessive noise and the strong probability of unwanted frequency harmonics. It was discovered during the investigation that the generator plug-in used in the 400 - 1000 MHz band produced substantial frequency harmonics until it had warmed up for an extensive period. Most of the measurements where this effect was suspected were repeated, but several of the measurement sets have unexplained variations from the calculated values below 1000 MHz but have very good agreement above 1000 MHz.

The great majority of the measurements display very good to excellent agreement with the calculated field distributions throughout the measured frequency band. Many times the agreement follows rather complex variations of both amplitude and phase. The overall impact of the comparisons is a very strong verification that the integral equation approach provides accurate solutions for the aperture fields and, consequently, all other field components in the cavities that have been treated during this investigation.

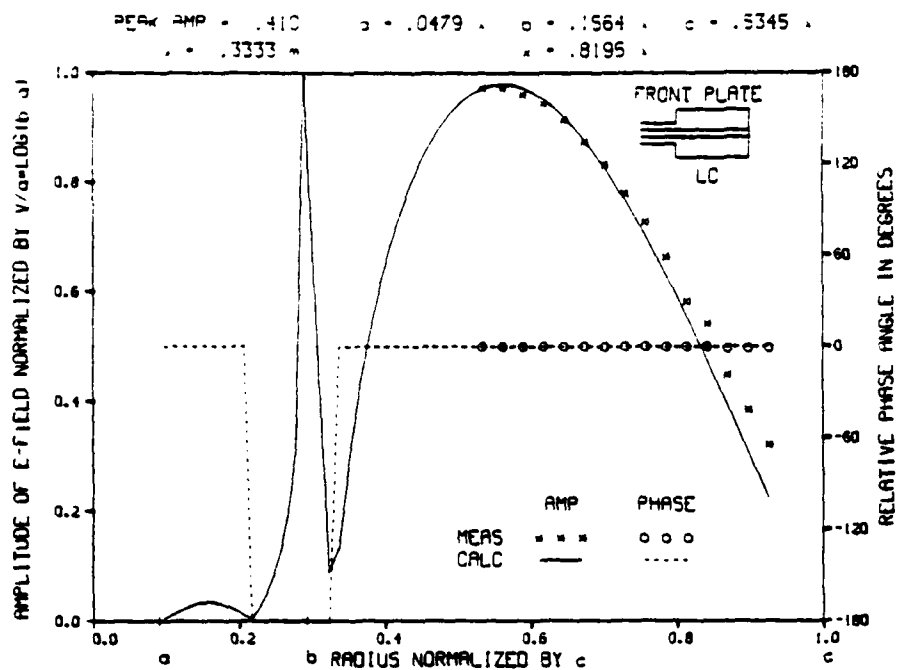


FIGURE 37 MEASURED AND CALCULATED Z COMPONENT OF ELECTRIC FIELD 900 MHZ

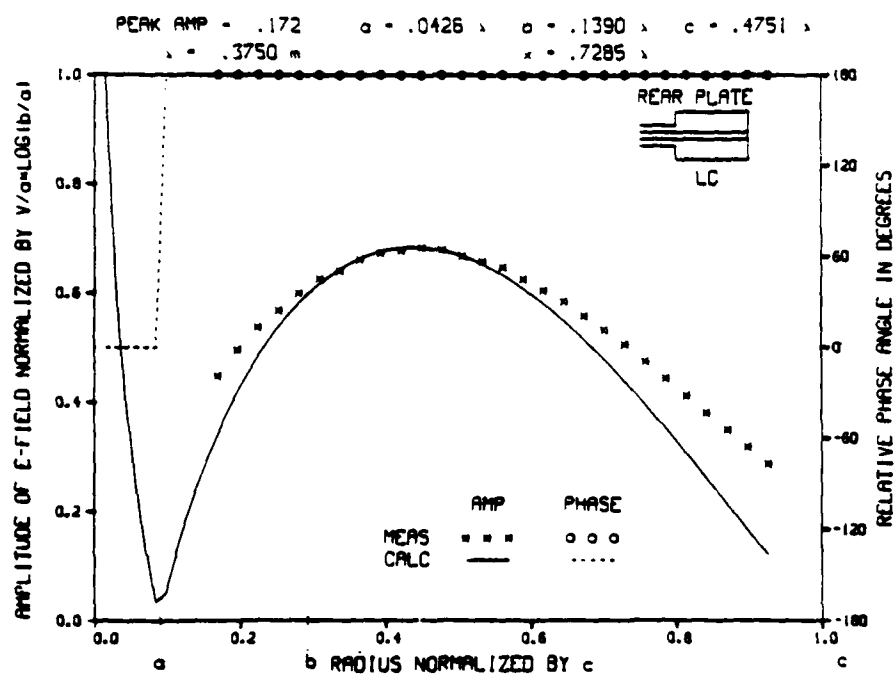
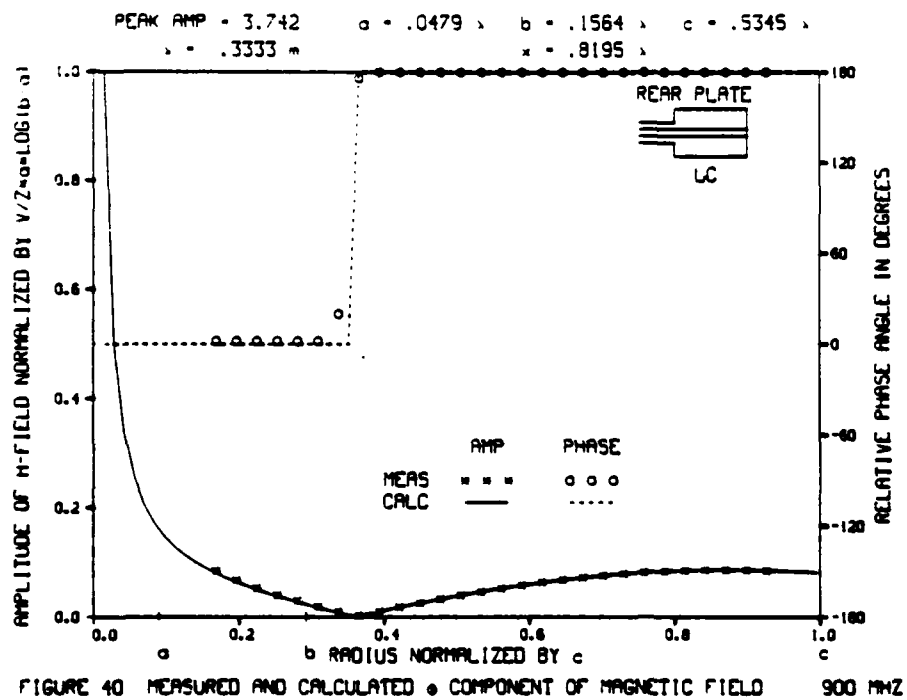
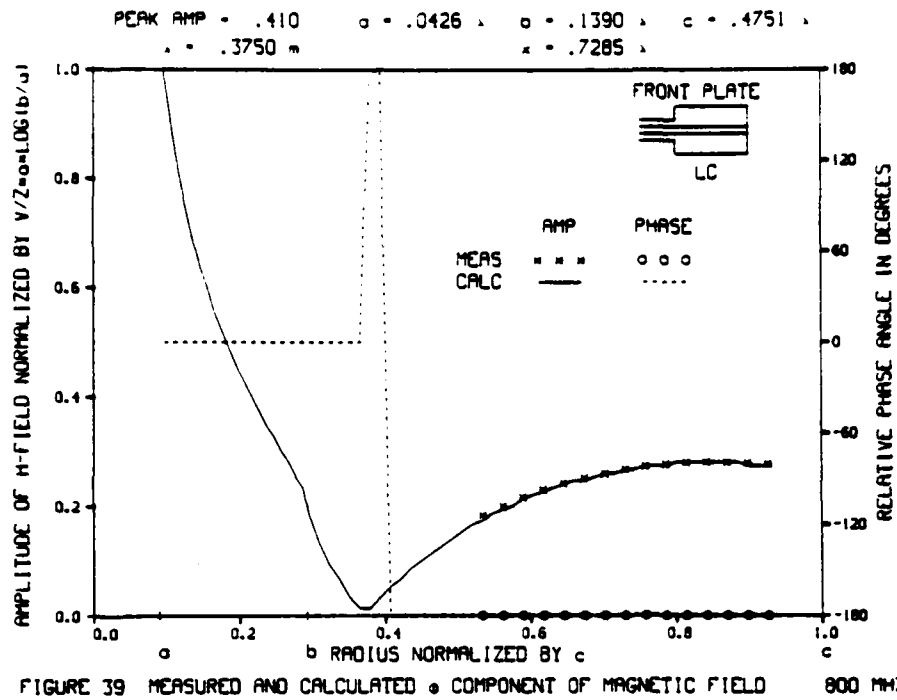


FIGURE 38 MEASURED AND CALCULATED Z COMPONENT OF ELECTRIC FIELD 800 MHZ



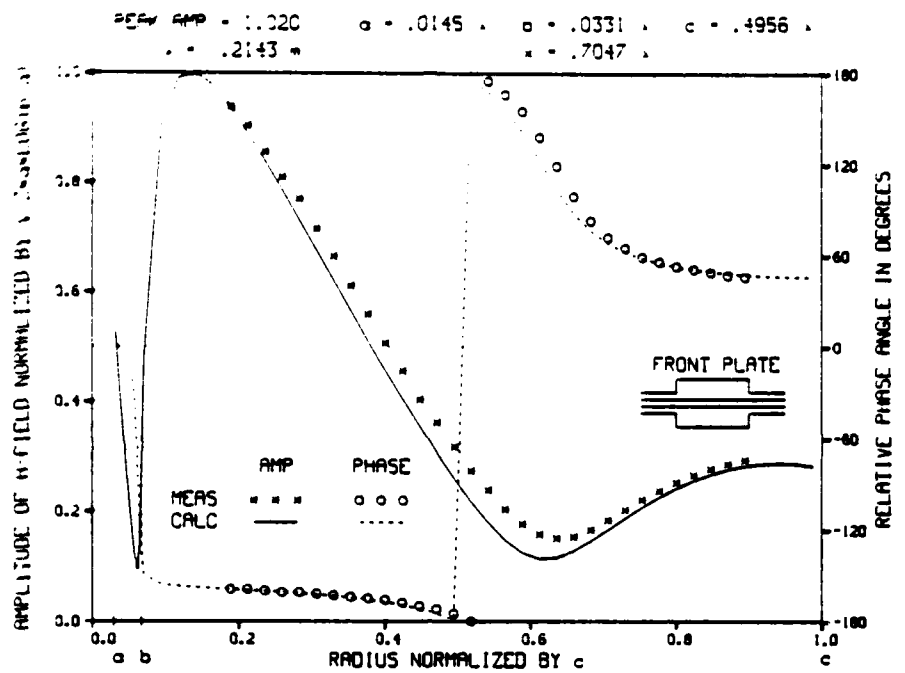


FIGURE 43 MEASURED AND CALCULATED θ COMPONENT OF MAGNETIC FIELD 1400 MHZ

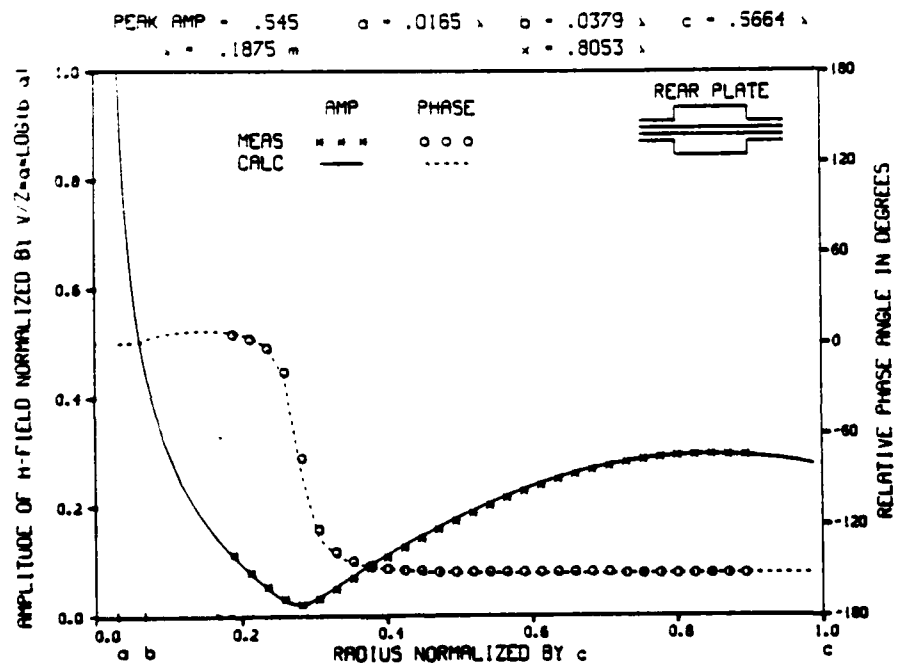


FIGURE 44 MEASURED AND CALCULATED θ COMPONENT OF MAGNETIC FIELD 1600 MHZ

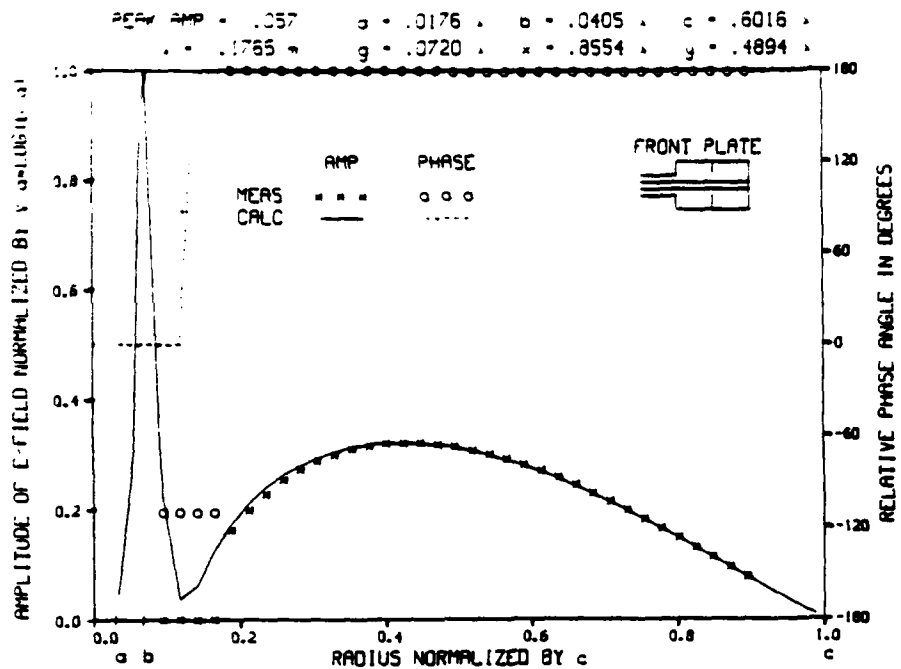


FIGURE 45 MEASURED AND CALCULATED Z COMPONENT OF ELECTRIC FIELD 1700 MHZ

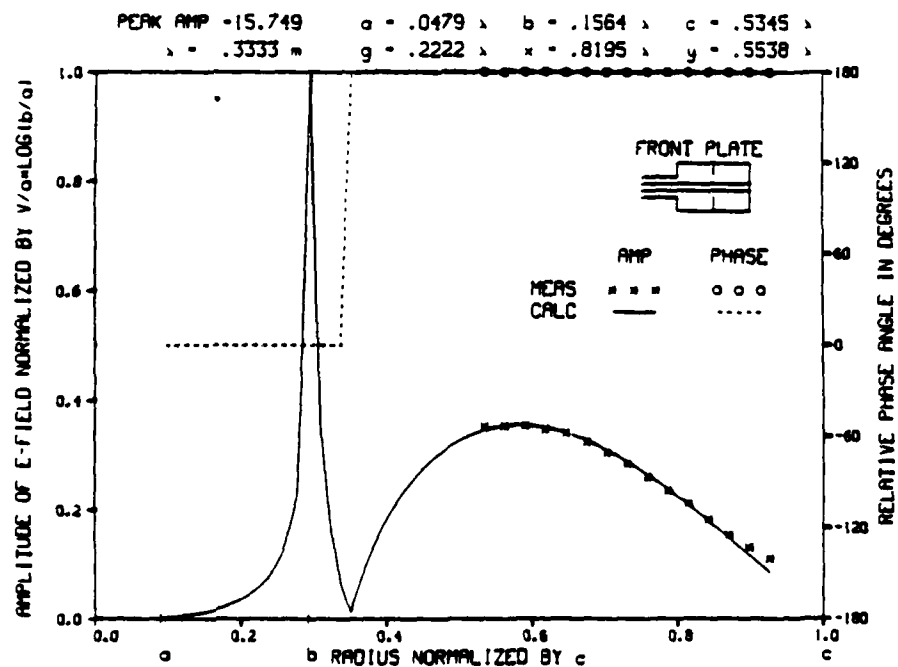


FIGURE 46 MEASURED AND CALCULATED Z COMPONENT OF ELECTRIC FIELD 900 MHZ

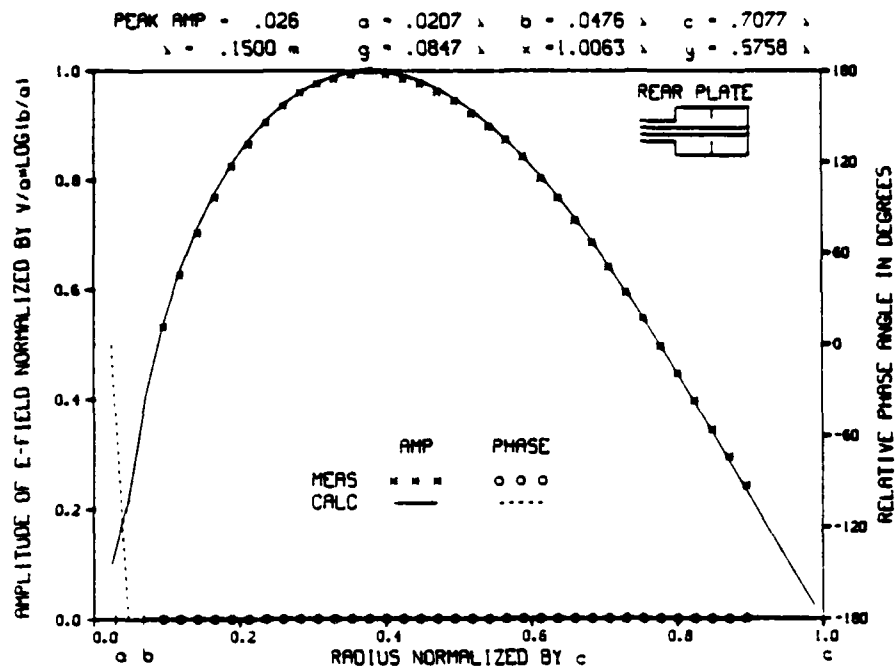


FIGURE 47 MEASURED AND CALCULATED Z COMPONENT OF ELECTRIC FIELD 2000 MHZ

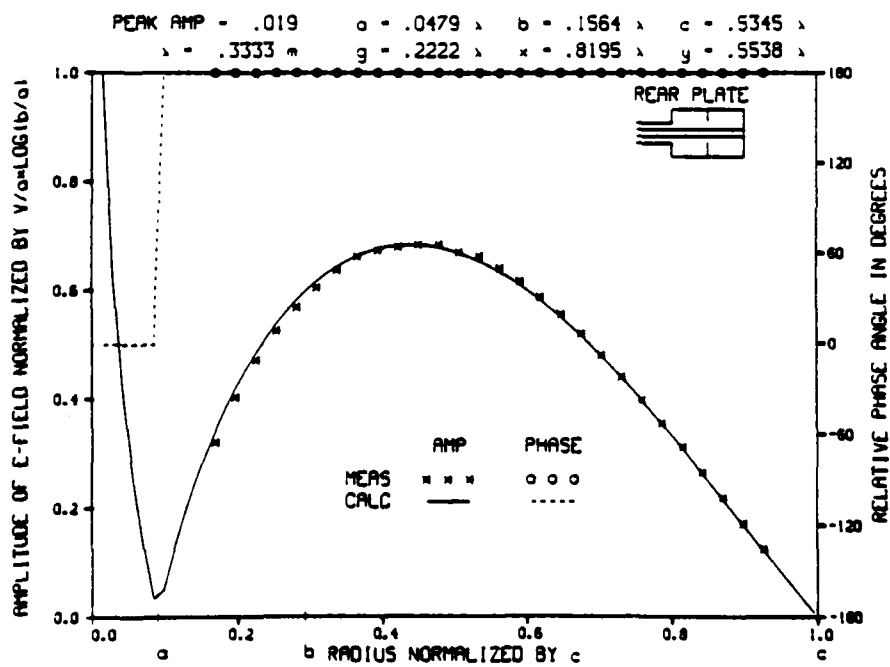


FIGURE 48 MEASURED AND CALCULATED Z COMPONENT OF ELECTRIC FIELD 900 MHZ

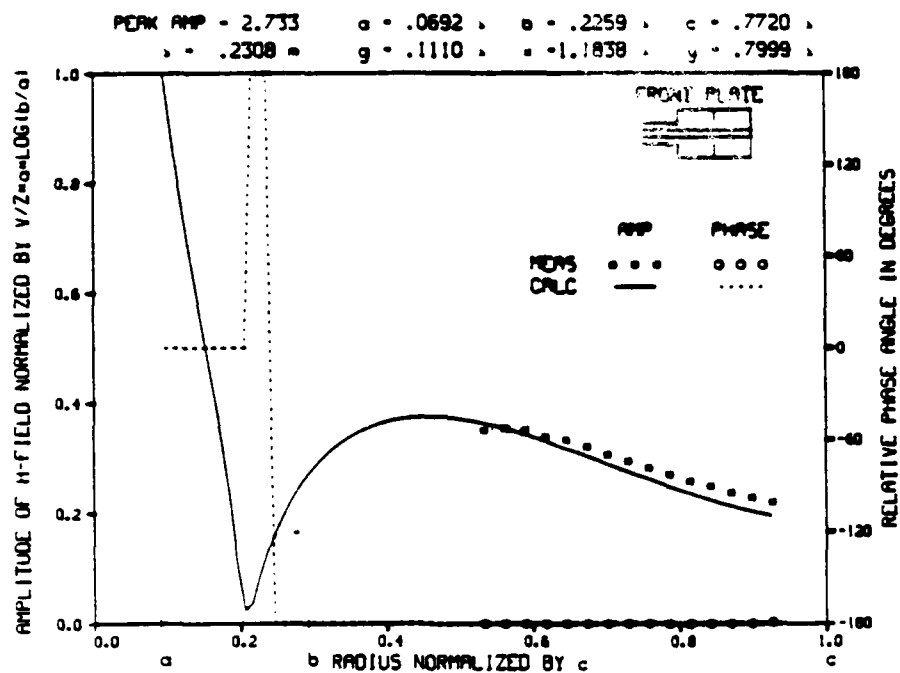


FIGURE 49 MEASURED AND CALCULATED • COMPONENT OF MAGNETIC FIELD 1300 MHZ

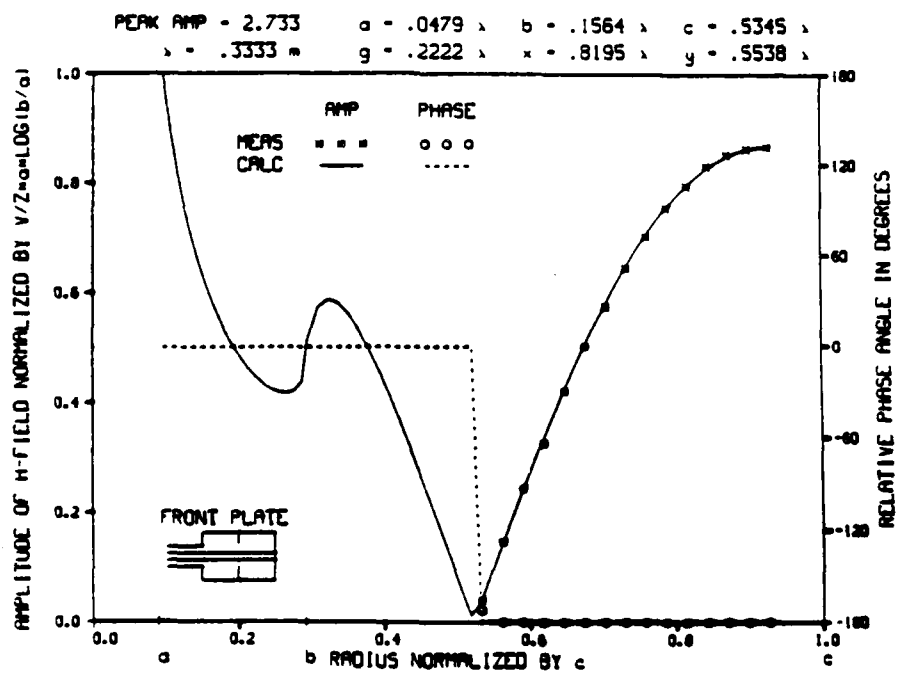
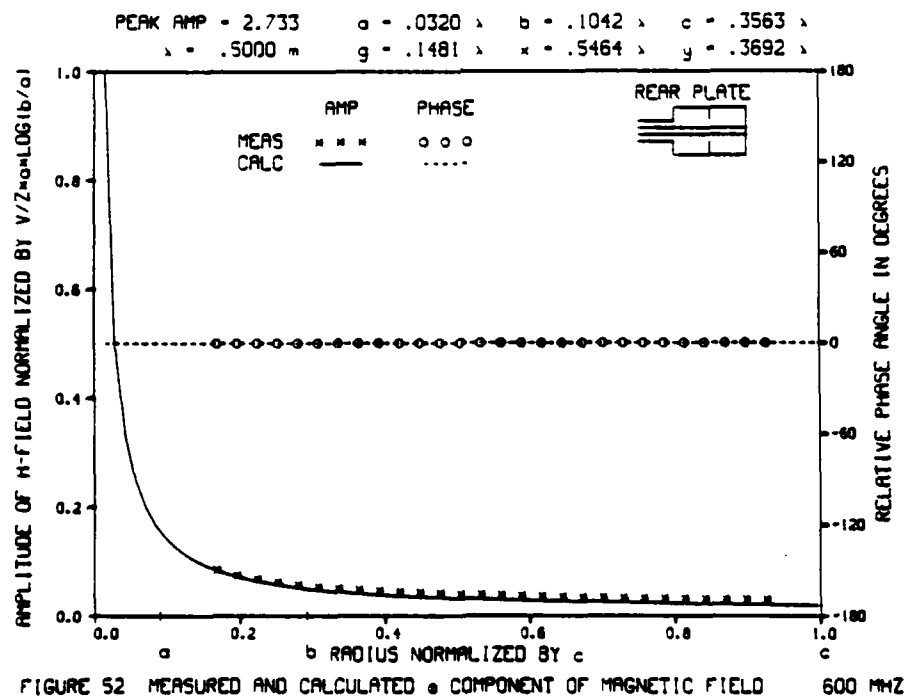
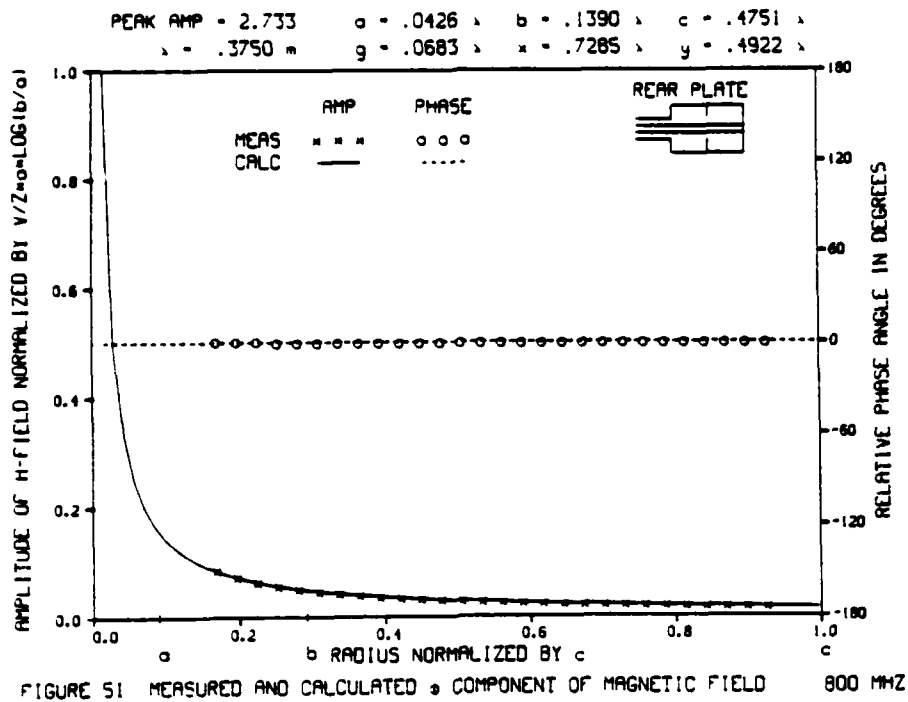
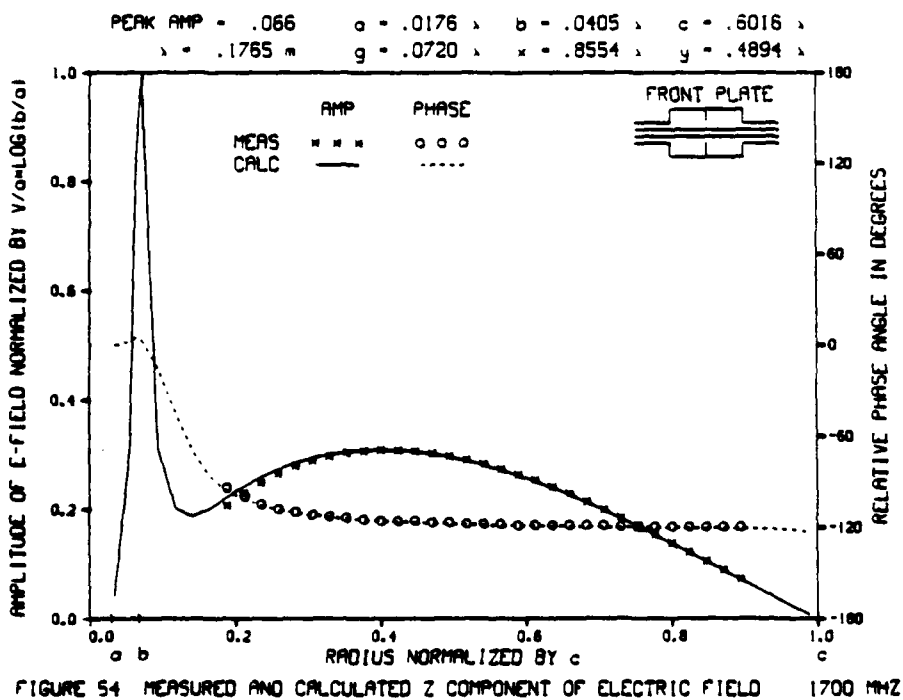
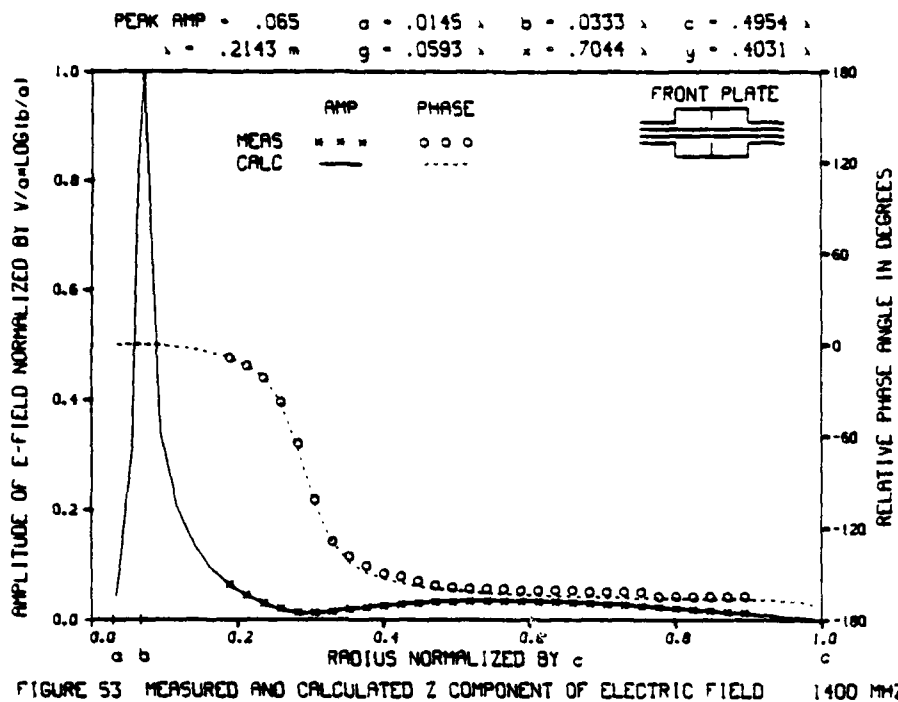


FIGURE 50 MEASURED AND CALCULATED • COMPONENT OF MAGNETIC FIELD 900 MHZ





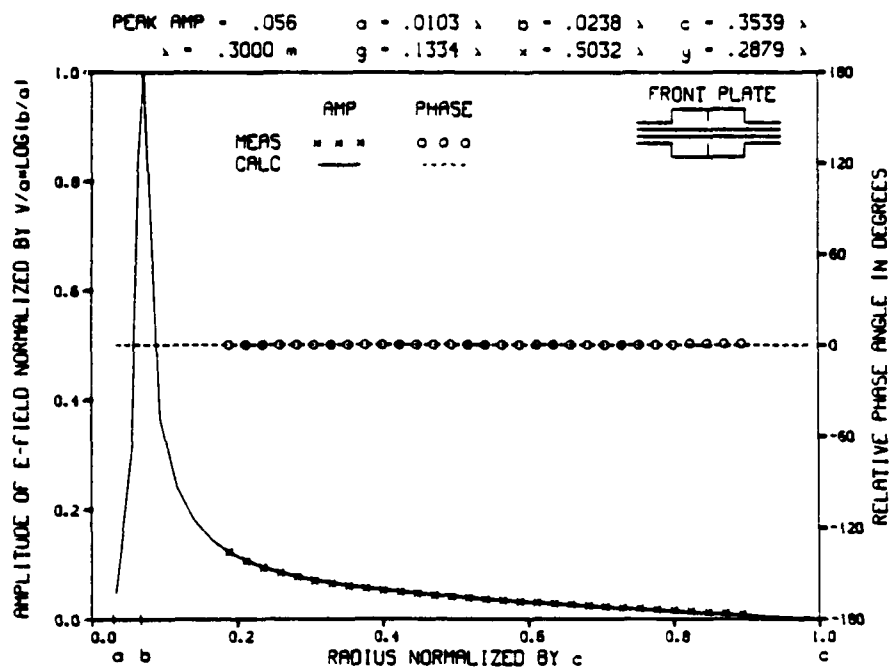


FIGURE 55 MEASURED AND CALCULATED Z COMPONENT OF ELECTRIC FIELD 1000 MHZ

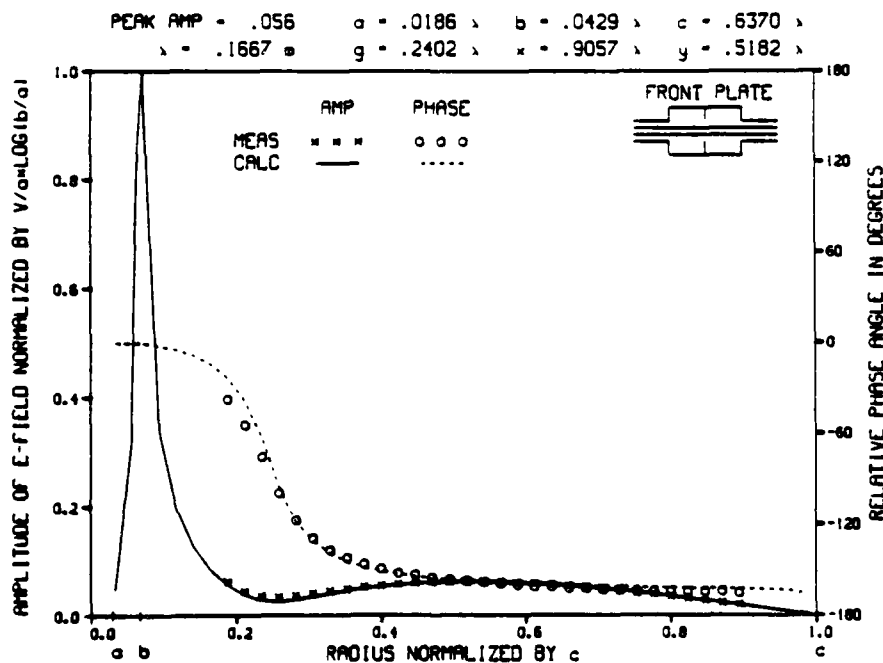


FIGURE 56 MEASURED AND CALCULATED Z COMPONENT OF ELECTRIC FIELD 1800 MHZ

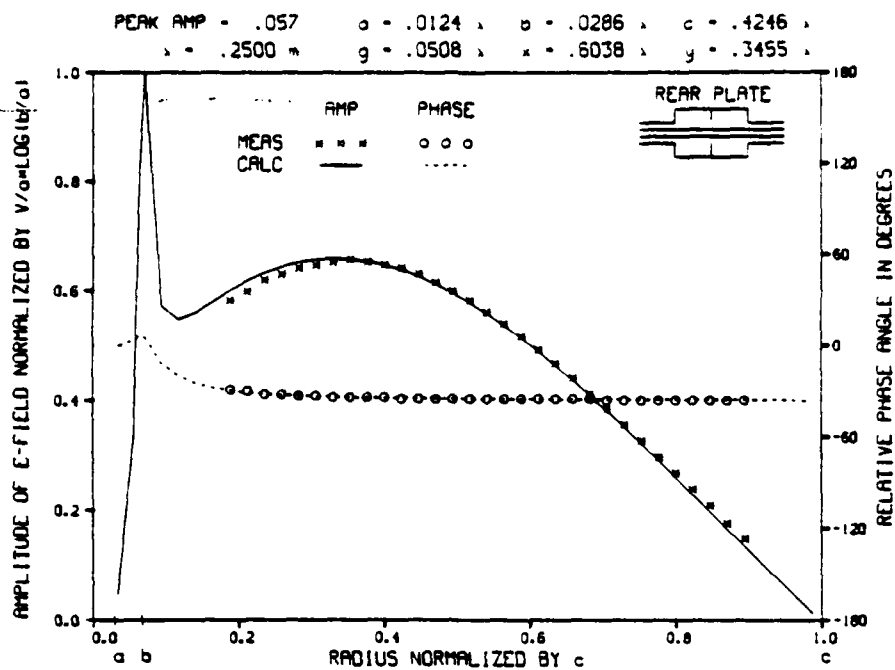


FIGURE 57 MEASURED AND CALCULATED Z COMPONENT OF ELECTRIC FIELD 1200 MHZ

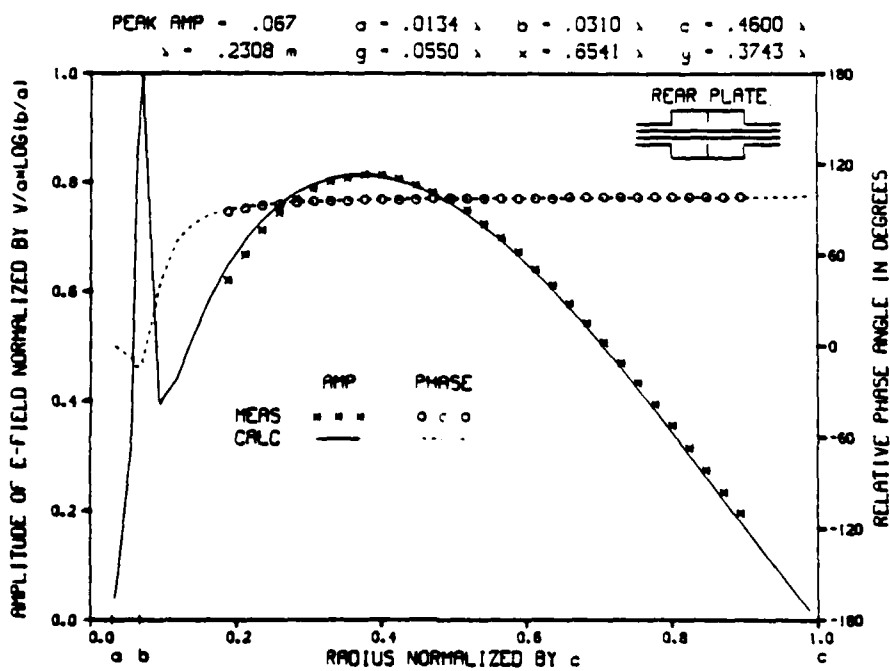


FIGURE 58 MEASURED AND CALCULATED Z COMPONENT OF ELECTRIC FIELD 1300 MHZ

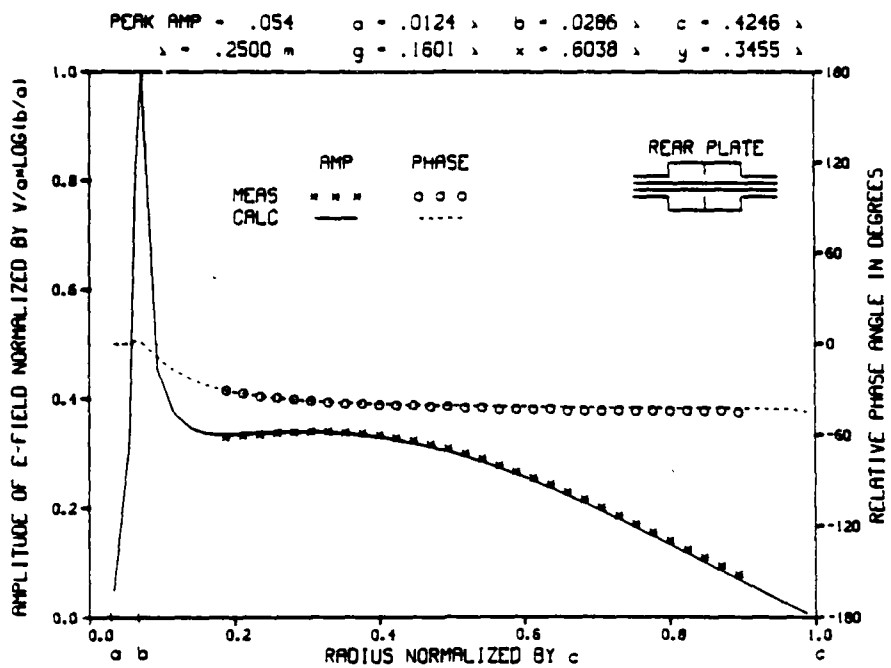


FIGURE 59 MEASURED AND CALCULATED Z COMPONENT OF ELECTRIC FIELD 1200 MHZ

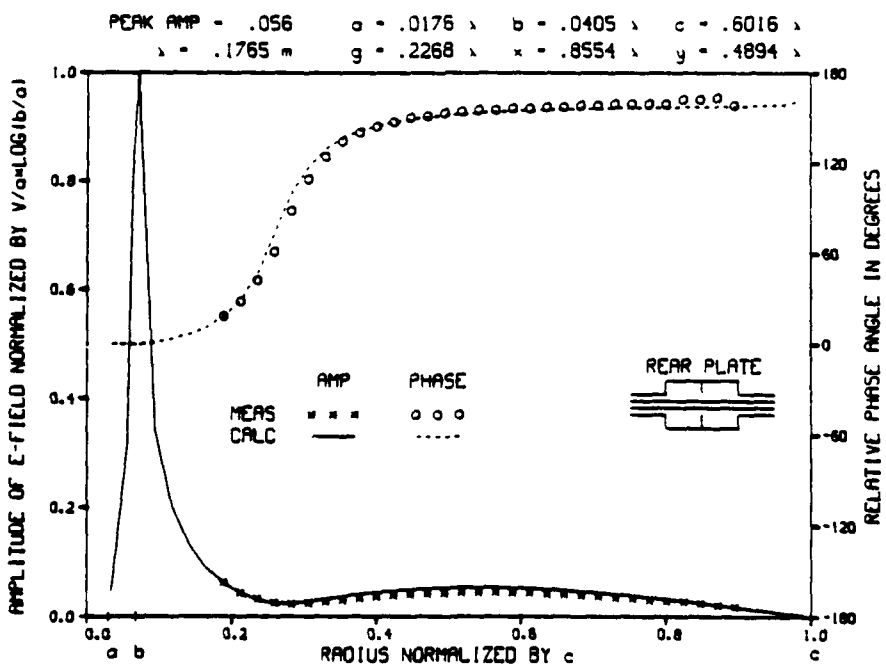


FIGURE 60 MEASURED AND CALCULATED Z COMPONENT OF ELECTRIC FIELD 1700 MHZ

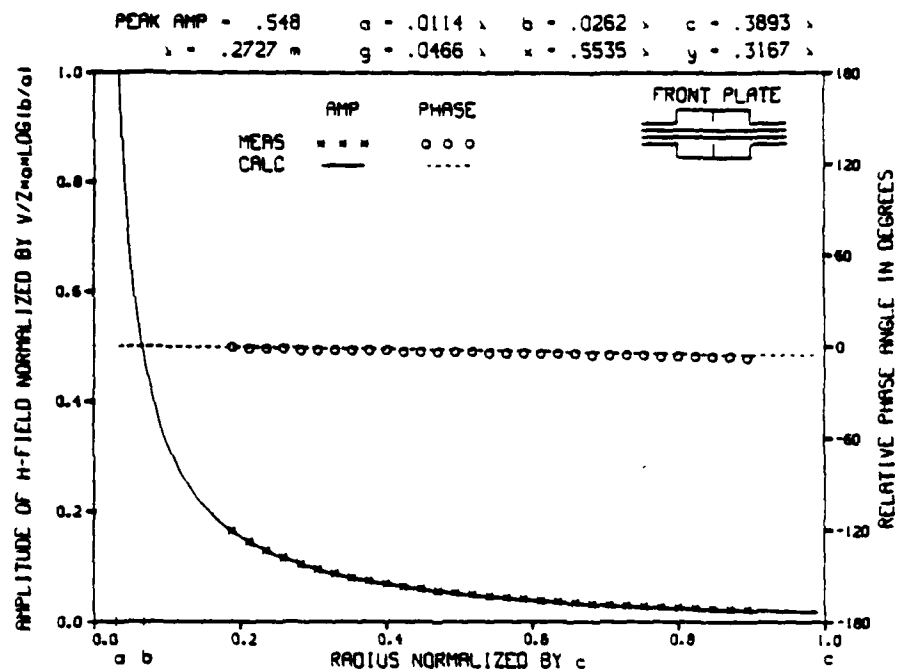


FIGURE 61 MEASURED AND CALCULATED θ COMPONENT OF MAGNETIC FIELD 1100 MHZ

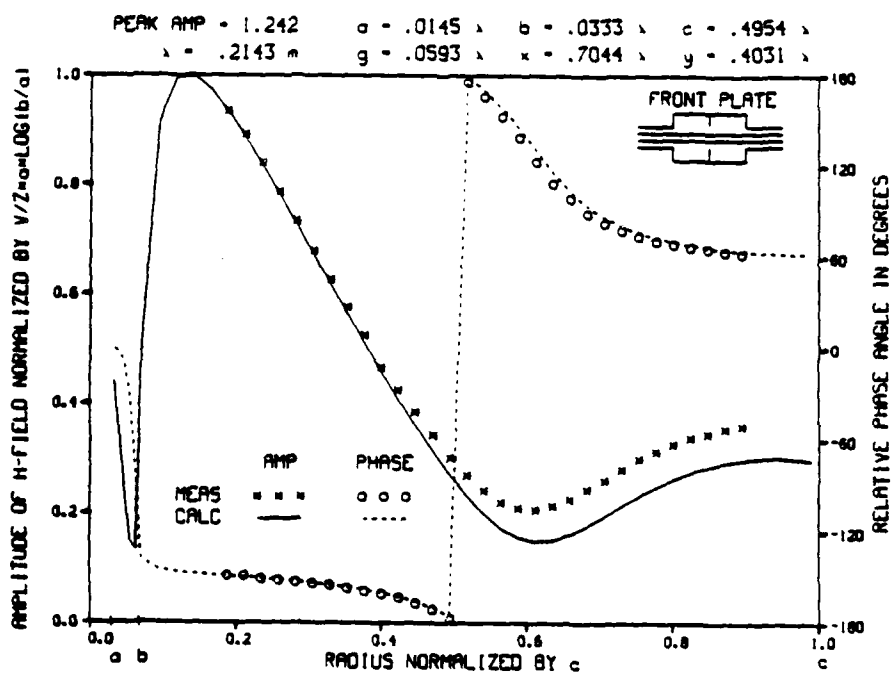
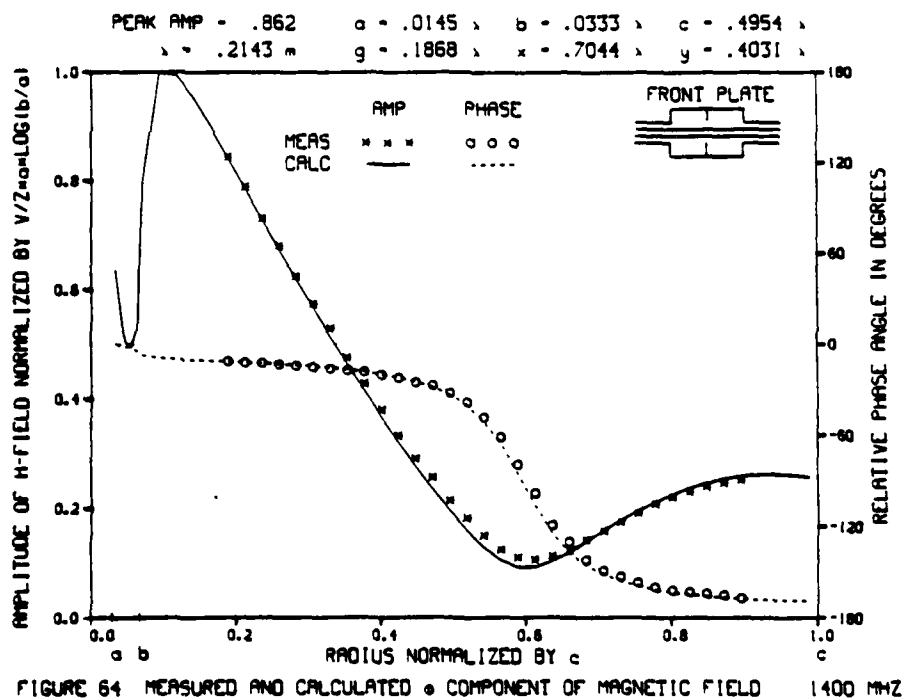
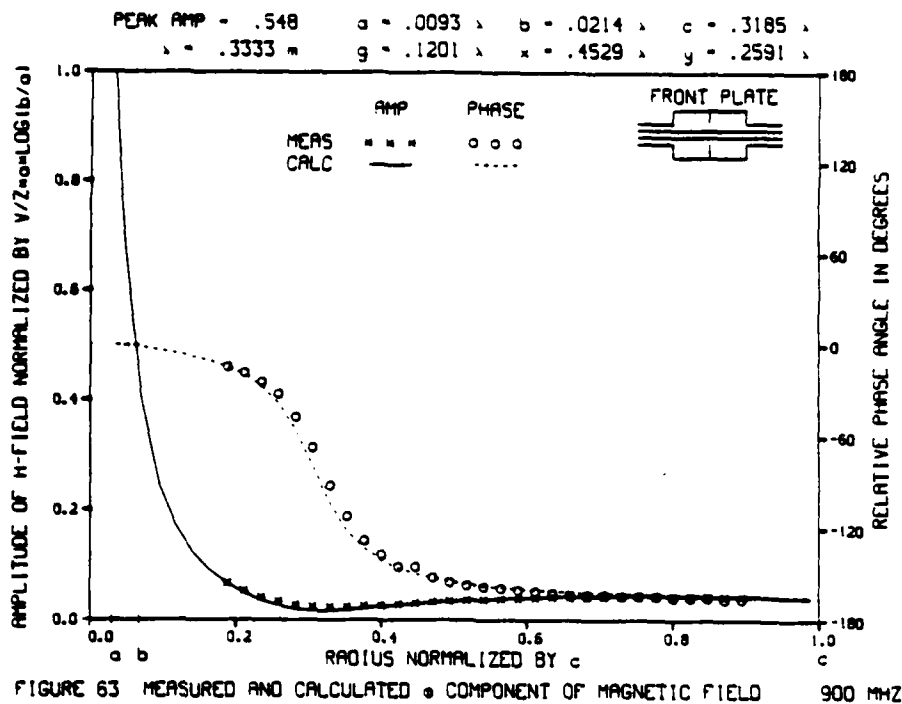
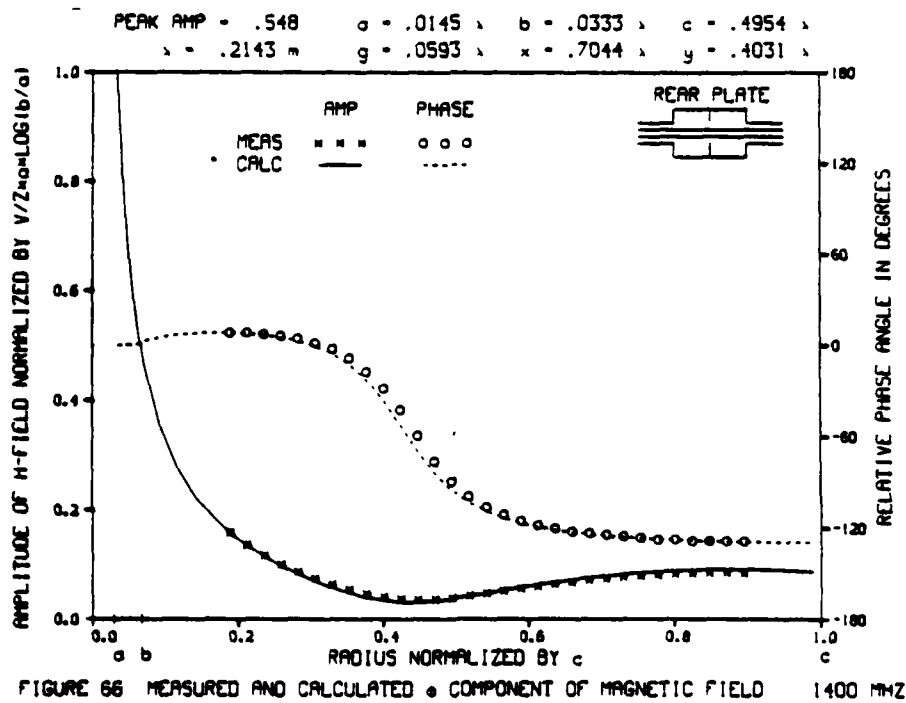
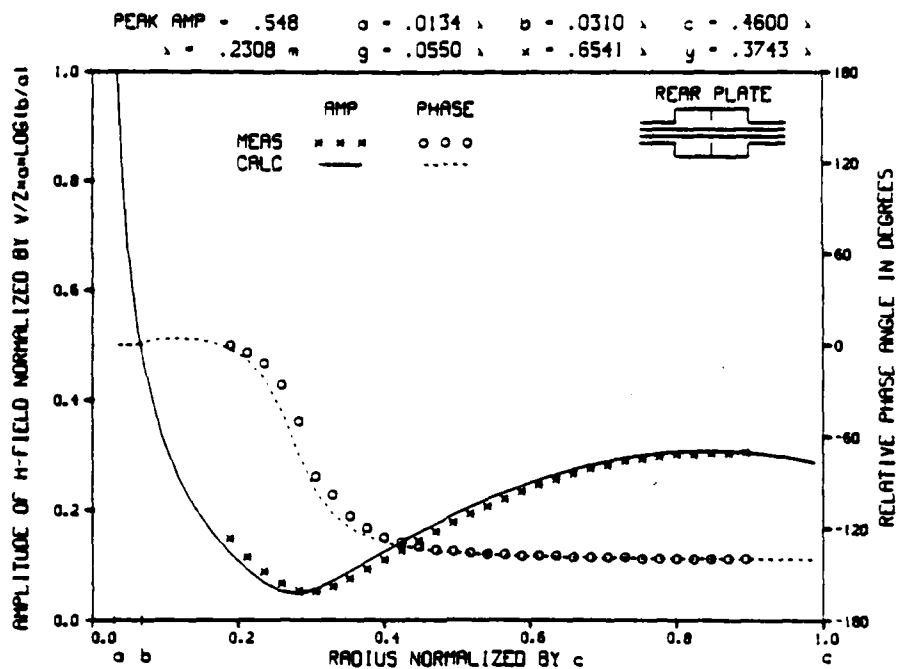
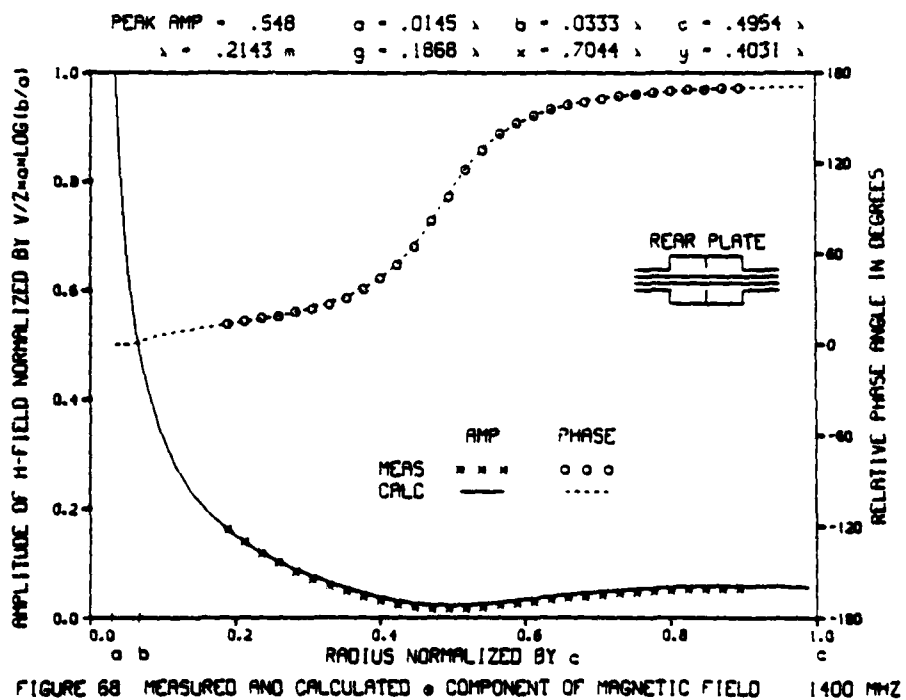
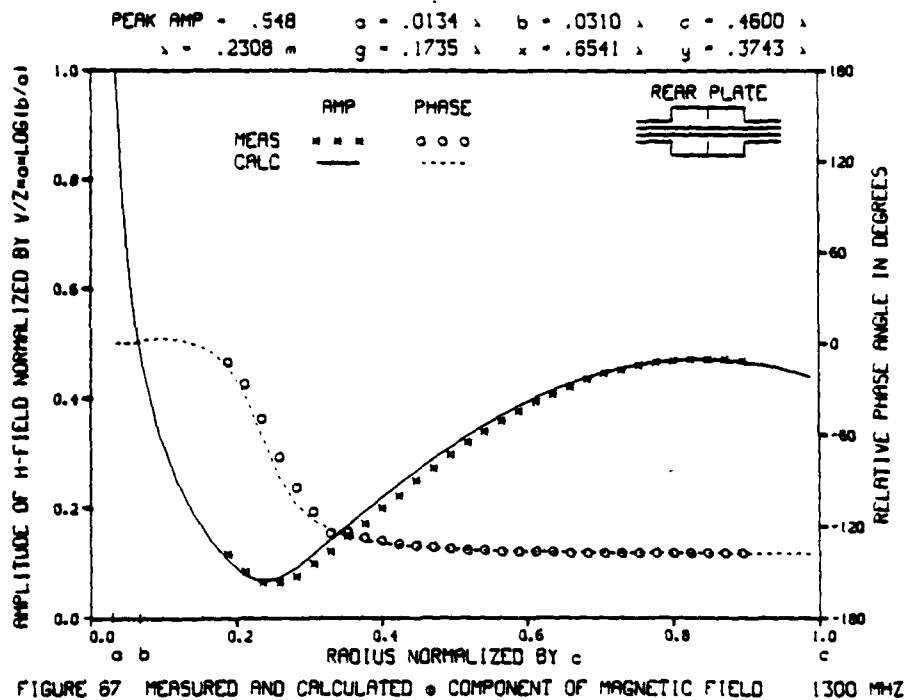


FIGURE 62 MEASURED AND CALCULATED θ COMPONENT OF MAGNETIC FIELD 1400 MHZ







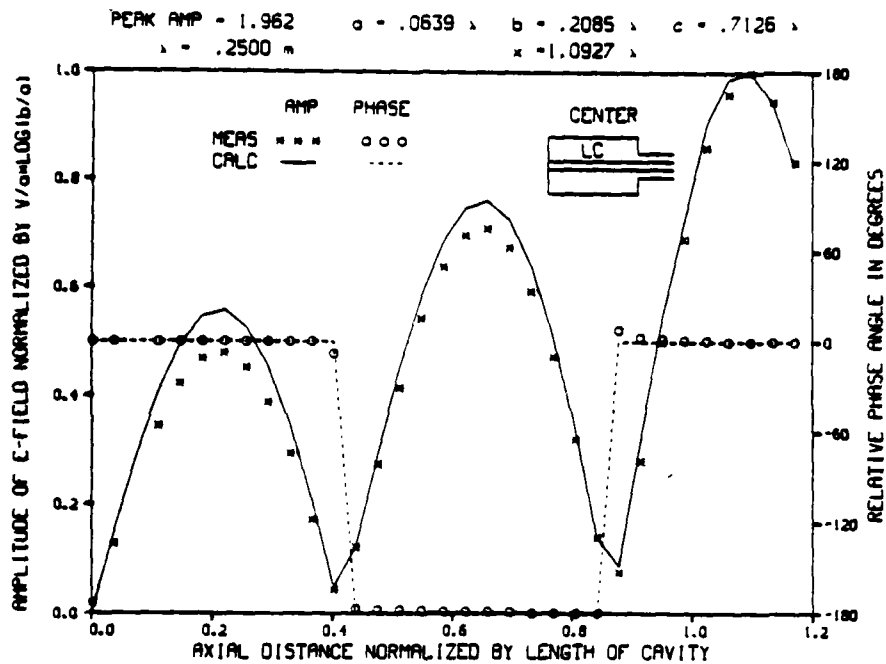


FIGURE 69 MEASURED AND CALCULATED μ COMPONENT OF ELECTRIC FIELD 1200 MHZ

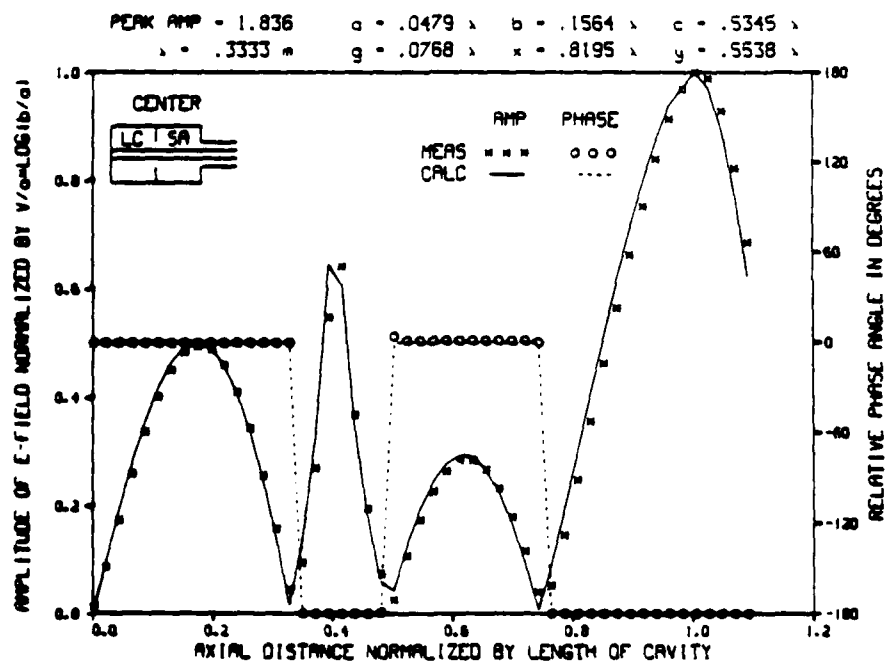


FIGURE 70 MEASURED AND CALCULATED μ COMPONENT OF ELECTRIC FIELD 900 MHZ

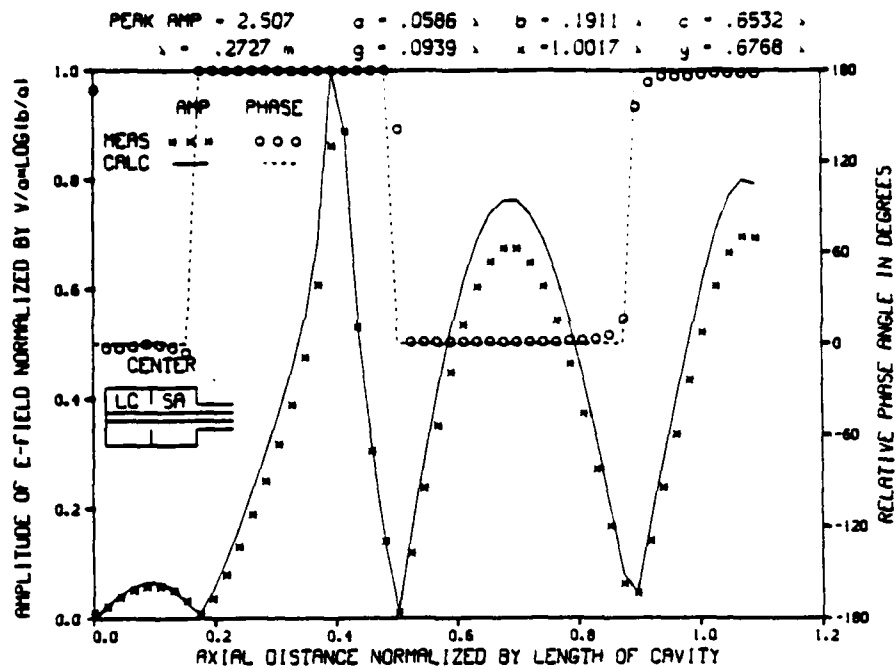


FIGURE 71 MEASURED AND CALCULATED, COMPONENT OF ELECTRIC FIELD 1100 MHZ

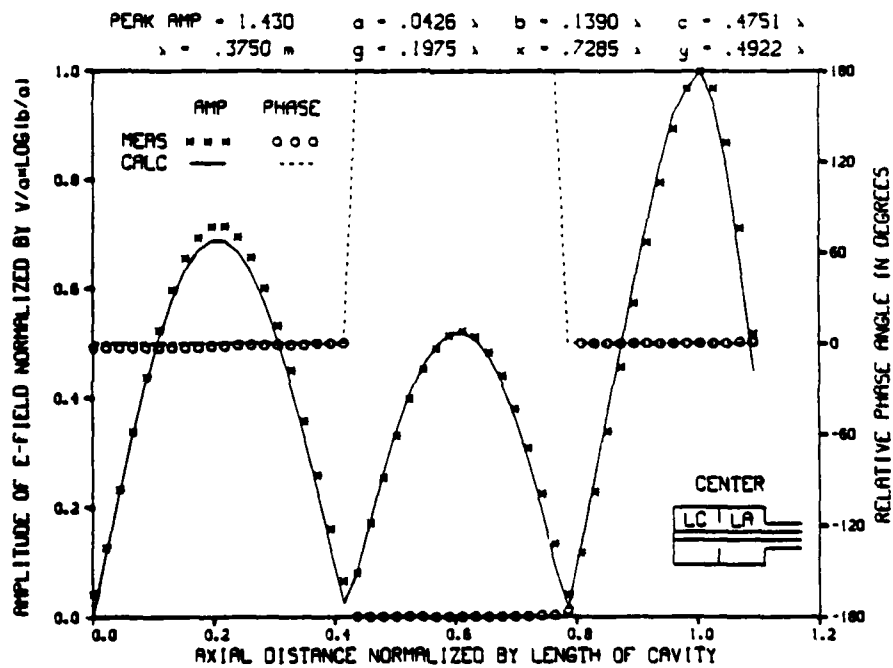
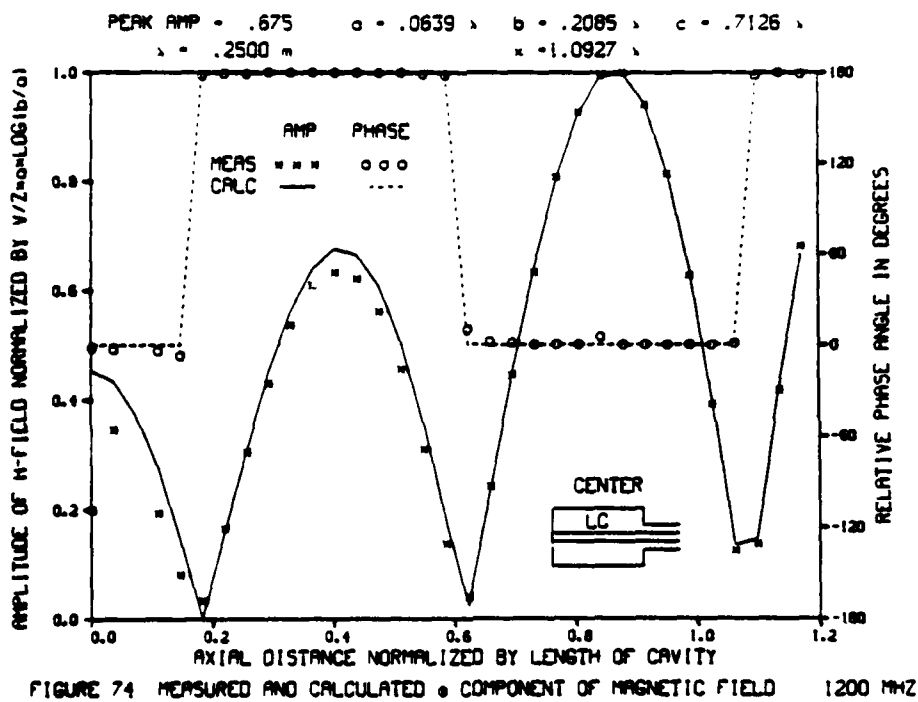
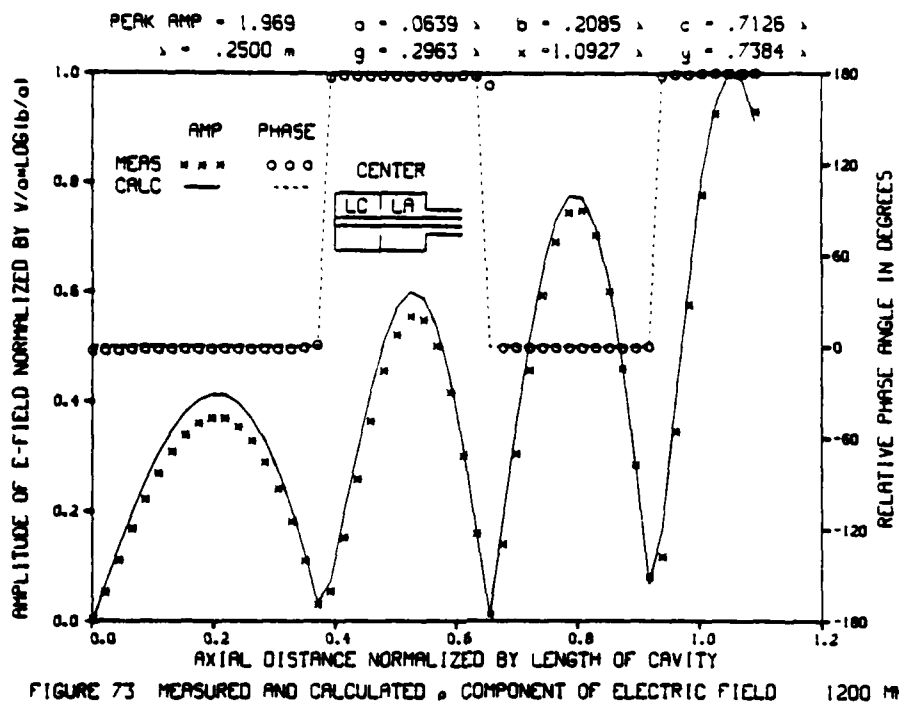


FIGURE 72 MEASURED AND CALCULATED, COMPONENT OF ELECTRIC FIELD 800 MHZ



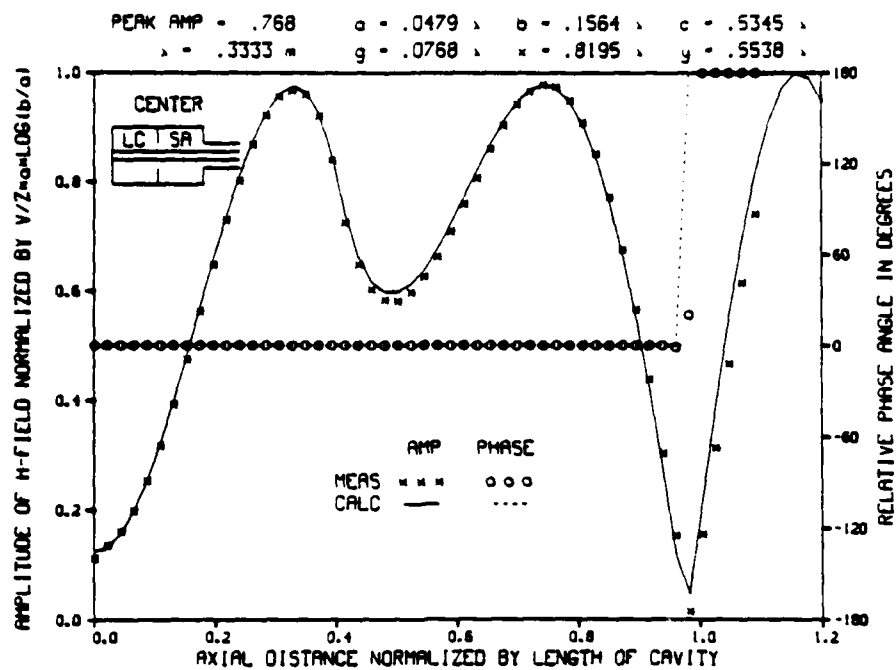


FIGURE 75 MEASURED AND CALCULATED • COMPONENT OF MAGNETIC FIELD 900 MHZ

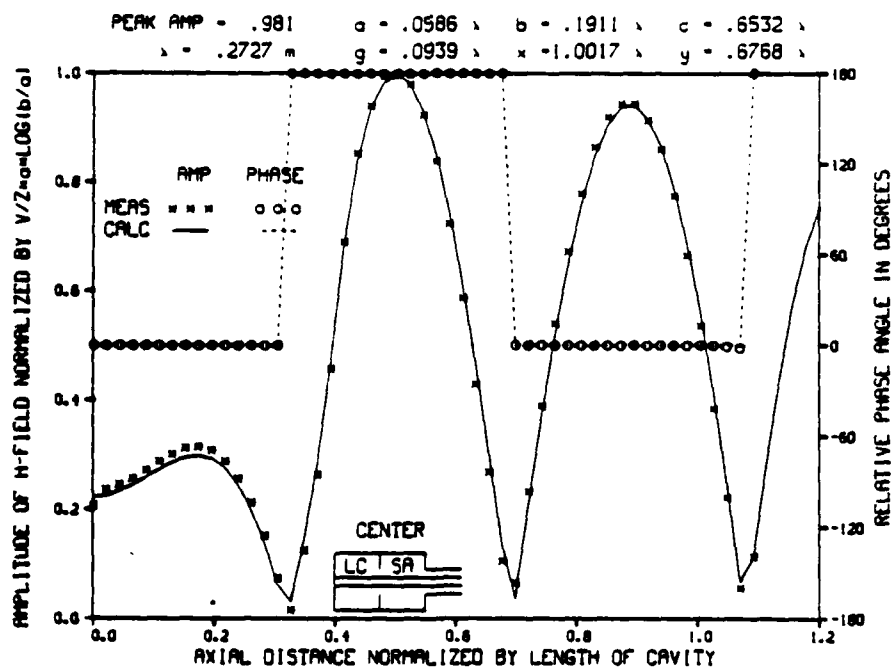


FIGURE 76 MEASURED AND CALCULATED • COMPONENT OF MAGNETIC FIELD 1100 MHZ

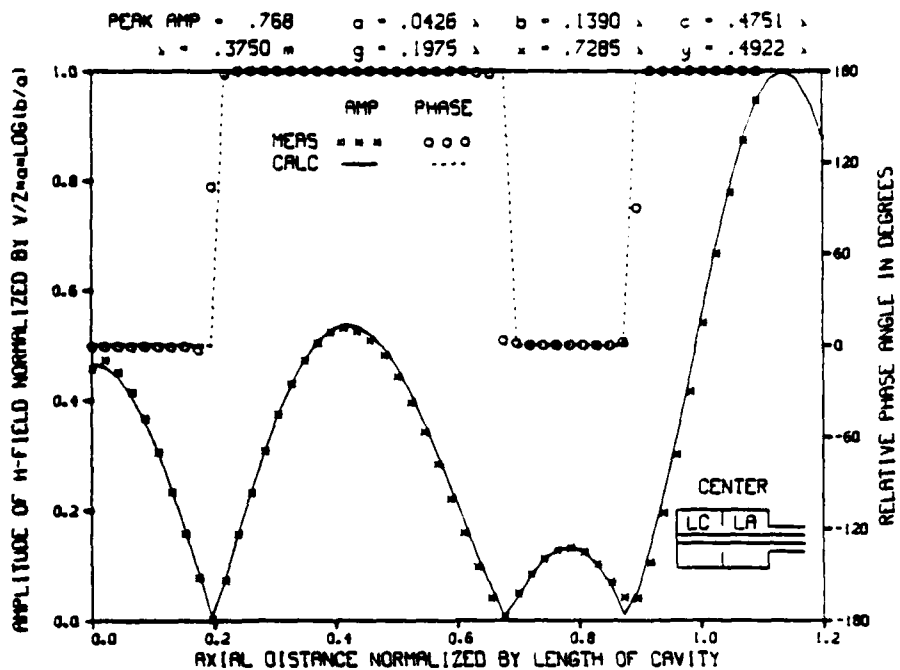


FIGURE 77 MEASURED AND CALCULATED θ COMPONENT OF MAGNETIC FIELD 800 MHZ

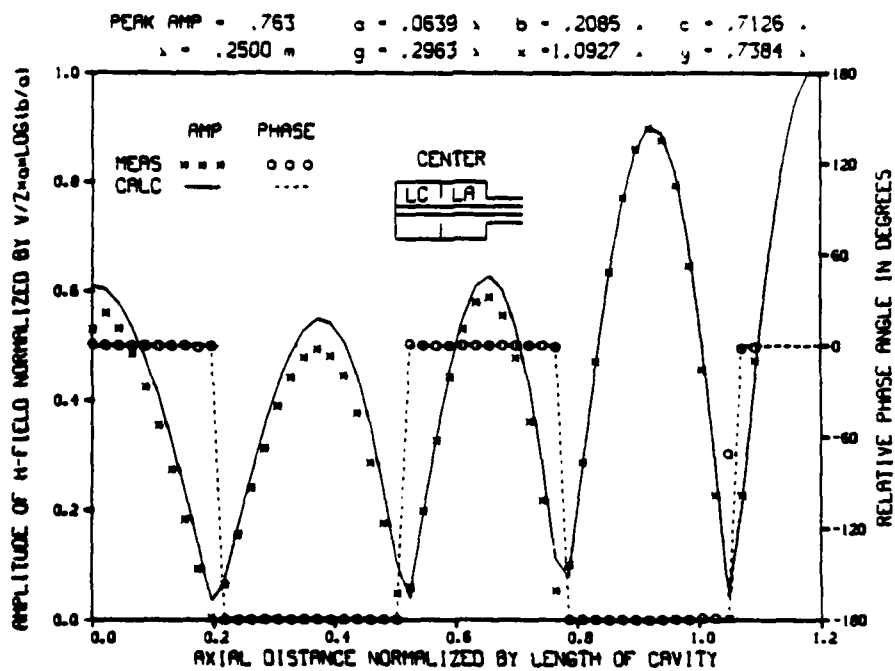


FIGURE 78 MEASURED AND CALCULATED θ COMPONENT OF MAGNETIC FIELD 1200 MHZ

CHAPTER IX

CONCLUSIONS

The primary objective of this investigation has been to develop a proven and practical technique for determining the electromagnetic properties of a set of planar discontinuities in coaxial waveguides. It is demonstrated early in this report that a knowledge of the transverse electric field distribution in the plane of the discontinuity (or discontinuities) is sufficient to characterize all electromagnetic properties of the structure. Accordingly, the bulk of the analysis has dealt with the derivation of tractable integral equations which can be solved to obtain these desired aperture field distributions. The technique for deriving such equations has proved to be quite general and has been easily extended to the treatment of coupled discontinuities. The general approach has also been applied to the related problem of the discontinuity occurring at the junction of a coaxial and circular waveguide where the coaxial center conductor is truncated.

A significant outcome of this effort is that any of the coaxial junctions, whether single or one of several forming a

complex structure, can be treated through the application of one general equation form. Use of such a general form is frequently cumbersome and experience has shown that three somewhat less general equation forms are more practical. The first of these general forms treats isolated discontinuities, the second treats discontinuities which are coupled to one other discontinuity, and the third treats discontinuities which are coupled to two other discontinuities, one on either side. The general equation form for the truncated coaxial center conductor may be similarly structured with an obvious limitation on the types of discontinuities to which this discontinuity may be simultaneously coupled.

The integral equations developed during this investigation have proved to be quite amenable to a straightforward numerical solution technique. The choice of an expansion function set for the aperture fields which allows analytic evaluation of the integrals significantly reduces the number of machine operations required and thus reduces the effect of this unavoidable source of error. Another very favorable factor is that the primary electromagnetic quantities of interest, e.g., admittance and internal field components, are computed from the integrals of the aperture fields, and integration is an operation which tends to reduce the effects of many distribution errors rather than enhance them.

A significant amount of effort during this investigation

was devoted to experimental measurements designed to verify the accuracy of the integral equation formulation and the numerical solution techniques. The comparisons between measured and calculated admittance values for three cavity structures demonstrated extremely good agreement. Significant differences between measured and calculated values appeared only at the highest frequencies measured and it is very probable that these differences are the result of experimental error. It is quite interesting to observe the exceptional agreement of the admittance calculated from transmission line theory with susceptance corrections from the Waveguide Handbook at lower frequencies, and then to observe the fairly rapid breakdown of this method as the frequency approaches the cutoff for the first higher-order mode.

The measurements of internal field components for nine different cavity structures and subsequent comparisons with calculated distributions has provided very impressive verification of the ability of the analytical technique to perform such calculations. There is not exact agreement for every measurement, but there is strong evidence that all such disagreements result from either instrumentation or experimental judgement errors. There are no cavity configurations where there is not exceptional agreement between measured and calculated field distributions for a majority of the frequencies sampled. The field distributions them-

selves provide an interesting study. There is generally little variation in the field distributions except near the transverse resonance frequencies. There is very little variation even at this frequency for measurements made at the rear end-plates of the one-port cavities. Measurements made on the end-plates of the two-port cavities generally display a gradual phase variation while the only phase variations observed for one-port cavity measurements are abrupt 180 degree shifts. If the primary goal of this effort had been to perform a rigorous characterization of several cavity structures, a substantial amount of additional data could have been generated and interesting comparisons drawn between field and admittance measurements over the frequency band. However, the amount of data obtained is more than adequate to verify the capability of the integral equation approach.

The descriptive term "practical", as applied in the first sentence of this chapter, can be interpreted to mean either useful or not excessively complicated to use, or, more likely, a given individual's combination of the two. A few suggested applications for the results of this investigation are given in Chapter I but this list does not emphasize possible microwave circuit applications. The demonstrations of the accuracy of the technique indicate possible applications in a large area of waveguide design problems where the expressions in the Waveguide Handbook have been used in

the past. The integral equation technique has given evidence of being more accurate for susceptance calculations than the expressions in the Waveguide Handbook for apertures that are small compared to the largest radial dimension. Examples presented in this report indicate that the accuracy of the aperture field solutions and, thus, the admittance calculations can be improved by increasing the number of expansion pulses used up to an, as yet, undetermined number. Increasing the number of series terms alone appears to have a less direct effect on convergence, but a larger number of pulses does require a larger number of series terms to achieve convergence. There is very likely a set of coaxial waveguide problems where either the requirements for extreme accuracy or extended bandwidth make the subject approach extremely appropriate. None of the publications listed in the Bibliography offer the means for calculating the admittance of coaxial discontinuities when higher-order modes are capable of propagation. The method of Wexler, Ref.[22], which can treat higher-order modes, could be modified to treat coaxial geometries; however, it is very cumbersome to treat more than a few such modes. It is the hope of the authors that the existence of this technique will play a role in developing useful applications for which it is well suited.

APPENDIX A

COMPLETENESS OF FIELD DERIVED FROM A MAGNETIC VECTOR POTENTIAL FOR A ROTATIONALLY SYMMETRIC WAVEGUIDE

All planar discontinuities in the coaxial waveguides considered in the present investigation are surfaces which support a transversely-directed electric current. The existence of such current components implies that a field description derived exclusively from a magnetic vector potential with only an axial component might not be complete. It is known that a field description which consists of the linear combination of all possible TEM, TM, and TE modes in a cylindrical waveguide is complete. In the present investigation, the TEM and TM modes are included so it remains to be determined whether or not there is possibly a necessary TE mode contribution to the field.

Within a cylindrical waveguide, all TE-mode field components can be derived from the axial component of an electric vector potential. The electric vector potential must satisfy the wave equation and for a coaxial region the general form is (note that the $m = 0$ term is not included)

$$F_z(\rho, \phi, z) = \sum_{m=-\infty}^{\infty} \sum_{n=1}^{\infty} a_{mn} Z_{mn}(z) e^{jm\phi} \Xi_{mn}(\rho) \quad (A-1)$$

where the axially-varying function $Z(z)$ is a solution of the harmonic equation

$$\frac{d^2 Z_{mn}(z)}{dz^2} + k_z^2 Z(z) = 0 \quad (A-2)$$

and Ξ_{mn} represents a set of solutions of Bessel's equation of order m . The form of Ξ_{mn} is dependent upon the requirement that the tangential component of the transverse electric field vanish at the walls of the waveguide. For a rotationally-symmetric waveguide with symmetric excitation, m must be zero and Eq. (A-1) becomes

$$F_z(\rho, z) = \sum_{n=1}^{\infty} a_n Z_n(z) \Xi_n(\rho) \quad (A-3)$$

The field components derived from this electric vector potential are

$$\begin{aligned} \vec{E} &= -\frac{1}{\epsilon} \nabla \times (\hat{z} F_z) \\ &= \sum_{n=1}^{\infty} \hat{\phi} \frac{a_n}{\epsilon} Z_n(z) \frac{d\Xi_n(\rho)}{d\rho} \end{aligned} \quad (A-4)$$

$$\begin{aligned} \vec{H} &= -j \frac{\omega}{k^2} [k^2 \hat{z} F_z + \nabla (\nabla \cdot \hat{z} F_z)] \\ &= -j \frac{\omega}{k^2} [k^2 \hat{z} F_z + \hat{\rho} \frac{\partial^2 F_z}{\partial \rho \partial z} + \hat{z} \frac{\partial^2 F_z}{\partial z^2}] \end{aligned} \quad (A-5)$$

For the field composed of TEM and TM modes to be incomplete, the ρ -directed current on the transverse surface must generate a field component which could be derived only from

an axially directed electric vector potential. A ϕ -independent, ρ -directed electric current generates only a ρ component of magnetic vector potential, A_ρ , and the field derived from A_ρ is given by

$$\begin{aligned}\vec{E} &= -j \frac{\omega}{k^2} [k^2 \hat{\rho} A_\rho + \nabla(\nabla \cdot \hat{\rho} A_\rho)] \\ &= -j \frac{\omega}{k^2} [k^2 \hat{\rho} A_\rho + \hat{\rho} \frac{\partial}{\partial \rho} \left\{ \frac{1}{\rho} \frac{\partial}{\partial \rho} (\rho A_\rho) \right\} + z \frac{\partial}{\partial z} \left\{ \frac{1}{\rho} \frac{\partial}{\partial \rho} (\rho A_\rho) \right\}] \quad (A-6)\end{aligned}$$

and

$$\begin{aligned}\vec{H} &= \frac{1}{\mu} \nabla \times \hat{\rho} A_\rho \\ &= -\frac{1}{\mu} \hat{\phi} \frac{\partial A_\rho}{\partial z} \quad (A-7)\end{aligned}$$

It should be noted that the scalar quantity A_ρ is not a solution to the wave equation and, therefore, is not useful in obtaining a solution for the field inside a waveguide. It is useful to note that the field components described by Eqs. (A-6) and (A-7) are precisely the same as those obtained from a ϕ -independent, axially directed component of magnetic vector potential, A_z . Furthermore, neither of the field components described by Eqs. (A-4) and (A-5) has a vector component that is common to the same field component of Eqs. (A-6) and (A-7). Therefore, there is no contribution to the field by a postulated F_z , so none is required for a complete field description.

APPENDIX B

PROCEDURE TO IMPROVE CONVERGENCE RATE OF BESSEL FUNCTION SERIES

An often productive procedure to increase the convergence rate of a given series consists of the termwise subtraction of a second series having a known sum and whose higher-order terms approach and eventually become equal to the corresponding terms of the first series. The sum of the initial series is then computed by adding the known sum of the second series to the series of difference terms. To illustrate the procedure, assume that the sum F of the following series is desired:

$$F = \sum_{n=1}^{\infty} f_n . \quad (B-1)$$

Next assume that there exists a second series with a known sum G

$$G = \sum_{n=1}^{\infty} g_n \quad (B-2)$$

whose individual terms have the following property

$$\lim_{n \rightarrow \infty} (f_n - g_n) = 0 . \quad (B-3)$$

If both series are convergent, then their sum or difference

is convergent, and Eq.(B-1) may be expressed

$$F = \sum_{n=1}^{\infty} (f_n - g_n) + G . \quad (B-4)$$

The difference series converges much more rapidly than either of the individual series. The rate of convergence is changed from a dependence upon how rapidly the magnitude of f_n approaches zero for increasing n to a function of how rapidly the individual f_n approaches the value of the corresponding g_n .

APPENDIX C

ASYMPTOTIC FORMS FOR EIGENFUNCTION EXPANSIONS OF FIELD COMPONENTS IN COAXIAL AND CIRCULAR WAVEGUIDES

A. Introduction

In order to apply the procedure described in Appendix B to the Bessel function series appearing in the definitions of the field components in coaxial and circular waveguides, the behavior of the series elements must be determined for increasing n . The roots of Bessel functions of the first and second kinds and of the function

$$\phi_n(\rho) = N_0(\gamma_n a) J_0(\gamma_n \rho) - J_0(\gamma_n a) N_0(\gamma_n \rho) \quad (C-1)$$

which is frequently obtained for coaxial geometries (with inner radius a), are increasing functions of n ; i.e., $\gamma_{n+1} > \gamma_n$ for $n+1 > n$, where γ_n denotes the n^{th} root of the particular function. Since the value of γ_n increases rapidly with n , the large argument forms of the Bessel functions become applicable. The following forms are used:

$$J_0(\gamma_n \rho) \underset{n \rightarrow \infty}{\sim} \sqrt{\frac{2}{\pi \gamma_n \rho}} \cos(\gamma_n \rho - \frac{\pi}{4}) \quad (C-2a)$$

$$N_0(\gamma_n \rho) \underset{n \rightarrow \infty}{\sim} \sqrt{\frac{2}{\pi \gamma_n \rho}} \sin(\gamma_n \rho - \frac{\pi}{4}) \quad (C-2b)$$

$$J_1(\gamma_n \rho) \xrightarrow{n \rightarrow \infty} \sqrt{\frac{2}{\pi \gamma_n \rho}} \cos(\gamma_n \rho - \frac{3\pi}{4}) \quad (C-2c)$$

$$N_1(\gamma_n \rho) \xrightarrow{n \rightarrow \infty} \sqrt{\frac{2}{\pi \gamma_n \rho}} \sin(\gamma_n \rho - \frac{3\pi}{4}) \quad (C-2d)$$

B. Asymptotic Form for H_ϕ in Coaxial Waveguide

With the assumption of no variation with ϕ , the transverse component of magnetic field in a coaxial waveguide is given by a positive and a negative traveling TEM-mode wave and an infinite sum of higher-order mode terms:

$$H_\phi = B_0^+ \frac{e^{-jkz}}{\eta \rho} - B_0^- \frac{e^{jkz}}{\eta \rho} + \frac{k}{\eta} \sum_{n=1}^{\infty} \frac{1}{\alpha_n} (B_n^+ e^{-j\alpha_n z} - B_n^- e^{j\alpha_n z}) \frac{d\phi_n}{d\rho}$$

where ϕ_n and α_n are defined by Eqs. (20) and (21), respectively. In this exercise, interest is limited to the higher-order mode terms which make up the infinite series. For a coaxial region between two discontinuities located at $z = s$ and t , $t > s$, the constants are defined

$$B_n^\pm = \frac{\pm e^{\pm j\alpha_n t}}{j2\sin\alpha_n(t-s) M_n^2} \int_h^b E_\rho^0 \rho \frac{d\phi_n}{d\rho} d\rho, \quad (C-3)$$

where the aperture electric field, E_ρ^0 , is defined by Eq. (31) and M_n^2 is defined by Eq. (36). The expression for the total TM contribution to the field is given by

$$H_\phi^{TM} = \frac{k}{\eta} \sum_{n=1}^{\infty} \left(\frac{\cos\alpha_n(t-z)}{j\sin\alpha_n(t-s) \alpha_n M_n^2} \int_h^b E_\rho^0 \rho \frac{d\phi_n}{d\rho} d\rho \right) \frac{d\phi_n}{d\rho}. \quad (C-4)$$

The aperture electric field may be expanded in a set of N pulses as defined by Eqs. (54) and (55). The integral is then evaluated to obtain

$$H_{\phi}^{TM} = \frac{k}{n} \sum_{n=1}^{\infty} \frac{\cos \alpha_n(t-z)}{j \sin \alpha_n(t-s) \alpha_n M_n^2} \left\{ \sum_{q=1}^N E_q [\phi_n(r_q^+) - \phi_n(r_q^-)] \right\} \frac{d\phi_n}{d\rho} \quad (C-5)$$

where r_q^+ and r_q^- are defined by Eq. (61). The expression may be rearranged to the form

$$H_{\phi}^{TM} = \frac{k}{n} \sum_{q=1}^N E_q \left[\sum_{n=1}^{\infty} \frac{\cos \alpha_n(t-z)}{j \sin \alpha_n(t-s)} \frac{\phi_n(r_q^+) - \phi_n(r_q^-)}{\alpha_n M_n^2} \frac{d\phi_n}{d\rho} \right].$$

Attention will now be directed toward the expression within the braces which is represented by $R_n(\rho)$:

$$R_n(\rho) = \frac{\phi_n(r_q^+) - \phi_n(r_q^-)}{\alpha_n M_n^2} \frac{d\phi_n}{d\rho}. \quad (C-6)$$

It is the expression given by Eq. (C-6) which determines the asymptotic behavior of the terms in the infinite series of Eq. (C-5). The elements of Eq. (C-6) are expanded in Bessel functions through the use of the definition for M_n^2 and the following

$$\frac{d\phi_n(\rho)}{d\rho} = -\gamma_n [N_0(\gamma_n a) J_1(\gamma_n \rho) - J_0(\gamma_n a) N_1(\gamma_n \rho)] \quad (C-7)$$

$$\begin{aligned}\phi_n(r_q^+) - \phi_n(r_q^-) &= [N_0(\gamma_n a)J_0(\gamma_n r_q^+) - J_0(\gamma_n a)N_0(\gamma_n r_q^+)] \\ &\quad - [N_0(\gamma_n a)J_0(\gamma_n r_q^-) - J_0(\gamma_n a)N_0(\gamma_n r_q^-)]. \quad (C-8)\end{aligned}$$

Substitution of the Bessel function forms into Eq. (C-6) yields the following expression:

$$\begin{aligned}R_n(\rho) &= \frac{-\gamma_n [N_0(\gamma_n a)J_1(\gamma_n \rho) - J_0(\gamma_n a)N_1(\gamma_n \rho)]}{\alpha_n \left\{ \frac{b^2 \gamma_n^2}{2} [N_0(\gamma_n a)J_1(\gamma_n b) - J_0(\gamma_n a)N_1(\gamma_n b)]^2 - \frac{2}{\pi^2} \right\}} \times \\ &\quad \{ [N_0(\gamma_n a)J_0(\gamma_n r_q^+) - J_0(\gamma_n a)N_0(\gamma_n r_q^+)] \\ &\quad - [N_0(\gamma_n a)J_0(\gamma_n r_q^-) - J_0(\gamma_n a)N_0(\gamma_n r_q^-)] \} \quad (C-9)\end{aligned}$$

The asymptotic forms of Eq. (C-2) are now substituted into Eq. (C-9) to yield

$$\begin{aligned}R_n(\rho) &= \frac{\frac{-2\gamma_n}{\alpha_n \pi \gamma_n \sqrt{a\rho}} [\sin(\gamma_n a - \frac{\pi}{4}) \cos(\gamma_n \rho - \frac{3\pi}{4}) - \cos(\gamma_n a - \frac{\pi}{4}) \sin(\gamma_n \rho - \frac{3\pi}{4})]}{\frac{4b^2 \gamma_n^2}{2ab\pi^2 \gamma_n^2} [\sin(\gamma_n a - \frac{\pi}{4}) \cos(\gamma_n b - \frac{3\pi}{4}) - \cos(\gamma_n a - \frac{\pi}{4}) \sin(\gamma_n b - \frac{3\pi}{4})]^2 - \frac{2}{\pi^2}} \times \\ &\quad \frac{2}{\pi \gamma_n} \frac{1}{\sqrt{a}} \left\{ \frac{1}{\sqrt{r_q^+}} [\sin(\gamma_n a - \frac{\pi}{4}) \cos(\gamma_n r_q^+ - \frac{\pi}{4}) - \cos(\gamma_n a - \frac{\pi}{4}) \sin(\gamma_n r_q^+ - \frac{\pi}{4})] \right. \\ &\quad \left. - \frac{1}{\sqrt{r_q^-}} [\sin(\gamma_n a - \frac{\pi}{4}) \cos(\gamma_n r_q^- - \frac{\pi}{4}) - \cos(\gamma_n a - \frac{\pi}{4}) \sin(\gamma_n r_q^- - \frac{\pi}{4})] \right\}. \quad (C-10)\end{aligned}$$

The trigonometric identity

$$\sin\phi \cos\theta - \cos\phi \sin\theta = \sin(\phi-\theta) \quad (C-11)$$

is employed to reduce Eq. (C-10) to the form

$$R_n(\rho) = \frac{-4\sin[\gamma_n(a-\rho) + \frac{\pi}{2}] \left[\frac{1}{\sqrt{r_q^+}} \sin[\gamma_n(a-r_q^+)] - \frac{1}{\sqrt{r_q^-}} \sin[\gamma_n(a-r_q^-)] \right]}{\pi^2 a \sqrt{\rho} \gamma_n \alpha_n \frac{2}{\pi^2} \left[\frac{b}{a} \sin^2[\gamma_n(a-b) - \frac{\pi}{2}] - 1 \right]}$$

The expression may be further reduced by noting that

$$\sin(\phi + \frac{\pi}{2}) = \cos\phi$$

which yields

$$R_n(\rho) = \frac{-2\cos[\gamma_n(a-\rho)] \left[\frac{1}{\sqrt{r_q^+}} \sin[\gamma_n(a-r_q^+)] - \frac{1}{\sqrt{r_q^-}} \sin[\gamma_n(a-r_q^-)] \right]}{a \sqrt{\rho} \gamma_n \alpha_n \frac{1}{a} \left[b \cos^2[\gamma_n(a-b)] - a \right]}$$

As n becomes larger, α_n approaches the value $-j\gamma_n$, yielding

$$R_n(\rho) = \frac{-2\cos[\gamma_n(a-\rho)] \left[\frac{1}{\sqrt{r_q^+}} \sin[\gamma_n(a-r_q^+)] - \frac{1}{\sqrt{r_q^-}} \sin[\gamma_n(a-r_q^-)] \right]}{-j\gamma_n^2 \sqrt{\rho} \left[b \cos^2[\gamma_n(a-b)] - a \right]}$$

As n becomes larger, γ_n approaches the value $\frac{n\pi}{b-a}$. The form of the expression then becomes

$$R_n(\rho) = \frac{-j2\cos\left[\frac{n\pi}{b-a}(a-\rho)\right] \left[\frac{1}{\sqrt{r_q^+}} \sin\left[\frac{n\pi}{b-a}(a-r_q^+)\right] - \frac{1}{\sqrt{r_q^-}} \sin\left[\frac{n\pi}{b-a}(a-r_q^-)\right] \right]}{\sqrt{\rho} \left(\frac{n\pi}{b-a}\right)^2 \left[b \cos^2\left[\frac{n\pi}{b-a}(a-b)\right] - a \right]}.$$

This expression may be simplified through the use of two trigonometric identities:

$$\cos^2(-n\pi) = 1$$

and

$$\cos\theta \sin\theta = \frac{1}{2} \sin(\theta+\theta) - \sin(\theta-\theta).$$

The expression now becomes

$$R_n(\rho) = \frac{-j(b-a)}{\pi^2 \sqrt{\rho}} \frac{1}{\sqrt{r_q^+}} \left[\frac{\sin(n\theta_1)}{n^2} - \frac{\sin(n\theta_2)}{n^2} \right] + \frac{1}{\sqrt{r_q^-}} \left[\frac{\sin(n\theta_3)}{n^2} - \frac{\sin(n\theta_4)}{n^2} \right] \quad (C-12)$$

where

$$\theta_1 = \frac{\pi}{b-a}(2a - \rho - r_q^+)$$

$$\theta_2 = \frac{\pi}{b-a}(r_q^+ - \rho)$$

$$\theta_3 = \frac{\pi}{b-a}(2a - \rho - r_q^-)$$

$$\theta_4 = \frac{\pi}{b-a}(r_q^- - \rho).$$

This exercise has demonstrated that the asymptotic (large

argument) form of the Bessel function expansion for H_{ϕ}^{TM} consists of four series which have the general form:

$$S(\theta) = \sum_{n=1}^{\infty} \frac{\sin(n\theta)}{n^2} \quad (C-13)$$

In order to apply the technique described in Appendix B, another series is required which has a known sum and whose individual elements have a form similar to those of Eq. (C-13). In Ref. [26], expression 604 is given as

$$\sum_{n=2}^{\infty} \frac{\sin(n\theta)}{n^2-1} = \frac{\sin\theta}{4} - \sin\theta \ln\{2\sin\frac{\theta}{2}\}, \quad 0 < \theta < 2\pi. \quad (C-14)$$

The procedure of Appendix B may now be employed to obtain a modified form of Eq. (C-12) which converges more rapidly. The resulting series expansion for H_{ϕ}^{TM} is

$$\begin{aligned} H_{\phi}^{TM} = & \frac{k}{\eta} \sum_{q=1}^N E_q \sum_{n=1}^{\infty} \frac{\cos\alpha_n(t-z)}{j\sin\alpha_n(t-s)} \left[\frac{\phi_n(r_q^+) - \phi_n(r_q^-)}{a_n M_n^2} \frac{d\phi_n(\rho)}{d\rho} \right] \\ & + \frac{j(b-a)}{\pi^2 \sqrt{\rho}} \frac{1}{n^2-1} \left[\frac{\sin(n\theta_1) - \sin(n\theta_2)}{\sqrt{r_q^+}} - \frac{\sin(n\theta_3) - \sin(n\theta_4)}{\sqrt{r_q^-}} \right] \\ & - \frac{j(b-a)}{\pi^2 \sqrt{\rho}} \frac{1}{\sqrt{r_q^+}} \left[\sin\theta_1 \left(\frac{1}{4} \ln\{2\sin\frac{\theta_1}{2}\} \right) - \sin\theta_2 \left(\frac{1}{4} \ln\{2\sin\frac{\theta_2}{2}\} \right) \right] \\ & \frac{1}{\sqrt{r_q^-}} \left[\sin\theta_3 \left(\frac{1}{4} \ln\{2\sin\frac{\theta_3}{2}\} \right) - \sin\theta_4 \left(\frac{1}{4} \ln\{2\sin\frac{\theta_4}{2}\} \right) \right]. \quad (C-15) \end{aligned}$$

Because the series of Eq.(C-14) begins with $n = 2$, the asymptotic terms are not evaluated for $n = 1$. Care must be taken that the arguments of the sine functions in Eq.(C-15) be in the range specified by Eq.(C-14). If the argument falls outside the range, the argument can be brought into the proper range by adding or subtracting multiples of 2π or by employing appropriate trigonometric relationships.

The sine and cosine functions in Eq.(C-5) are not included in the derivation of the asymptotic form for two reasons: the first is that these terms are not always present and the second is that when the terms are present, they are easily treated because of the behavior of hyperbolic functions. The behavior of the quotient $\cos\alpha_n(t-z)/j\sin\alpha_n(t-s)$ as n increases is primarily dependent on the value of z . Since α_n approaches $-j\gamma_n$ for large n , the trigonometric functions become hyperbolic functions with the following behavior:

For $z = s$:

$$\lim_{n \rightarrow \infty} \frac{\cos\alpha_n(t-s)}{\sin\alpha_n(t-s)} \rightarrow \lim_{n \rightarrow \infty} \frac{\cosh\gamma_n(t-s)}{-j\sinh\gamma_n(t-s)} \rightarrow j \quad (C-16)$$

For $z = \zeta$: $s < \zeta \leq t$

$$\lim_{n \rightarrow \infty} \frac{\cos\alpha_n(t-\zeta)}{\sin\alpha_n(t-s)} \rightarrow \lim_{n \rightarrow \infty} \frac{\cos\gamma_n(t-\zeta)}{-j\sinh\gamma_n(t-s)} \rightarrow 0 \quad (C-17)$$

AD-A103 056

MISSISSIPPI UNIV UNIVERSITY

F/G 20/3

AN ANALYTICAL AND EXPERIMENTAL INVESTIGATION OF PLANAR DISCONTINUITIES (U)

MAR 81 M G HARRISON, C M BUTLER

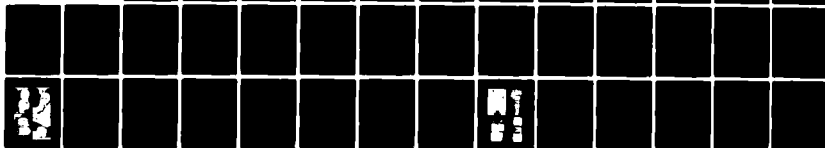
AFOSR-77-3464

UNCLASSIFIED

AFWL-TR-79-187

NL

3 of 3
A-103 056



END

DATE

FILED

9-81

DTIC

An inspection of Eq.(C-5) will verify that the asymptotic form of Eq.(C-16) normally occurs in conjunction with a $\frac{1}{j}$ factor. Since the product of j and $\frac{1}{j}$ is unity, the limit of the quotient $\cos\alpha_n(t-s)/j\sin\alpha_n(t-s)$ as n increases without bound is unity and, therefore, it does not enter into the asymptotic form for H_ϕ^{TM} . An even more advantageous result is obtained when the quotient is of the form given by Eq.(C-17). These factors approach zero so rapidly with increasing n that it is unnecessary to employ the procedure of Appendix to obtain rapid convergence.

C. Asymptotic Form for E_ρ in Coaxial Waveguide

An expression for the higher-order mode expansion of E_ρ in the same coaxial region for which Eq.(C-4) is defined is given by

$$E_\rho^{TM} = \sum_{n=1}^{\infty} \left[\frac{\sin\alpha_n(t-z)}{\sin\alpha_n(t-s)} \frac{1}{M_n^2} \int_h^b E_\rho^0 \rho \frac{d\phi_n}{d\rho} d\rho \right] \frac{d\phi_n}{d\rho} \quad (C-18)$$

The only difference between Eq.(C-5) and Eq.(C-18) which would affect the asymptotic form of the latter is the lack of the $1/\alpha_n$ term found in the former. The use of this fact allows the derivation of the asymptotic form $S_n(\rho)$ equivalent to $R_n(\rho)$ for H^{TM} by multiplying Eq.(C-12) by the asymptotic form of α_n :

$$\lim_{n \rightarrow \infty} \alpha_n \rightarrow \frac{-jn\pi}{b-a}$$

The resulting expression for $S_n(\rho)$ is given by

$$S_n(\rho) = \frac{-1}{\pi\sqrt{\rho}} \frac{1}{\sqrt{r_q^+}} \left(\frac{\sin(n\theta_1)}{n} \frac{\sin(n\theta_2)}{n} \right) \frac{1}{\sqrt{r_q^-}} \left(\frac{\sin(n\theta_3)}{n} \frac{\sin(n\theta_4)}{n} \right) . \quad (C-19)$$

The definitions of the θ_n are the same as those given for Eq.(C-12). The convergence improving procedure of Appendix B can now be applied by employing expression number 508 of Ref.[26]:

$$\sum_{n=1}^{\infty} \frac{\sin(n\theta)}{n} = \frac{1}{2}(\pi - \theta) \quad , \quad 0 < \theta < 2\pi . \quad (C-20)$$

D. Asymptotic Form for E_z in Coaxial Waveguide

The z-directed component of electric field has no TEM component and is defined entirely by its higher-order mode expansion. An expression for E_z which is valid in the same coaxial region as that for Eqs.(C-4) and (C-18) is given by

$$E_z = \sum_{n=1}^{\infty} \left(\frac{\cos\alpha_n(t-z)}{j\sin\alpha_n(t-s)} \frac{\gamma_n^2}{\alpha_n M_n^2} \int_h^b E_{\rho}^o \rho \frac{d\phi_n}{d\rho} d\rho \right) \phi_n . \quad (C-21)$$

The process for obtaining the asymptotic form is begun by substituting the large argument forms of the Bessel functions into Eq.(C-21) and results in the expression:

$$T_n(\rho) = \gamma_n^2 [N_0(\gamma_n a) J_0(\gamma_n \rho) - J_0(\gamma_n a) N_0(\gamma_n \rho)] \\ \alpha_n \left(\frac{b^2 \gamma_n^2}{2} [N_0(\gamma_n a) J_1(\gamma_n b) - J_0(\gamma_n a) N_0(\gamma_n b)]^2 - \frac{2}{\pi^2} \right) \\ \{ [N_0(\gamma_n a) J_0(\gamma_n r_q^+) - J_0(\gamma_n a) N_0(\gamma_n r_q^+)] \\ [N_0(\gamma_n a) J_0(\gamma_n r_q^-) - J_0(\gamma_n a) N_0(\gamma_n r_q^-)] \} . \quad (C-22)$$

After the steps outlined in Eqs.(C-7) through (C-12) are followed, an asymptotic expression for $T_n(\rho)$ is obtained:

$$T_n(\rho) = \frac{j}{\pi^2 \sqrt{\rho}} \frac{1}{\sqrt{r_q^+}} \left(\frac{\cos(n\theta_1)}{n} - \frac{\cos(n\theta_2)}{n} \right) \\ \frac{1}{\sqrt{r_q^-}} \left(\frac{\cos(n\theta_3)}{n} - \frac{\cos(n\theta_4)}{n} \right) . \quad (C-23)$$

The θ_n are the same as those defined for Eq.(C-12). The convergence improving procedure of Appendix B may be applied with the use of expression number 503 of Ref.[26]:

$$\sum_{n=1}^{\infty} \frac{\cos(n\theta)}{n} = -\ln\{2\sin\frac{\theta}{2}\} , \quad 0 < \theta < 2\pi . \quad (C-24)$$

E. Asymptotic Form for H_ϕ in Circular Waveguide

The field in a circular waveguide consists only of higher-order modes. The field expansion is different from that of a coaxial region and, consequently, the asymptotic

forms for the individual field components are different. In Chapter VI, it is shown that the transverse component of magnetic field is proportional to the following expression:

$$H_{\phi}^C = \frac{k}{\eta} \sum_{n=1}^{\infty} \frac{2 \cos \alpha_n (t-z)}{j \sin \alpha_n (t-s) b^2 \alpha_n J_1^2(\lambda_n b)} \int_a^b E_{\rho}^O \rho J_1(\lambda_n \rho) J_1(\lambda_n \rho) . \quad (C-25)$$

After E_{ρ}^O is expanded in a set of weighted pulses defined by Eq.(31), the integral is evaluated and a function $Q_n(\rho)$ is extracted:

$$Q_n(\rho) = \frac{-2 J_1(\lambda_n \rho)}{\lambda_n b^2 \alpha_n J_1^2(\lambda_n b)} [J_0(\lambda_n r_q^+) - J_0(\lambda_n r_q^-)] . \quad (C-26)$$

Substitution of the asymptotic forms for the Bessel functions into Eq.(C-26) yields

$$Q_n(\rho) = \frac{-2 \frac{2}{\pi \lambda_n} \cos(\lambda_n \rho - \frac{3\pi}{4}) \frac{2}{\pi \lambda_n}}{\lambda_n b^2 \alpha_n \sqrt{\rho} \frac{2}{\pi \lambda_n b} \cos^2(\lambda_n b - \frac{3\pi}{4})} \left[\frac{1}{\sqrt{r_q^+}} \cos(\lambda_n r_q^+ - \frac{\pi}{4}) - \frac{1}{\sqrt{r_q^-}} \cos(\lambda_n r_q^- - \frac{\pi}{4}) \right] . \quad (C-27)$$

The trigonometric identity

$$\cos \phi \cos \theta = \frac{1}{2} [\cos(\phi + \theta) + \cos(\phi - \theta)] \quad (C-28)$$

is now employed to yield

$$Q_n(\rho) = \frac{-1}{\alpha_n \lambda_n b \sqrt{\rho} \cos^2(\lambda_n b - \frac{3\pi}{4})} \left\{ \frac{1}{\sqrt{r_q^+}} \{ \cos[\lambda_n(\rho + r_q^+) - \pi] \right. \\ \left. + \cos[\lambda_n(\rho - r_q^+) - \frac{\pi}{2}] \} - \frac{1}{\sqrt{r_q^-}} \{ \cos[\lambda_n(\rho + r_q^-) - \pi] + \cos[\lambda_n(\rho - r_q^-) - \frac{\pi}{2}] \} \right\}.$$

Three additional identities:

$$\cos(\phi - \pi) = -\cos\phi, \quad (C-29a)$$

$$\cos(\phi - \frac{\pi}{2}) = \sin\phi, \quad (C-29b)$$

and

$$\cos^2\phi = \frac{1}{2}[\cos 2\phi + 1], \quad (C-29c)$$

are used to obtain

$$Q_n(\rho) = \frac{-2}{\alpha_n \lambda_n b \sqrt{\rho} [-\sin(2\lambda_n b) + 1]} \left\{ \frac{1}{\sqrt{r_q^+}} \{ -\cos[\lambda_n(\rho + r_q^+)] \right. \\ \left. + \sin[\lambda_n(\rho - r_q^+)] \} - \frac{1}{\sqrt{r_q^-}} \{ -\cos[\lambda_n(\rho + r_q^-)] + \sin[\lambda_n(\rho - r_q^-)] \} \right\}.$$

For increasing n :

$$\alpha_n \rightarrow -j\lambda_n \quad (C-30a)$$

and

$$\lambda_n \rightarrow \frac{(n - \frac{1}{2})\pi}{b}. \quad (C-30b)$$

The asymptotic form of $Q_n(\rho)$ is now given by

$$Q_n(\rho) = \frac{-2}{-jb \frac{(n-\frac{1}{2})^2 \pi^2}{b^2} \sqrt{\rho} \left[-\sin\left[\frac{2(n-\frac{1}{2})\pi}{b}b\right] + 1 \right]} \times$$

$$\left\{ \frac{1}{\sqrt{r_q^+}} \left\{ \sin\left[\frac{(n-\frac{1}{2})\pi}{b}(\rho-r_q^+)\right] - \cos\left[\frac{(n-\frac{1}{2})\pi}{b}(\rho+r_q^+)\right] \right\} \right. \\ \left. - \frac{1}{\sqrt{r_q^-}} \left\{ \sin\left[\frac{(n-\frac{1}{2})\pi}{b}(\rho-r_q^-)\right] - \cos\left[\frac{(n-\frac{1}{2})\pi}{b}(\rho+r_q^-)\right] \right\} \right\} .$$

Note that: $\sin[(2n-\frac{1}{2})\pi] = -1$.

The asymptotic expression for $Q_n(\)$ may be presented more compactly by

$$Q_n(\rho) = \frac{-jb}{(n-\frac{1}{2})^2 \pi^2 \sqrt{\rho}} \left\{ \frac{1}{\sqrt{r_q^+}} \left\{ \sin(n-\frac{1}{2})\phi_1 - \cos(n-\frac{1}{2})\phi_2 \right\} \right. \\ \left. - \frac{1}{\sqrt{r_q^-}} \left\{ \sin(n-\frac{1}{2})\phi_3 - \cos(n-\frac{1}{2})\phi_4 \right\} \right\} , \quad (C-31)$$

where

$$\phi_1 = \frac{\pi}{b}(\rho-r_q^+) ,$$

$$\phi_2 = \frac{\pi}{b}(\rho+r_q^+) ,$$

$$\phi_3 = \frac{\pi}{b}(\rho-r_q^-) ,$$

and

$$\phi_4 = \frac{\pi}{b}(\rho+r_q^-) .$$

The use of the trigonometric identities:

$$\sin(\phi - \theta) = \sin\phi \cos\theta - \cos\phi \sin\theta \quad (\text{C-32})$$

and

$$\cos(\phi - \theta) = \cos\phi \cos\theta + \sin\phi \sin\theta, \quad (\text{C-33})$$

results in the expression

$$\begin{aligned} Q_n(\rho) = & \frac{-jb}{(n-\frac{1}{4})^2 \pi^2 \sqrt{\rho}} \left\{ \frac{1}{\sqrt{r_q^+}} \left\{ \cos\frac{\phi_1}{4} \sin(n\phi_1) - \sin\frac{\phi_1}{4} \cos(n\phi_1) \right. \right. \\ & - \cos\frac{\phi_2}{4} \cos(n\phi_2) - \sin\frac{\phi_2}{4} \sin(n\phi_2) \left. \right\} - \frac{1}{\sqrt{r_q^-}} \left\{ \cos\frac{\phi_3}{4} \sin(n\phi_3) \right. \\ & \left. \left. - \sin\frac{\phi_3}{4} \cos(n\phi_3) - \cos\frac{\phi_4}{4} \cos(n\phi_4) - \sin\frac{\phi_4}{4} \sin(n\phi_4) \right\} \right\}. \quad (\text{C-34}) \end{aligned}$$

The procedure of Appendix B may now be applied by employing Eq.(C-14) for the sine series and one of the following expressions from Ref.[26]: (The second expression is #605.)

$$\sum_{n=1}^{\infty} \frac{\cos(n\phi)}{n^2} = \frac{\pi^2}{6} - \frac{\pi\phi}{2} + \frac{\phi^2}{4}, \quad 0 < \phi < 2\pi \quad (\text{C-35})$$

$$\sum_{n=2}^{\infty} \frac{\cos(n\phi)}{n^2-1} = \frac{1}{2} + \frac{1}{2}\cos\phi - \frac{1}{2}(\pi-\phi)\sin\phi, \quad 0 < \phi < 2\pi \quad (\text{C-36})$$

If the series with n^2-1 in the denominator are used, the $n = 1$ terms are neglected.

F. Asymptotic Form for E_ρ in Circular Waveguide

The asymptotic form for E can be obtained from that for H_ϕ by multiplying the latter by α_n . For very large n , α_n approaches $-j(n-\frac{1}{4})\pi/b$, and the subsequent multiplication of Eq.(C-34) by this factor yields the expression

$$V_n(\rho) = \frac{-1}{(n-\frac{1}{4}) \pi \sqrt{\rho}} \left\{ \frac{1}{\sqrt{r_q^+}} \cos \frac{\hat{\phi}_1}{4} \sin(n\hat{\phi}_1) - \sin \frac{\hat{\phi}_1}{4} \cos(n\hat{\phi}_1) \right. \\ - \cos \frac{\hat{\phi}_2}{4} \cos(n\hat{\phi}_2) - \sin \frac{\hat{\phi}_2}{4} \sin(n\hat{\phi}_2) \Big\} - \frac{1}{\sqrt{r_q^-}} \left\{ \cos \frac{\hat{\phi}_3}{4} \sin(n\hat{\phi}_3) \right. \\ \left. - \sin \frac{\hat{\phi}_3}{4} \cos(n\hat{\phi}_3) - \cos \frac{\hat{\phi}_4}{4} \cos(n\hat{\phi}_4) - \sin \frac{\hat{\phi}_4}{4} \sin(n\hat{\phi}_4) \right\} . \quad (C-37)$$

The convergence improving procedure of Appendix B may be applied through the use of the series in Eqs.(C-20) and (C-24).

APPENDIX D

PROPERTIES OF SOLUTIONS TO BESSEL'S EQUATION

1. Introduction

In the present analysis, frequent use of various Bessel functions (solutions to Bessel's equation) is made and, thus, for convenience, pertinent properties are developed and summarized here.

2. Orthogonality

Bessel's equation is

$$\frac{1}{x} \frac{d}{dx} \left\{ x \frac{d}{dx} f_n(\lambda x) \right\} + \left(\lambda^2 - \frac{n^2}{x^2} \right) f_n(\lambda x) = 0$$

where f_n is any solution. Consider two solutions $B_n(\lambda_q x)$ and $Z_m(\gamma_p x)$ of

$$\frac{1}{x} \frac{d}{dx} \left\{ x \frac{d}{dx} B_n(\lambda_q x) \right\} + \left(\lambda_q^2 - \frac{n^2}{x^2} \right) B_n(\lambda_q x) = 0 \quad (D-1a)$$

and

$$\frac{1}{x} \frac{d}{dx} \left\{ x \frac{d}{dx} Z_m(\gamma_p x) \right\} + \left(\gamma_p^2 - \frac{m^2}{x^2} \right) Z_m(\gamma_p x) = 0 \quad (D-1b)$$

Multiply Eq. (D-1a) by $x Z_m(\gamma_p x)$ and Eq. (D-1b) by $x B_n(\lambda_q x)$ to obtain

$$- z_m(\gamma_p x) \frac{d}{dx} \left(x \frac{d}{dx} B_n(\lambda_q x) \right) + \left(\lambda_q^2 - \frac{n^2}{x^2} \right) x z_m(\gamma_p x) B_n(\lambda_q x) = 0 \quad (D-2a)$$

and

$$B_n(\lambda_q x) \frac{d}{dx} \left(x \frac{d}{dx} z_m(\gamma_p x) \right) + \left(\gamma_p^2 - \frac{m^2}{x^2} \right) x z_m(\gamma_p x) B_n(\lambda_q x) = 0 \quad (D-2b)$$

Subtract Eq. (D-2b) from Eq. (D-2a) and integrate over (a,b):

$$\begin{aligned} \int_{x=a}^b \left[z_m \frac{d}{dx} \left(x \frac{d}{dx} B_n \right) - B_n \frac{d}{dx} \left(x \frac{d}{dx} z_m \right) \right] dx \\ = \int_{x=a}^b \left[\left(\gamma_p^2 - \lambda_q^2 \right) + \frac{1}{x^2} (n^2 - m^2) \right] x z_m B_n dx \end{aligned} \quad (D-3)$$

The left side of Eq. (D-3), after one integration by parts, reduces to

$$\begin{aligned} \int_{x=a}^b \left[z_m \frac{d}{dx} \left(x \frac{d}{dx} B_n \right) - B_n \frac{d}{dx} \left(x \frac{d}{dx} z_m \right) \right] dx \\ = \left[x z_m \frac{d}{dx} B_n - x B_n \frac{d}{dx} z_m \right]_{x=a}^b \\ - \int_{x=a}^b \left[x \left(\frac{d}{dx} B_n \right) \left(\frac{d}{dx} z_m \right) - x \left(\frac{d}{dx} z_m \right) \left(\frac{d}{dx} B_n \right) \right] dx \\ = \left[x z_m \frac{d}{dx} B_n - x B_n \frac{d}{dx} z_m \right]_{x=a}^b \end{aligned}$$

so that one may write

$$\begin{aligned}
 & (\gamma_p^2 - \lambda_q^2) \int_{x=a}^b x Z_m B_n dx + (n^2 - m^2) \int_{x=a}^b \frac{1}{x} Z_m B_n dx \\
 & = \left[x Z_m \frac{d}{dx} B_n - B_n \frac{d}{dx} Z_m \right]_{x=a}^b \quad (D-4)
 \end{aligned}$$

Eq. (D-4) serves as the basis for determination of various useful properties of solutions to Bessel's equation. These properties are developed in turn below. When $m=n$, Eq. (D-4) reduces to

$$\begin{aligned}
 & (\gamma_p^2 - \lambda_q^2) \int_{x=a}^b x Z_n(\gamma_p x) B_n(\lambda_q x) dx \\
 & = \left[x \left(Z_n(\gamma_p x) \frac{d}{dx} B_n(\lambda_q x) - B_n(\lambda_q x) \frac{d}{dx} Z_n(\gamma_p x) \right) \right]_{x=a}^b \quad (D-5)
 \end{aligned}$$

Observe that:

$$\int_{x=a}^b x Z_n(\gamma_p x) B_n(\lambda_q x) dx = 0 \quad (D-6)$$

if $\gamma_p^2 \neq \lambda_q^2$ and if the following is true:

$$\left[x \left(Z_n(\gamma_p x) \frac{d}{dx} B_n(\lambda_q x) - B_n(\lambda_q x) \frac{d}{dx} Z_n(\gamma_p x) \right) \right]_{x=a}^b = 0 \quad (D-7)$$

Z_n and B_n can be the same solution to Bessel's equation or different solutions; e.g., J_n , N_n , or combinations of these. If the term within the braces of Eq.(D-7) is zero at both a and b , or one is zero at a and the other at b , the condition is satisfied.

Another condition which leads to similar results is

$$x \frac{d}{dx} Z_n + Z_n = 0 \quad (D-8a)$$

$$x \frac{d}{dx} B_n + B_n = 0 \quad (D-8b)$$

at $x=a$ and at $x=b$ as can be seen from the following simplification of the left-hand side of Eq.(D-7) subject to Eq.(D-8):

$$\left[\left(Z_n(\gamma_p b) [-B_n(\lambda_q b)] - B_n(\lambda_q b) [Z_n(\gamma_p b)] \right) - \left(Z_n(\gamma_p a) [-B_n(\lambda_q a)] - B_n(\lambda_q a) [Z_n(\gamma_p a)] \right) \right] = 0 \quad (D-9)$$

It is worth noting that Eq.(D-9) follows from Eq.(D-8) also in the special case that $Z_n = B_n$ (the eigenvalues are maintained distinct).

If Eq.(D-1a) is replaced by the zero eigenvalue equation below:

$$\frac{1}{x} \frac{d}{dx} \left(x \frac{d}{dx} R_n(x) \right) - \frac{n^2}{x^2} R_n(x) = 0$$

and the preceding procedure is repeated, one arrives at

$$\gamma_p^2 \int_{x=a}^b x z_n(\gamma_p x) R_n(x) dx$$

$$= \left[x \left(z_n(\gamma_p x) \frac{d}{dx} R_n(x) - R_n(x) \frac{d}{dx} z_n(\gamma_p x) \right) \right]_{x=a}^b \quad (D-10)$$

which shows that the solution $R_n(x)$ for the zero eigenvalue exhibits the same property as those associated with non-zero eigenvalues.

3. Normalization

If Bessel's equation is multiplied by $2x^2 \frac{d}{dx} f_n(\lambda x)$, one obtains

$$2x \frac{d}{dx} f_n \frac{d}{dx} (x \frac{d}{dx} f_n) + 2(\lambda^2 x^2 - n^2) \frac{d}{dx} f_n f_n = 0$$

or

$$\frac{d}{dx} \left([x \frac{d}{dx} f_n]^2 \right) - n^2 \frac{d}{dx} [f_n^2] + \lambda^2 \left(2x^2 \frac{d}{dx} f_n f_n \right) = 0 \quad (D-11)$$

By direct differentiation, one obtains

$$\frac{d}{dx} [x^2 f_n^2] = 2x^2 f_n \frac{d}{dx} f_n + 2x f_n^2$$

or

$$2x^2 f_n \frac{d}{dx} f_n = \frac{d}{dx} [x^2 f_n^2] - 2x f_n^2$$

which enables one to reduce Eq. (D-11) to

$$2\lambda^2 x f_n^2 = \frac{d}{dx} \left([x \frac{d}{dx} f_n]^2 \right) + \lambda^2 \frac{d}{dx} [x^2 f_n^2] - n^2 \frac{d}{dx} [f_n^2] \quad (D-12)$$

Integration of both sides of Eq. (D-12) yields the following result:

$$\int_{x=a}^b x f_n^2(\lambda x) dx = \frac{1}{2\lambda^2} \left[\left(x \frac{d}{dx} f_n(\lambda x) \right)^2 + \lambda^2 x^2 f_n^2(\lambda x) - n^2 f_n^2(\lambda x) \right]_{x=a}^b \quad (D-13)$$

Another form which is useful in applications follows from use of the identity (valid for any solution to Bessel's equation):

$$x \frac{d}{dx} f_n(\lambda x) = n f_n(\lambda x) - \lambda x f_{n+1}(\lambda x)$$

in Eq. (D-13).

$$\int_{x=a}^b x f_n^2(\lambda x) dx = \left[\frac{x^2}{2} \left(f_n^2(\lambda x) - f_{n+1}(\lambda x) f_{n-1}(\lambda x) \right) \right]_{x=a}^b \quad (D-14a)$$

for $n \neq 0$. When $n=0$, $\frac{d}{dx} f_0(\lambda x) = -\lambda f_1(\lambda x)$ and Eq. (D-13) is reduced to

$$\int_{x=a}^b x f_0^2(\lambda x) dx = \frac{1}{2} \left[x^2 f_1^2(\lambda x) + x^2 f_0^2(\lambda x) \right]_{x=a}^b \quad (D-14b)$$

4. Orthogonality of ϕ_p

The function ϕ_p , commonly found in problems dealing with coaxial geometries, is defined by

$$\phi_p(x) = N_0(\lambda_p a) J_0(\lambda_p x) - J_0(\lambda_p a) N_0(\lambda_p x) \quad (D-15)$$

where a and b are the inner and outer radii, respectively, of the coaxial structure and the eigenvalues λ_p are the roots of

$$J_0(\lambda_p a) N_0(\lambda_p b) - N_0(\lambda_p a) J_0(\lambda_p b) = 0 \quad (D-16)$$

Since $\phi_p(x)$ is a solution to Bessel's equation, one can write from Eq. (D-6)

$$\begin{aligned} (\lambda_p^2 - \lambda_q^2) \int_{x=a}^b x \phi_p(x) \phi_q(x) dx \\ = \left[x \left(\phi_p(x) \frac{d}{dx} \phi_q(x) - \phi_q(x) \frac{d}{dx} \phi_p(x) \right) \right]_{x=a}^b \end{aligned} \quad (D-17)$$

Notice that the right-hand side of Eq. (D-17) is zero at the upper limit because $\phi_p(b)$ and $\phi_q(b)$ are zero due to the conditions that λ_p and λ_q are the appropriate associated roots. At the lower limit, each ϕ_p and ϕ_q is identically zero regardless of the values of the roots. Hence, clearly ϕ_p and ϕ_q are orthogonal.

5. Norm of ϕ_p

From Eq. (D-14b) we see that for (order) $n=0$:

$$\begin{aligned} \int_{x=a}^b x \phi_p^2(x) dx = \\ \frac{1}{2} \left[x^2 \left(N_0(\lambda_p a) J_1(\lambda_p x) - J_0(\lambda_p a) N_1(\lambda_p x) \right)^2 + x^2 \phi_p^2(x) \right]_{x=a}^b \end{aligned}$$

which, because of the boundary conditions on $\phi_p(x)$ at $x = a$ and $x = b$, reduces to

$$\int_{x=a}^b x \phi_p^2(x) dx = \frac{1}{2} \left[x^2 \left(N_0(\lambda_p a) J_1(\lambda_p x) - J_0(\lambda_p a) N_1(\lambda_p x) \right)^2 \right]_{x=a}^b$$

or

$$\begin{aligned} \int_{x=a}^b x \phi_p^2(x) dx &= \frac{1}{2} \left[b^2 \left(N_0(\lambda_p a) J_1(\lambda_p b) - J_0(\lambda_p a) N_1(\lambda_p b) \right)^2 \right. \\ &\quad \left. - a^2 \left(N_0(\lambda_p a) J_1(\lambda_p a) - J_0(\lambda_p a) N_1(\lambda_p a) \right)^2 \right]. \end{aligned}$$

Since the coefficient of a^2 above is in the form of a Wronskian squared, one has

$$\int_{x=a}^b x \phi_p^2(x) dx = \frac{b^2}{2} \left(N_0(\lambda_p a) J_1(\lambda_p b) - J_0(\lambda_p a) N_1(\lambda_p b) \right)^2 - \frac{2}{\pi^2 \lambda_p^2}. \quad (D-18)$$

Another form is

$$N_p^2 = \int_{x=a}^b x \phi_p^2(x) dx = \frac{1}{2} \frac{1}{\lambda_p^2} \left[\left(x \frac{d}{dx} \phi_p(x) \right)^2 \right]_{x=a}^b. \quad (D-19)$$

6. Orthogonality of $\frac{d}{dx} \phi_p(x)$

The eigenfunction $\frac{d}{dx} \phi_p(x)$ is

$$\frac{d}{dx} \phi_p(x) = -\lambda_p [N_0(\lambda_p a) J_1(\lambda_p x) - J_0(\lambda_p a) N_1(\lambda_p x)] \quad (D-20)$$

where the λ_p are the roots of Eq. (D-17). Notice that the boundary conditions on $\frac{d}{dx} \phi_p(x)$ are given by

$$\frac{d}{dx} \left(x \phi_p \right) = 0 \quad \text{at } x = a, b \quad (\text{D-21})$$

and

$$\frac{1}{x} \frac{d}{dx} \left(x \frac{d\phi_p}{dx} \right) + \left(\lambda_p^2 - \frac{1}{x} \right) \phi_p = 0, \quad (\text{D-22})$$

from which it may be concluded that

$$x \left\{ \frac{d}{dx} \left(\frac{d}{dx} \phi_p(x) \right) \right\} + \frac{d}{dx} \phi_p(x) = 0 \quad \text{at } x = a, b. \quad (\text{D-23})$$

Hence, the procedure leading to Eq. (D-9) ensures the orthogonality of $\frac{d}{dx} \phi_p(x)$.

If one considers the zero eigenvalue equation and the corresponding eigenfunction, $\frac{1}{x}$, the orthogonality of $\frac{1}{x}$ and $\frac{d}{dx} \phi_p(x)$, subject to the weight function x , can be demonstrated by writing

$$\int_{x=a}^b x \left(\frac{1}{x} \right) \left(\frac{d}{dx} \phi_p(x) \right) dx = \phi_p(b) - \phi_p(a) \quad (\text{D-24})$$

which reduces to, in view of the boundary conditions,

$$\begin{aligned} \int_{x=a}^b x \left(\frac{d}{dx} \phi_p(x) \right)^2 dx &= \frac{x^2}{2} \left(\frac{d}{dx} \phi_p(x) \right)^2 \Big|_{x=a}^b \\ &= \lambda_p^2 \left[\frac{x^2}{2} [N_0(\lambda_p a) J_1(\lambda_p x) - J_0(\lambda_p a) N_1(\lambda_p x)]^2 \right]_{x=a}^b. \end{aligned} \quad (\text{D-25})$$

7. Norm of $\frac{1}{x}$

The eigenfunction corresponding to the zero eigenvalue has the following norm, with respect to the weight function x ,

$$\int_{x=a}^b x \left(\frac{1}{x} \right)^2 dx = \ln \frac{b}{a} . \quad (D-26)$$

8. Summary

For convenience, the orthogonality properties and norms developed in this Appendix are summarized below.

Orthogonality

$$\int_{x=a}^b x \phi_p(x) \phi_q(x) dx = 0 , \quad p \neq q \quad (D-27)$$

$$\int_{x=a}^b x \left(\frac{d}{dx} \phi_p(x) \right) \left(\frac{d}{dx} \phi_q(x) \right) dx = 0 , \quad p \neq q \quad (D-28)$$

$$\int_{x=a}^b x \left(\frac{d}{dx} \phi_p(x) \right) \left(\frac{1}{x} \right) dx = 0 , \quad \lambda_p^2 \neq 0 \quad (D-29)$$

Norms

$$\begin{aligned} N_p^2 &= \int_{x=a}^b x \phi_p^2(x) dx = \frac{b^2}{2\lambda_p^2} \left(\frac{d}{dx} \phi_p(x) \right)^2 - \frac{2}{\pi^2 \lambda_p^2} \\ &= \frac{b^2}{2} \left[N_0(\lambda_p a) J_1(\lambda_p b) - J_0(\lambda_p a) N_1(\lambda_p b) \right]^2 - \frac{2}{\pi^2 \lambda_p^2} \end{aligned} \quad (D-30)$$

$$\begin{aligned}
M_p^2 &= \int_{x=a}^b x \left(\frac{d}{dx} \phi_p(x) \right)^2 dx = \frac{b^2}{2} \left(\frac{d}{dx} \phi_p(x) \right)^2 - \frac{2}{\pi^2} \\
&= \frac{b^2 \lambda_p^2}{2} \left(N_0(\lambda_p a) J_1(\lambda_p b) - J_0(\lambda_p a) N_1(\lambda_p b) \right)^2 - \frac{2}{\pi^2} \quad (D-31)
\end{aligned}$$

$$\int_{x=a}^b x \left(\frac{1}{x} \right)^2 dx = \ln \frac{b}{a} \quad (D-32)$$

APPENDIX E

DETAILS OF COAXIAL CAVITY CONSTRUCTION

1. Introduction

Two sets of coaxial cavity structures were fabricated in order to perform the experimental investigations described in Chapters VII and VIII. The two sets of cavities are functionally quite similar but differ greatly in construction detail and materials. The primary reason for this difference is that one set is almost twice the diameter of the other and the smaller set was constructed from the largest, cylindrical, brass pipe available. Each set consists of two cavity (waveguide) sections having identical cross sections, but different lengths, plus interchangeable end plates which give the cavities one- or two-port characteristics. In addition, each set includes two very thin partitions with centered, circular apertures (of different sizes) which are used to divide the cavities into multiple sections. All cavity components are made of brass in order to achieve boundary conditions of high electrical conductivity. Following are short physical descriptions of each set of cavities and appropriate construction details.

2. Smaller Coaxial Cavity

The geometry and dimensions of the smaller of the two sets of coaxial cavities are given in Figure E-1 and Table E-1. The cavity sections were cut from a section of approximately eight inch inner diameter, red brass pipe and were bored on a lathe to their final inner diameters after the 1/4 inch thick flanges were soldered on each end. As indicated in Table E-1, the shorter cavity section required a slightly larger bore to achieve a circular cross section which left it 0.04 cm larger in inner diameter than the other section. In order to position the inner conductor as near to perfect center as possible, the end plates and cavity sections were aligned by inserting steel pins through precisely positioned holes drilled in flanges and the end plates. After insertion of the pins, nuts and bolts were used to securely fasten the adjacent parts together. Use of the available pieces allowed four different cavity configurations to be realized:

1. One-section, one-port cavity
2. One-section, two-port cavity
3. Two-section, one-port cavity
4. Two-section, two-port cavity

It should be noted that configurations 3 and 4 have the options of no partition between the sections or a partition with

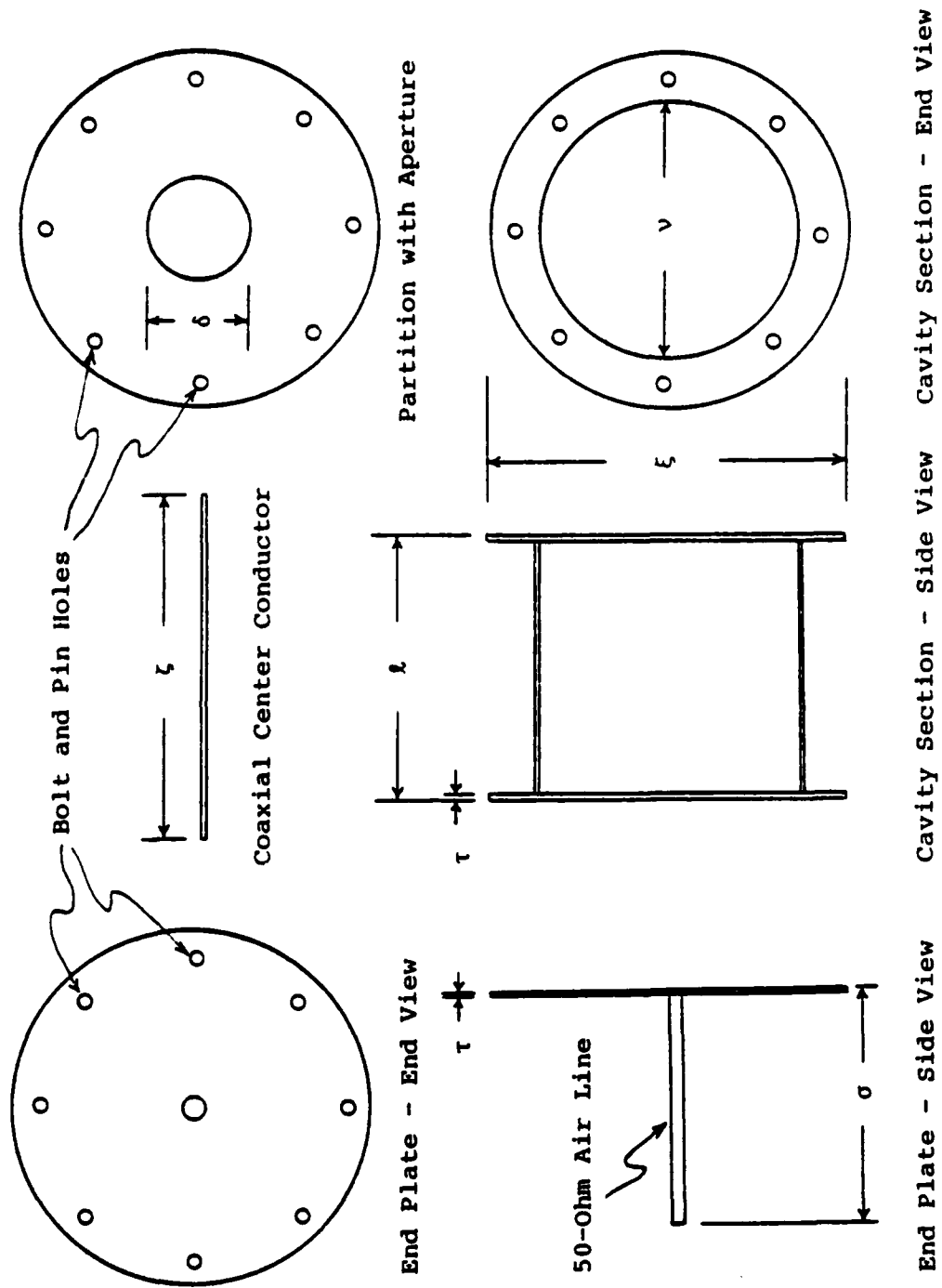


Figure E-1. Illustration of Components of Smaller Coaxial Cavity Set

TABLE E-1. DIMENSIONS OF COMPONENTS OF SMALLER SET OF CAVITIES

Cavity Component	l [cm]	ξ [cm]	v [cm]	δ [cm]	σ [cm]	τ [cm]	ζ [cm]
Long Cavity Section	15.095	30.48	21.232			0.635	
Short Cavity Section	8.637	30.48	21.273			0.635	
Front End Plate		29.84			11.684	0.318	
Rear End Plate		29.84			13.472	0.318	
Partition with Large Aperture		29.80		8.006		0.051	
Partition with Small Aperture		29.80		2.540		0.051	
One-Port Rod							26.799
Two-Port Rod							40.300
Rod Used with Partition							48.939

TABLE E-2. COMPARISONS OF ADMITTANCES OF TRANSMISSION LINES WITH DIFFERENT RODS FOR COAXIAL CENTER CONDUCTOR

Transmission Line Section	OD of Inner Conductor [cm]	ID of Outer Conductor [cm]	Admittance [mhos]
GenRad 50-Ohm Feed Line			
GenRad Center Rod	0.6205	1.428	0.020000
Nominal $\frac{1}{4}$ -inch Rod	0.6350	1.428	0.020565
$\frac{1}{4}$ -inch Rod - 0.005"	0.6223	1.428	0.020065
$\frac{1}{4}$ -inch Rod + 0.005"	0.6477	1.428	0.021080
Long Cavity Section			
GenRad Center Rod	0.6205	21.232	0.004718
Nominal $\frac{1}{4}$ -inch Rod	0.6350	21.232	0.004749
$\frac{1}{4}$ -inch Rod - 0.005"	0.6223	21.232	0.004722
$\frac{1}{4}$ -inch Rod + 0.005"	0.6477	21.232	0.004770
Short Cavity Section			
GenRad Center Rod	0.6205	21.273	0.004715
Nominal $\frac{1}{4}$ -inch Rod	0.6350	21.273	0.004746
$\frac{1}{4}$ -inch Rod - 0.005"	0.6223	21.273	0.004719
$\frac{1}{4}$ -inch Rod + 0.005"	0.6477	21.273	0.004773

one of two aperture sizes. Thus, there are eight possible cavity variations available from the four basic configurations.

The coaxial outer conductors which were soldered to the end plates to form feed lines to the cavity are GenRad Type 874, 50-ohm, air line sections. The companion, 50-ohm inner conductors were used for cavity configurations 1 and 2. These rods have a diameter of 0.6205 cm (0.2443 inches). The inner conductors of the two-section cavities were constructed of circular, brass rod with a diameter of 0.635 ± 0.013 cm (0.250 ± 0.005 inches). The possible variations in the characteristic impedances of the feed lines and the cavity sections is presented in Table E-2. This change in inner conductor diameter is included in the appropriate calculations. The only impact would be in matching the 50-ohm load for the two-port cavity configuration. Comparisons of measured and calculated results for these cases show no effects.

In order to allow the insertion and movement of probes designed to sample the field inside the cavity, radial slots, 0.3175 cm (1/8 inch) wide, were cut in each of the end plates. These slots were designed to be parallel to the direction of current flow on the end plates and, thus, provide minimum disturbance to the field within the cavity. The orientation of the slots also served to inhibit the excitation of any higher-order modes which might be associated with ϕ -directed currents.

The use of the brass pipe, the 1/4 inch brass flanges, and the 1/8 inch brass end plates made these cavity configurations very durable and heavy. It was possible to tighten the flange bolts very firmly in order to enhance electrical conductivity at the interfaces. The excellent agreement between measured and calculated field and admittance values for the smaller cavities demonstrates that the cavities contain no electrical abnormalities. Photographs of cavity components are presented in Figure E-2.

3. Larger Coaxial Cavity

The geometry and dimensions of the larger set of coaxial cavities are given in Figure E-3 and Table E-3. The cavity sections were formed from 0.005 cm (0.020 inch) thick brass sheets which were rolled into circular cylinders and soldered to 1/8 inch thick brass flanges which serve to hold the cylinders in shape. The axial seams where the sheet brass ends join were filled with solder and sanded smooth. Because both cavity sections were constructed simultaneously, the inner diameter (average of four measurements) of one section agrees to within 0.1 cm of the other. The cavity sections and end plates are joined by the use of alignment pins and bolts passing through holes in the flanges as was done for the smaller set of cavities. The inner conductor was constructed from a 3.195 cm (1.258 inch) diameter brass pipe. The outer conduc-

tor of the feed-line section was constructed from a 10.424 cm (4.104 inch) inner diameter, brass pipe.

The feed point on the feed line was a GenRad 50-ohm connector mounted on the sedi of the outer conductor with the center pin of the connector extending down to the inner conductor of the feed line. The end of the feed line not attached to the cavity was blocked off with a moveable aluminum plug which served as a shorting plate. Because of the difficulty of fabricating a matched load for the non-standard coaxial line, only one-port versions of the large cavities were constructed. This resulted in two possible cavity configurations:

1. One-section, one-port cavity
2. Two-section, one-port cavity

Two partitions with different aperture sizes were constructed for use with the two-section cavity. The relevant dimensions of the larger cavity set are given in Table E-3 and admittances of different waveguide segments are given in Table E-4.

Slots for field probe insertion were cut into the cavity end plates as was done for the smaller cavity set. In addition, an axial slot was cut in the inner conductor to allow sampling of the interior field along the axial coordinate. This slot extended well into the feed-line section and would serve quite well for a slotted line for admittance measurements. The extremely large standing wave ratios caused by

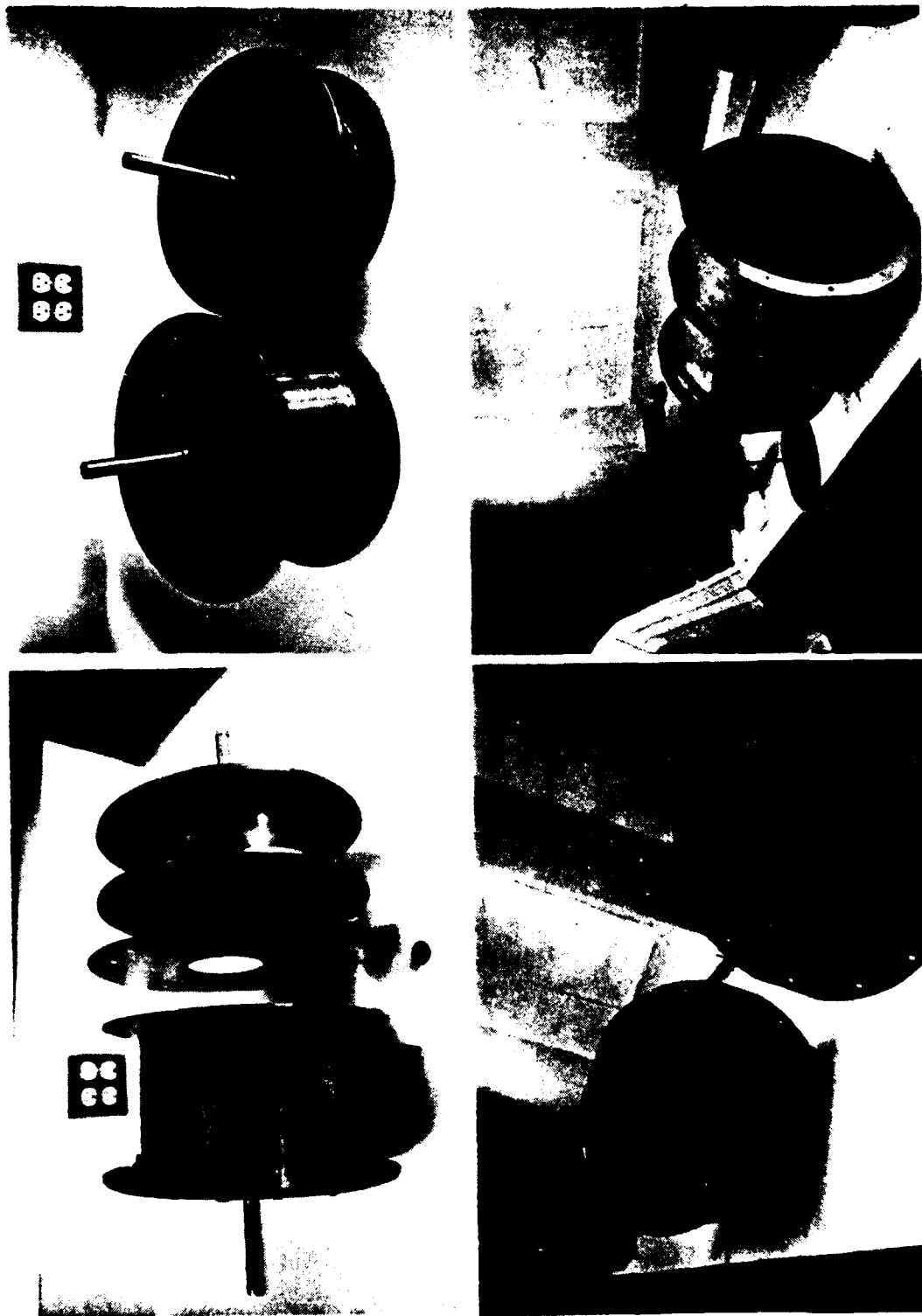


Figure E-2. Photographs of Small and Large Cavity Sets

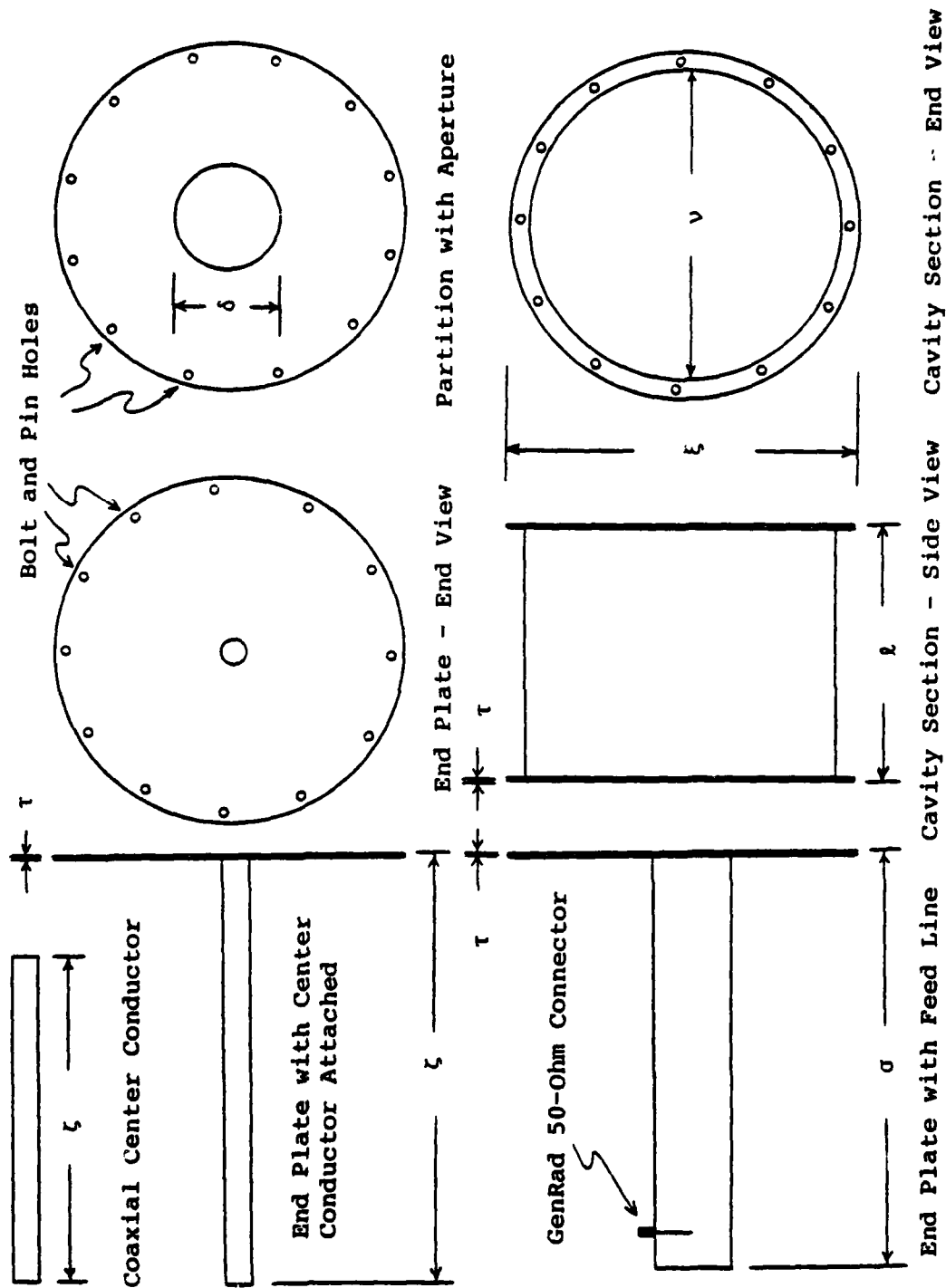


Figure E-3. Illustration of Components of Larger Cavity Set

TABLE E-3. DIMENSIONS OF COMPONENTS OF LARGER SET OF CAVITIES

Cavity Component	l [cm]	ξ [cm]	v [cm]	δ [cm]	σ [cm]	τ [cm]	ζ [cm]
Long Cavity Section	27.318	41.28	35.631			0.159	
Short Cavity Section	18.459	41.28	35.551			0.159	
End Plate with Inner Conductor		41.28			177.01	0.159	
End Plate with Outer Conductor		41.28			105.41	0.159	
Partition with Large Aperture		41.00		14.813		0.051	
Partition with Small Aperture		41.00		5.121		0.051	
Truncated Coaxial Center Conductor							174.31

TABLE E-4. ADMITTANCE OF EACH SECTION OF LARGER SET OF CAVITIES

Transmission Line Section	OD of Inner Conductor [cm]	ID of Outer Conductor [cm]	Admittance [mhos]
Feed Line Section	3.195	10.424	0.014094
Long Cavity Section	3.195	35.631	0.006911
Short Cavity Section	3.195	35.551	0.006917

the one-port cavity configuration made such measurements impractical.

There was some difficulty in obtaining extremely tight interfaces between the equally-spaced bolts which hold the flanges together. During the measurements, C-clamps were used to tighten these joints although tests made at several frequencies did not show any significant effect due to adding the clamps. The agreement between measured and calculated results on the end plates of the larger cavities, while generally good to very good, did not attain the almost complete consistency of the end-plate measurements for the smaller cavity set. The greater difficulty in obtaining very tight flange junctions is one likely cause for such disagreements. The very good agreement between measured and calculated data at the surface of the coaxial inner conductor of the large cavity contributes strong support to the idea that the impedance mismatch of the one-port cavities makes it extremely difficult to couple sufficient energy into the cavity to perform accurate measurements.

APPENDIX F

DESCRIPTIONS OF ELECTRIC AND MAGNETIC FIELD PROBES

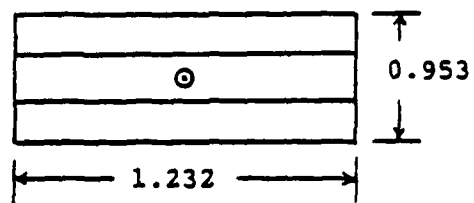
1. Introduction

Two types of probes were fabricated in order to sample the interior field of the coaxial cavities. The electric field or "charge" probe consists of a short, thin electrical conductor (in this case, the inner conductor of a short piece of 0.035 inch semi-rigid coaxial cable) which is oriented normal to the perfectly-conducting wall of the cavity. The normal component of the electric field induces a small current on the conductor which, in turn, creates a potential difference between the conductor and the cavity wall which is detectable by a network analyzer operating in a vector voltmeter mode. The magnetic field or "current" probe is composed of a semi-circular loop of 0.035 inch coax with the outer conductor grounded to the probe transport at both ends. A short section of the outer conductor is cut away at the center of the loop to expose a short piece of the inner conductor. The component of magnetic field tangential to the cavity wall induces a current on the loop and, in turn, creates a potential difference between the outer and inner conductors of the coaxial loop. This potential difference is again detected by a network ana-

lyzer. The basic probe designs have been in use by Professor R. W. P. King and others for many years. The rest of this appendix describes the particular probe transport designs used for the end plates and the center conductor of the cavities.

2. End-Plate Probes

Front and side views of the electric and magnetic field probes used to sample the cavity field at the inner surface of the cavity end plates are presented in Figure F-1. The probes are mounted on brass transports which have a T-shaped cross section for insertion into and sliding back and forth in a $1/8$ inch (0.3175 cm) wide slot. The bottoms of the probe transports are designed to be flush with the inside surface of the end plates. Good electrical contact between the probe transport and the cavity end plate is very important in order to obtain a valid reading from the network analyzer. It is also important that the probe transport slide easily in the slot to facilitate making measurements. These two contradicting requirements add an element of art to the science of probe manufacture and use. Adequate pressure on the top of the probe transport during measurements can ensure a good electrical contact with the cavity end plate. It is important that the bottom of the probe transport be flush with the inner surface of the end plate in order that the probe see no sharp corners or other discontinuities in its neighborhood.



All dimensions
are in centimeters

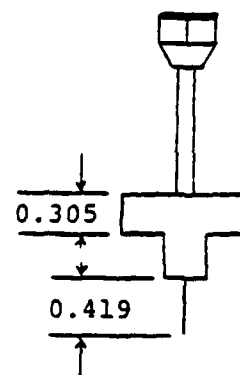
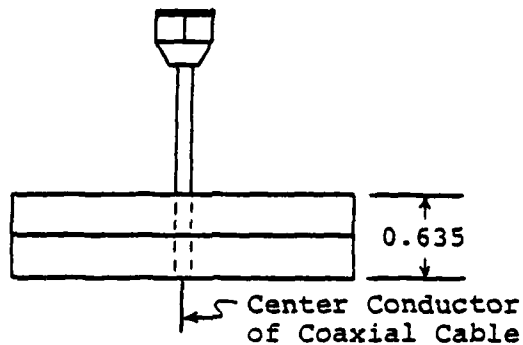
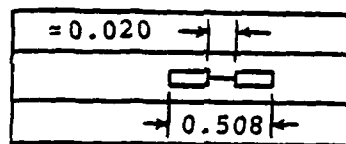


Figure F-1a. Orthogonal Views of Electric Field Probe for End Plates



Brass Probe Transport

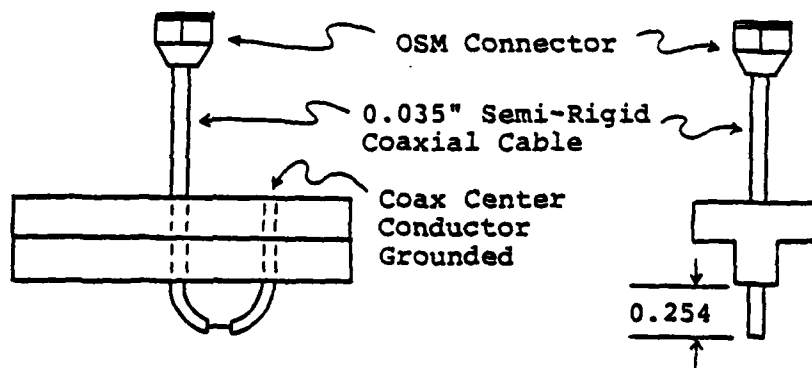


Figure F-1b. Orthogonal Views of Magnetic Field Probe for End Plates

Since the end plates on the small cavities are 1/8 inch thick and those of the large cavities are 1/16 inch thick, a small, flat, 1/16 inch thick clip is used to adjust the depth of the probe transport to the thickness of the thinner end plates. A photograph of the two probes (with a quarter for size comparison) is shown in Figure F-2.

3. Center Conductor Probes

Drawings of the electric and magnetic field probes used to sample the cavity field at the outer surface of the coaxial inner conductor are presented in Figure F-3. The probes are mounted on 1/8 inch-thick, brass guides which are in turn mounted on thin, brass plates. The plates have been contoured to fit the outside of a brass, cylindrical probe transport and make a snug fit with the inner surface of the brass pipe which forms the coaxial center conductor. The thin plates are secured to the sides of the cylindrical probe transports by miniature screws. The coaxial lead from each probe passes into a hole in the side of the cylinder and emerges from the hole at one of the flat ends. The probe transport slides easily inside the brass pipe because of thick, Teflon disks which are fastened to each end of the brass cylinder. The disks are slightly larger than the cylinders and make the sliding contact with the inner walls of the pipe. The thin brass plates make the primary electrical contact with the brass pipe. The

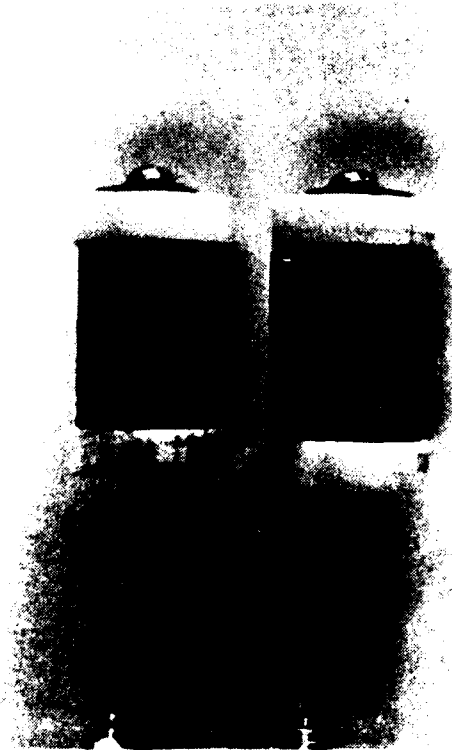
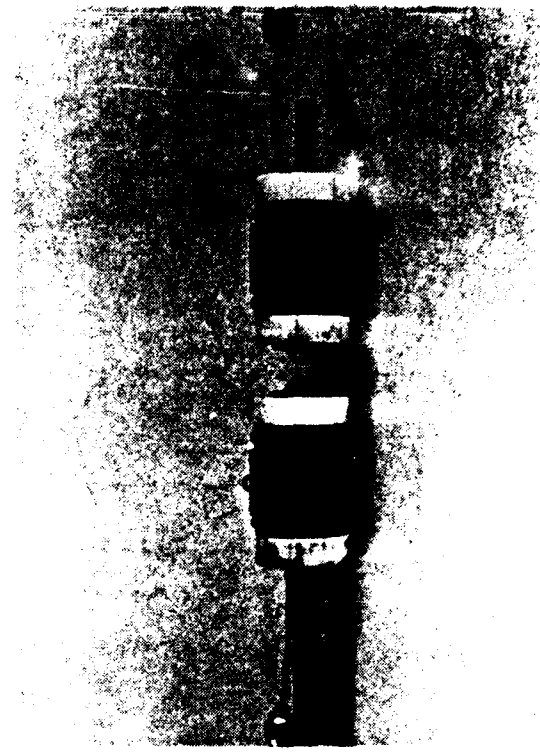


Figure F-2. Photographs of Electric and Magnetic Field Probes

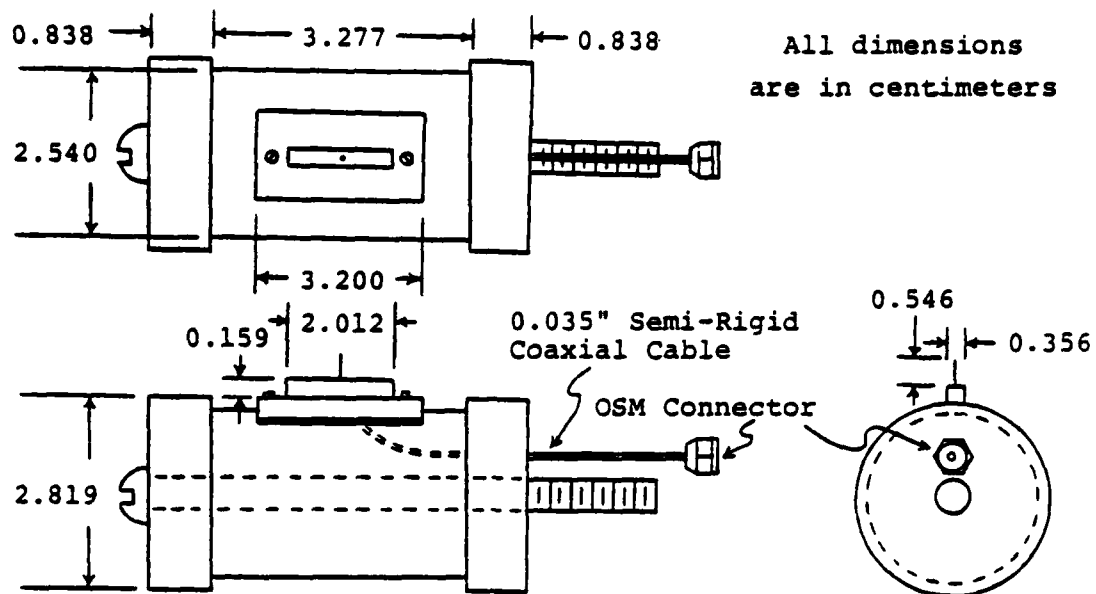


Figure F-3a. Orthogonal Views of Electric Field Probe for Coaxial Center Conductor

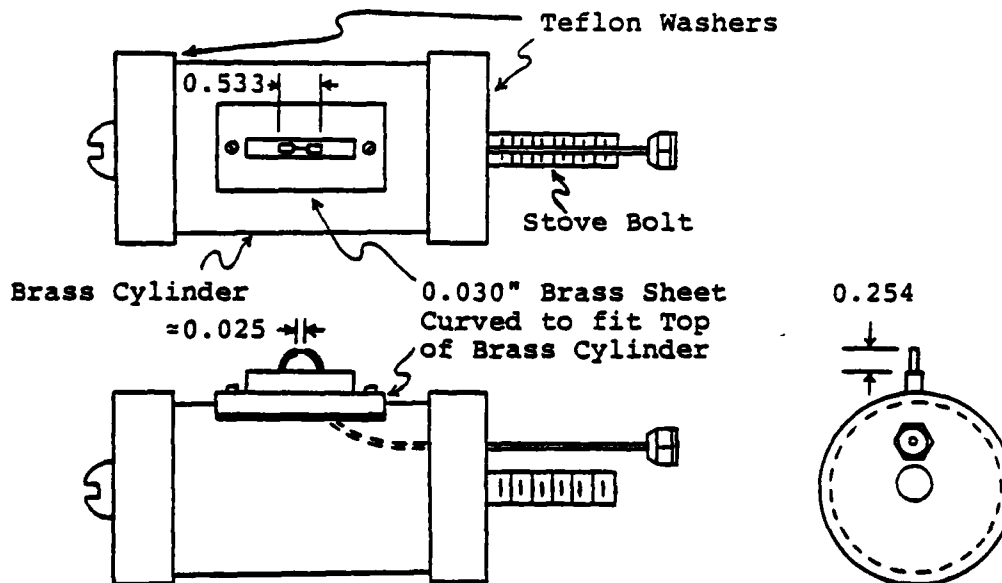


Figure F-3b. Orthogonal Views of Magnetic Field Probe for Coaxial Center Conductor

tops of the brass guides are designed to be flush with the outer surface of the brass pipe.

The probe transports are positioned by moving a long, thin, brass tube whose end has been threaded to receive a bolt which passes through the center of the brass cylinder. The flexible probe lead enters a hole in the side of the thin tube (just behind the threaded section), passes through the inside of the tube, and exits at the far end of the tube. A marker was placed near the far end of the tube for use in recording the position of the probe inside the cavity. Two photographs of the magnetic and electric field probes are presented in Figure F-2.

BIBLIOGRAPHY

- [1] N. Marcuvitz, Editor, Waveguide Handbook. New York: McGraw-Hill, 1950; Reprinted, New York: Dover, 1965.
- [2] J. S. Schwinger and D. S. Saxon, Discontinuities in Waveguides. New York: Gordon and Breach, 1968.
- [3] R. E. Collin, Field Theory of Guided Waves. New York: McGraw-Hill, 1960.
- [4] L. Lewin, Advanced Theory of Waveguides. London: Iliffe & Sons, 1951.
- [5] L. Lewin, "On the Resolution of a Class of Waveguide Discontinuity Problems by the Use of Singular Integral Equations," IRE Transactions on Microwave Theory and Techniques, Vol. MTT-9, pp. 321-332, July 1961.
- [6] L. Lewin, Theory of Waveguides. New York: Wiley, 1968.
- [7] J. R. Whinnery and H. W. Jamieson, "Equivalent Circuits for Discontinuities in Transmission Lines," Proceedings of the IRE, Vol. 32, pp. 98-115, February 1944.
- [8] J. R. Whinnery, H. W. Jamieson, and T. E. Robbins, "Coaxial Line Discontinuities," Proceedings of the IRE, Vol. 32, pp. 695-709, November 1944.
- [9] R. F. Harrington, Field Computation by Moment Methods. New York: McMillan, 1968.
- [10] P. I. Somlo, "The Discontinuity Capacitance and the Effective Position of a Shielded Open Circuit in a Coaxial Line," Proceedings of the IRE (Australia), Vol. 28, pp. 7-9, January 1967.
- [11] P. I. Somlo, "The Computation of Coaxial Line Step Discontinuities," IEEE Transactions on Microwave Theory and Techniques, Vol. MTT-15, pp. 48-52, January 1967.

- [12] D. Woods, "Shielded-Open-Circuit Discontinuity Capacitance of a Coaxial Line," Proceedings of the Institution of Electrical Engineers, Vol. 119, pp. 1691-1692, December 1972.
- [13] A. Jurkus, "Computation of Step Discontinuities in Coaxial Line," IEEE Transactions on Microwave Theory and Techniques, Vol. MTT-20, pp. 708-709, October 1972.
- [14] E. W. Risley, "Discontinuity Capacitance of a Coaxial Line Terminated in a Circular Waveguide," IEEE Transactions on Microwave Theory and Techniques, Vol. MTT-17, pp. 86-92, February 1969.
- [15] E. W. Risley, "Discontinuity Capacitance of a Coaxial Line Terminated in a Circular Waveguide: Part II--Lower Bound Solution," IEEE Transactions on Microwave Theory and Techniques, Vol. MTT-21, pp. 564-566, August 1973.
- [16] J. B. Davies, "A Least-Squares Boundary Residual Method for the Numerical Solution of Scattering Problems," IEEE Transactions on Microwave Theory and Techniques, Vol. MTT-21, pp. 99-104, February 1973.
- [17] M. Razaz and J. B. Davies, "Admittance of a Coaxial-to-Circular Waveguide Junction," Electronics Letters, Vol. 10, pp. 324-326, July 1974.
- [18] H. Oraizi and J. Perini, "A Numerical Method for the Solution of the Junction of Cylindrical Waveguides," IEEE Transactions on Microwave Theory and Techniques, Vol. MTT-21, pp. 640-642, September 1973.
- [19] R. Jansen, "On the Performance of the Least-Squares Method for Waveguide Junctions and Discontinuities," IEEE Transactions on Microwave Theory and Techniques, Vol. MTT-23, pp. 434-436,
- [20] H. J. A. LaRiviere and J. B. Davies, "The Solution of Electromagnetic Eigenvalue Problems by Least-Squares Boundary Residuals," IEEE Transactions on Microwave Theory and Techniques, Vol. MTT-23, pp. 436-441,
- [21] M. Razaz and J. B. Davies, "Capacitance of the Abrupt Transition from Coaxial-to-Circular Waveguide," IEEE Transactions on Microwave Theory and Techniques, Vol. MTT-27, June 1979.

- [22] A. Wexler, "Solution of Waveguide Discontinuities by Modal Analysis," IEEE Transactions on Microwave Theory and Techniques, Vol. MTT-15, pp. 508-517, September 1967.
- [23] C. M. Butler, "Introduction to Moment Methods with Simple Applications," chapter in Theoretical Methods for Determining the Interaction of Electromagnetic Waves with Structures, to be published subsequent to a short course of the same name at the NATO Advanced Study Institute, University of East Anglia, Norwich, England, July-August 1979.
- [24] C. M. Butler, Private Communication, 1979.
- [25] E. L. Ginzton, Microwave Measurements. New York: McGraw-Hill, 1957.
- [26] L. B. W. Jolley, Summation of Series. New York: Dover, 1961.

